IceCube Preliminary Design Document

October 11, 2001/ Revision: 1.24

The IceCube Collaboration

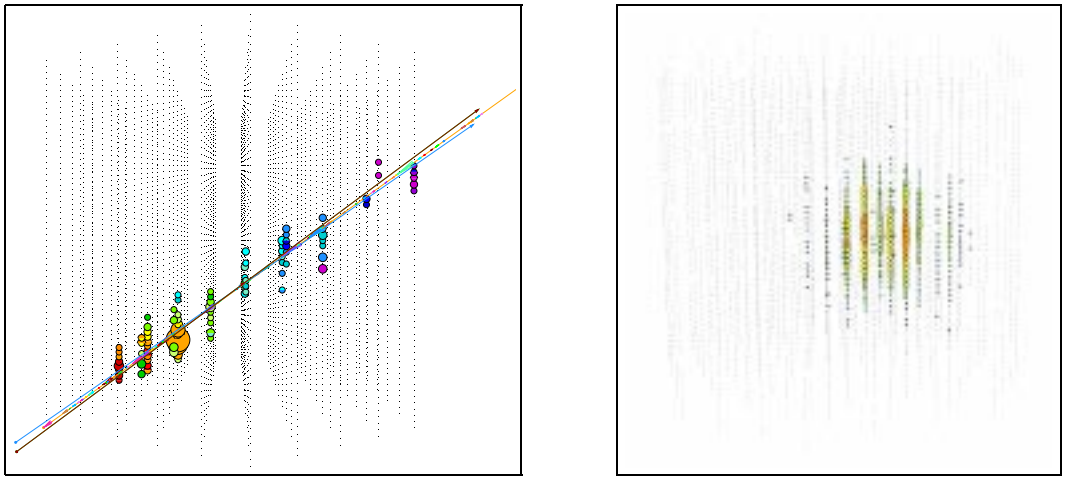

Simulated interactions of a 10 TeV ν_μ (top left), 375 TeV ν_e (top right), and 1 PeV ν_τ (bottom) in IceCube.

The IceCube Collaboration

J. Ahrens[12], J.R. Alonso[8], J.N. Bahcall[6], X. Bai[1], T. Becka[12], K.-H. Becker[2], D. Berley[13], D. Bertrand[3], D.Z. Besson, A. Biron[5], B. Bless[16], S. Böser[5], C. Bohm[21], O. Botner[20], A. Bouchta[5,23], S. Carius[7], J. Cavin[18], A. Chen[17], W. Chinowsky[8], D. Chirkin[10,2], J. Conrad[20], J. Cooley[17], C.G.S. Costa[3], D.F. Cowen[15], C. De Clercq[22], T. DeYoung[17], P. Desiati[5], J.-P. Dewulf[3], B. Dingus[17], P. Doksus[17], P.A. Evenson[1], A.R. Fazely[9], T. Feser[12], J.-M. Frère[3], T.K. Gaisser[1], J. Gallagher[16], M. Gaug[5], A. Goldschmidt[8], A. Hallgren[20], F. Halzen[17], K. Hanson[15], R. Hardtke[17], T. Hauschildt[5], M. Hellwig[12], P. Herquet[14], G.C. Hill[17], P.O. Hulth[21], K. Hultqvist[21], S. Hundertmark[11], J. Jacobsen[8], G.S. Japaridze[4], A. Karle[17], R. Koch[18], L. Köpke[12], M. Kowalski[5], J.I. Lamoureux[8], H. Leich[5], M. Leuthold[5], P. Lindahl[7], J. Madsen[19], P. Marciniewski[20], H.S. Matis[8], C.P. McParland[8], P. Miočinović[10], R. Morse[17], T. Neunhöffer[12], P. Niessen[5,22], D.R. Nygren[8], H. Ogelman[17], Ph. Olbrechts[22], R. Paulos[17], C. Pérez de los Heros[20], P.B. Price[10], G.T. Przybylski[8], K. Rawlins[17], W. Rhode[2], M. Ribordy[5], S. Richter[17], H.-G. Sander[12], T. Schmidt[5], D. Schneider[17], D. Seckel[1], M. Solarz[10], L. Sparke[16], G.M. Spiczak[1], C. Spiering[5], T. Stanev[1], D. Steele[17], P. Steffen[5], R.G. Stokstad[8], O. Streicher[5], P. Sudhoff[5], K.-H. Sulanke[5], I. Taboada[15], C. Walck[21], C. Weinheimer[12], C.H. Wiebusch[5,23], R. Wischnewski[5], H. Wissing[5], K. Woschnagg[10]

(1) Bartol Research Institute, University of Delaware, Newark, DE 19716, USA
(2) Fachbereich 8 Physik, BUGH Wuppertal, D-42097 Wuppertal, Germany
(3) Université Libre de Bruxelles, Science Faculty CP230, Boulevard du Triomphe, B-1050 Brussels, Belgium
(4) CTSPS, Clark-Atlanta University, Atlanta, GA 30314, USA
(5) DESY-Zeuthen, D-15735 Zeuthen, Germany
(6) Institute for Advanced Study, Princeton, NJ 08540, USA
(7) Dept. of Technology, Kalmar University, S-39182 Kalmar, Sweden
(8) Lawrence Berkeley National Laboratory, Berkeley, CA 94720, USA
(9) Department of Physics, Southern University and A&M College, Baton Rouge, LA 70813, USA
(10) Dept. of Physics, University of California, Berkeley, CA 94720, USA
(11) Dept. of Physics and Astronomy, University of California, Irvine, CA 92697, USA
(12) Institute of Physics, University of Mainz, Staudinger Weg 7, D-55099 Mainz, Germany
(13) Dept. of Physics, University of Maryland, College Park, MD 20742, USA
(14) University of Mons-Hainaut, 7000 Mons, Belgium
(15) Dept. of Physics and Astronomy, University of Pennsylvania, Philadelphia, PA 19104, USA
(16) Dept. of Astronomy, University of Wisconsin, Madison, WI 53706, USA
(17) Dept. of Physics, University of Wisconsin, Madison, WI 53706, USA
(18) SSEC, University of Wisconsin, Madison, WI 53706, USA
(19) Physics Department, University of Wisconsin, River Falls, WI 54022, USA
(20) Division of High Energy Physics, Uppsala University, S-75121 Uppsala, Sweden
(21) Fysikum, Stockholm University, S-11385 Stockholm, Sweden
(22) Vrije Universiteit Brussel, Dienst ELEM, B-1050 Brussel, Belgium
(23) Present address: CERN, CH-1211, Genève 23, Switzerland

Contents

Contacts/Authors of this Document

Section 1:	D. Cowen (Penn)
Section 2:	T. Gaisser (Bartol), F. Halzen (UW-Madison)
Section 3:	T. Gaisser (Bartol), F. Halzen (UW-Madison)
Section 4:	T. Gaisser (Bartol)
Section 5:	D. Cowen (Penn), K. Hanson (Penn), G. Hill (UW-Madison), A. Karle (UW-Madison)
Section 6:	C. Spiering (DESY)
Section 7:	J. Jacobsen (LBNL), A. Karle (UW-Madison), C. McParland (LBNL), D. Nygren (LBNL)
Section 8:	D. Cowen (Penn), P. Herquet (Mons), J. Lamoureux (LBNL), C. McParland (LBNL), D. Schneider (UW-Madison)
Section 9:	P.O. Hulth (Stockholm)
Section 10:	A. Karle (UW-Madison), B. Morse (UW-Madison)
Section 11:	E. Richards (UW-Madison)
Section 12:	P.O. Hulth (Stockholm)

1 Document Overview

This document describes a conceptual design for the proposed IceCube Neutrino Observatory at the South Pole. An Executive Summary is provided in section 2. Section 3 gives the scientific motivation for constructing a kilometer-scale device optimized for detection of cosmological neutrinos with ultrahigh energies in the TeV to PeV range. Section 4 briefly reviews the current status of the field of neutrino astronomy, and section 5 details the expected performance of the IceCube neutrino telescope, with emphasis on the scientific goals outlined in section 3.

Most of the remainder of the document focuses on technical aspects of the IceCube detector. Section 6 lists the technical requirements the IceCube detector must meet in order to attain the desired scientific goals, and section 7 gives a complete conceptual description of the IceCube detector itself. Section 8 describes how the data produced by this detector will be processed and made available for high-level analysis, and section 9 shows how the collaboration will organize itself to perform these analyses.

An explanation of how drilling, deployment and the associated logistics will be handled is given in section 10. Section 11 describes what quality assurance procedures will be implemented to ensure initial and continued success in deployment, data acquisition and data processing. Finally, section 12 shows how the AMANDA and IceCube detectors will be integrated to maximize the overall science output.

This and other documents are on the Web at http://www.ssec.wisc.edu/a3ri/icecube/.

2 Executive Summary

The IceCube Project at the South Pole is a logical extension of the research and development work performed over the past several years by the AMANDA Collaboration. The optical properties of ice deep below the Pole have been established, and the detection of high-energy neutrinos has been demonstrated with the existing detector. This accomplishment represents a proof of concept for commissioning a new instrument, IceCube, with superior detector performance and an effective telescope size at or above the kilometer-scale.

IceCube scientific goals require that the detector have an effective area for muons generated by cosmic neutrinos of one square kilometer. The detector will utilize South Pole ice instrumented at depth with optical sensors that detect the Cherenkov light from secondary particles produced in interactions of high-energy neutrinos inside or near the instrumented volume.

The design for the IceCube neutrino telescope is an array of 4800 photomultiplier tubes (PMTs) each enclosed in a transparent pressure sphere to comprise an optical module (OM) similar to those in AMANDA. In the IceCube design, 80 strings are regularly spaced by 125 m over an area of approximately one square kilometer, with OMs at depths of 1.4 to 2.4 km below the surface. Each string consists of OMs connected electrically and mechanically to a long cable, which brings OM signals to the surface. The array is deployed one string at a time. For each string, a hot-water drill creates a hole in the ice to a depth of about 2.4 km. The drill is then removed from the hole and a string with 60 OMs spaced by 17 m is deployed before the water freezes. The signal cables from all the strings are brought to a central location, which houses the data acquisition electronics, other electronics, and computing equipment.

Each OM contains a PMT that detects individual photons of Cherenkov light generated in the optically clear ice by muons and electrons moving with velocities near the speed of light. Signal events consist primarily of upgoing muons produced in neutrino interactions in the bedrock or the ice. In addition, the detector can discriminate electromagnetic and hadronic showers ("cascades") from interactions of ν_e and ν_τ inside the detector volume provided they are sufficiently energetic (a few 100 TeV or higher). Background events are mainly downward-going muons from cosmic ray interactions in the atmosphere above the detector. The background is monitored for calibration purposes by the IceTop air shower array covering the detector.

Signals from the optical modules are digitized and transmitted to the surface such that a photon's time of arrival at an OM can be determined to within a few nanoseconds. The electronics at the surface determines when an event has occurred (e.g., that a muon traversed or passed near the array) and records the information for subsequent event reconstruction and analysis.

At the South Pole site (see fig. 1), a computer system accepts the data from the event trigger through the data acquisition system. The event rate, which is dominated by down-going cosmic ray muons, is estimated to be 1–2 kHz. This will produce a large amount of data and requires filtering and compression of this data stream at the South Pole. There are two ways for the data to be transported to the Northern Hemisphere. The first and preferred method is via satellite transmission. The second method is by hand-carrying the data tapes north once the station reopens in the austral summer. Even in this case, a reduced set of data must be

transferred daily by satellite to monitor the detector and to access important data. Once at the data archive, the data are catalogued, unpacked, checked, filtered, and calibrated. Interesting events are reconstructed and distributed to the collaboration for scientific analysis.

The technology that will be employed in IceCube has been developed, tested, and demonstrated in AMANDA deployments, in laboratory testing, and in simulations. This includes the instrument architecture, technology, deployment, calibration, and scientific utilization of the proposed detector. There have been yearly improvements in the AMANDA system, especially in the OMs, and in the overall quality of the information obtained from the detector. In the 1999/2000 season, a string was deployed with optical modules containing readout electronics inside the module. The information is sent digitally to the surface over twisted-pair electrical cable. This option eliminates the need for optical fiber cables and simplifies calibration of the detector elements. This digital technology is the baseline technology of IceCube.

For more details and references, see `http://www.ssec.wisc.edu/a3ri/icecube/`.

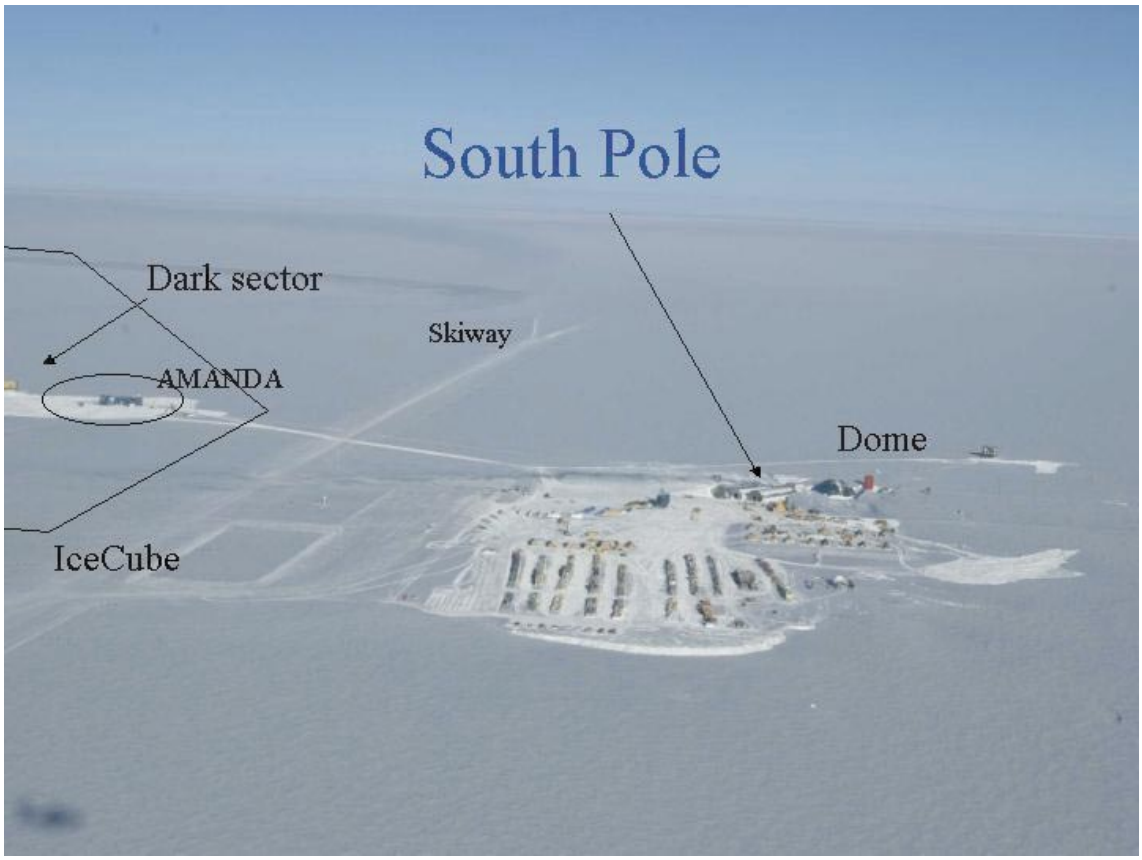

Figure 1: The South Pole site, showing the residential dome and associated buildings, the skiway where planes land, the dark sector with the Martin A. Pomerantz Observatory in which the AMANDA electronics are housed, and a rough outline of where IceCube strings are to be placed.

3 Science Motivation for Kilometer-Scale Detectors

The construction of neutrino telescopes is overwhelmingly motivated by their discovery potential in astronomy, astrophysics, cosmology and particle physics. To maximize this potential, one must design an instrument with the largest possible effective telescope area to overcome the small neutrino cross section with matter, and the best possible angular and energy resolution to address the wide diversity of possible signals. A well-designed neutrino telescope can

- search for high energy neutrinos from transient sources like Gamma Ray Bursts (GRB) or Supernova bursts;
- search for steady and variable sources of high energy neutrinos, e.g. Active Galactic Nuclei (AGN) or Supernova Remnants (SNR);
- search for the source(s) of the cosmic-rays;
- search for Weakly Interacting Massive Particles (WIMPs) which may constitute dark matter;
- search for neutrinos from the decay of superheavy particles related to topological defects;
- search for magnetic monopoles and other exotic particles like strange quark matter;
- monitor our Galaxy for MeV neutrinos from supernova explosions and operate within the worldwide SNEWS triangulation network;
- search for unexpected phenomena.

In practice, the observed fluxes of cosmic-rays and gamma rays set the scale of a neutrino telescope. With minimal model-dependence, one can estimate the very high energy cosmic neutrino fluxes by scaling to the observed energy density in high-energy cosmic-rays, or to the measured fluxes of non-thermal high-energy gamma rays. The basic assumption in calculating the expected neutrino fluxes is that some fraction of cosmic-rays will interact in their sources to produce neutrinos.

Although they are not yet identified, the sources of the highest energy cosmic radiation very likely involve extremely dense regions with exceptional gravitational forces such as supermassive black holes, collapse of massive stars or mergers of black holes and neutron stars. With accretion and intense radiation fields as ingredients, some fraction of the particles accelerated in such environments will likely produce pions in hadronic collisions with ambient gas and/or by photoproduction. In either case, the neutral pions decay to photons, while charged pions include neutrinos among their decay products with spectra related to the observed gamma-ray spectra. In the first part of this section, we discuss estimates based on this relationship and conclude that a km-scale detector is needed to observe neutrino signals from known classes of high energy astrophysical sources.

The baseline design of the detector maximizes sensitivity to ν_μ-induced muons from below with energies in the TeV to PeV range, where the acceptance is enhanced by the increasing neutrino cross section and muon range but the Earth is still largely transparent to neutrinos. Good angular resolution is required to distinguish possible point sources from background, while energy resolution is needed to enhance the signal from astrophysical sources, which are expected to have flatter energy spectra than that of the atmospheric neutrino background.

A standard technique to search for high energy neutrinos of astrophysical origin is to look for upgoing muons induced by ν_μ that have penetrated the Earth. The signal is given by the convolution

$$\text{Signal} \;\sim\; \text{Area} \otimes R_\mu \, N_A \otimes \sigma_\nu \otimes \phi_\nu, \tag{1}$$

where R_μ is the muon range in g/cm^2 and N_A is Avogadro's number. The range and cross section both increase linearly with energy into the TeV region, after which the rate of increase slows. Neutrinos with $E_\nu < 100$ TeV are not strongly attenuated by the Earth, and much of the solid angle away from the nadir remains accessible up to 1 PeV [16]. Thus the optimum range for ν_μ-induced upgoing muons is from a TeV to a PeV. Also in this energy range the muon energy loss is greater than minimum ionizing, which is a potential way to discriminate against the background of atmospheric neutrinos, which have a steeply falling spectrum. We will return to the importance of energy measurement further on.

The generic cosmic accelerator is believed to produce neutrinos in the flux ratio $\nu_e : \nu_\mu : \nu_\tau :: 1 : 2 : 0$. With neutrino oscillations, however, at the detection point this ratio becomes $1 : 1 : 1$. This is especially interesting for neutrino telescopes because the ν_τ is not absorbed in the Earth like the ν_e and ν_μ due to the charged current regeneration effect (as discussed below). Instead, ν_τ's with energies exceeding roughly 1 PeV pass through the Earth and emerge with an energy of roughly 1 PeV. IceCube is well-suited to detecting neutrinos in this energy range and will have full 4π sensitivity to this potential signal.

In the second part of this section we discuss several other important scientific goals which depend on the sensitivity of the detector to neutrinos of much higher energies and of much lower energies. On the one hand, we will discuss detecting and measuring the energy of PeV–EeV ν_e, ν_μ and ν_τ interactions. On the other, we will consider the detection of low energy muon-neutrinos from the annihilation of dark matter particles and the detection of MeV electron-antineutrinos from galactic supernovae. We describe how the baseline design can address these objectives as well.

3.1 High-Energy Neutrinos Associated with Cosmic Particle Accelerators

We estimate the range of possible neutrino signals in three ways: first on the basis of an energetics argument, second by referring to some particular models, and third by comparing to known sources of TeV photons.

3.1.1 Energy Considerations

Models for the origin of the highest energy cosmic-rays typically predict associated neutrino fluxes. A requirement on the sources is that they must provide sufficient power to supply the observed energy in the galactic or extragalactic component of the cosmic radiation. The assumption that comparable amounts of energy go into high-energy neutrinos allows an estimate of the corresponding neutrino signal that is independent of the specific nature of the sources, but which depends only on their distribution in the universe.

In the case of galactic cosmic-rays, the energy flux carried by neutrinos is much lower than that carried by the parent cosmic-rays because the charged particles are trapped locally as they propagate diffusively in the turbulent galactic magnetic fields. Thus an observer inside the galaxy has several chances to see a given cosmic ray particle, but only one chance to see a neutrino that passes directly out of the galaxy. Nevertheless, there is a chance that some nearby galactic sources could be visible in neutrinos in a km-scale detector. Examples will be discussed in the next section.

In contrast, the neutrino energy flux for a cosmological distribution of sources can be comparable to or larger than the observed cosmic-ray energy flux. The flux depends on how the sources have evolved over cosmological time scales–provided that the fraction of accelerated protons that interact near the source is large. One natural scenario that gives comparable energy in neutrinos and cosmic rays occurs when protons remain trapped in the acceleration region until they suffer inelastic collisions, while secondary neutrons escape and decay to become cosmic-ray protons. It is generally believed that sources of the ultra-high energy cosmic-rays are indeed extragalactic, or at least not confined to the plane of the galaxy. There is some evidence for a transition from one particle population to another somewhere above 10^{18} eV as well as for a trend from heavy toward lighter composition. Measurements of the cosmic-ray spectrum above 10^{17} eV are summarized in fig. 2.

We now wish to estimate the neutrino signal expected if the energy in neutrinos is comparable to the energy in the extra-galactic component of the cosmic radiation. The first step is to determine what fraction of the observed spectrum is the extra-galactic component. It is generally assumed that the acceleration processes produce a power-law spectrum $\propto E^{-\alpha}$ with differential index $\alpha = 2$ or slightly higher [8, 10]. But the measured spectrum has an index close to $\alpha = 3$, so it is not clear just how to normalize with an extra-galactic component with a much harder spectrum.

As an illustration, the lower heavy line in fig. 2 shows a spectrum with $\alpha = 2$ and an exponential cutoff at 5×10^{19} eV to represent the Greisen-Zatsepin-Kuzmin (GZK) effect [11]. Particles with energies above the GZK cutoff have interaction lengths in the microwave background of order 50 Mpc or less and must therefore be from a local or exotic component (indicated by *Super-GZK* in the figure), which we do not consider for the moment. If the excess of data above the curve for $E < 10^{19}$ eV in fig. 2 is attributed to the tail of the galactic cosmic-ray spectrum, then the energy in a universal component of the cosmic radiation may be estimated. Integrating the energy content under the $\alpha = 2$ curve gives for the energy density in cosmic rays of extragalactic origin, $\rho_{EG} \sim 2 \times 10^{-19}$ eV. The estimated power calculated from ρ_{EG} is

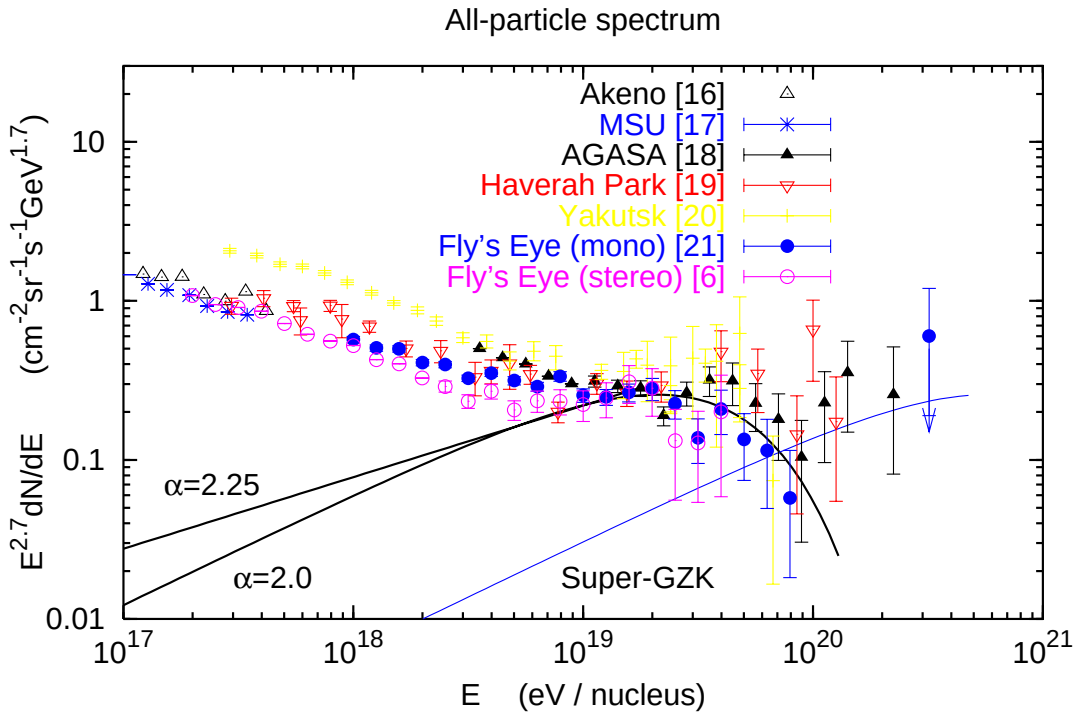

Figure 2: The high energy cosmic-rays spectrum. See text for explanation of curves. Data are from Refs. [1, 2, 3, 4, 5, 6, 7]

consistent with that observed from AGN and GRBs.

Shifting the normalization point lower (or higher) by half a decade in energy would increase (decrease) this estimate by roughly a factor of two. This is comparable to the systematic differences among the different measurements of the spectrum. If the spectrum is steeper (indicated by the upper solid curve in fig. 2, as expected for acceleration by relativistic shocks [12, 13, 14]) then the energy content will be somewhat [15] larger.

Using our estimate of the energy in the extragalactic component of the cosmic-ray spectrum and assuming a spectral index $\alpha \sim 2.0$ for the neutrinos as well as the cosmic-rays, one predicts a neutrino event rate of $f \times 30$ events/km^2/yr [17], where f is the efficiency for production of neutrinos relative to cosmic rays. For $f = 0.3$ this estimate gives a diffuse flux at the level of $E_\nu^2 dN/dE_\nu \sim 10^{-8}$ GeVcm^{-2}sr^{-1}, which is comparable to the "upper bound" estimate of Waxman & Bahcall [8] before accounting for the likely effect of evolution of sources over cosmological times.

In a sense, this estimate is conservative, and there are several ways in which the neutrino flux could be larger:

- When cosmological evolution is included, estimates based on association with sources of

ultrahigh energy cosmic-rays would be expected to be a factor of five higher if the sources are assumed to evolve similarly to the rate of star formation [8, 9, 18]. This is because the ultrahigh energy protons from high redshift would be attenuated by photoproduction and pair production while the neutrinos would not. Thus the neutrino flux would be greater for a given cosmic-ray flux at the normalization point.

- If the spectrum of extragalactic cosmic-rays to which the normalization is made has $\alpha > 2.0$, then the corresponding estimated neutrino flux and signal in the TeV to PeV range could also be larger.
- If the sources are not transparent and the cosmic-rays are partially absorbed in the source, the neutrino flux could be larger (assuming there is sufficient power in the sources).
- If, for a class of sources, the particular sources that produce the highest energy cosmic-rays are different from the ones that produce the highest neutrino fluxes.

The above discussion is summarized in Fig. 3.

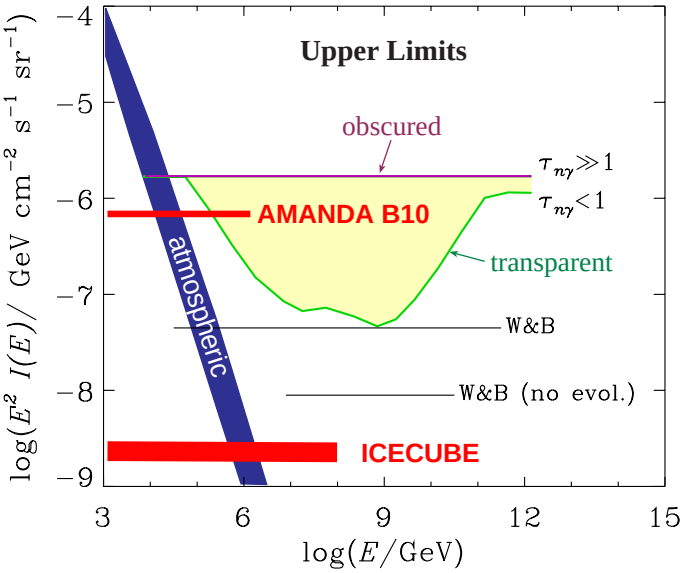

Figure 3: Cosmic-ray bounds on extragalactic neutrino fluxes. The generic bound obtained by Mannheim, Protheroe and Rachen [18] for the optically thin ($\tau_{n\gamma} < 1$) and thick case ($\tau_{n\gamma} \gg 1$) are shown together with the limit inferred from Waxman and Bahcall [8] with and without source evolution. They are compared to the present AMANDA limit and to the limit expected from three years of IceCube operation.

3.1.2 Estimates Based on Models

We may summarize the previous paragraphs by saying that an argument based on energetics coupled with a natural association between cosmic particle accelerators and their secondary neutrino beams suggests that a km-scale detector will be needed to see the neutrinos. A similar conclusion is reached by relating the neutrino flux to the source of the highest energy cosmic-rays in the context of specific models.

In a recent review [19] Learned and Mannheim have summarized recent work on models of AGN, GRB and other sources of high energy astrophysical neutrinos. As relevant examples, we quote here just two new papers that appeared since ref. [19]. Schuster, Pohl and Schlickeiser [20] work out the consequences of a model of AGN blazars [21] in which the TeV γ-rays come from decay of neutral pions produced in proton-proton collisions as a relativistic cloud of dense plasma plows into the ambient interstellar medium of the host galaxy. In this picture, there is a similar flux of TeV neutrinos from decay of charged pions. They conclude that the neutrino flux from a typical bright TeV γ-blazar would be detectable at the 3 σ level above atmospheric background in an exposure of a km^2-year. During an extended flare, such as occurred for Mrk501 from March to September of 1997 [22, 23, 24], the rate would be correspondingly higher in this model (see below).

The frequently quoted estimates [25, 26] of neutrino production in GRB sources by collisions of extremely energetic protons with MeV photons in the gamma-ray jets typically produces ~ 100 TeV neutrinos at a level sufficient to produce a few events per km^2-year. Now Mészáros and Waxman [27] argue that in gamma-ray bursts that involve collapse of massive progenitors, there will be an earlier phase of production of multi-TeV neutrinos from collisions of energetic protons with X-rays as the jet pushes through the envelope of the progenitor. They predict that there may also be a class of collapses so massive that the jets do not emerge. These would not appear as visible gamma-ray bursts but would generate neutrino bursts. The event rates estimated range from a few hundred to a thousand per year over the whole sky, depending on the ratio of "choked" to "bursting" fireballs. The northern hemisphere bursts would be detectable by IceCube.

3.1.3 Neutrinos as a Diagnostic of TeV Gamma-Ray Sources

The question whether the intriguing sources of TeV γ-rays such as Markarian 421, 501 are cosmic proton accelerators has not yet been answered. Most experts argue that the photons are produced by radiative processes from accelerated electrons. There are, however, some hints that this may not be the case. For example, the spectrum of Mrk501 during the extended (six month) flare in 1997 [22] entends to above 20 TeV, which strains the electronic models because of the short synchrotron loss time for electrons. However, only neutrinos can provide incontrovertible evidence of proton acceleration.

For the case of the Mrk501 flare, it is possible to estimate the associated neutrino flux and signal that would be expected if the observed photons are produced from decay of neutral pions. The neutrino flux is closely related to the photon flux at the source. If the pion production

mechanism is photoproduction by protons, then the energy in muon neutrinos will be about 1/4 the energy in photons. If the pions are produced in proton-gas collisions, then the energy in muon neutrinos and the energy in photons will be comparable. To obtain the source spectrum of photons, it is necessary first to account for the attenuation of photons during propagation through the infrared background radiation. This has been estimated by Konopelko et al. [28]. They find a source photon spectrum that extends from below a TeV to above 20 TeV with a power law differential spectral index of $\alpha = 2$. Starting from the six-month average flux in Ref. [22] and correcting for the infra-red absorption, one would expect 10–100 ν_μ events per km^2 of effective area in four months, depending on the origin of the produced pions (photo-production or proton-gas interactions).

In principle, high-energy neutrino astronomy has the potential to discriminate between hadronic and electromagnetic origin of the TeV emission from objects as diverse as supernova remnants, gamma-ray bursts and active galactic nuclei. The fluxes are likely to be low, however. Estimates for a variety of sources show that reasonable expectations are at the level of a few events per km^2-year. Moreover, the estimates depend on how many interactions the photons experience in the source as well as whether all observed photons are hadronic in origin. As an example of the latter point, the hadronic model of Bednarek and Protheroe [29] for the CRAB nebula attributes only the high-energy end of the photon spectrum to decay of neutral pions. For a range of parameters their model predicts a signal from < 1 to as much as 4 events per km^2·yr with $E_\mu > 1$ TeV. The corresponding rate from atmospheric background within a 1° cone is ≈ 0.4.

3.2 Other Science Opportunities

So far we have focussed on detection of muons from below the horizon produced by muon neutrinos in the TeV-PeV regime, such as may be associated with GRB sources, AGN or other cosmic accelerators observed as TeV gamma-ray emitters. Neutrinos of both higher and lower energies can also be measured with IceCube. This capability will allow us to address other science that ranges from WIMP annihilation and supernova explosions to ν_τ appearance to neutrinos from topological defects of supermassive relic particles.

3.2.1 WIMPs and Other Sources of Sub-TeV ν_μ

So far we have assumed an IceCube energy threshold of 0.4 TeV or higher. It is important to note that it will be possible to detect muon-neutrinos of significantly lower energy. If the track of the secondary muon is close to an individual string, its length can be deduced from the arrival times of Cherenkov photons detected by nearby PMTs. A good measurement requires nanosecond timing in several modules. Requiring, conservatively, signals in five modules separated by 17 m, the minimum tracklength is $\sim$ 70 m for a muon energy of $\sim$ 15 GeV. Requiring further that the distance from the string to the track is significantly less than the scattering length, 10 m for instance, yields a detection volume of 25 megaton with a threshold of less than 20 GeV for a source directly below the detector, in particular for neutrinos from annihilation of WIMPS

trapped in the center of the Earth. For other directions the energy threshold is higher and the efficiency for a given energy is correspondingly lower. The cuts on track-length and proximity to a string can be relaxed if the detector would be exposed to an accelerator beam. During the short beam spills the detector is free of background and requirements on track measurement can be reduced thus increasing the target volume. On the other hand, the neutrino beam would be at some angle to the strings, depending on the location of the accelerator, which would reduce the acceptance.

Several science missions would benefit from a reduced threshold in a limited volume, e.g. the search for dark matter. If Weakly Interacting Massive Particles (WIMPs) make up the dark matter of the universe, they would also populate the galactic halo of our own Galaxy. They would be captured by the Earth or the Sun where they would annihilate pairwise, producing high-energy muon neutrinos that can be detected by neutrino telescopes. A favorite WIMP candidate is the lightest neutralino which arises in the Minimal Supersymmetric Model (MSSM). In general, IceCube's reach as a dark matter detector is complementary to that of direct search detectors because of its good sensitivity to larger neutralino masses, typically higher than a few hundred GeV. In addition, the rates depend on the capture and annihilation rates of the WIMPs in the Earth or Sun rather than their cross sections for interaction in the detector. High energy neutrinos produced in the annihilation of galactic neutralino dark matter have characterisitic energies of $1/4 \sim 1/6$ the mass of the parent particles. A reduction in neutrino threshold therefore results in increased sensitivity to lower masses. The standard IceCube geometry presents an effective area of 0.7 km^2 for WIMPs with mass > 50 GeV annihilating in the core of the Earth. For WIMPS in the Sun, because of the less favorable geometry, the effective area increases from $\sim$ .01 km^2 for $m_W = 50$ GeV and approaches 0.7 km^2 for TeV WIMPS. The situation is most favorable for WIMPS above the threshold for decay into weak intermediate bosons, where IceCube is competitive with specialized future detectors such as GENIUS and CRESST in the search for neutralino dark matter anticipated in supersymmetric theories [45].

Another reason for maintaining sensitivity to $\sim$ 10 GeV neutrinos is that these may be produced in GRBs along with high energy neutrinos. Bahcall and Meszaros [46] have argued that a gamma-ray burst "fireball" is likely to contain an admixture of neutrons, in addition to protons, in essentially all progenitor scenarios. Inelastic collisions between protons and neutrons in the fireball produce muon neutrinos (antineutrinos) of $\sim$10 GeV energy as well as electron neutrinos (antineutrinos) of $\sim$5 GeV, which could produce $\sim$7 events/year in km-scale detectors, if the neutron abundance is comparable to that of protons. With a reduced threshold and exploiting coincidence in timing with the GRB, this flux may be observable.

A low threshold also preserves the capability discussed in connection with AMANDA (see sec. 12) to detect secondary muons from TeV-energy gamma rays produced in the atmosphere *above* the detector. These are guaranteed fluxes, calculable from the observed fluxes. The technique could be particularly revealing in GRB studies.

3.2.2 Atmospheric Neutrinos

Neutrinos produced locally by interactions of cosmic-rays in the atmosphere constitute the foreground for neutrinos of astrophysical origin. They are both background and calibration source. The energy spectrum of atmospheric neutrinos is steep, falling approximately like E^{-3} and steepening to $E^{-3.7}$ for $E \gg 1$ TeV. Above ~ 10 GeV the flux of ν_e falls even more quickly, and above ~ 100 effects of oscillations are also negligible. Thus atmospheric muon-neutrinos are a known calibration source up to a TeV and beyond. There is a characteristic factor of two excess of neutrinos from near the horizontal as compared to the vertical. Measuring the rate and angular dependence of atmospheric ν_μ-induced muons is therefore a benchmark measurement for IceCube.

The component of "prompt" ν_μ from charm decay has a harder spectrum than the component from decay of charged kaons and pions. It is expected to become the dominant source of atmospheric neutrinos above an energy of perhaps 100 TeV. The exact level of the prompt component is rather poorly known, and it could present a significant background for diffuse astrophysical neutrinos. If it is sufficiently large, it could be measured by IceCube as a hardening the neutrino energy spectrum by one power of the energy.

With a sufficiently low energy threshold, IceCube could also play a role in confirming the compelling indications that atmospheric neutrinos oscillate. Studies of systematics and backgrounds show, however, that significant progress would require smaller spacing of OMs along a string than presently planned. Such a specialized effort would be warranted only if ongoing experiments fail to prove oscillation of atmospheric neutrinos before IceCube construction.

3.2.3 PeV and EeV Neutrinos

The interactions of neutrinos with PeV energies and higher will have spectacular signatures in IceCube. (The simulated 6 PeV neutrino in fig. 16 illustrates this point.) Since the Earth becomes increasingly opaque to neutrinos with energy in the PeV range and higher, it is necessary to use events from horizontal and downgoing neutrinos. Fortunately, setting an energy threshold in the PeV energy region is high enough to be above atmospheric backgrounds. In this energy region the observed muon events in IceCube will be dominated by muon neutrinos interacting in the ice or atmosphere *above* the detector and near the horizon. PeV cascades from ν_e interactions in the detector volume also contribute at a somewhat lower rate. Tau neutrinos will also show up as cascades, as described below. Upgoing neutrinos are suppressed by an order of magnitude. Due to the Earth's opacity, the zenith angle distribution of neutrinos associated with EeV signals will have a striking signature. For a detailed discussion, see [36, 38].

With a threshold for cascades below the PeV region, IceCube will be complementary to detectors such as Auger, OWL and RICE which have thresholds of 10 EeV and higher. The lower threshold means that comparable event rates may be possible with IceCube even though its effective volume is much smaller.

The high-energy capability of IceCube will allow us to attack a major scientific problem, the existence of particles whose energy apparently exceeds the GZK cutoff. Speculations re-

garding their origin include heavy relics from the early Universe and topological defects which are remnant cosmic structures associated with phase transitions in grand unified gauge theories [30, 31, 32]. Interactions of ultra-high energy neutrinos with massive neutrinos in the galactic halo is also a possibility [33]. Such models would predict a sizeable flux of neutrinos in a much higher range of energy than the neutrinos associated with the GRB and AGN models mentioned above. Some limits on the highest predictions of neutrino fluxes are emerging from analysis of horizontal air showers, but there is still considerable phase space for exploration. Detection of neutrinos produced in interactions leading to the GZK cutoff is also a possibility, although their level is relatively low. Specific examples include:

- generic topological defects with grand-unified mass scale M_X of order 10^{15} GeV and a particle decay spectrum consistent with all present observational constraints[30] might yield 10 events/year;
- neutrinos produced by superheavy relics whose decay products include highest energy cosmic-rays[35], also 10 events/year;
- superheavy relics [31, 32], which we normalize to the Z-burst scenario[33] where the observed cosmic-rays with $\sim 10^{20}$ eV energy, and above, are locally produced by the interaction of super-energetic neutrinos with the cosmic neutrino background could give as many as 30 events/year;
- the flux of neutrinos produced in the interactions of cosmic rays with the microwave background[37]. This flux, which originally inspired the concept of a km-scale neutrino detector, would only give one or two events per year, or less depending on how the sources evolve over cosmological time scales.

3.2.4 Tau Neutrino Detection

Interest in detection of τ neutrinos is motivated by the evidence for neutrino oscillations from SuperKamiokande [39] and SNO [40]. Production of ν_τ in hadronic interactions or photoproduction is suppressed relative to ν_e and ν_μ by several orders of magnitude. In the absence of new physics, ν_τ of astrophysical origin would therefore be virtually undetectable. If, however, there is large mixing in the $\nu_\mu \leftrightarrow \nu_\tau$ channel, then over astrophysical distances fluxes of ν_τ would be comparable to ν_μ.

Tau neutrinos of sufficiently high energy can in principle be identified in several ways in a km-scale neutrino detector. Perhaps the most striking signature would be the characteristic double bang events [41] in which the production and decay of a τ lepton would be seen as two separated bursts in the detector. It may also be possible to identify "lollipop" events in which a ν_τ with energy >PeV creates a long minimum-ionizing track that enters the detector and ends in a huge burst as the τ lepton decays to a final state with hadrons or an electron. The entering τ, because of its large mass, would emit fewer bremsstrahlung photons than a muon of similar energy. Such events would be detected from above or near the horizontal since the Earth is opaque to neutrinos with energies at or above the PeV region.

At still higher energies, the Earth becomes completely opaque to ν_e and ν_μ fluxes but it remains transparent to ν_τ flux [42]. In essence, ν_τ charged current interactions create a tau lepton, which decays before losing all its energy, and which always has a ν_τ as one of its decay products. This ultimately results in an upgoing ν_τ flux in the 100 TeV energy range. In what follows we discuss only the "double-bang" signature, which gives a conservative estimate of possible rates.

In a charged current ν_τ deep inelastic scattering (DIS) interaction with a nucleus, a τ lepton of energy $(1-y)E_{\nu_\tau}$ is produced as well as a hadronic shower of energy yE_{ν_τ} which is initiated in the fragmentation of the nucleus. Here y is the fraction of energy transferred to the hadronic vertex in the interaction. The τ lepton travels on average a distance R_τ along the medium before decaying given by:

$$R_\tau = \frac{E_\tau}{m_\tau} ct_0 = \frac{(1-y)E_{\nu_\tau}}{m_\tau} ct_0 \tag{2}$$

where E_τ and m_τ are the energy and mass of the τ respectively and t_0 is its rest lifetime. In its decay it produces another ν_τ and an electromagnetic or hadronic shower $\sim 82\%$ of the times. Assuming a typical detector dimension D, there are several conditions that have to be fulfilled for the detection of a double bang event induced by a ν_τ:

- The ν_τ has to interact through a charged current DIS interaction producing a hadronic shower contained inside the instrumented volume of the detector ($\sim D^3$).
- The τ lepton must decay inside the detector to a final state that produces an electromagnetic or hadronic shower which again has to be contained inside the device.
- R_τ has to be large enough so that both showers are sufficiently separated from each other to be distinguished.
- The showers have to be energetic enough to trigger the detector.

Using these criteria we can estimate the probability of detecting a double bang event in a neutrino telescope of linear dimension $D = 1$ km such as IceCube using a simple Monte Carlo. We take the energy threshold for detecting showers to be $E_{\rm shower} \sim 1$ TeV and fix 250 m as the minimum distance the τ has to travel to distinguish the Cherenkov light from both showers. This (conservative) number is mainly determined by the 125 m separation between strings since detection by separated strings is needed to establish the double burst for a horizontal event. This distance corresponds to a minimum energy of ~ 5 PeV for the τ lepton. The requirement that both bursts occur inside the detector sets an upper limit of ~ 20 PeV. With these constraints, one would expect at most a few events per year given current limits on neutrino fluxes from AMANDA. This conclusion is consistent with the result of Athar et al. [43], who find some tens of double bang events per year in the original AGN model [44] which is somewhat above current limits.

3.2.5 Neutrinos from Supernovae

A high energy neutrino telescope in deep Antarctic ice is sensitive to the stream of low energy neutrinos produced by a galactic supernova Although 10-20 MeV energy is far below the AMANDA/IceCube trigger threshold, a supernova would be detected by higher counting rates in individual PMTs over a time window of 5-10 s. The enhancement in rate of a single PMT is buried in PMT dark noise. However, by summing the signals from *all* PMTs a significant excess would be observed. Limits obtained with AMANDA have been submitted for publication [47]. Relatively low background counting rates in ice (relative to water) make this possible.

Most of the energy released by a supernova is liberated in a burst lasting about ten seconds. Roughly equal energies are carried by each neutrino species with a thermal spectrum of temperature 2–4 MeV. Since the $\bar{\nu}_e$ cross-section on protons in the detector is significantly larger than the interaction cross sections for the other neutrino flavors, $\bar{\nu}_e$ events dominate the signal by a large factor after detection efficiency is taken into account. In this reaction, free protons absorb the antineutrino to produce a neutron and a positron which is approximately isotropically emitted with an energy close to that of the initial neutrino. A thermal spectrum of temperature 4 MeV, when folded with an inverse beta decay cross section which increases with the square of the neutrino energy, yields an observed positron energy distribution which peaks in the vicinity of 20 MeV. The track-length of a 20 MeV positron in ice is roughly 12 centimeters and therefore over 3000 Cherenkov photons are produced.

AMANDA and IceCube can contribute to the SuperNova Early Warning Network [48]. A recent analysis [47] shows that 70% of the galatic disk can be monitored for a supernova like SN1987A using a selected set of low noise AMANDA PMTs. Given a known template for time evolution of the pulse, the resulting accuracy in timing could be 14 ms for AMANDA-II and as good as 1-3 ms for IceCube. The resulting angular resolution depends on the orientation of the triangulation grid with respect to the supernova. The three detectors SuperK, SNO and IceCube will achieve typical resolution of 5 to 20 degrees. This is to be compared with the accuracy of about 5° achieved from the measured electron direction in a detector like SuperK.

Simultaneous detection of high energy and lower energy MeV neutrinos from a supernova is an exciting capability of a high energy neutrino telescope with supernova sensitivity. Loeb and Waxman [49] have shown that when a type II supernova shock breaks out of its progenitor star, it becomes collisionless and may accelerate protons to TeV-energy or higher. Inelastic nuclear collisions of these protons produce a $\sim$1 hr long flash of TeV neutrinos about 10 hr after the thermal neutrino burst from the cooling neutron star. A Galactic supernova in a red supergiant star would produce a neutrino flux of $\sim 10^{-4}\,\mathrm{erg/cm^2\,s}$. A $\mathrm{km^2}$ neutrino detector will detect $\sim$100 muons, thus allowing one to constrain both supernova models and neutrino properties. All these opportunities will be greatly enhanced by a low threshold associated with short tracks detected by individual strings.

3.3 Summary

The main goal of the IceCube project is the detection of extraterrestrial sources of very high energy neutrinos [19, 50, 51].

- IceCube will reach a sensitivity for diffuse fluxes of a few $10^{-9} \cdot E^{-2}$ GeV^{-1} cm^{-2} s^{-1}, which is more than one order of magnitude below conservative "upper bounds" derived from cosmic-ray observations, and three orders of magnitude below bounds derived from gamma ray observations alone. The published AMANDA limit has already improved previous experimental limits by more than a factor 10 and will be improved by AMANDA-II and IceCube by roughly an additional 1.0 and 2.5 orders of magnitude, respectively. Within this range of sensitivity, models predict between "several" and thousands of events per year.
- Point source searches will reach a sensitivity of at least 10^{-12} cm^{-2} s^{-1} for energies greater than about 10 TeV. This is nearly two orders of magnitude below the observed Mrk501 TeV gamma-ray flux during its flaring phase. Predictions for some steady or quasi-steady sources reach a few tens of events per year.
- Supernova models predict 10-100 events shortly before and after the SN burst.
- Gamma Ray Bursts are expected to yield 10-100 events per year.
- IceCube has also significant EeV capabilities. Event numbers predicted by top-down scenarios (like topological defects) lead to 1-30 events per year, comparable to expectations for dedicated EeV experiments.
- IceCube has a realistic chance to identify tau neutrinos via "double-bang" events, with up to 100 events per year expected for certain topological defect models.

IceCube is a multi-purpose detector. Beside high energy neutrino astronomy, it can be used to investigate a series of other questions:

- Magnetic monopoles: Present limits for the flux of relativistic monopoles can be improved by two orders of magnitude. This is a factor of 1000 below the Parker bound [52]. One also can search for slow monopoles catalyzing proton decay, or for strange quark matter.
- Neutrinos from WIMP annihilation: IceCube can play a complementary role to future direct detection experiments, particularly for high WIMP masses. The instrument is unique for TeV dark matter.
- MeV neutrinos from supernova bursts: IceCube will detect a supernova burst over the whole Galaxy, and as far as the Magellanic clouds.
- As a by-product, neutrino oscillations, physics (and gamma-ray astronomy) with downgoing muons, or even questions of glaciology can be investigated.

Discovery of any single one of the high energy signals listed above would unquestionably make IceCube a resounding success. However, as a detector one hundred times larger than AMANDA and one thousand times larger than any underground detector, IceCube will be opening a new window on the universe, and as such holds out even greater promise: the exciting discovery of unanticipated phenomena.

4 Status of High Energy Neutrino Astronomy

The science of high energy neutrino astronomy is compelling. The main challenge is therefore to develop a reliable, expandable and affordable detector technology. The diagram in fig. 4 shows

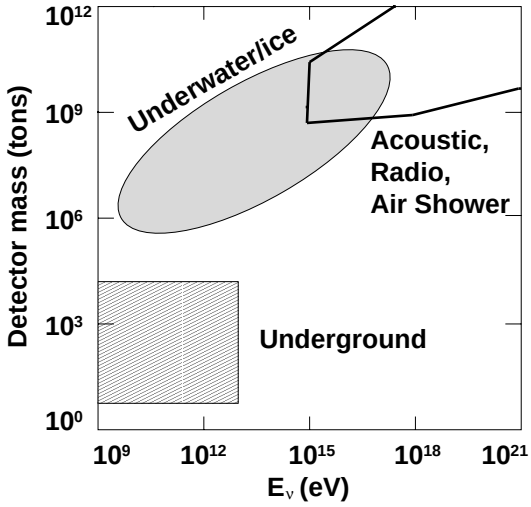

Figure 4: Schematic representation [70] of the physics reach of various types of detectors in detector mass versus neutrino energy space.

schematically the range of various detectors in the space of volume vs. neutrino energy. IMB and Kamioka are so far the only detectors that have observed neutrinos from outside the solar system, with the detection of SN1987A. With its large volume and great sensitivity, Super-Kamiokande has pushed the frontiers of the study of atmospheric neutrinos in the sub-GeV and multi-GeV energy range, SNO and Super-Kamiokande have done the same with solar neutrinos, with SNO recently providing the first clear evidence of solar neutrino oscillations. There is significant activity with several underground detectors, including Borexino and KamLand, pushing toward lower energy and higher energy resolution on the solar neutrino frontier. Super-Kamiokande, along with Frejus, MACRO and Soudan, have also provided important limits on fluxes of high energy neutrinos.

With the termination of the pioneering DUMAND experiment, the efforts in water are, at present, spearheaded by the Baikal experiment [71]. The Baikal Neutrino Telescope is deployed in Lake Baikal, Siberia, 3.6 km from shore at a depth of 1.1 km. An umbrella-like frame holds 8 strings, each instrumented with 24 pairs of 37-cm diameter *QUASAR* photomultiplier tubes (PMT). Two PMTs in a pair are switched in coincidence in order to suppress background from natural radioactivity and bioluminescence. Operating with 144 optical modules since April 1997, the *NT-200* detector has been completed in April 1998 with 192 optical modules (OM). The Baikal detector is well understood, and the first atmospheric neutrinos have been identified.

The Baikal site is competitive with deep oceans, although the smaller absorption length

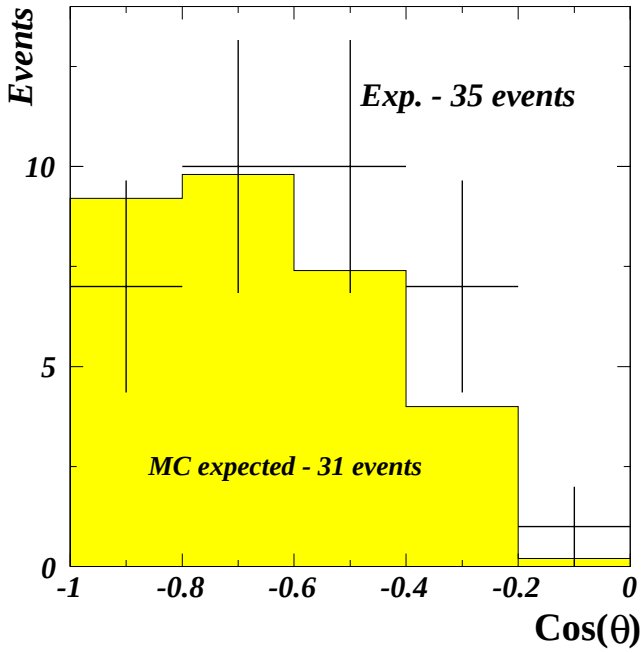

Figure 5: Angular distribution of muon tracks in the Lake Baikal NT-200 experiment after all final cuts have been applied [73].

of Čerenkov light in lake water requires a somewhat denser spacing of the OMs. This does, however, result in a lower threshold which may be a definite advantage, for instance for oscillation measurements and WIMP searches. They have shown that their shallow depth of 1 km does not represent a serious drawback. By far the most significant advantage is the site with a seasonal ice cover which allows reliable and inexpensive deployment and repair of detector elements from a stable platform.

With data taken with the Baikal NT-200 detector, the Baikal collaboration has shown that atmospheric muons can be reconstructed with sufficient accuracy to identify atmospheric neutrinos, as illustrated in fig. 5. The neutrino events are isolated from the cosmic ray muon background by imposing a restriction on the chi-square of the Čerenkov fit, and by requiring consistency between the reconstructed trajectory and the spatial locations of the OMs reporting signals.

In the following years, *NT-200* will be operated as a neutrino telescope with an effective area between $10^3 \sim 5 \times 10^3$ m^2, depending on energy. Presumably too small to detect neutrinos from extraterrestrial sources, *NT-200* will serve as the prototype for a larger telescope. For instance, with 2000 OMs, a threshold of $10 \sim 20$ GeV and an effective area of $5 \times 10^4 \sim 10^5$ m^2, an expanded Baikal telescope would fill the gap between present underground detectors and planned high threshold detectors of km^3 size. Its key advantage would be low threshold.

The Baikal experiment represents a proof of concept for deep ocean projects. These have the advantage of larger depth and optically superior water. Their challenge is to find reliable and affordable solutions to a variety of technological challenges for deploying a deep underwater detector. Several groups are confronting the problem; both NESTOR and ANTARES are developing rather different detector concepts in the Mediterranean.

The NESTOR collaboration [74], as part of a series of ongoing technology tests, is testing the umbrella structure which will hold the OMs. They have already deployed two aluminum "floors," 34 m in diameter, to a depth of 2600 m. Mechanical robustness was demonstrated by towing the structure, submerged below 2000 m, from shore to the site and back. These tests should soon be repeated with fully instrumented floors. The actual detector will consist of a tower of 12 six-legged floors vertically separated by 30 m. Each floor contains 14 OMs with four times the photocathode area of the commercial 8 inch photomultipliers used by AMANDA and ANTARES.

The detector concept is patterned along the Baikal design. The symmetric up/down orientation of the OMs will result in uniform angular acceptance and the relatively close spacings in a low threshold. NESTOR does have the advantage of a superb site off the coast of Southern Greece, possibly the best in the Mediterranean. The detector can be deployed below 3.5 km relatively close to shore. With the attenuation length peaking at 55 m near 470 nm the site is optically superior to that of all other deep water sites investigated for neutrino astronomy.

The ANTARES collaboration [72] is investigating the suitability of a 2400 m-deep Mediterranean site off Toulon, France. The site is a trade-off between acceptable optical properties of the water and easy access to ocean technology. Their detector concept indeed requires remotely operated vehicles for making underwater connections. First results on water quality are very encouraging with an attenuation length of 40 m at 467 nm and a scattering length exceeding 100 m. Random noise exceeding 50 khz per OM is eliminated by requiring coincidences between neighboring OMs, as is done in the Lake Baikal design. Unlike other water experiments, they will point all photomultipliers sideways in order to avoid the effects of biofouling. The problem is significant at the Toulon site, but only affects the upper pole region of the OM. Relatively weak intensity and long duration bioluminescence results in an acceptable deadtime of the detector. They have demonstrated their capability to deploy and retrieve a string, and have reconstructed down-going muons with 8 OMs deployed on the test string.

With the study of atmospheric neutrino oscillations as a top priority, they had planned to deploy in 2001-2003 10 strings instrumented over 400 m with 100 OMs. After study of the underwater currents they decided that they can space the strings by 100 m, and possibly by 60 m. The ANTARES detector will consist of 13 strings, each equipped with 30 storeys and 3 PMTs per storey. The large photocathode density of the array will allow the study of atmospheric neutrino oscillations in the range $255 < L/E < 2550\,\mathrm{km\,GeV^{-1}}$ with neutrinos in the energy range $5 < E_\nu < 50$ GeV. This detector will have an area of about $3 \times 10^4\,\mathrm{m^2}$ for 1 TeV muons–similar to AMANDA-II–and is planned to be fully deployed by the end of 2003.

A new R&D initiative based in Catania, Sicily has been mapping Mediterranean sites, studying mechanical structures and low power electronics. One must hope that with a successful pioneering neutrino detector of $10^{-3}\,\mathrm{km^3}$ in Lake Baikal, a forthcoming $10^{-2}\,\mathrm{km^3}$ detector near

Toulon, the Mediterranean efforts will converge on a 10^{-1} km^3 detector possibly at the NESTOR site.

As in many other fields, high energy neutrino astronomy would ideally have two or more independent experiments sensitive to the same energy regime. Such redundancy allows one to perform vital crosschecks and (hopefully) discovery verification. It is therefore in the best interests of the community that projects other than AMANDA and IceCube succeed. In addition, a detector in the northern hemisphere would provide the community with full TeV–PeV neutrino sky coverage, while at the same time having considerable coverage overlap regions.

4.1 Status of AMANDA

The AMANDA-B10 results presented below provide a proof-of-concept for a high energy neutrino telescope at the South Pole. We focus first on the detection of neutrinos and compare them to the predicted flux of atmospheric neutrinos. Possible backgrounds will be discussed. We then apply the results to the search for high energy neutrinos of astrophysical origin, such as a diffuse flux of HE neutrinos, point-like sources and gamma-ray bursts.

It is important to note that due to its size and shape, AMANDA-B10 is not highly sensitive to high energy neutrino fluxes expected from sources such as AGN and GRBs. The much larger AMANDA-II detector has significantly more sensitivity, and data from this device is currently being analyzed. However, only with IceCube will the sensitivity levels be high enough to reach predicted high energy neutrino flux levels.

4.1.1 Atmospheric Neutrinos

The results presented here are based on data taken during the austral winter of 1997. The effective livetime has been determined to be 130.1 days for the selected data. The method of calibration and the characteristics of the optical sensors are very similar to the 4 string prototype array described in ref. [53]. Simulations predict a rate of a few tens of events per day from atmospheric neutrinos above a threshold of 30-50 GeV, compared to $6 \cdot 10^6$ events from cosmic ray muons, as shown in fig. 6.

The analysis of the atmospheric neutrino sample with the AMANDA-B10 array has been performed independently by two working groups in the collaboration. Both groups come to very similar and statistically consistent results while the methods are quite different and partially independent. The figures and the method presented here are based on one analysis [56].

Neutrinos are identified by looking for upward going muons. We use a maximum likelihood method [57], incorporating a detailed description of the scattering and absorption of photons in the ice, to reconstruct muon tracks from the measured photon arrival times. Events are reconstructed with a Bayesian method [58], in which the likelihood function is multiplied by a prior probability function. The prior function contains the zenith angle information in fig. 6. By accounting in the reconstruction for the fact that the flux of downgoing muons from cosmic rays is more than 5 orders of magnitude larger than that of upgoing neutrino-induced muons, the number of downgoing muons that are misreconstructed as upgoing is greatly reduced. A small

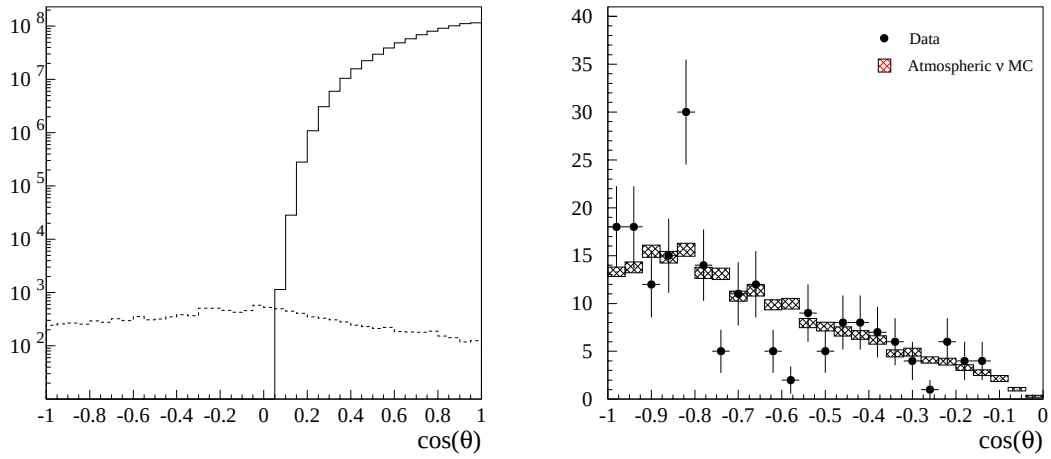

Figure 6: Left: The zenith angle distribution of AMANDA triggers. The solid line represents triggers from downgoing cosmic ray muons. The dashed line shows triggers produced by atmospheric neutrinos. Right: The zenith angle distribution of upward reconstructed events. The size of the hatched boxes indicates the statistical precision of the atmospheric neutrino simulation.

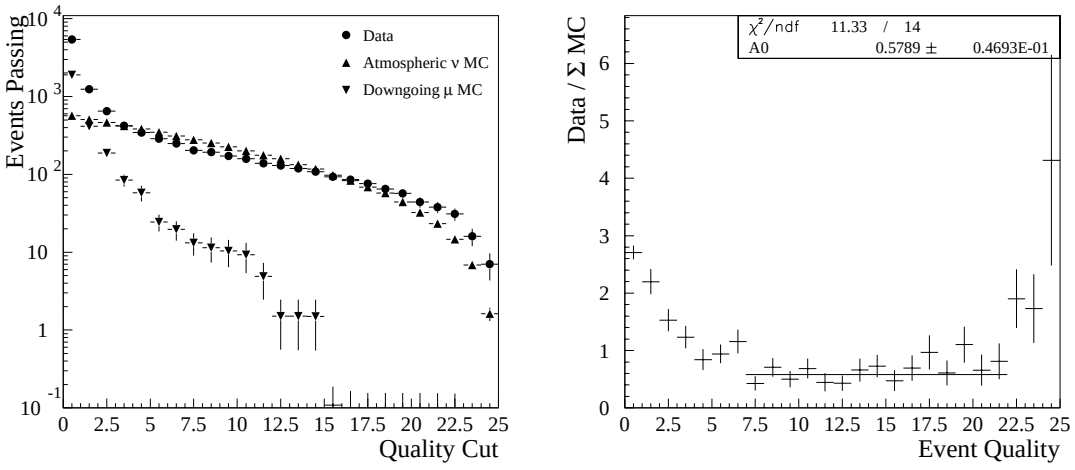

Figure 7: Event quality. Left: Passing rates of events above a certain quality level is shown for background MC, atmospheric neutrino MC and experimental data. Right: Differential presentation of the ratio data/MC.

fraction of the downgoing muons ($5 \cdot 10^{-6}$) are reconstructed as upward and form a background to the neutrino-induced events. This background is removed by applying quality criteria to the time profiles of the observed photons as well as to their spatial distribution in the array. A measure of the event quality has been defined by combining six quality variables into a single parameter. A high event quality is reached when the values of all six parameters agree with the characteristics of a correctly reconstructed muon track. By making increasingly stringent cuts on the event quality the background of a total of $1.2 \cdot 10^9$ events is reduced by a factor of approximately 10^8, while retaining about 5% of the neutrino signal. The distribution of the single quality parameter for experimental data and for a Monte Carlo simulation of atmospheric neutrinos is shown in fig. 7. It compares the number of events passing various levels of cuts; i.e., the integral number of events above a given quality. At low qualities, the data set is dominated by misreconstructed downgoing muons, most of which are reproduced in the Monte Carlo. At higher cut levels, the passing rates of data closely track the simulated neutrino events, and the predicted background contamination is very low.

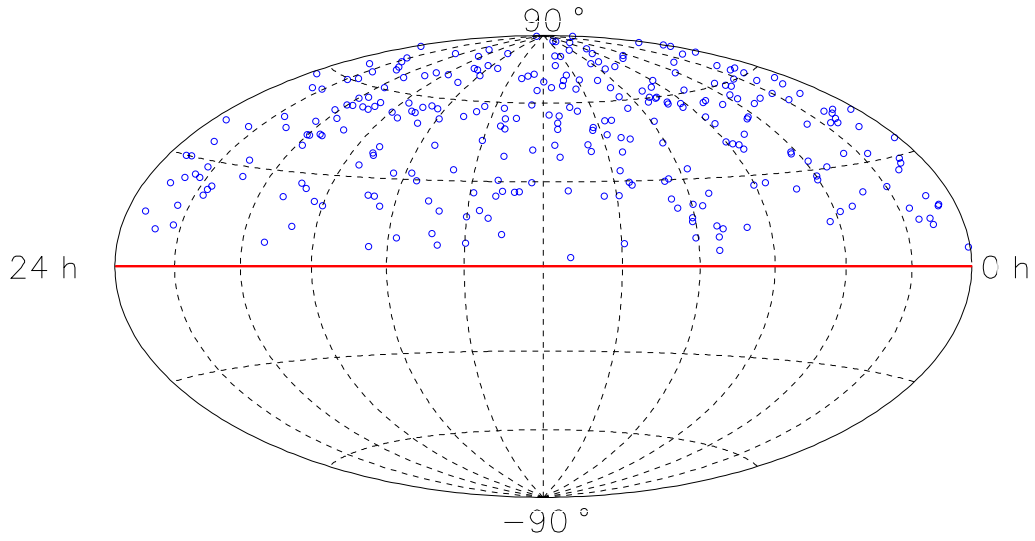

Figure 8: Neutrino sky of upgoing events as seen with AMANDA-B10. The background of non neutrino events is estimated to less than 10%.

We can investigate the agreement between data and Monte Carlo more systematically by

	Experimental Data	MC: Atmospheric Neutrinos
Triggered	$1.2 \cdot 10^9$	4600
Reconstructed upward	$5 \cdot 10^3$	571
Upward going	204	279

Table 1: Event numbers are given at various cutlevels: Experimental data and atmnospheric neutrino Monte Carlo.

comparing the differential number of events, rather than the total number of events passing various levels of cuts. This is done in fig. 7 (right), where the ratios of the number of events observed to those predicted from the combined signal and background simulations are shown. One can see that at low quality levels there is an excess in the number of misreconstructed events observed. This is mainly due to instrumental effects such as cross talk which are not well described in the detector Monte Carlo. There is also an excess, though statistically less significant, at very high quality levels, which is caused by slight inaccuracies in the description of the optical parameters of the ice. Nevertheless, over the bulk of the range there is close agreement between the data and the simulations, apart from an overall normalization factor. In the range where the line is shown the ratio of Data/MC is about 0.6. Counting all events above the quality cut (7.0) this ratio is 0.70. It should be emphasized that the quality parameter is a combination of all six quality parameters, and so the flat line in fig. 7 demonstrates agreement not only in individual cut parameters but also quantitative agreement in the correlations between cut parameters.

The zenith angle distribution for the 204 events is shown in fig. 6, and compared to that for the signal simulation. In the figure the Monte Carlo events were normalized to the observed events. The achieved agreement in the absolute flux of atmospheric neutrinos is consistent with the systematic uncertainties of the absolute sensitivity and the flux of high energy atmospheric neutrinos. The shape of the zenith distribution of data is statistically consistent with the prediction from atmospheric neutrinos. The zenith distribution reflects the angular acceptance of the narrow but tall detector. A skyplot of these events is shown in fig. 8. 223 events were found in an independent analysis. The overlap of 119 events with the sample presented here is within expectations. The observation of atmospheric neutrinos at a rate consistent with Monte Carlo prediction establishes AMANDA-B10 as a neutrino telescope.

4.1.2 Pointing Resolution

In order to establish AMANDA as a neutrino telescope, one more step is needed. That is the verification that AMANDA does indeed reconstruct the direction of events correctly in sky coordinates. This is done by analyzing events that are measured coincidently by AMANDA in the deep ice and by surface air shower detectors. In the 1997 data set we have three independent detectors at the surface in operation: the SPASE-1 air shower array, the SPASE-2 array, and the GASP air cherenkov detector. All three experiments agree on the average absolute pointing

of the AMANDA array to within 1–2 degrees (sky coordinates) [55]. A full agreement with the true direction is achieved in azimuth, and a small offest of order 1 degree is observed in the in the zenith angle (data and Monte Carlo). The offset is relatively small compared to the size of a search bin ($\sim$ 5 degrees half angle) for point sources. These instruments were also used to verify the angular resolution (median angular error) of about 3 degrees.

The observation of atmospheric neutrinos together with the verification of the angular resolution establishes AMANDA as a functioning neutrino telescope. From here we search the neutrino sky for various sources. Depending on the type of the investigated neutrino signal hypothesis (diffuse flux, point sources, GRB, WIMPs, etc.), we re-optimize the background rejection strategy.

4.1.3 Search for a diffuse high energy neutrino flux

The search for a diffuse neutrino flux of astronomical origin follows naturally from the observation of a diffuse flux of neutrinos generated in the atmosphere. Neutrinos from generic astrophysical sources are expected to extend to higher energies while the energy spectrum of atmospheric neutrinos falls off steeply with increasing energy. A very simple and robust measure of the energy of the observed muons is the number of optical modules (OM) that observed at least one photoelectron in a given event. Figure 9 shows the energy distribution of events that pass the neutrino filter as predicted for a) atmospheric neutrinos and b) an assumed energy spectrum for astrophysical neutrinos following a power law of $dN/dE_\nu = 10^{-5} E_\nu^{-2}\,\mathrm{cm}^{-2}\,\mathrm{s}^{-1}\,\mathrm{sr}^{-1}\,\mathrm{GeV}^{-1}$. When using the number of fired OMs as a measure of energy we obtain the distributions given in fig. 9. The assumed astronomical neutrino flux would generate a significant excess at high multiplicities of fired photomultipliers. A preliminary analysis does not show such an excess. This leads to a preliminary upper limit [65] (90%C.L.) of $dN/dE_\nu \sim 10^{-6} E_\nu^{-2}\,\mathrm{cm}^{-2}\,\mathrm{s}^{-1}\,\mathrm{sr}^{-1}\,\mathrm{GeV}^{-1}$. However, the systematics of this analysis with respect to the high energy sensitivity is still subject to further investigation. A re-analysis with an updated version of the Monte Carlo simulation is underway.

This sensitivity on the diffuse neutrino flux is below previously stated upper limits by experiments such as BAIKAL [71], SPS-DUMAND [66], AMANDA-A [67], and FREJUS [68], and comparable to a limit presented by BAIKAL [75].

It is comparable to the AGN prediction by Salamon and Stecker [63] and approaches the prediction of Protheroe [69].

4.1.4 Point Sources

The search for point sources allows us to measure the background off-source. Searches have been performed for specific point sources as well as all sky searches. The median angular resolution of the AMANDA-B10 array is 3 degrees. Thus, one hemisphere consists of 319 bins. Again the search strategy is optimized for the expected energy spectrum. The size of the search bins, the effective area and the livetime of the array enter the calculation of a neutrino flux limit. In absence of a signal we calculate upper limits to a neutrino flux from point sources. The

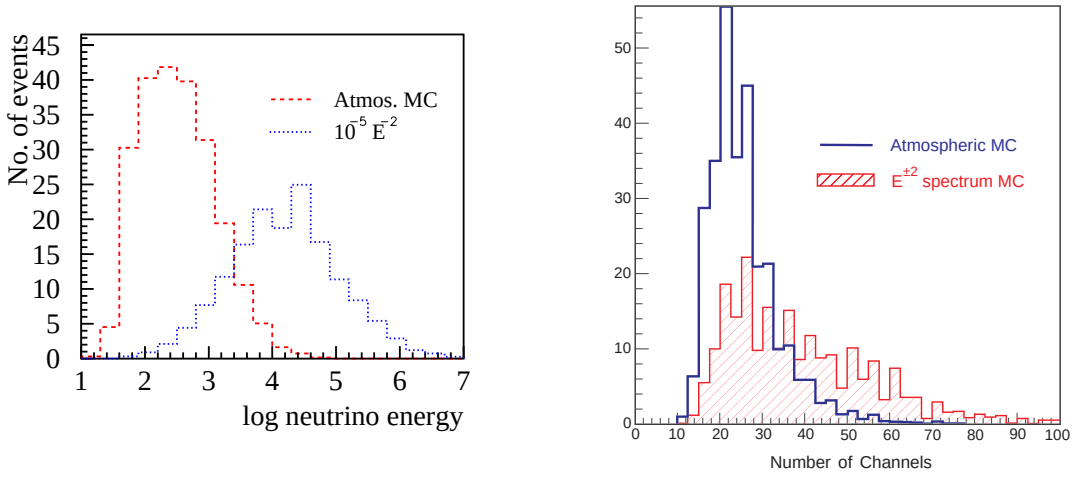

Figure 9: Left: Monte Carlo simulation of the energy spectrum of atmospheric neutrinos shown in the skyplot in fig. 8. Also shown is the energy spectrum of neutrinos generated by a neutrino flux of a E_ν^{-2}-type energy spectrum (see text).

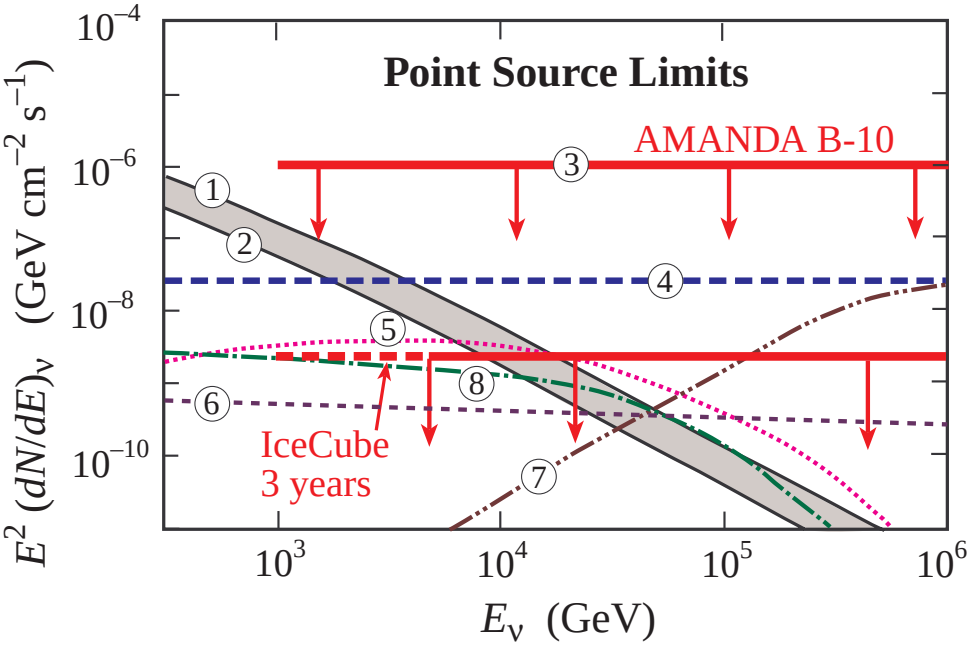

Figure 10: Predictions of high energy $\nu_\mu + \bar{\nu}_\mu$ fluxes from astrophysical sources are shown. Also shown are the preliminary average upper limit as obtained with AMANDA-B10 (3), as well as the sensitivity of the proposed IceCube array after three years of operation. The atmospheric neutrino flux [59] in 2×2 degree bin is given as reference: (1) horizontal, (2) vertical. Models: (4) 3C273 pp neutrinos [60], (5) Crab Nebula [61], (6) Coma Cluster [62], (7) 3C273 $p\gamma$ neutrinos [63], (8) Supernova IC443 [64].

preliminary average neutrino flux limits are at a level of $dN/dE_\nu \sim 10^{-6} E_\nu^{-2}\,\mathrm{cm}^{-2}\,\mathrm{s}^{-1}\,\mathrm{GeV}^{-1}$.

The limit in case of Mrk501 is of particular interest. Here our neutrino flux limit is only about a factor of 10 above the gamma emission of this blazar, during its high state in 1997. The sensitivity of the AMANDA array is thus beginning to approach observed fluxes of gamma rays.

Figure 10 shows the expected neutrino fluxes from various sources, together with the current preliminary AMANDA upper limit (90% C.L.). The atmospheric neutrino background is given for a 2×2 degree bin. Detailed simulations have been performed of IceCube, the proposed km-scale neutrino array. The achievable upper limit for an assumed E^{-2}-type spectrum for point sources is indicated in the figure.

4.1.5 Gamma-Ray Bursts

According to the relativistic fireball model, gamma-ray bursts (GRBs) are expected to be astrophysical sources of high energy neutrinos. The expected neutrino event rate in AMANDA has been determined from a full MC simulation of the GRB signal and the detector. GRB neutrinos are generated following a broken power law energy-spectrum [78]. Figure 11 shows the energy spectrum of Monte Carlo events that triggered events in the AMANDA array. The search strategy has been optimized for this hypothetical signal. The number of expected events depends strongly on the assumed Lorentz factor. This scenario predicts event rates ranging from 10^{-4} events ($\Gamma = 1000$) to 1 event ($\Gamma = 100$) for the given data sample.

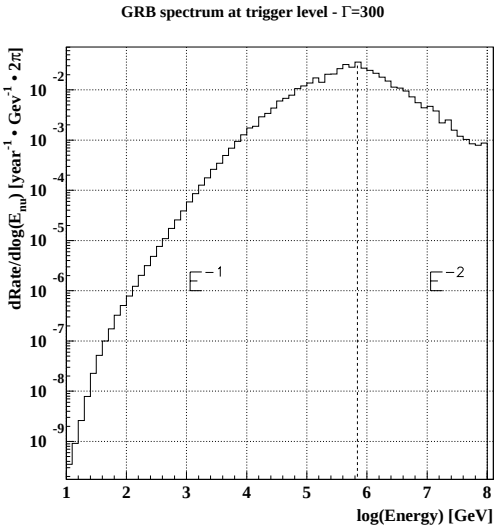

Figure 11: The energy spectrum of a neutrino flux as expected from gamma ray bursts triggered by AMANDA (Monte Carlo simulation).

With $\sim 1/3$ sky coverage, the BATSE satellite instrument detected 304 gamma-ray bursts in 1997. AMANDA data for 78 gamma-ray northern hemisphere bursts detected on-board the BATSE satellite were examined for coincident neutrino emission. Because the time window of

coincidence is rather short, typically of order 10 seconds per burst, there is very little background from cosmic rays and atmospheric neutrinos. No excess of neutrinos has been found above a background of 17.2 events for all 78 bursts.

4.1.6 WIMPs

AMANDA can be used to search for non-baryonic dark matter in the form of weakly interacting massive particles (WIMPs). The non observation of an excess of vertically upgoing muons has been used to set a limit on the flux of neutrinos from WIMP annihilations in the center of the Earth [79]. With only 132 days of exposure in 1997, AMANDA has reached a sensitivity in the region of high WIMP masses ($\geq$ 500 GeV) that begins to constrain the theoretically allowed parameter space. It is comparable in sensitivity to other detectors with much longer livetimes.

Figure 12 shows the present AMANDA limit after 132 days observation time in comparison with the limits obtained from long-year exposure of MACRO, Baksan and SuperK [80]. Note that the AMANDA limit is determined including (currently) large systematic uncertainties (the other experiments did not include their comparatively small uncertainties).

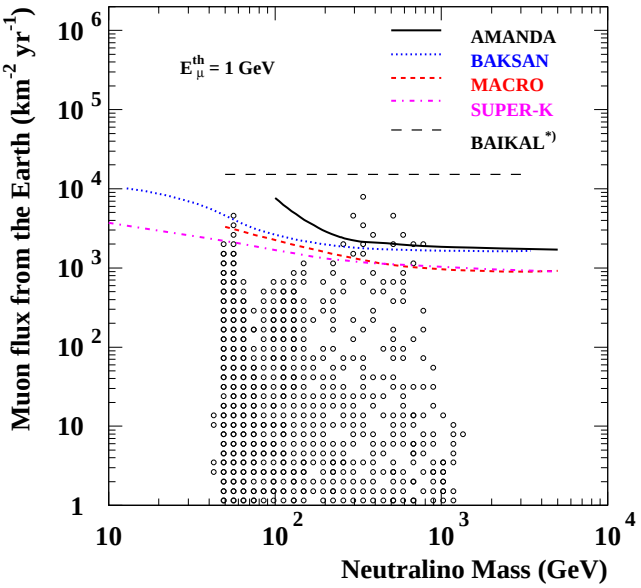

Figure 12: Upper limits on the flux of upgoing muons from WIMP annihilation in the Earth obtained in AMANDA, Baksan, Macro, Super-K and and Baikal (normalized to 1 GeV threshold). (Note: The Baikal limit is a muon flux limit from the center of the Earth, without MSSM model assumptions.)

4.1.7 Supernovae

By monitoring bursts of low energy neutrinos AMANDA can be used to detect the gravitational collapse of supernovae in the galaxy. This method takes advantage of the low noise characteristics (300–1500 Hz/PMT) of the optical sensors in the deep ice.

Figure 13 shows, for 215 days of live time in 1997/98 and all stable AMANDA-B10 PMTs, the distribution of the deviation $\Delta\mu$ of the average noise rate from its mean value. Each data point is the average over a 10 s interval. Accepting every 10 s interval with $\Delta\mu > 4$ Hz (see the vertical line) as a supernova event, would result in one fake alarm per year. This corresponds to a 90% efficiency for a SN-1987A-like supernova event loacted at a distance of 9.8 kpc (the distance to center of Galaxy is about 8 kpc). A robust on-line monitor could be operated with a slightly higher threshold covering about 70% of the Galaxy. With AMANDA-II and an improved supression of non-Poissonian noise we will monitor more than 90% of the Galaxy.

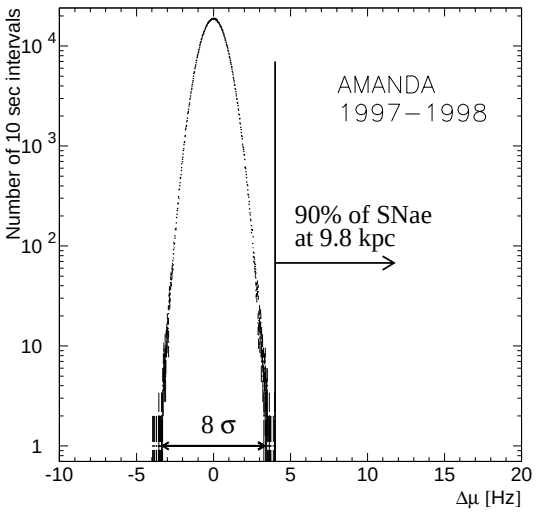

Figure 13: Distribution of the deviation $\Delta\mu$ of the average noise rate from its mean value, for 215 days of live time. The vertical line is set at the level where we get a rate of one background event per year. 90% of the supernova neutrino bursts located at 9.8 kpc distance would be seen above that cut.

4.1.8 Magnetic Monopoles

A magnetic monopole with unit magnetic Dirac charge and a velocity of β close to 1 would emit Cherenkov light along its path, exceeding that of of a bare relativistic muon by a factor of 8300. From the non-observation of events with this clear signature, a limit of $0.62 \cdot 10^{-16}$ cm^{-2} s^{-1} sr^{-1} for highly relativistic monopoles has been derived. This limit, illustrated in fig. 53, is a factor of 20 below the Parker bound and a factor of four below other best limits.

4.1.9 Summary of AMANDA Status

The detection of atmospheric neutrinos in agreement with expectation and the calibration of downgoing muons with surface detectors establish AMANDA-B10 as a neutrino telescope. Since February 2000, the significantly larger and improved AMANDA-II array has been collecting data. Its effective area for high energy neutrinos is about three times that of the AMANDA-B10 array. At the same time improved angular resolution and background rejection potential are available. The analysis of these data is under way and will improve the given results significantly.

5 Expected IceCube Performance

5.1 Introduction

In this section we describe how well the IceCube detector will perform and show that it will reach the scientific goals described in Section 3. This performance depends crucially on signal detection efficiency, background rejection, and calibration of the detector response to high-level variables such as energy and direction and low-level variables such as hit times and amplitudes. Therefore, estimates of IceCube signal sensitivities and limit levels for a variety of potential signals are given, as well as descriptions of techniques for high-level calibration of the detector response (low-level calibrations are discussed separately in section 7). We also describe studies of the detector configuration in order to maximize detector performance.

5.2 Atmospheric Neutrinos

The largest contribution to the ν flux from non-transient sources in the energy range of several hundreds of MeV to at least several hundreds of TeV is atmospheric neutrinos. The atmospheric ν flux is dominated by the muon component, increasing from a 2:1 $\nu_\mu : \nu_e$ ratio at low energies $E_\nu \sim 1$ GeV to 30:1 at $E_\nu \sim 100$ TeV so that the atmospheric ν "background" to UHE cascades is somewhat smaller than for UHE muons. The following sections will address the use of atmospheric neutrinos as a calibration source at lower energies, and their rejection as a background source at higher energies.

5.3 Muon-Neutrino-Induced Muons

5.3.1 Simulation

Muon events have been generated with the neutrino simulation package `nusim` [133, 134]. Neutrinos, sampled from an E_ν^{-1} spectrum, are propagated through the earth, taking full account of the earth's density profile. Neutral current regeneration of the neutrinos is treated exactly using a recursive propagation algorithm. Simulation of a generic E_ν^{-1} spectrum allows for the final events to be re-weighted to any desired neutrino source spectrum, whether it be an atmospheric neutrino spectrum ($E_\nu^{-3.7}$), a generic E_ν^{-2} spectrum for AGN neutrinos, or any other spectrum predicted in the literature.

The absorption of neutrinos in the Earth is an important effect, see fig. 14. For energies below a few tens of TeV, the full lower hemisphere is visible, whereas at energies above a few PeV the angular acceptance is reduced to zenith angles smaller than 30 degrees below horizon.

Neutrinos have been generated up to a maximum energy of 100 PeV which was set by technical limitations. Eight million events from downgoing muons which constitute the main source of background have been simulated and are used to demonstrate efficient background rejection. Muons were propagated with full simulation of stochastic energy loss. The detector

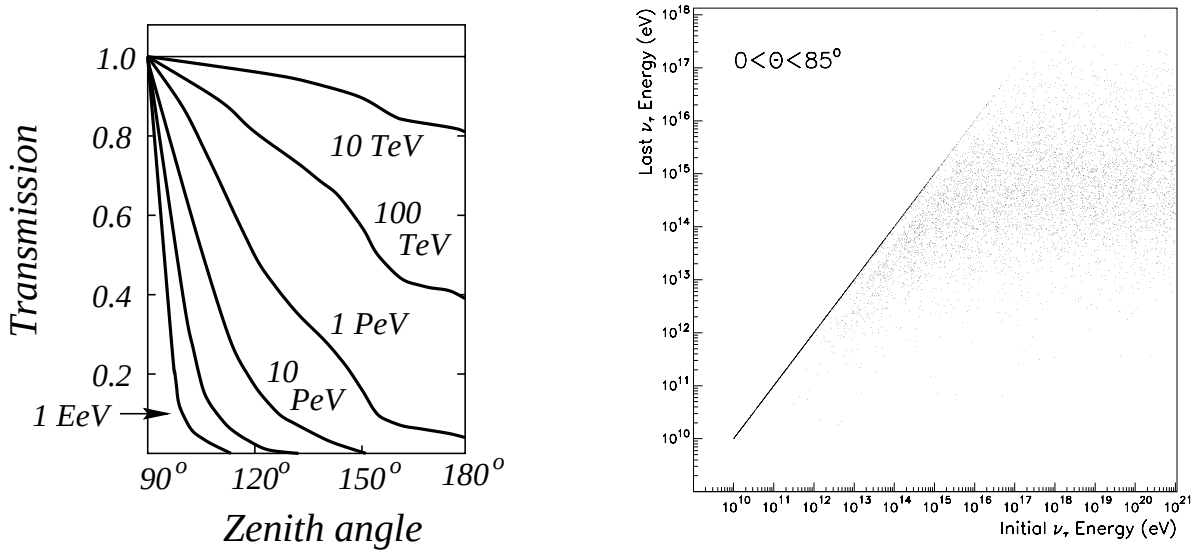

Figure 14: Left plot: Transmission coefficient of the Earth for electron and muon neutrinos as a function of energy and zenith angle [126]. Tau neutrinos have a transmission coefficient of $\sim$1 due to ν_τ regeneration effects, but their energies are degraded. Right plot: Energy of exiting ν_τ as a function of energy of entering ν_τ, showing effect of energy degradation due to passage through the Earth [42].

simulation was performed with the AMANDA simulation package `amasim`. Ice inhomogenities have been neglected for this study but will be included in the future. We simulated PMTs of 10 in diameter but did not take into account the possible increase in light collection efficiency due to a proposed wavelength shifter coating applied to the outer OM surfaces. The noise of the PMTs has been conservatively assumed to be 500 Hz (i.e. higher than the design goal of 300 Hz). A trigger was defined by the condition of at least 5 hits in a local coincidence. A local coincidence is defined with respect to the four nearest neighbors, and for a time window of 1 μs.

Signal Monte Carlo muon events are shown in figs. 15 and 16, where the muon energies are 10 TeV and 6 PeV, respectively.

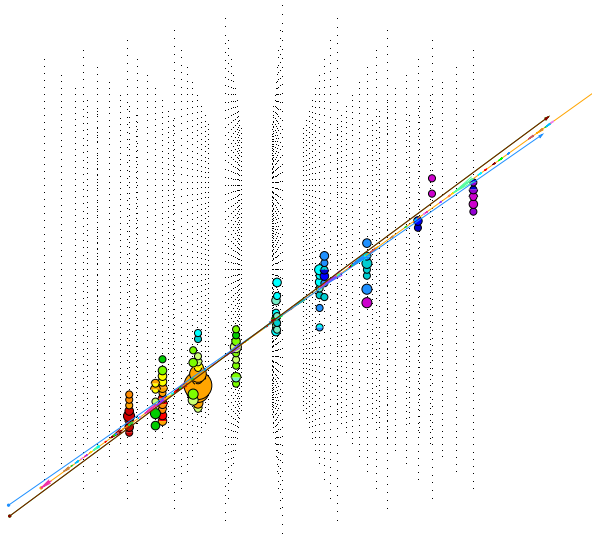

Figure 15: A simulated 10 TeV muon track in IceCube. Colored circles represent hit channels, with red circles hit earliest and violet circles latest. Circle size corresponds to number of detected photons.

5.3.2 Reconstruction and Background Rejection

The reconstruction was done in several steps using the AMANDA reconstruction package `recoos`. The start values for the full fit are obtained from two simple fast approximations called line-fit and dipole-fit (see [151] for details). As a first reduction step with respect to downgoing muons, relatively weak cuts on the zenith angle obtained from these fast approximations have been applied. These cuts have passing rates of 0.91, 0.78 and 0.04 with respect to the sample from AGN neutrinos, atmospheric neutrinos and downgoing muons, respectively.

Next, a full likelihood fit was performed (see [150] and [151]). This fit yields a series of parameters which can be used for selecting events with high quality reconstruction and for further reduction of background. The cuts chosen are the following:

- zenith angle θ obtained from the likelihood fit larger than 85°, and $-\log L < 10$, where L is the likelihood;

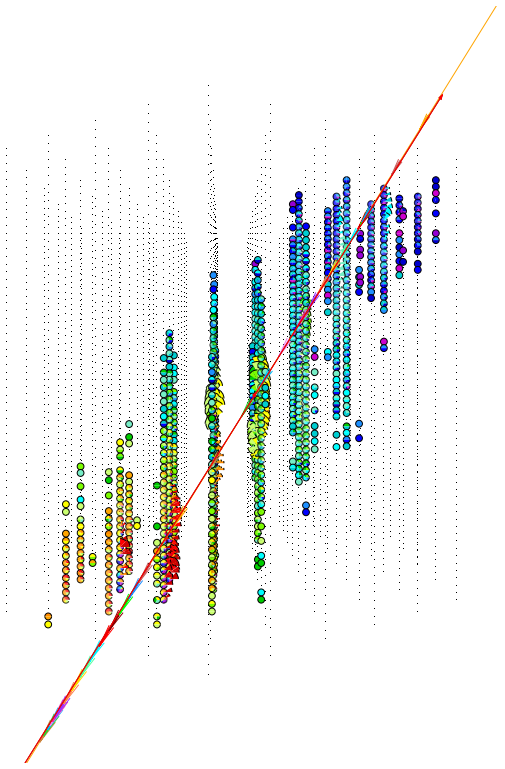

Figure 16: A simulated 6 PeV muon track in IceCube. Colored circles represent hit channels, with red circles hit earliest and violet circles latest. Circle size corresponds to number of detected photons.

- ≥ 5 hits with a time residual between –15 ns and +150 ns ("direct hits"), where the photon did not undergo many scattering interactions);
- length of the projection of the direct-hit OMs to the reconstructed track larger than 150 m;
- difference between the zenith angles obtained from line fit and likelihood fit smaller than 10 degrees;
- the absolute value of the *smoothness*, smaller than 0.5.[1]

Note that the standard cuts listed above result in a passing rate of 53% for AGN neutrinos and reduce the background from downgoing muons by $3 \cdot 10^{-6}$. As shown in fig. 17, this background is concentrated close to the horizon. It can be easily rejected by a further zenith cut (if lower energies should be accepted), or by cuts on the number of channels (if one focuses to the separation of higher energies). Figure 17 also shows the background from uncorrelated coincident air showers (bottom right) which can produce two hit clusters, and earlier one at the bottom and a later one at the top of the array. Such events are not rejected by a simple angular cut, giving the relatively high passing rate after angular cuts compared to muons from single air showers. However, these events are easily identified by the subsequent cuts, in particular the cut on the smoothness.

Results are shown for the "standard configuration" (triangular pattern, 16 m vertical spacing[2], 125 m interstring distance). Numbers at the top corner give the number of events and the passing rates. For AGN neutrinos, a flux of $2 \times 10^{-7} \cdot E^{-2}$ GeV^{-1} cm^{-2} s^{-1} sr^{-1} has been assumed, resulting in 4265 events.[3]

We have investigated the physics performance of the IceCube detector for different configurations, starting from the default configuration and going into the direction of both smaller and larger spacings [139]. Early results on similar IceCube simulations have been presented in [124, 125]. Whereas in [139] only configurations with about 5000 OMs and equidistant spacing are considered [124, 125] cover also options with twice or half the number of OMs, and nested configurations.

The basic pattern is shown in fig. 18. Apart from the triangular pattern, we also simulated rectangular patterns, which yield similar results. The circle in fig. 18 indicates an area of one square kilometer. The configuration includes 80 strings and 60 OMs per string. For a vertical spacing of 16 m, this results in an instrumented length of 944 m. The top layer of OMs was assumed to be at a depth of 1400 m. Table 2 summarizes the studied configurations.

The two following tables give the number of triggered and accepted events per year for the various configurations. Table 3 gives results for atmospheric neutrinos. Numbers in table 4 are for AGN neutrinos, again assuming a flux of $2 \times 10^{-7} \cdot E^{-2}$ GeV^{-1} cm^{-2} s^{-1} sr^{-1}. The upper

[1] The smoothness S measures the homogenity of the distribution of hits along the track. Exactly equidistant hits would give $S = 0$, all hits at the starting point of the track $S = +1$ and all hits at the endpoint $S = -1$.

[2] The 16 m vertical spacing was chosen for this study before 17 m became the baseline design.

[3] An AGN neutrino flux of roughly $10^{-7} \cdot E^{-2}$GeV^{-1} cm^{-2} s^{-1} sr^{-1} is roughly the flux to which AMANDA is sensitive. It is otherwise arbitrary.

vertical / horizontal	100 m	125 m	150 m	175 m
12 m	X	X	X	-
16 m	X	X	X	-
20 m	X	X	X	X

Table 2: Simulated configurations. Columns indicate different string spacings, rows different spacings of OMs along a string. An "X" indicates that the particular configuration was simulated.

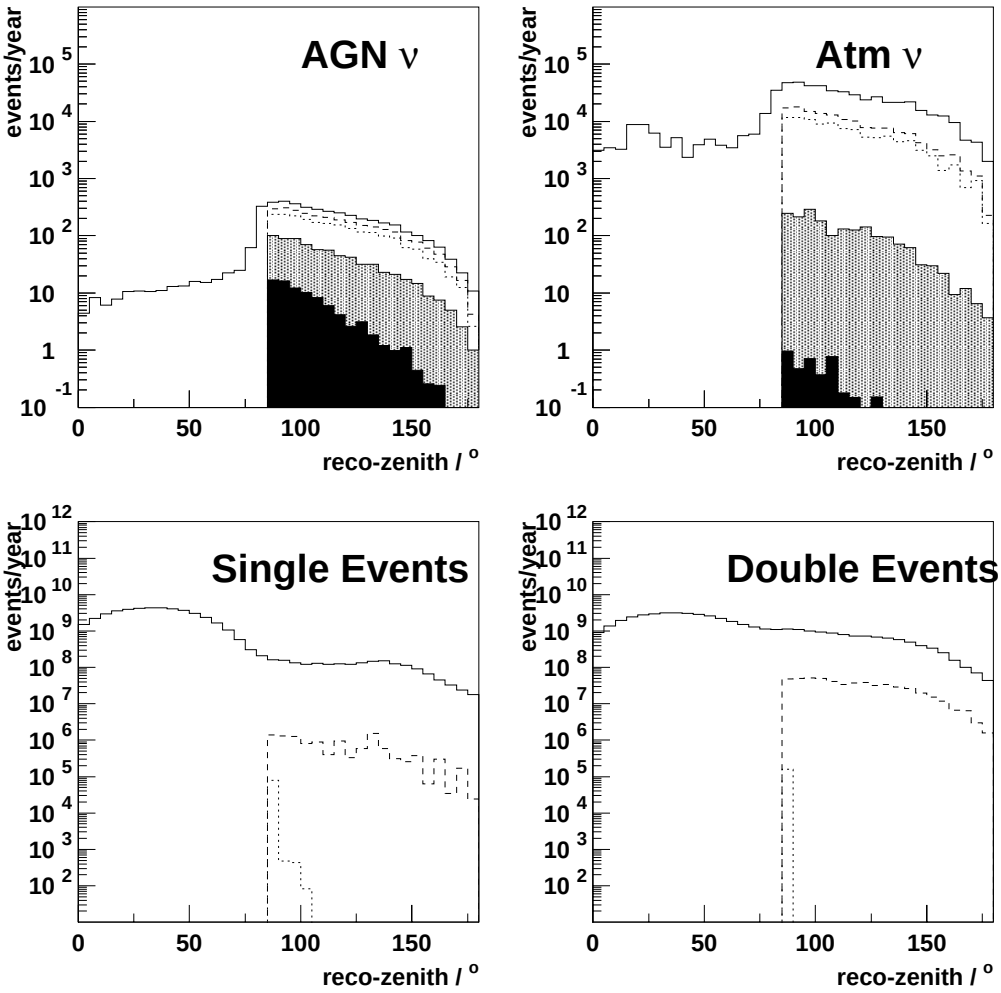

Figure 17: Distribution of the reconstructed zenith angle after trigger (full upper line), and the 3 cuts on the zenith angles (dashed line), the remaining four quality cuts (dotted line). The shaded histogram gives the energy spectrum after an additional cut on the number of hit PMTs at $N_{ch} > 50$. The dark histogram corresponds to a cut at $N_{ch} > 180$. The bottom histograms show the background expected from single air showers (left) and from accidentally coinciding air showers (right). Note that neutrinos have been generated only between 80 and 180 degrees, hence the cut-off at 80 degrees after quality cuts.

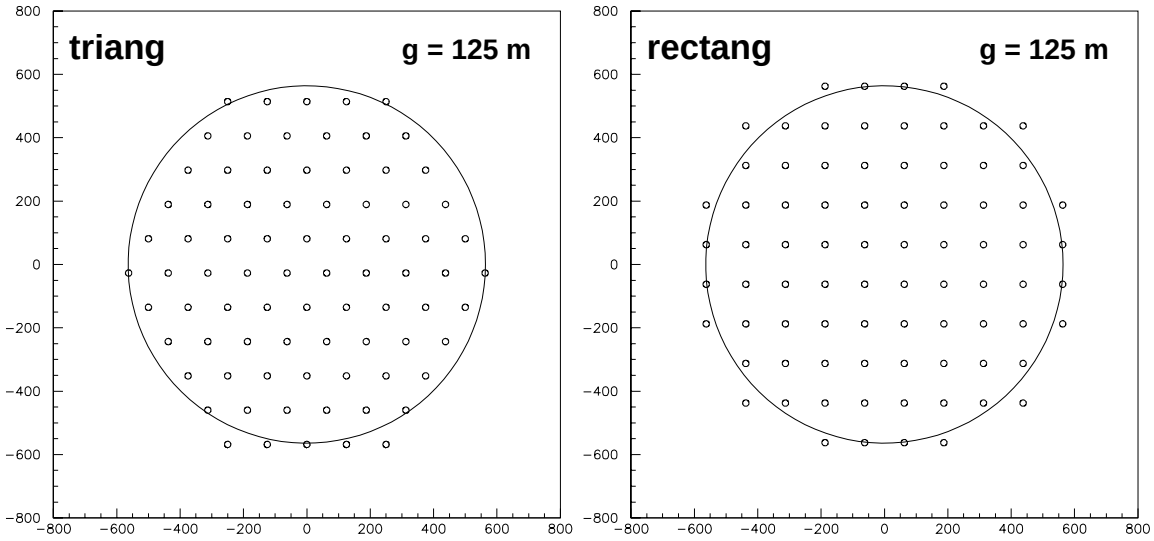

Figure 18: Top view of the two principal string patterns investigated here. *left:* triangular pattern, *right:* rectangular pattern (both shown for a string spacing of 125 m). Scales are in meters.

vertical/horizontal	100 m	125 m	150 m	175 m
12 m	2.9 k	3.6 k	4.3 k	-
	1.5 k	*1.8 k*	*2.2 k*	-
16 m	3.4 k	4.3 k	5.5 k	-
	1.9 k	*2.3 k*	*2.5 k*	-
20 m	4.0 k	4.9 k	5.7 k	6.5 k
	2.1 k	*2.4 k*	*2.6 k*	*2.8 k*

Table 4: Number of triggered and accepted neutrino events per year (in thousands) assuming a flux of $2 \times 10^{-7} \cdot E^{-2}$ GeV^{-1} cm^{-2} s^{-1} sr^{-1}. The upper numbers refer to triggered events, the lower numbers in italics to the events after quality cuts.

numbers refer to triggered events, the lower numbers (in italics) to events after reconstruction and quality cuts.

vertical/horizontal	100 m	125 m	150 m	175 m
12 m	600 k	620 k	640 k	-
	140 k	*130 k*	*120 k*	-
16 m	590 k	600 k	620 k	-
	140 k	*130 k*	*110 k*	-
20 m	580 k	590 k	600 k	560 k
	140 k	*110 k*	*90 k*	*60 k*

Table 3: Number of triggered and accepted events per year for atmospheric neutrinos (in thousands). The upper numbers refer to triggered events, the lower numbers in italics to the events after quality cuts.

Clearly, larger spacing is preferable for the AGN case but tends to suppress more atmospheric neutrinos after quality cuts. Going from 125 m string spacing to 150 m gives a 10% increase in accepted AGN events. The rectangular configuration gives a 5% increase in events rate. Decreasing the spacing to 12 m/100 m gives 30% loss in AGN neutrinos, but a slight increase for atmospheric neutrinos. The angular resolution for all configurations is ≤ 1 degree.

5.3.3 Sensitivity to Diffuse Sources of Muon Neutrinos

We calculate the sensitivity of the detector to diffuse fluxes of neutrinos with a generic E^{-2} spectrum, expected for sources such as active galactic nuclei (AGN). For the purposes of these calculations we assume a source strength for muon-neutrinos and antineutrinos of a level $\mathrm{E}^2 \mathrm{d}N/dE = 10^{-7} \mathrm{GeV\,cm^{-2}\,s^{-1}\,sr^{-1}}$. We use the Model Rejection Potential formalism [132, 135], and the associated "model rejection factor" (MRF), to optimize the limit analysis. Figure 19 shows the results of the minimization of the MRF for the hit multiplicity (N_{ch}) cut and an exposure time of three years. The top left figure shows the differential numbers of events expected for both the E^{-2} spectrum (blue solid line) and for the atmospheric neutrinos (red dashed line). The top right plot shows the same quantities as an integral distribution. Also shown is the Feldman-Cousins 90% confidence level average upper limit. As the background falls toward zero, this classical average upper limit converges toward a value of 2.44. The best limit is obtained where the model rejection factor, $(\bar{\mu}(n_b)/n_s)$, is minimised (bottom left plot).This occurs for a cut of 168 channels, where 120.9 signal events would be expected upon a background of 17.2. The average upper limit for this background is 8.4, leading to a MRF $= 6.9 \times 10^{-2}$, and therefore to a flux limit of $\mathrm{E}^2 dN/dE = 6.9 \times 10^{-7} \mathrm{GeV\,cm^{-2}\,s^{-1}\,sr^{-1}}$. The bottom right plot shows the parent neutrino energy distribution for those events with multiplicity above the optimal cut of 168 channels. The multiplicity cut corresponds to a minimum energy of about 30 TeV, and to a typical neutrino energy of 1 PeV. Table 5 summarises the results of the MRF optimization for exposure times of one and three years.

time (yrs)	N_{ch} cut	$S(\geq N_{ch})$	$B(\geq N_{ch})$	$\bar{\mu}(B(\geq N_{ch}))$	limit $(= E^{-2}dN/dE \times \frac{\mu}{S})$
1	175	53.1	5.4	5.3	1.0×10^{-8}
3	221	93.1	3.2	4.5	4.8×10^{-9}

Table 5: IceCube model rejection factor for an $E^2 dN/dE = 10^{-7}\mathrm{cm}^{-2}\mathrm{s}^{-1}\mathrm{sr}^{-1}\mathrm{GeV}^2$ flux as a function of exposure time.

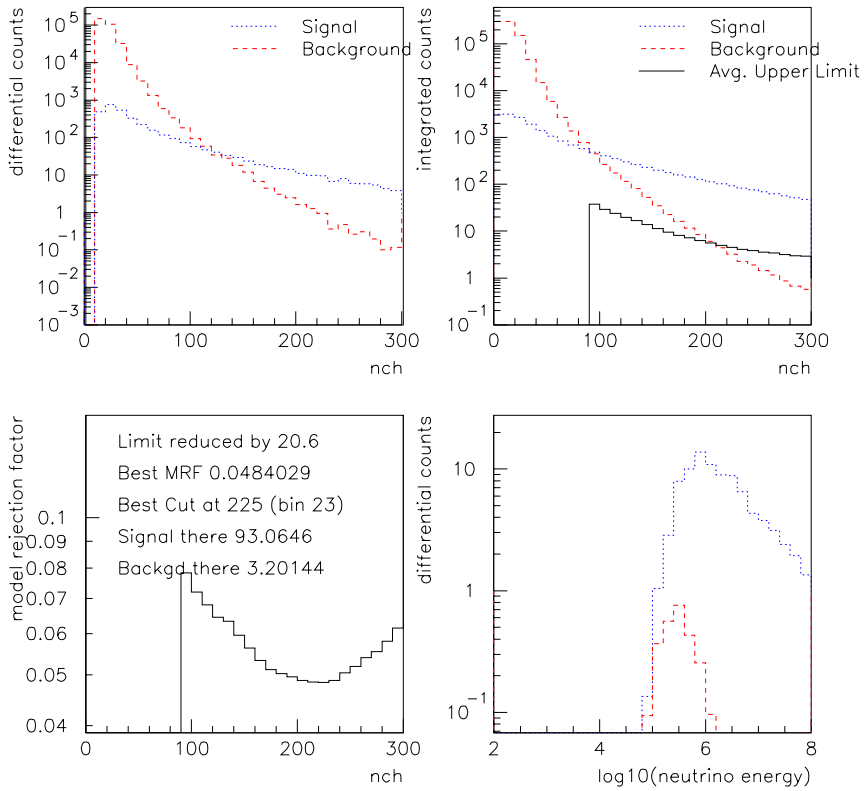

Figure 19: Model rejection potential optimization for a diffuse flux: *Top left:* differential N_{ch} distribution for atmospheric neutrinos (dashed histogram) and AGN neutrinos (full histogram), assuming a flux of $10^{-7} \cdot E^{-2}\,\mathrm{GeV}^{-1}\,\mathrm{cm}^{-2}\,\mathrm{s}^{-1}\,\mathrm{sr}^{-1}$ for AGN neutrinos. *Top right:* integral N_{ch} distribution, with the average upper limit shown as a solid line. *Bottom left:* Model rejection factor. *Bottom right:* Distribution of neutrino energies for those events with hit multiplicity N_{ch} greater than the optimal cut. We see that the N_{ch} cut corresponds to neutrino energies greater than ~ 30 TeV and that the detector is sensitive to diffuse E^{-2} neutrinos of energy of order 1 PeV (solid blue line). The red dashed line shows the energies of the atmospheric neutrinos that pass the cuts.

5.3.4 Sensitivity to Muon Neutrino Point Sources

The sensitivity of IceCube for point sources of neutrinos has been assessed. Since the background may be greatly reduced by cutting to a small angular region about the direction of the point source, the multiplicity cut (N_{ch}) can be relaxed. The sensitivity has been checked in two ways, first by averaging the sensitivity over the upward going hemisphere, and second by looking at a point source from a specific zenith angle.

For each exposure time tested, we optimise in both angular bin size and N_{ch}. Figure 20 shows the pointing accuracy of the array. Ninety percent of events reconstruct to within 4° of the true direction, and 60% to within 1°. The MRF results from varying angular bin and exposure time are shown in table 6. These show that a signal strength of the level $dN/dE = 10^{-7}\mathrm{cm}^{-2}\mathrm{s}^{-1}\mathrm{sr}^{-1}\mathrm{GeV}^{2}$ would produce a very significant signal in IceCube, and in its absence, very constrained upper limits would be obtained. For both exposure times, the best choice of angular cut is about 1°, but the limit is ultimately not very sensitive to the choice of angular cut, suggesting that a smaller cut, to enhance the significance of a possible observation, may be warranted. Although the cuts have been optimised to minimise the MRF, thereby optimising the limit setting potential of the detector, we can make some basic estimates of the level of a point source flux needed to give a significant detection of a signal in the exposure time. A chance probability of $\sim 10^{-7}$ for a background fluctuation corresponds roughly to a "5 sigma" observation. For any quoted background level, we can calculate the number of events needed to get this chance probability. For the case of 1 year exposure with a 1° angular bin, the expected background is 0.53 events. If 8 events were observed, this would give the required chance probability of $\sim 10^{-7}$. A signal strength of $8 - 0.5 = 7.5$ events is about 1/5 of the number of events expected from the $dN/dE = 10^{-7}\mathrm{cm}^{-2}\mathrm{s}^{-1}\mathrm{sr}^{-1}\mathrm{GeV}^{2}$ flux, therefore a point source of level $dN/dE \sim 2 \times 10^{-8}\mathrm{cm}^{-2}\mathrm{s}^{-1}\mathrm{sr}^{-1}\mathrm{GeV}^{2}$ would be required to produce a "5 sigma" observation in one year of live time. Of course, this analysis assumes that we only look at a single candidate source. If we do a full sky search, we must pay a penalty for statistical trials. There are about 6500 bins of 1° radius in a half sky (upgoing neutrino) search, so a significance of $\sim 10^{-9}$ would be needed for an unknown point source to give a $\sim 10^{-7}$ result after the trials are accounted for. This requires that about 10 events are observed (the chance probability to observe 10 or more events from a backgrpound of 0.53 is 3×10^{-10}), increasing the required signal strength by about 30%.

Table 7 shows the MRF results for a point source at a zenith angle of 130°. The limit setting potential is slightly less than the average seen in table 6. Figure 21 shows the model rejection potential optimization for a point source.

5.3.5 Sensitivity to Muon Neutrinos from Gamma-Ray Bursts

Recently, Waxman and Bahcall [94] have proposed that gamma-ray bursts (GRBs) might be sources of neutrinos. The search for neutrinos from GRBs is simplified over that of a point source, due to the time stamp available from satellite observations of the gamma rays from the burst. In the Waxman-Bahcall model the neutrinos are expected to arrive within approximately

t (y)	$\Delta\psi$	N_{ch} cut	$S(\geq N_{ch})$	$B(\geq N_{ch})$	$\bar{\mu}(B(\geq N_{ch}))$	limit $(= E^{-2}dN/dE \times \frac{\mu}{S})$
1	0.5	25.5	43.1	0.53	2.9	6.7×10^{-9}
1	**1.0**	**32.5**	**60.6**	**0.91**	**3.2**	$\mathbf{5.3 \times 10^{-9}}$
1	2.0	42.5	55.6	1.10	3.4	6.0×10^{-9}
1	5.0	55.5	43.9	2.20	4.0	9.0×10^{-9}
3	0.5	32.5	110.2	0.67	3.0	2.7×10^{-9}
3	**1.0**	**42.5**	**137.6**	**0.82**	**3.1**	$\mathbf{2.3 \times 10^{-9}}$
3	2.0	53.5	128.8	1.25	3.5	2.7×10^{-9}

Table 6: IceCube model rejection factor for a point source, averaged over zenith angles $90-180^\circ$ with flux $E^2dN/dE = 10^{-7}\mathrm{cm}^{-2}\mathrm{s}^{-1}\mathrm{GeV}^2$. The optimum choice of cuts for both exposure times are highlighted in bold.

time (yrs)	$\Delta\psi$	N_{ch} cut	$S(\geq N_{ch})$	$B(\geq N_{ch})$	$\bar{\mu}(B(\geq N_{ch}))$	limit $(= E^{-2}dN/dE \times \frac{\mu}{S})$
1	0.5	24.5	36.6	0.71	3.0	8.2×10^{-9}
1	**1.0**	**33.5**	**47.7**	**1.0**	**3.3**	$\mathbf{6.9 \times 10^{-9}}$
1	2.0	41.5	45.8	2.2	4.0	8.8×10^{-9}
1	5.0	64.5	25.6	1.6	3.7	1.4×10^{-8}
3	0.5	29.5	98.0	1.2	3.4	3.5×10^{-9}
3	**1.0**	**33.5**	**143.2**	**3.0**	**4.4**	$\mathbf{3.1 \times 10^{-9}}$
3	2.0	42.5	132.8	5.8	5.5	4.1×10^{-9}

Table 7: IceCube model rejection factor for an point source at 130° zenith angle, with flux $E^2dN/dE = 10^{-7}\mathrm{cm}^{-2}\mathrm{s}^{-1}\mathrm{GeV}^2$.

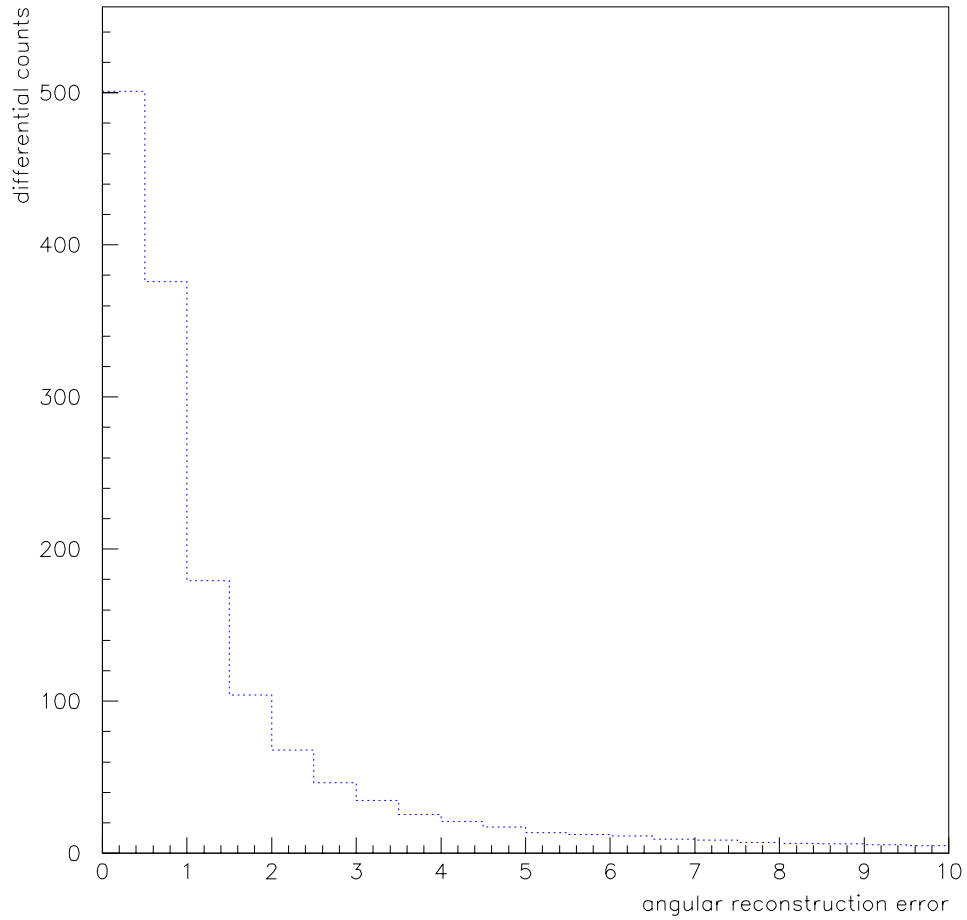

Figure 20: IceCube angular resolution for E^{-2} point sources: 80% of events reconstruct to within 2° of the true direction.

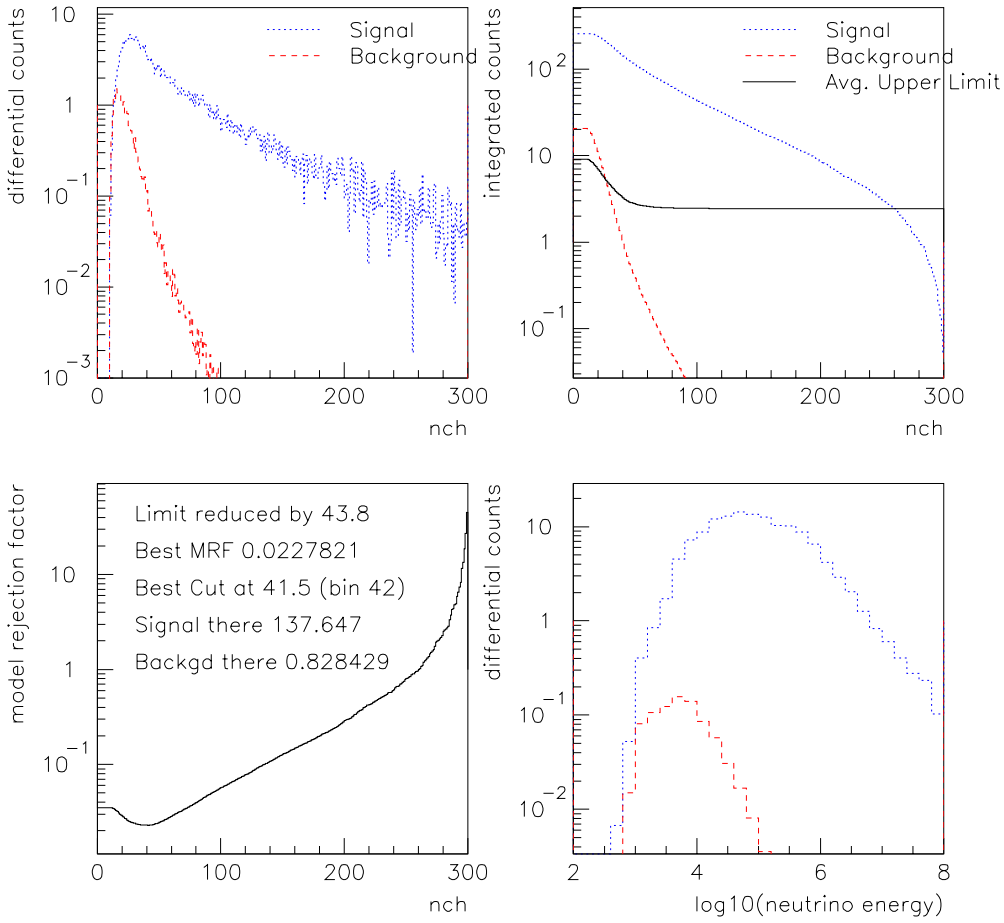

Figure 21: Model rejection potential optimization for a point source: *Top left:* differential N_{ch} distribution for atmospheric neutrinos (dashed histogram) and AGN neutrinos (full histogram), assuming a flux of $10^{-7} \cdot E^{-2}$ GeV^{-1} cm^{-2} s^{-1} sr^{-1} for AGN neutrinos. *Top right:* integral N_{ch} distribution. Solid line – average upper limit *Bottom left:* Model rejection factor. *Bottom right:* Distribution of neutrino energies for those events with hit multiplicity N_{ch} greater than the optimal cut. We see that the N_{ch} cut corresponds to neutrino energies greater than $\sim$ 1 TeV and that the detector is sensitive to diffuse E^{-2} neutrinos of energy of order 100 TeV (solid blue line). The red dashed line shows the energies of the atmospheric neutrinos that pass the cuts.

10 seconds of the gamma rays. The IceCube detector will reconstruct neutrino-induced muons from GRBs to less than ten degrees of the true direction (fig. 22).

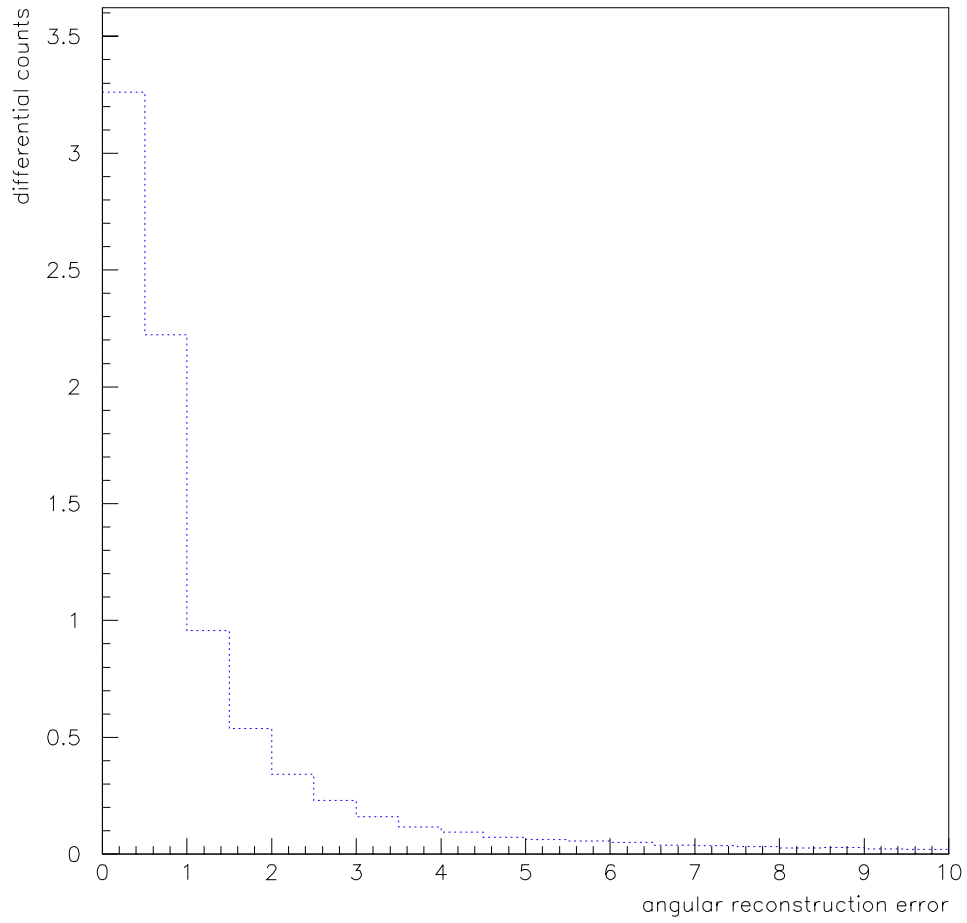

Figure 22: IceCube angular resolution for gamma-ray bursts.

The Waxman-Bahcall flux corresponds to the expected neutrino flux from 1000 GRBs. Within a 10° angular search bin and 10 second time window, we would expect a total of 15 upgoing muon events from 1000 GRBs after quality cuts were applied to remove the most obvious mis-reconstructed downgoing muons. The atmospheric neutrino background is negligible (total 0.32 events) but about 500 misreconstructed downgoing muons would remain. Tightening the cuts to the final cut set discussed previously removes the last of the muon background, reduces the atmospheric neutrino background to 0.23 events, and retains 12 GRB induced neu-

trino events. It should be noted that more Monte-Carlo simulations are needed to further check the belief that the background of mis-reconstructed downgoing muons is indeed zero.

Optimising the N_{ch} cut leads to a cut of $N_{ch} = 12.5$ and model rejection factor of 0.22, a severe constraint on the Waxman-Bahcall model. Since the GRB search is essentially background free, the improvement in the limit goes nearly linearly with the increasing number of GRBs searched. This behaviour is shown in table 8. It is interesting that the observation of only 210 GRBs is enough to rule out the Waxman-Bahcall model at 90% classical confidence.

Since the angular cut and time window search can be made so tight, the GRB searches are close to background-free. Then the observation of even a few events would be very significant. For 300 GRBs searched, and a 2°, window, the Waxman-Bahcall model predicts about 3 events, on an atmospheric neutrino background of 0.003. The chance probability of observing 3 or greater events given a background of 0.003 is about 5×10^{-9}.

Table 8 shows that the MRF is insensitive to the choice of angular bin size. In this case, a choice of a smaller search window would be preferred, in order to reduce the background (for limited signal loss) and give a more significant observation of a potential signal. Ultimately however, the uncertainty in the knowledge of the GRB direction (from the satellite observation) will limit how small the angular search bin can be made. Figure 23 shows the model rejection potential optimization for GRBs.

n_{bursts}	$\Delta\psi$	N_{ch} cut	$S(\geq N_{ch})$	$B(\geq N_{ch})$	$\bar{\mu}(B(\geq N_{ch}))$	limit $(= E^{-2}dN/dE \times \frac{\mu}{S})$
100	2.0	1.5	0.98	0.001	2.4	2.49
	5.0	1.5	1.13	0.005	2.4	2.16
	10.0	1.5	1.19	0.02	2.46	2.06
	20.0	1.5	1.20	0.086	2.51	2.07
	30.0	12.5	1.22	0.19	2.60	2.12
210	10	1.5	2.50	0.045	2.49	0.99
300	2.0	1.5	2.94	0.003	2.44	0.829
	5.0	1.5	3.40	0.016	2.45	0.721
	10.0	1.5	3.51	0.065	2.46	0.70
	20.0	1.5	3.66	0.26	2.66	0.72
1000	2.0	1.5	9.81	0.009	2.45	0.249
	5.0	1.5	11.34	0.05	2.48	0.219
	10.0	12.5	11.9	0.215	2.62	0.22
	20.0	20.5	11.3	0.471	2.83	0.25

Table 8: IceCube model rejection factor for a Gamma-ray burst search.

5.3.6 Possible Improvements

The sensitivities given above could change in reality. We estimate that uncertainties in ice modelling might change them by up to 50%–in either direction. Use of an energy estimator

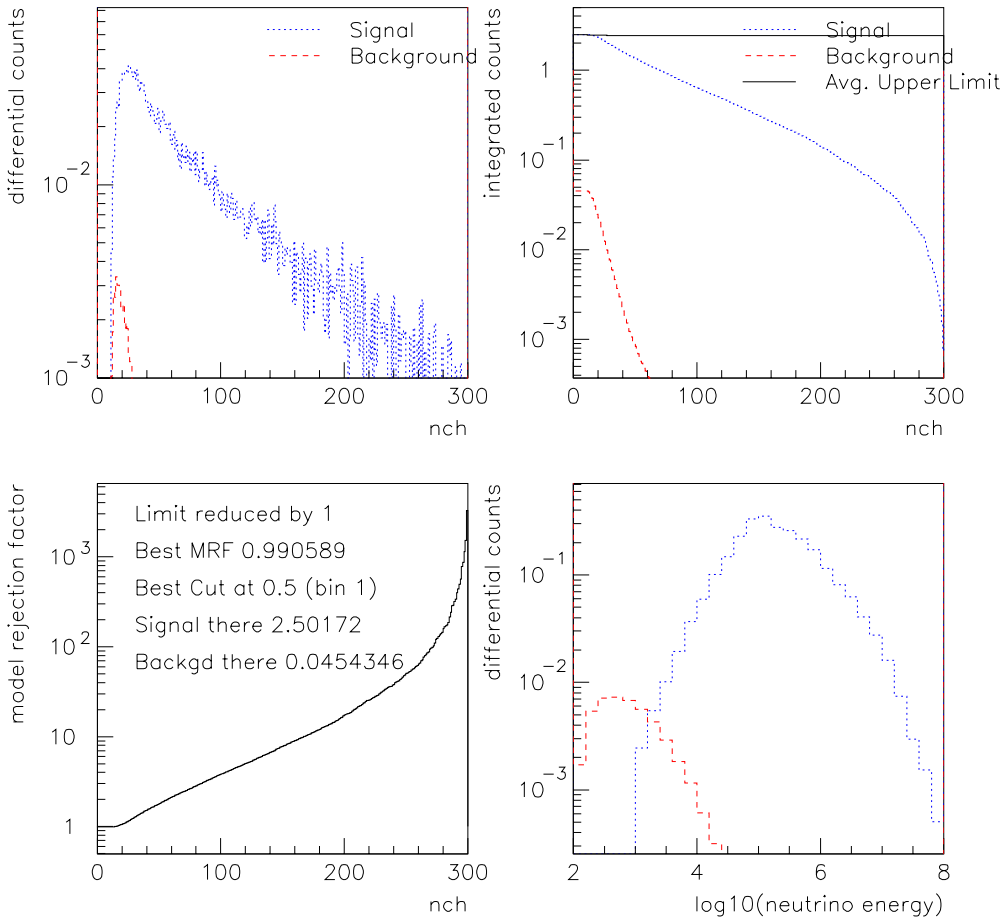

Figure 23: Model rejection potential optimization for gamma-ray bursts: *Top left:* differential N_{ch} distribution for atmospheric neutrinos (dashed histogram) and WB GRBs (full histogram). *Top right:* integral N_{ch} distribution. Dotted line – average upper limit. *Bottom left:* model rejection factor. *Bottom right:* Distribution of neutrino energies for those events with hit multiplicity N_{ch} greater than the optimal cut. We see that the N_{ch} cut corresponds to neutrino energies greater than ~ 1 TeV and that the detector is sensitive to diffuse E^{-2} neutrinos of energy of order 100 TeV (dashed blue line). The red dashed line shows the energies of the atmospheric neutrinos that pass the cuts.

better than N_{ch} may result in an improvement of up to 30%. Use of wavelength shifter could enhance the sensitivity of the OMs by up to 35% and result in higher signal efficiency and improved background rejection. The application of reconstruction methods which make use of the full waveform instead of using only the time of the first arriving photon will lead to a better angular reconstruction, in particular for high-energy events (see Section 5.6). We hope to reach an accuracy of about 0.5 degrees for moderate cuts, resulting in a slightly better point source sensitivity. Neutrinos with >100 PeV have not been taken into account in the present simulation. Their inclusion will also result in a better limit. Other lines of improvement are selection of cuts with a better passing rate for for AGN neutrinos (giving possibly a 10–15% effect), and a change of the configuration to larger spacing, which is discussed in section 5.8.

5.4 Electromagnetic and Hadronic Cascades

The charged current interaction of UHE electron neutrinos and the neutral current interactions of UHE neutrinos of all active flavors will produce large localized depositions of energy in the IceCube detector. The signature of these electromagnetic or hadronic showers (cascades) is a bright, pointlike source of Čerenkov light[4] as shown in fig. 24. To be detected, cascades must occur near or within the active detector volume, and consequently the effective volume for their detection is substantially smaller than that of muons. However, cascades have the advantage that their energies can be measured more accurately than muon events, making it easier to separate UHE cascades from background. This is especially true for ν_{e} charged current and "double bang" ν_τ interactions, where the resulting cascades give a fairly accurate measure of the energy of the parent neutrino.

5.4.1 Simulation

Cascade events were generated using one of three generators depending on the study:

- Reconstruction studies and effective volume calculations were performed using a very simple Perl script which throws isotropic cascade vertices uniformly throughout a cylindrical volume 1.5 km tall and 1.5 km in radius surrounding the detector. These events are generated with a E_{cas}^{-1} energy spectrum from 100 GeV to 1 EeV.

- The atmospheric neutrino signal was generated by `casim`, a weighted Monte Carlo package which produces cascade events with a E_{cas}^{-1} spectrum from 10 GeV to 100 TeV. The atmospheric neutrino flux is taken from Lipari [95]. The weight of each event is recorded to allow biasing back to the physical energy spectrum.

- The expected signal for ultrahigh-energy cascades from diffuse sources or GRBs was simulated using code which propagates a given neutrino flux through the Earth, taking into

[4]The pointlike approximation for cascades holds to very high energies as the logitudinal development of the shower is only logarithmically dependent on the shower energy.

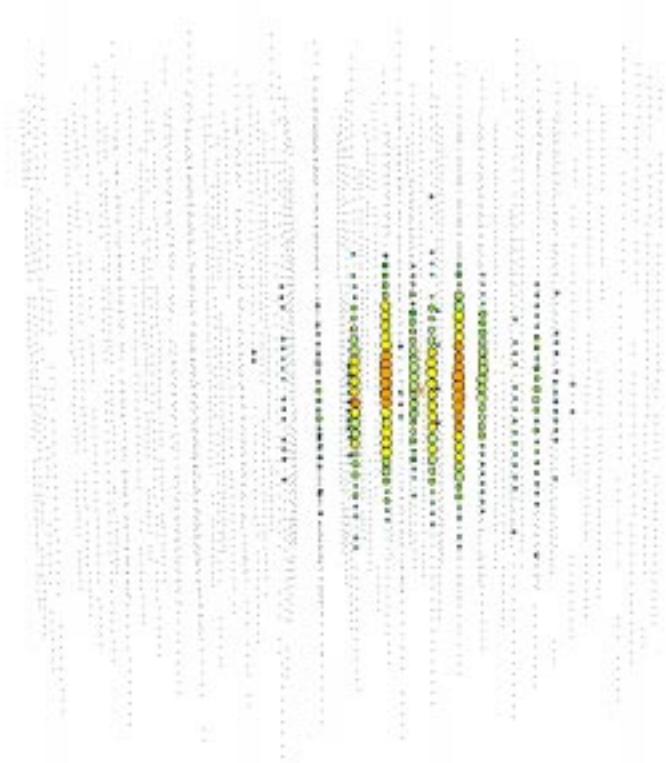

Figure 24: A 375 TeV cascade in IceCube. Colored circles represent hit channels, with red circles hit earliest and violet circles latest. Circle size corresponds to number of detected photons.

account both neutrino absorption and neutral-current regeneration and generates neutrino-nucleus interaction vertices in a homogeneous volume of ice surrounding the detector over the full 4π steradians of solid angle. In order to realistically simulate the overburden of material in the upper hemisphere, the simulation code models the south polar ice as a spherical cap on the Earth. This package generates unweighted events. Several energy spectra were sampled for 100 GeV $< E_\nu <$ 1 EeV, each corresponding to a distinct astrophysical source models. They are dealt with in finer detail in the appropriate sections.

These vertices are then passed to the detector simulation package, `amasim`, which generates PMT hits in the array and builds them into events. Triggers were generated on a coincidence of five hits in 2.5 μs. Additionally, a feature of `amasim` was enabled that preserves pulse amplitude information for each pulse in the event that a single OM receives multiple hits. [5] This additional information approximated waveform readout in IceCube.

5.4.2 Reconstruction

Applying algorithms developed for AMANDA on simulated IceCube data, we have estimated the vertex, direction, and energy resolutions of cascades in IceCube. We have also estimated these resolutions using newly developed algorithms tailored to IceCube data. Estimates using AMANDA algorithms are conservative since they rely primarily on the arrival times of the first photons in each PMT, while in IceCube we will have access to much more detailed waveform information. Estimates using new algorithms are also conservative since we anticipate using the waveform information in a more complete manner than presented here.

The AMANDA algorithm for reconstructing the vertex position and time is based on a model of the scattering and absorption of Čerenkov light in the ice. It maximizes a likelihood function which depends on a parametrization of the probability distribution of observing one photon with a given time delay at some distance from the source. The AMANDA algorithm for reconstructing direction and energy is also a maximum likelihood fit which uses a parametrization of the expected number of photons at each PMT as a function of cascade energy and the relative cascade-PMT direction.

Applying these algorithms to simulated IceCube cascades with contained vertex positions (vertices at least 100 m from the edge of the detector), resulted in energy and zenith angle resolutions which were better than in AMANDA. The resolutions are as follows:

- Energy: 11% in $\log_{10}$ E (AMANDA: >40%)
- Zenith: 27° in zenith angle (AMANDA: 27°)
- Vertex: 3 m in x, y; 2 m in z (AMANDA: 6.4 m in x, y; 5.3 m in z)

These resolutions are illustrated in fig. 25.

[5] In AMANDA, the peak ADC hardware only records a single peak value per ADC gate, and thus, normally, the multiple pulse information is suppressed in `amasim`.

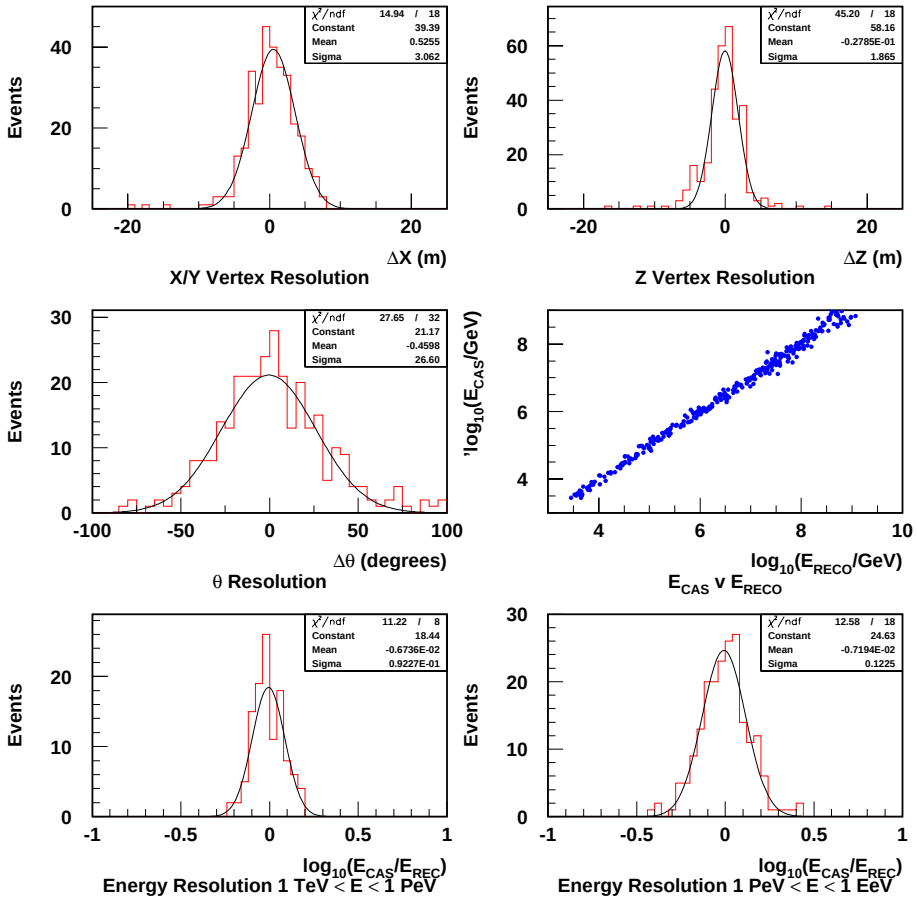

Figure 25: Vertex, direction, and energy resolutions for simulated IceCube cascades, using AMANDA multiphoton reconstruction algorithms. These reconstructions are evaluated after all cuts which are listed later in the subsection 5.4.2 on background rejection.

Ultimately, we anticipate that we will construct a likelihood function which uses the full waveform information from each PMT, maximizing the probability that each PMT observed a particular waveform as a function of cascade ($\vec{r}$,t,E,$\vec{d}$). Moreover, waveform readout will dramatically increase the dynamic range of the PMTs. Cascade reconstructions in particular would benefit from this enhancement due to the nature of the cascade signal: OMs very close to the cascade vertex are expected to receive thousands of Čerenkov γs, but simultaneously the detector must be able to resolve the single γ hits at large distances for accurate energy reconstruction.

Techniques for suppressing the cosmic ray muon events in IceCube have been borrowed from AMANDA cascade analyses. The very large instrumented volume of IceCube makes cosmic-ray muon rejection very efficient using quick algorithms based on event topology and total charge information. Once these fast filters have reduced the data volume down to manageable levels, maximum likelihood fits are performed to reconstruct the cascade vertex, direction, and energy and further cuts are made on these output quantities.

It should be noted that these cuts were contructed to optimize HE events ($E > 10$ TeV) and consequently, they are not efficient at passing the lower energy atmospheric neutrinos. In fact, in a search for high energy galactic or extragalactic neutrinos, atmospheric neutrinos themselves constitute a background.

The selection criteria are now explained. First, the tensor of inertia is evaluated about the center of gravity of the hits and is diagonalized to find its eigenvalues. The ratio of the smallest eigenvalue to the sum of the eigenvalues, $L_1/\sum L_i$, provides an estimate of the *sphericity* of the event: muons tend towards enlongated hit patterns while cascades produce hits more or less spherically symmetric about their centers. Next, a *line fit* is performed. The line fit is an analytic approximation that all hits lie along a straight line moving at the speed of light. This heuristic provides a measure of the time flow of the hits in an event. Cascades and muons separate into two clearly distinct populations via the parameter $|v_{LF}|$, the *velocity of the linefit*. Monte Carlo simulations indicate that cuts on these two variables suppress much of the background and accept most of the cascade signal.

While the above criteria reduce the background by almost two orders of magnitude there still remain at least four orders before the level of the signals is approached. An additional cut on the total charge generated by the detected photoelectrons, $\sum Q$, is applied which reduces even the high-energy Corsika-generated cosmic-ray muons almost another two orders of magntiude at the expense of loss of signal sensitivity below about 10 TeV. A cut was applied on the likelihood of the cascade reconstruction, $\mathcal{L}_{cas} < 6$, eliminating all but two events of the (admittedly small) simulated high energy background sample. Finally, a containment cut was made which required the center of gravity of the hits, weighted with ADC amplitude, to fall within a cylindrical volume centered on the detector center, 750 m in height, 450 m in radius (0.48 km^3). This eliminates all background events in the sampled sets.

Background was estimated using two different physics generators for cosmic ray muons: the basiev program generates proton primaries up to energies of 1 PeV. Beyond that, heavier elements constitute a large portion of the cosmic-ray primaries and the Corsika air shower package is used which accurately simulates the composition of the cosmic-ray primaries and the high-

energy interactions up to very high energies, exceeding 10^{20} eV. The calculated live times of the atmospheric muon samples are 80 seconds and 16 hours, respectively for the basiev and Corsika sets. Therefore, background was estimated for higher cut levels which left no background in the sample sets. This was done by fitting background versus a cut variable well below threshold and integrating the extrapolated variable above threshold. Clearly, a more thorough study necessitates additional background sampling. The results of the background suppression cuts on these data sets as well as signal acceptance on diffuse (E^{-2}) and atmospheric neutrino fluxes are presented in table 9.

Cut Level	Diffuse Signal	ATM ν Signal	basiev $E_{CR} < 1\,PeV$	Corsika $E_{CR} > 1\,PeV$
Trigger	981	22500	1.17×10^{11}	2.22×10^{8}
$L_1/\sum L$	842	10650	8.03×10^{8}	7.76×10^{6}
$\lvert v_{LF}\rvert$	676	5470	1.47×10^{8}	2.34×10^{6}
$\sum Q$	461	470	13	5.68×10^{4}
$\mathcal{L}_{\mathrm{mpe}} < 6$	447	397	~ 0	1.96×10^{3}
$\rho < 450\,\mathrm{m}, \lvert z\rvert < 375\,\mathrm{m}$	180	217	~ 0	~ 50

Table 9: Event rates of various sources of signal and background versus cut level. The numbers quoted are in units of expected events per year. In the case of the diffuse neutrino flux, the rate is scaled for a flux of $E^2\Phi_\nu = 10^{-7}\,(\mathrm{GeV}\cdot\mathrm{cm}\cdot\mathrm{s}\cdot\mathrm{sr})^{-1}$.

There is also the possibility for strong cosmic-ray muon background suppression with the surface array, IceTop. In the high-energy region where muon bremsstrahlung begins to look like a signal the surface array becomes relevant in two ways. Air showers with energy in the PeV range and above will trigger the surface array with high efficiency, and this trigger can be used to veto and study this source of background. At higher energy the surface array will also have some veto power for showers with cores outside the physical boundary of the array.

5.4.3 Effective Volume

The effective trigger volume, V_{eff}, is defined as the equivalent volume in which the detector achieves 100% efficiency and is calculated from a simulation of cascades thrown in a much larger volume, V_{gen}, by

$$V_{eff}(E_{cas}) = \frac{n_{trig}(E_{cas})}{n_{gen}(E_{cas})} \times V_{gen}$$

and ranges from about 1 km^3 at 1 TeV to 4 km^3 at 100 PeV (see fig. 26). A more realistic effective volume has been calculated that takes into account the background rejection criteria discussed in the previous section. "Background Rejection I" refers to cuts made that remove background that is expected to remain after vetoing cosmic-ray events that trigger the IceTop surface array. The effective volume drops to zero below about 1 TeV because of a high charge

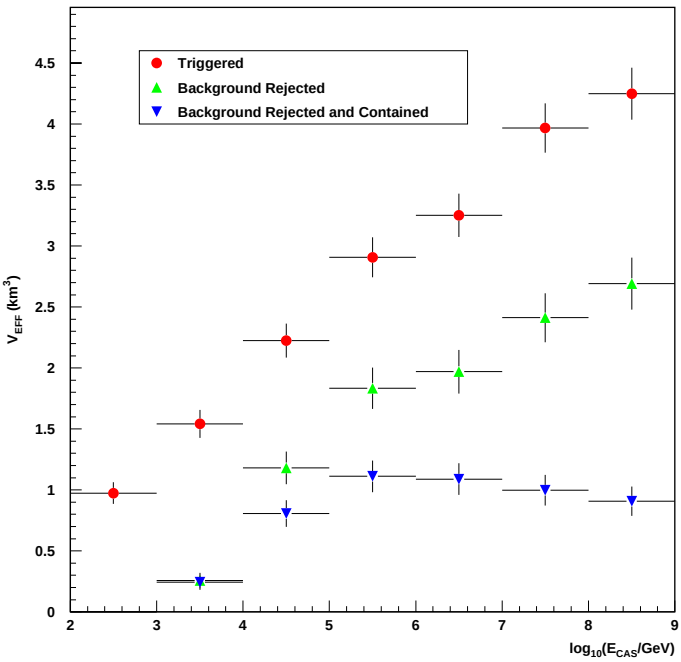

Figure 26: Effective volume for neutrino induced cascades at trigger level (circles), after background suppression cuts (upward triangles), and both background cuts and requiring that the cascade falls within the volume of instrumented ice (downward triangles). The trigger is here defined as five hits within a multiplicity window of 7.0 microseconds.

requirement, reaches 1 km^3 at 10 TeV, and grows to about 2.5 km^3 at 100 PeV. "Background Rejection II" cuts further require that the center of gravity of the hits be contained well inside the detector instrumented volume. This additional cut reduces cosmic-ray muon background to zero independent of any IceTop veto at the cost of reducing the fiducial volume to ~ 0.5 km^3.

5.4.4 Sensitivity to Atmospheric ν

Examination of table 9 shows that there is a very prominent signal of atmospheric ν (ATM ν) at trigger level (fig. 27). Since they are produced with a much softer spectrum than the expected spectra of extragalactic neutrinos, most of this signal populates the medium and high energy regions from the lower energy threshold of IceCube ($\sim$ 100 GeV to several tens of TeV) and is reduced by more than 90% by the $\sum Q$ cut. It may possible to recover some of this lost signal by tuning the cuts for low energy neutrinos. For example, the high charge cut could be lowered and supplemented with a cut on the zenith angle of the muon reconstruction to reject downgoing fakes.

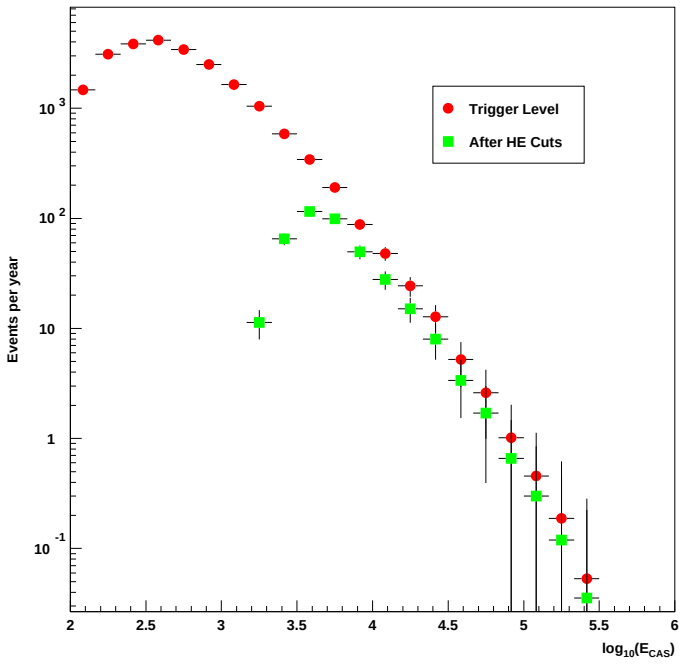

Figure 27: Triggers versus energy and events passing background rejection cuts versus energy for atmospheric neutrinos (Lipari flux [95].)

5.4.5 Sensitivity to Point Sources

With present reconstruction techniques, the poor angular resolution of ν-induced cascades in the IceCube detector makes it difficult to perform a point source search in these channels. However, new reconstruction techniques which take advantage of waveform information may improve upon this situation.

5.4.6 Sensitivity to Diffuse ν_e Sources

Earth absorption plays a significant role in the UHE neutrino flux at the IceCube detector. Figure 28 shows the zenith angle dependence on the event rate and demonstrates the effect: Earth shadowing begins attenuating the event rate below the horizon at several tens of TeV. The shadowing steepens with energy until, above energies $E_\nu > 10$ PeV, the earth is almost totally opaque to neutrinos. Fold into this the fact that the target volume for $\nu \rightarrow$ cascade, being closer to the detector than for $\nu \rightarrow \mu$ vertices, is symmetrically distributed both above and below the detector so that cascades do not suffer a reduced amount of target material for downgoing events. These two observations together imply that the upper hemisphere is especially important for the detection of UHE ν-induced showers and the ability to cleanly separate UHE neutrino-induced showers from cosmic-ray muon background is another trump held by cascade analyses. The differential event rate of UHE cascades in IceCube versus energy for a flux of $E^2\Phi_\nu = 10^{-7}\,(\mathrm{GeV}\cdot\mathrm{cm}\cdot\mathrm{s}\cdot\mathrm{sr})^{-1}$ is shown in fig. 29. The squares represent the trigger rate and the triangles represent the event rate after all background rejection cuts have been applied.

5.4.7 Sensitivity to GRBs

GRBs are another hypothesized source of UHE extragalactic neutrinos. For these sources, Waxman and Bahcall [127, 128] propose a flux that is very soft, falling as E^{-1} until a break energy of several hundred TeV when the spectrum turns down to fall as E^{-2}. Folding in the ν cross-section, one obtains the result of an increasing interaction rate (in $\log E$) until the break energy, and thus a very high-energy source of ν-induced cascades in the detector visible above the background (fig. 30). The authors also predict that the ν and γ bursts are very closely correlated in time so that the IceCube detector can restrict searches to time windows centered on burst events observed by one of the several gamma-ray satellites. However, if the GRB fluence is close to the W&B prediction, IceCube could still detect a cluster of cascade events from such a burst without "triggering" on satellite observations.

A GRB search in the cascade channel has a distinct advantage over the muon channel search which offsets the smaller effective volume of high-energy cascades versus muons: background rejection is based on event topology. That is, cascades do not look like atmospheric muons, therefore the upper hemisphere does not need to be excluded from a cascade GRB search, making IceCube sensitive to both northern and southern hemisphere GRBs.

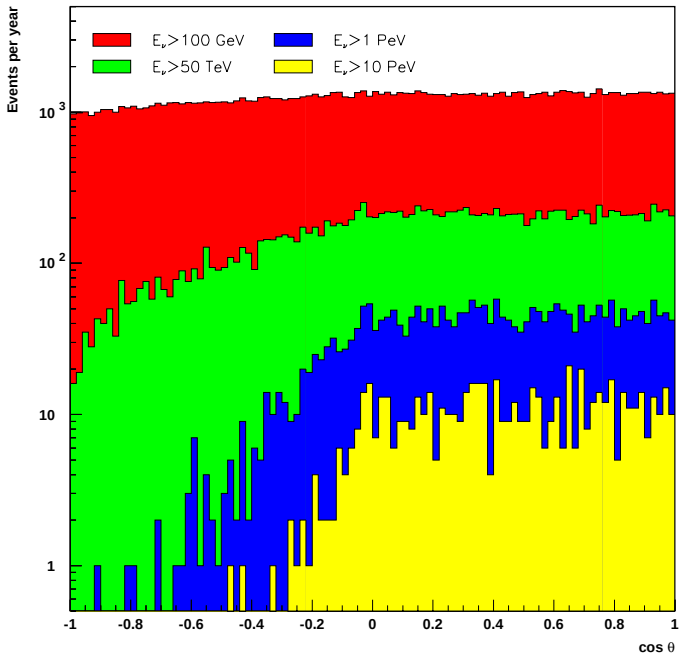

Figure 28: Distribution of UHE ν-induced cascades versus zenith angle at generator level for a generic E^{-2} flux. The assumed source flux is $E^2\Phi = 10^{-7}\,(\mathrm{GeV}\cdot\mathrm{cm}\cdot\mathrm{s}\cdot\mathrm{sr})^{-1}$.

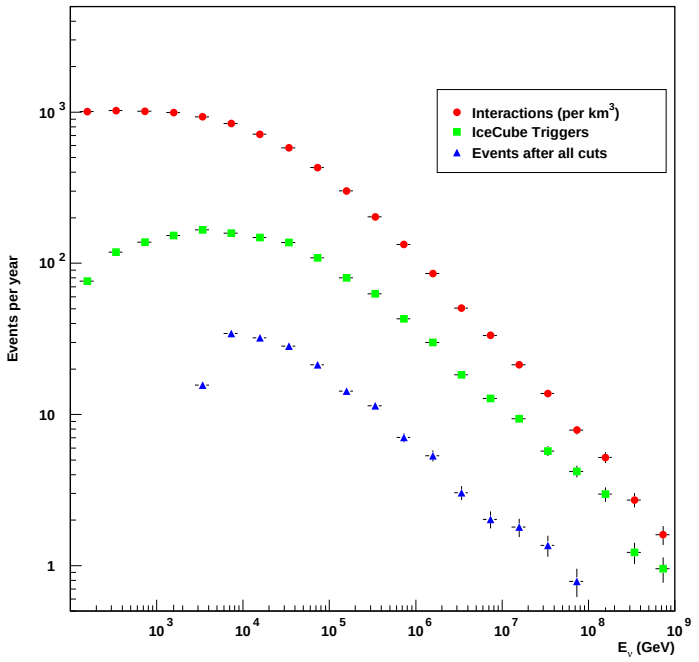

Figure 29: UHE ν interactions (circles, scaled to $\mathrm{km}^{-3}\cdot\mathrm{year}^{-1}$), triggers in IceCube (squares), and events passing background rejection cuts (triangles), versus energy for flux $E^2\Phi_{\nu+\bar{\nu}} = 10^{-7}\,(\mathrm{GeV}\cdot\mathrm{cm}\cdot\mathrm{s}\cdot\mathrm{sr})^{-1}$.

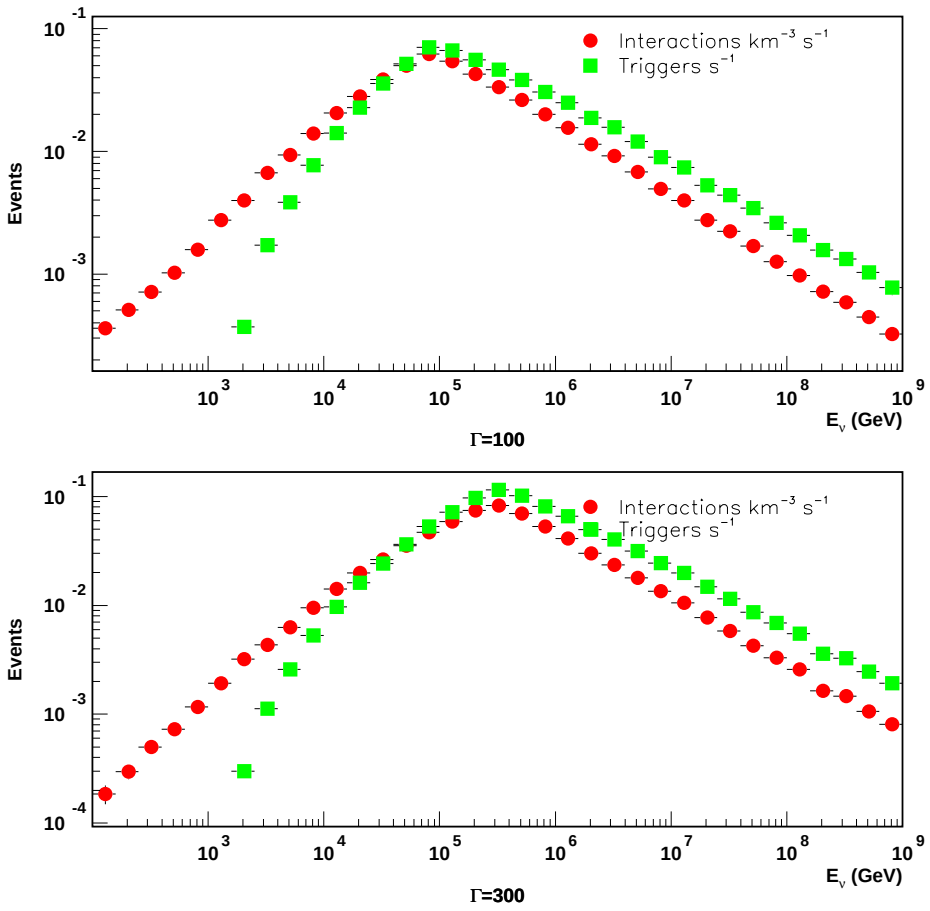

Figure 30: GRB ν-induced cascade event rate predictions following the Waxman-Bahcall model for two choices of the Lorentz factor, Γ. The y-axis is in units of s^{-1} making the integrated expected rate of events in a km^3 detector about 0.5 Hz and 0.9 Hz for the choices $\Gamma = 100$ and $\Gamma = 300$, respectively.

5.4.8 Possible Improvements

High energy cascade reconstruction will benefit greatly from the waveform readout of IceCube which is not yet fully simulated. Many improvements could be made to the reconstruction algorithms which are currently not equipped to make use of the detailed hit information that comes with waveform readout. These are likely to improve cascade identification at high energies. At lower energies, better cuts need to be developed that reject background but preserve the neutrino signal. Containment cuts that use the outer portion of IceCube as a veto shield should allow sub-TeV cascade events to be identified.

5.5 Tau Neutrinos

In this section we expand on the discussion found in secs. 3.2.4 on ν_τ kinematics, detection probability and event rates in IceCube. High energy tau neutrinos can be distinguished from other signals by either their "double bang" or "lollipop" topologies. These topologies are diagrammed in fig. 31. Preliminary studies of the lollipop topology have only just begun, so we will focus on the double bang topology in what follows. Double bang events are those in which

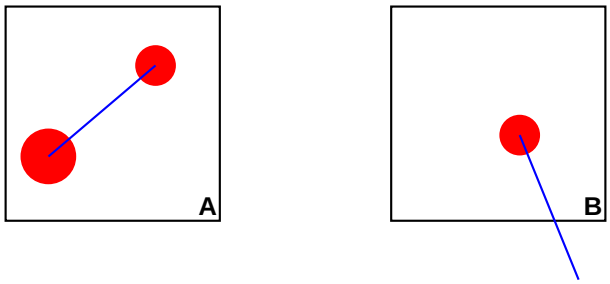

Figure 31: The "double bang" (A) and "lollipop" (B) signatures which tau neutrino interactions can create. These signatures are also discussed in section 5.6.1.

the production and decay of a τ lepton can be identified [118]. Figure 32 shows a simulated CC ν_τ double bang event in IceCube.

We have calculated the probability of detecting a double bang event in a neutrino telescope of linear dimension $D = 1$ km such as IceCube. We have developed a very simple Monte Carlo for this purpose in which the detector is considered as one dimensional. We have taken the energy threshold for detecting showers to be $E_{\rm shower} \sim 1$ TeV. We have conservatively fixed to 250 m the minimum distance the τ has to travel to clearly distinguish the Čerenkov light from both showers. This number is determined by the separation between strings which is 125 m. (In principle this number could go much lower if other double bang topologies are considered.) Our Monte Carlo accounts for the fluctuations in the fraction of energy transferred to the τ in the interaction, as well as for the fluctuations in its range. The result of the Monte Carlo is shown in fig. 33 along with the probability of observing a ν_μ-induced muon. Also shown is the

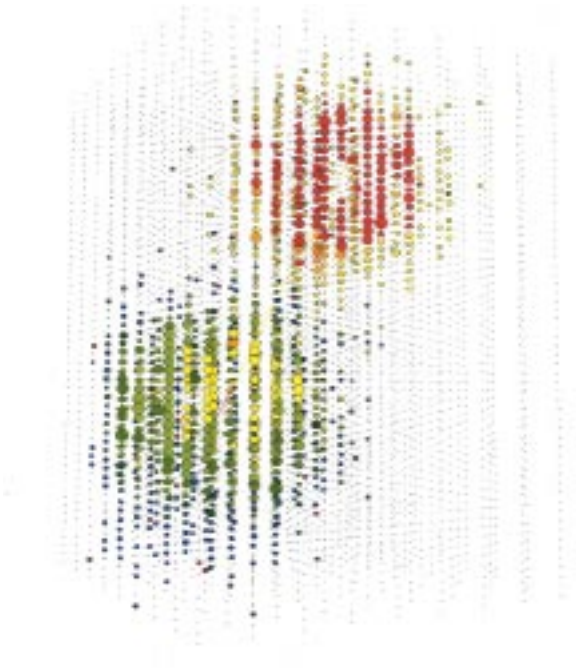

Figure 32: A double-bang ν_τ event with an energy of a few PeV in IceCube. Colored circles represent hit channels, with red circles hit earliest and violet circles latest. Circle size corresponds to number of detected photons.

probability of observing a double bang event as obtained in [119] using the expression:

$$P_\tau(E, E_\tau^{\min}) = \rho N_A \int^{1-\frac{E_\tau^{\min}}{E}} dy[D - R_\tau] \frac{d\sigma^{CC}(E, y)}{dy}, \tag{3}$$

where ρ is the density of the medium and N_A is Avogadro's number. $E_\tau^{\min}$ is the minimum energy of the τ, it is automatically fixed imposing that $R_\tau \geq 250$ m. This expression uses average values for R_τ and hence at $E_{\nu_\tau} \leq E_\tau^{\min}$ the probability of observing a double bang vanishes since the average range of the τ is smaller than 250 m. The probability calculated with this expression has a broad maximum which is determined by the condition that R_τ has to be larger than 250 m but smaller than the size of the detector. Assuming an average value of $y \sim 0.25$ at these energies and using eq. 2 this corresponds to E_{ν_τ} between roughly 7 PeV and 27 PeV.

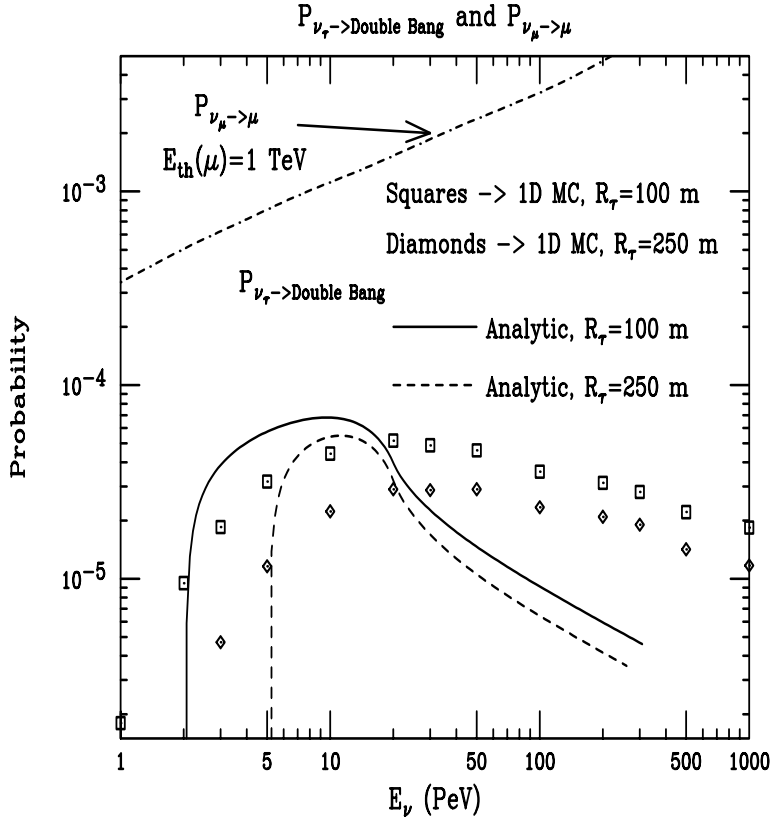

Figure 33: Probability of detecting ν_τ induced double bang events in IceCube obtained with Monte Carlo simulation and using the analytic expression given by of [119] (Eq.2). The probability is shown for $R_\tau = 100$ m and 250 m. Also shown is the probability of detecting a ν_μ-induced muon.

Due to fluctuations in R_τ, even ν_τ's with energy below $E_\tau^{\rm min}$ are going to produce τ's that travel more than 250 m. This explains why our probability doesn't vanish at $E_{\nu_\tau} < E_\tau^{\rm min}$ as happens to the one given by eq. (3). It also has a longer tail at high energies because fluctuations in the τ range and in its energy prevent a fraction of high energy ν_τ's from producing a τ that travels a distance larger than the dimension of the detector.

5.5.1 Tau Neutrino Event Rates

We calculate the number of ν_τ events in the standard way [93], convoluting the probability of observing the double bang events with the $\nu_\tau + \bar{\nu}_\tau$ flux:

$$N_{\rm events} = A_{\rm eff} \int \Phi_{\nu_\tau + \bar{\nu}_\tau}(E_{\nu_\tau}) P_{\nu_\tau \rightarrow \text{ double bang}}(E_{\nu_\tau}) dE_{\nu_\tau} \tag{4}$$

where we will take $A_{\rm eff} = 1$ km^2. $P_{\nu_\tau \rightarrow \text{ double bang}}$ is the probability of observing a double bang event as shown in fig. 33.

By far the largest uncertainty in this expression is the $\nu_\tau + \bar{\nu}_\tau$ flux. Tau neutrino production is expected to be very small in most astrophysical scenarios where ν's are produced in pp or pγ collisions. Several calculations suggest a ratio [119] $F_{\nu_\tau/\nu_\mu} \sim 10^{-5}$. Oscillation scenarios in which ν_μ's convert themselves into ν_τ's may be the most promising sources of ν_τ's. Making the assumption that $F_{\nu_\tau/\nu_\mu} = 0.5$ we obtain the number of events in table 10 for representative $\nu_\mu + \bar{\nu}_\mu$ fluxes in the literature. In fig. 34 we also show the energy distribution of the events. They all resemble the shape of the probability function of fig. 33. For more details and references, see reference [83].

It is important to note that with neutrino oscillations a generic cosmic accelerator which produces neutrinos in the flux ratio $\nu_e : \nu_\mu : \nu_\tau :: 1 : 2 : 0$ will result in neutrinos in the flux ratio of $1 : 1 : 1$ at the detection point. With a $1 : 1 : 1$ ratio the numbers of double bang events in table 10 would grow by a factor of two.

5.5.2 Tau Neutrino Simulations

Although tau neutrinos are clearly a promising analysis to pursue, at present no IceCube simulations of tau neutrinos have been run, due to lack of time and manpower. Many of the simulation tools used for muons and cascades are applicable, so it is anticipated that this deficit will be remedied in the near future.

5.6 Neutrino Flavor Differentiation with Waveform Digitization

Waveform digitization will provide a wealth of information which undoubtedly will lead to improvements in many aspects of event reconstruction. Since work in this area has only just begun, this section presents a qualitative picture of what can be achieved with waveforms, with a focus on neutrino flavor differentiation. The signatures produced by electron, muon and tau neutrinos are as follows:

Table 10: Double bang events per km^2 per year in 2π stereoradian for representative $\nu_\mu + \bar{\nu}_\mu$ fluxes in the literature assuming $F_{\nu_\tau/\nu_\mu} = 0.5$. Attenuation has been taken into account to calculate ν_μ events but not for ν_τ events. The GRB event rate takes into account fluctuations in distance, gamma factor and energy of the GRB's normalizing to 1000 GRB's/year. The TD's models correspond to maximal predictions of fig.2 in reference [103]. The neutrino flux from the decay of Superheavy Relics is taken from reference [104]. The numbers of double bang events grow by a factor of two if one takes into account recent neutrino oscillation results and uses instead $F_{\nu_\tau/\nu_\mu} = 1$.

Flux	Double Bang events	$\nu_\mu + \bar{\nu}_\mu$ (upgoing) events
$10^{-6}\ E^{-2}$(cm^2 s sr)$^{-1}$	6	10,779
GRB (Fluctuation model)	~ 1	43
TD, $M_X = 10^{14}$ GeV, $Q_0 = 6.31 \times 10^{-35}$, p=0	146	58,665
TD, $M_X = 10^{14}$ GeV, $Q_0 = 6.31 \times 10^{-35}$, p=1	6×10^{-2}	12
TD, $M_X = 10^{14}$ GeV, $Q_0 = 6.31 \times 10^{-35}$, p=2	1.5×10^{-2}	3
TD, $M_X = 10^{15}$ GeV, $Q_0 = 1.77 \times 10^{-34}$, p=0	120	48,605
TD, $M_X = 10^{15}$ GeV, $Q_0 = 1.58 \times 10^{-34}$, p=1	5.5×10^{-2}	9
TD, $M_X = 10^{15}$ GeV, $Q_0 = 1.12 \times 10^{-34}$, p=2	1.1×10^{-2}	2
Superheavy Relics $M_X = 10^{14}$ GeV	3×10^{-2}	4×10^{-4}

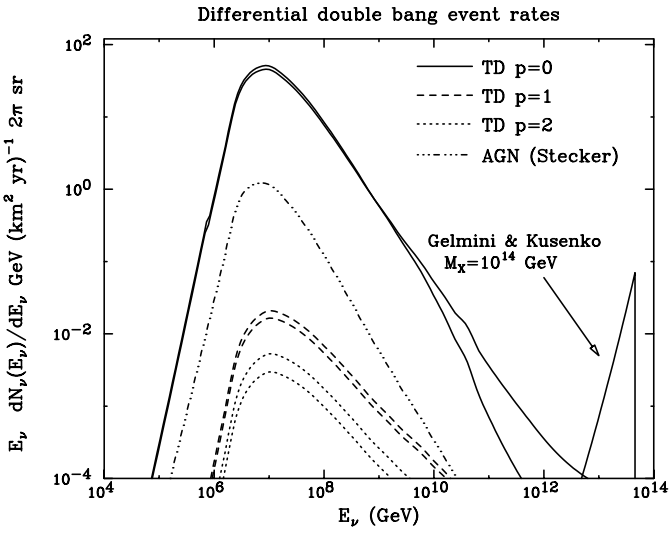

Figure 34: Differential ν_τ induced double bang event rates for different fluxes assuming $F_{\nu_\tau/\nu_\mu} = 0.5$. The upper lines at 10^7 GeV for the Topological Defect models correspond to $M_X = 10^{14}$ GeV and the lower ones to $M_X = 10^{15}$ GeV.

- Charged current electron neutrino interactions and neutral current neutrino interactions produce an electromagnetic and/or hadronic shower at the point of interaction. The cascade generated in this reaction will, depending on energy, extend from a few to more than 10 m, a scale small compared to the spacings of IceCube strings. Therefore, cascades will be treated as pointlike events in what follows. As seen in fig. 24, cascades produce a characteristic spherical pattern.

- Charged current muon neutrino interactions produce an initial hadronic shower, which may or may not be detected, and a muon. At energies exceeding roughly 500 GeV, the muon loses substantial amounts of energy stochastically in radiative processes.

- Tau events can have the characteristic "double bang" signature, which originates from the production and then decay of a tau particle. The first shower comes from the charged current interaction of the ν_τ with a nucleon. The products of this interaction are a tau lepton and a hadronic shower. The dissipation of the energy in the hadronic shower produces the first "bang."

  The second shower happens when the tau travels a short distance and then decays into a tau neutrino. This reaction also causes a hadronic shower. The dissipation of this shower is what produces the second "bang." This energy range at which these event signatures are generated are from a few PeV to a few tens of PeV.

  Alternatively, tau events can have the characteristic "lollipop" signature, which is created when the first bang described above is not detected but the tau lepton and the second bang caused by its decay are. These events can be distinguished from muons by the lower level of light produced by the heavier tau lepton in flight.

The energy regimes best-suited to the detection of each neutrino flavor are illustrated in fig. 35.

Figure 36 shows the average photoelectron density observed at an OM as a function of the distance of closest approach of the muon track. Stochastic energy losses have been excluded from the calculation. As expected, the closer the muon is to an OM, the more photoelectrons the OM sees.

Figure 37 shows the photoelectron density as a function of the distance between an OM and the high energy cascade vertex. In this case, the shower has inital energy of 1 PeV. Again, the closer the shower occurs to an OM, the more photoelectrons that module will see. At distances greater than 150 m, the photon flux drops by about one order of magnitude every 60 m.

5.6.1 Photon Flux Distribution Generated by High Energy Cascades

In this section we discuss the spatial photon flux density distribution as generated by high energy cascades. The light profile of electromagnatic and hadronic cascades can be assumed to be identical as shown by [105]. Simulations in this report are based on electromagnetic cascades. Hadronic cascades differ only in the absolute light output, which is roughly 20% lower than for electromagnetic cascades. The simulations include the orientation of the optical sensor. The

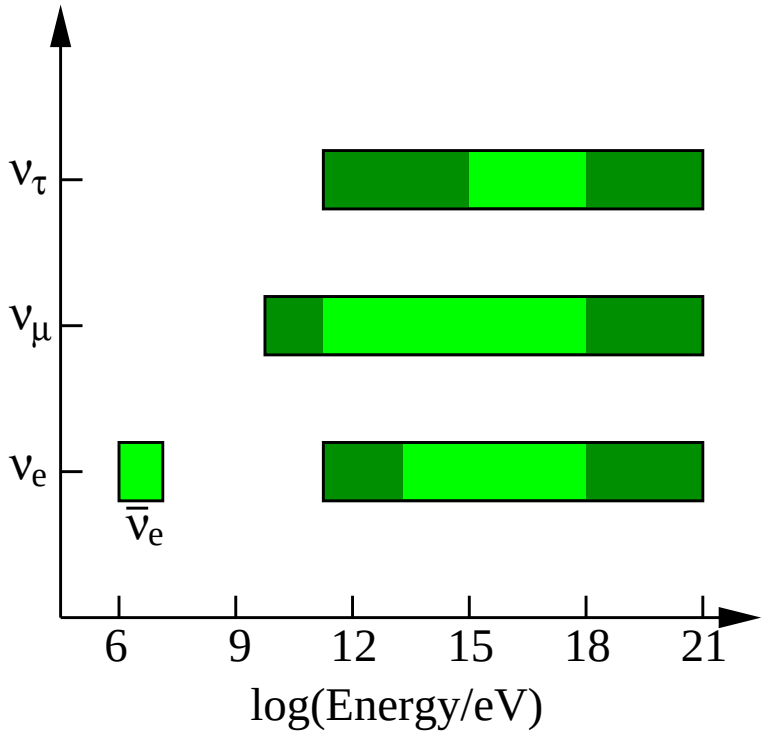

Figure 35: Energy regimes best-suited to the detection of each neutrino flavor.

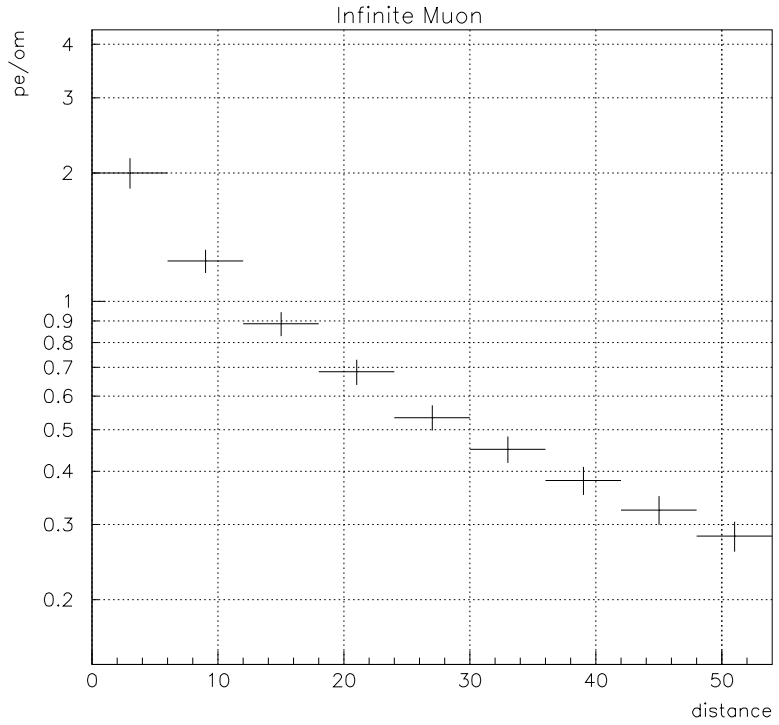

Figure 36: Average photoelectron density observed at an OM as a function of the distance of closest approach of the muon track. Stochastic energy losses are excluded. The number of photoelectrons is based on the Čerenkov radiation of the relativistic charged particle in the medium ice.

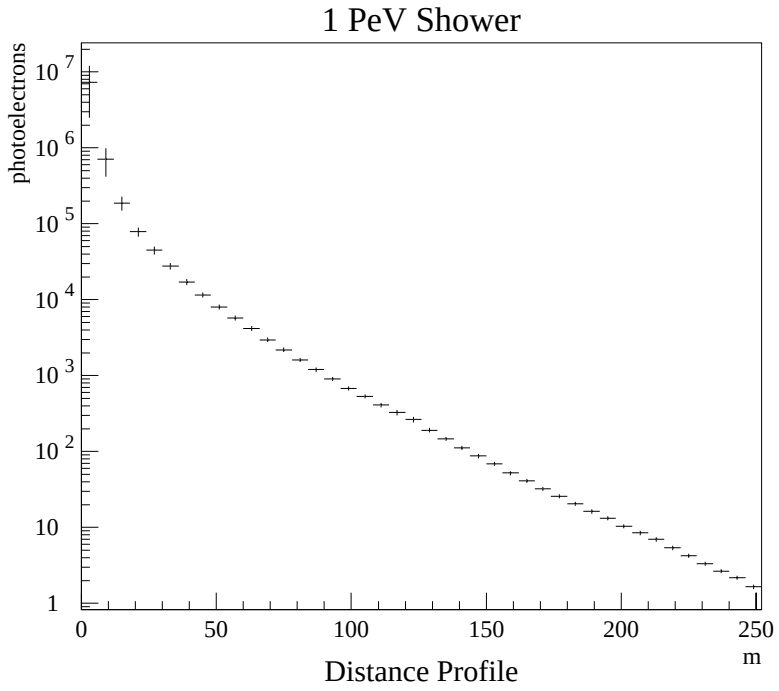

Figure 37: Average photoelectron density as a function of the distance from the vertex of an electromagnetic cascade of 1 PeV energy.

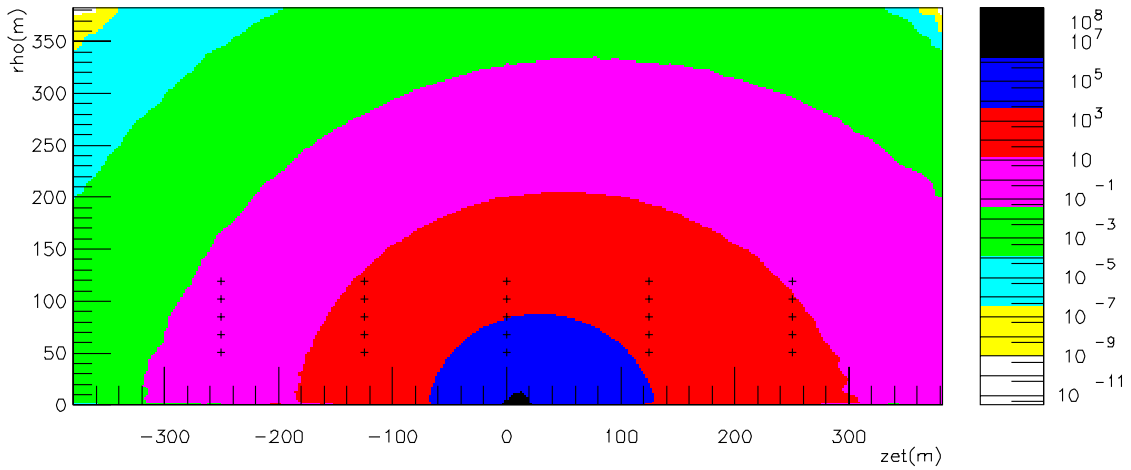

Figure 38: Integrated number of photoelectrons over a 2.5 μs period from a 1 PeV cascade as seen by downward facing OMs.

quantum efficiency is assumed to be 20% and the diameter of the PMT 25 cm. The spectral sensitivity is based on the Hamamatsu datasheet. The glass transmission of the pressure housing is based on the instrument housings manufactured by Benthos Co. which are currently in use by AMANDA.

In the following we focus on the integrated number of photoelectrons observed by an optical sensor in 2.5 μs of recording time. The time window of 2.5 μs is long enough to integrate over the full length of the expected pulses for cascades in the energy range discussed in this document (up to 100 PeV). (N.B.: The integrated number of photoelectrons scales linearly with the cascade energy.)

Figure 38 shows the spatial distribution of the integrated number of photoelectrons over a 2.5 μs time period. The light emission generated by the 1 PeV cascade is assumed to be cylindrically symmetric. Therefore we can project the density profile in a two dimensional graph, using cylindrical coordinates (rho, zet). In this and the following figures the light emission occurs at the origin (0,0). The shower itself is assumed to be pointlike. The direction of the shower points to the right (positive z). Thus the density is peaked in the forward direction. However, due to scattering of photons in the ice, the light is *eventually* distributed in all directions. On a scale of 400 m by 800 m as shown in the figure, which is very large compared to the effective scattering length of the ice (24 m) the emission becomes approximately spherical.

One can see that the symmetry of the light distribution is shifted in the forward direction by about one scattering length. The OMs are pointing downward in this simuation. A grid of OMs has been marked in the figure with a horizontal spacing of 125 m and a vertical spacing of 17 m, corresponding to the IceCube baseline design.

Figure 39 shows the maximum number of photoelectrons to strike a downward-facing OM

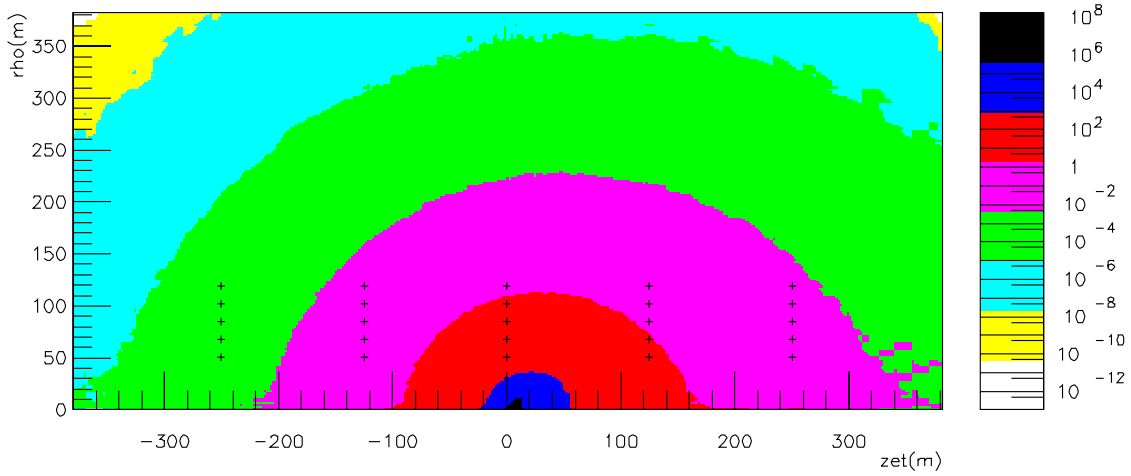

Figure 39: Expected peak photocathode current or the maximum number of photoelectrons/ns from a 1 PeV cascade as seen by downward facing OMs.

per 10 ns bin for a 1 PeV shower. This figure can be used to derive the regions in which the PMT will saturate. For events relevant for IceCube the saturation depends primarily on the photocathode current. The figure gives the peak cathode current (in photoelectrons and ns). A dynamic range of 150 pe/ns can be used.

Figures 40, 41 and 42 show how pulse shapes increase with distance from the OM for a 100 TeV, 1 PeV and 100 PeV cascade. Therefore the peak amplitude (max pe) drops less strongly than the integrated number of photoelectrons. As these plots clearly show, waveforms will provide us with richly detailed information from which quantities such as cascade energy and direction can be estimated. IceCube OMs will be linear up to at least 150 pe per 10 ns bin, which means that a 100 TeV (1 PeV) cascade can be recorded linearly from distances as close as 30 m (50 m).

5.6.2 ν_τ Event Signatures

Tau neutrinos can produce distinctive "double bang" and "lollipop" signatures in IceCube, as described earlier in section 5.5. Waveform information is particularly well matched to the extraction of these signatures. Although detailed reconstruction algorithms have not yet been written, the following figures should make it clear that sufficiently energetic tau neutrinos can in principle be reconstructed and extracted from IceCube data.

Figure 43 shows the integrated number of photoelectrons from a double bang tau event of about 10 PeV primary energy as seen by downward facing OMs. The decay length of the tau lepton was 225 m. Figure 44 depicts the leading edge times of pulses from a tau lollipop event. Note how the incoming tau leaves a small but clearly distinguishable set of early pulses prior to its decay in to a large cascade. Figure 45 shows the pulse shapes as a function of time generated at various OMs for a double bang 10 PeV tau event. Note the distinctive double-peaked structure in OMs at $z = 125$ m from the first vertex: the first peak is from the interaction of the ν_τ; the second from the tau lepton decay. Figure 46 shows a tau event where the decay length of the tau was 300 m. At this distance, no single OM receives significant pulses from the two cascades, but timing measurements still show quite clearly that two distinct cascades were detected. Note that in figs. 43-46 the tau was generated travelling horizontally. That makes this analysis a conservative one because the horizontal orientation is the least favorable one for reconstructing such events.

5.6.3 Summary

The studies of individual events gives insight in the variety of pulse shapes that are expected in IceCube. The waveforms depend strongly on the following parameters:

- Energy: The integral of a given pulse shape depends strictly linearly on the energy of a given event.
- Distance: The width of the pulse shape increases in an unambiguous way as a function of position and orientation of the sensor with respect to the event. The distance of the event

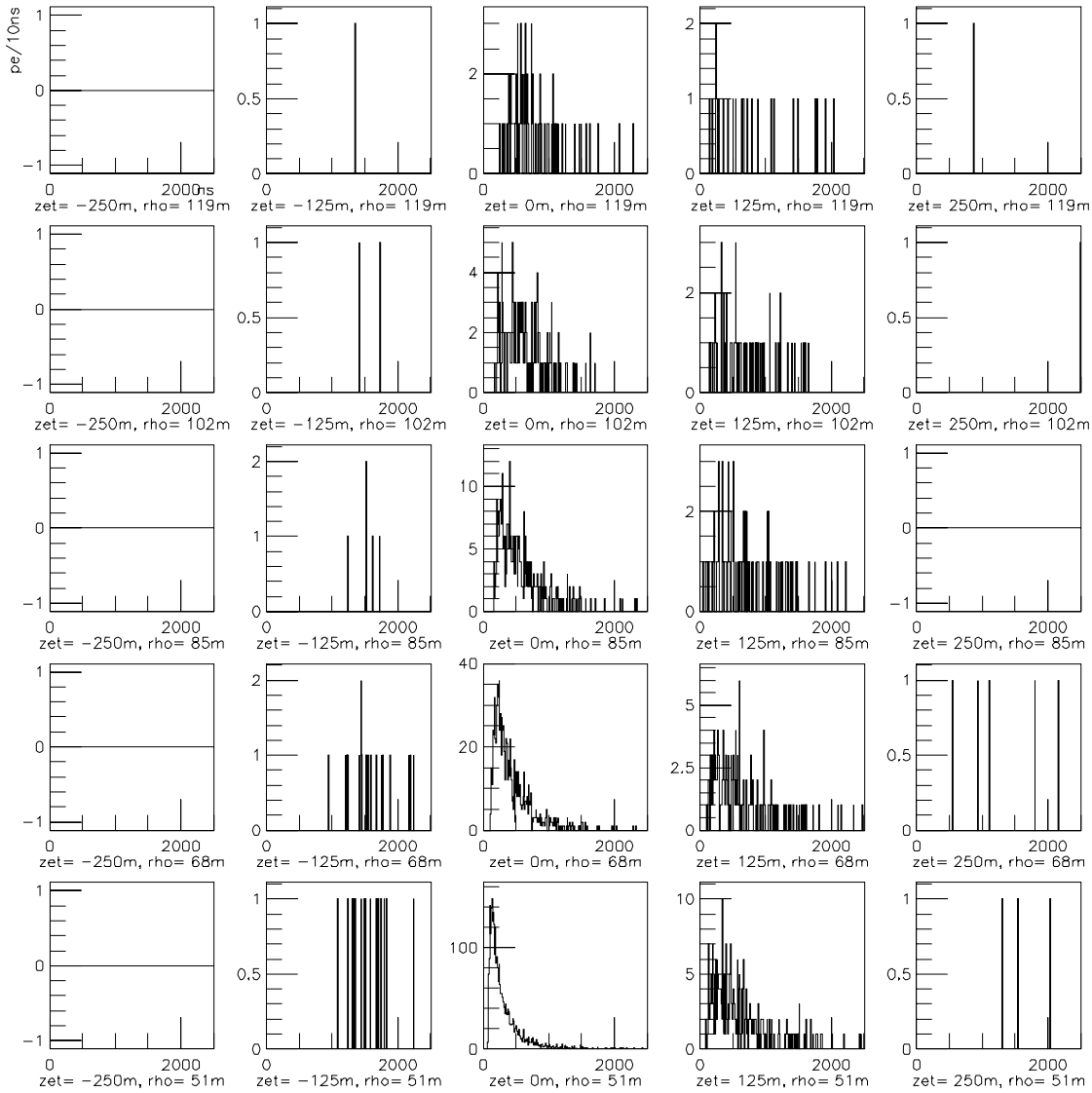

Figure 40: Pulse shapes generated by a 100 TeV cascade as observed by optical sensors in the positions marked in fig. 38. The amplitudes are given in photoelectrons per 10 ns interval, as seen by a 100 Msps waveform digitizer.

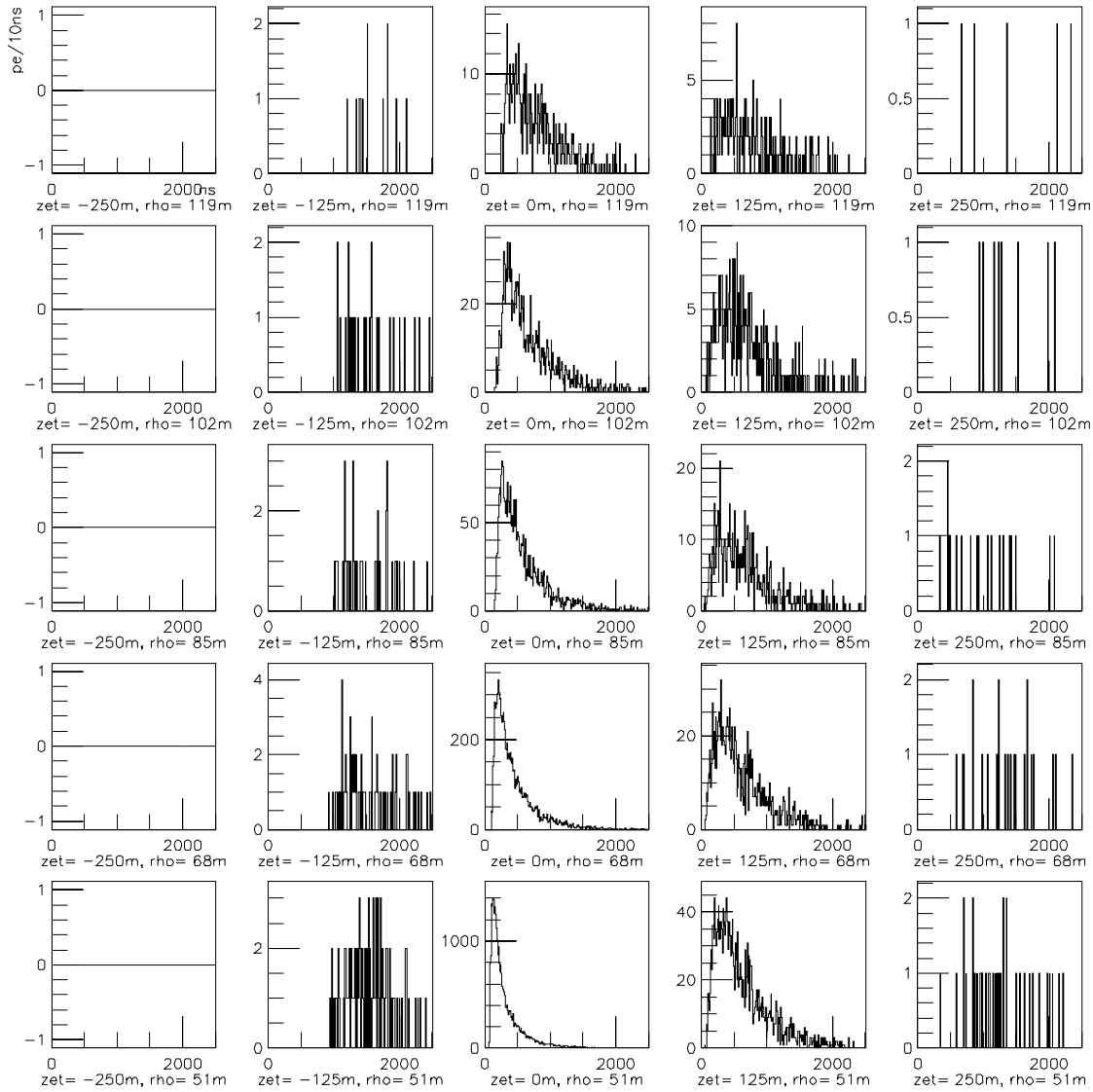

Figure 41: Pulse shapes generated by a 1 PeV cascade as observed by optical sensors in the positions marked in fig. 38. The amplitudes are given in photoelectrons per 10 ns interval, as seen by a 100 Msps waveform digitizer.

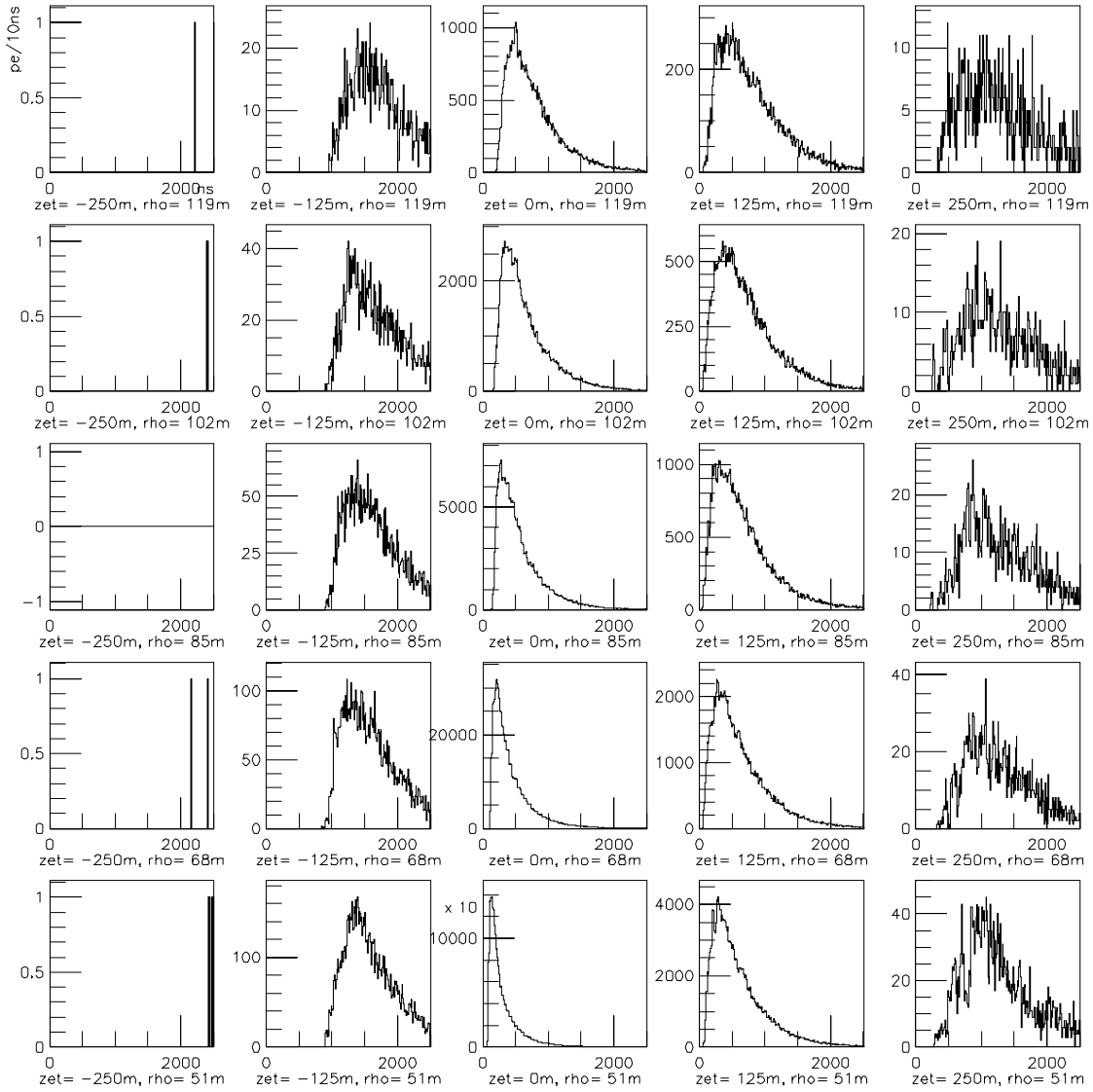

Figure 42: Pulse shapes generated by a 100 PeV cascade as observed by optical sensors in the positions marked in fig. 38. The amplitudes are given in photoelectrons per 10 ns interval, as seen by a 100 Msps waveform digitizer. The pulses on strings 3 and 4 exceed the dynamic range of the photomultiplier. Only at larger distances there will be many sensors that are outside the region of saturation.

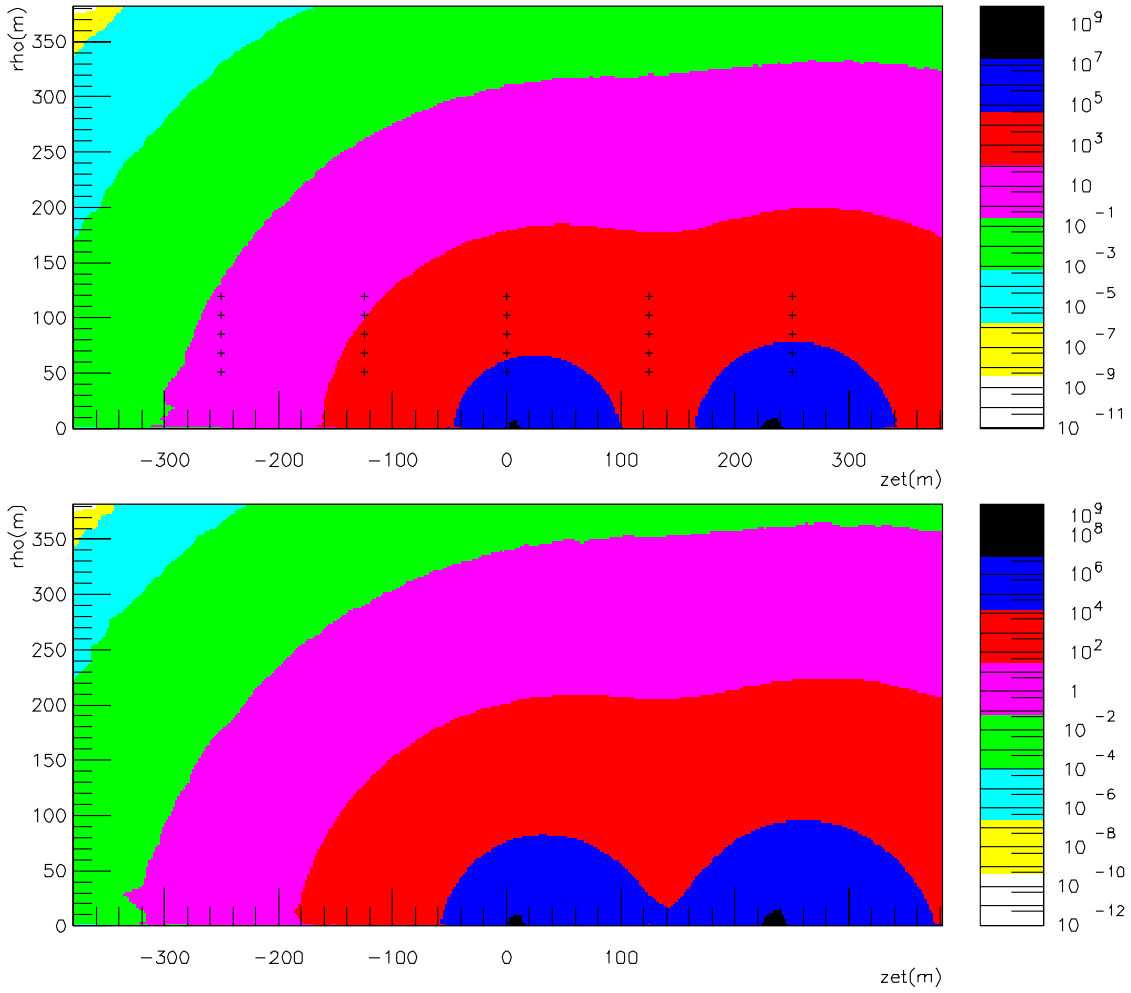

Figure 43: *Top:* Integrated number of photoelectrons from a tau event of about 10 PeV primary energy as seen by downward facing OMs. *Bottom:* Same, but for upward facing OMs. The energy of the tau was about 10 PeV and its decay length was 225 m.

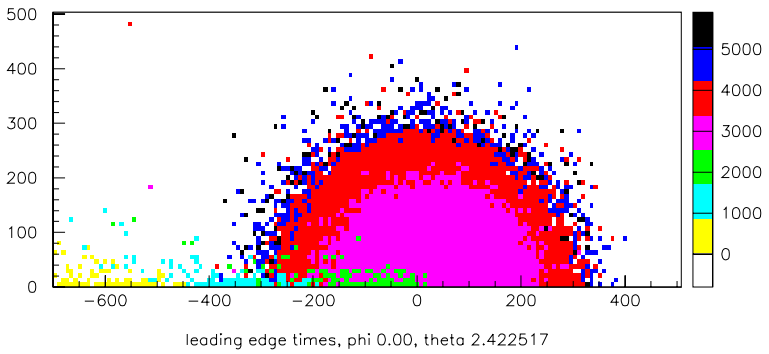

Figure 44: Leading edge times of pulses from a tau "lollipop" event of about 10 PeV primary energy as seen by downward facing OMs. The times are color-coded and shown as a function of ρ versus z. Note that the earliest times (in yellow, cyan and green) are due to the minimum ionizing tau, and the remaining hits in the event at later times are due to the cascade from the tau decay.

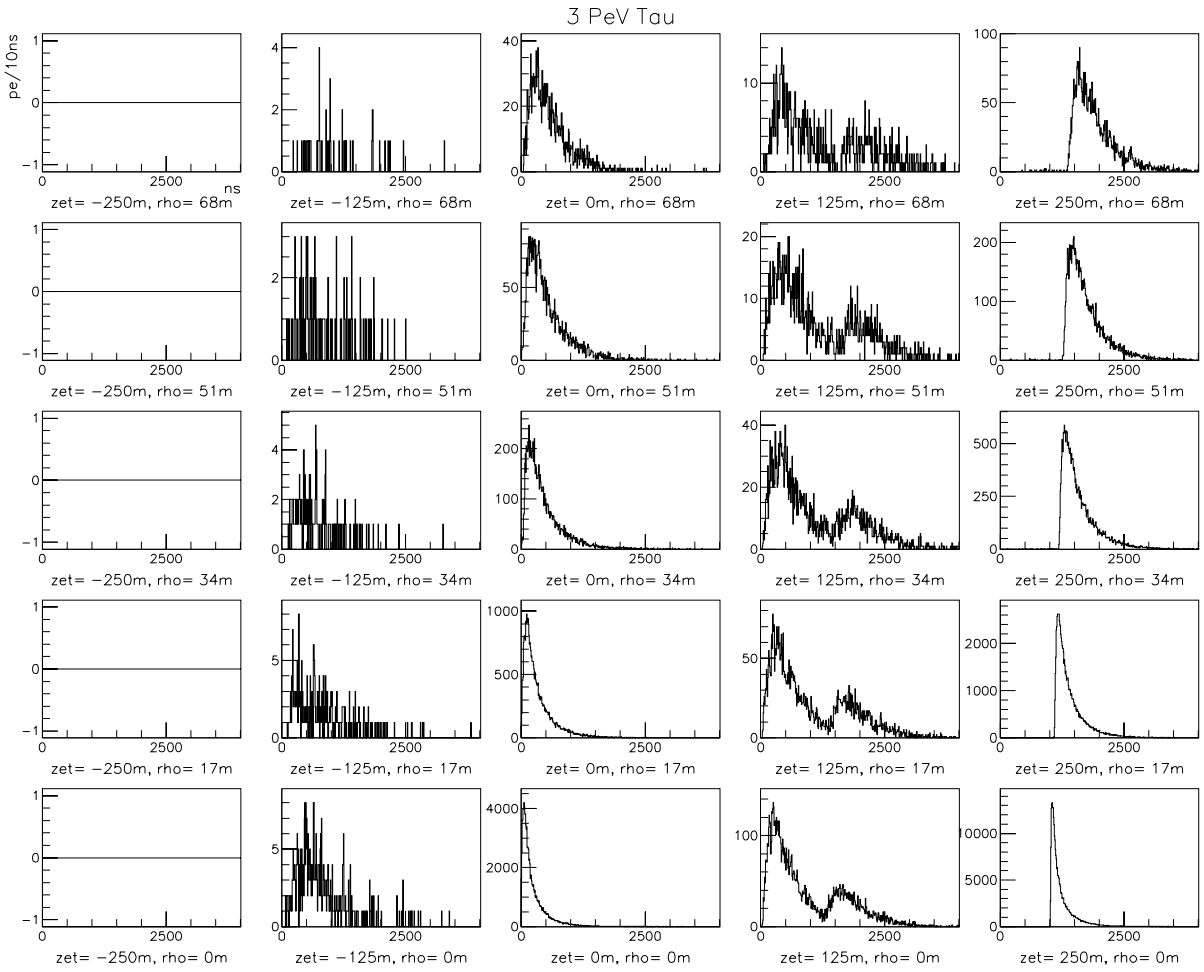

Figure 45: Pulse shapes generated by a tau event of about 10 PeV primary energy, similar to that in fig. 43. The amplitudes are given in photoelectrons per 10 ns interval. The tau decay length was 225 m.

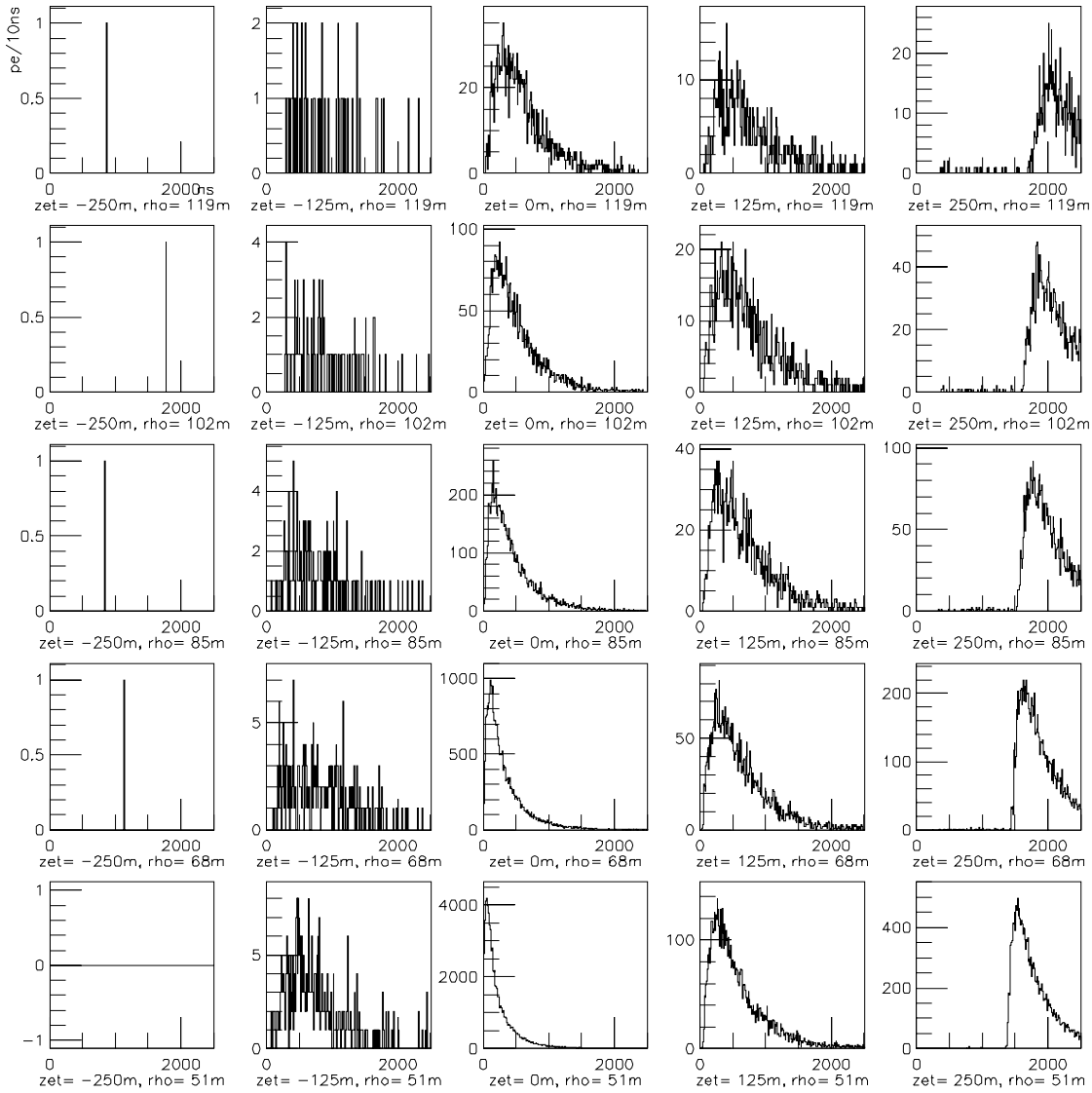

Figure 46: Pulse shapes generated by a tau event of about 10 PeV primary energy, similar to that in fig. 45, but the decay length of the tau lepton was 300 m. At this decay length, single OMs do not have double peaked pulse shapes as at 225 m, but it is still clear from the timing profiles that two cascades occurred in the detector.

is the dominant parameter to determine the width of the pulse.

- Lepton flavor: Muon tracks generated by ν_μ, cascades as generated by ν_e or neutral current interaction, and finally ν_τ interactions generated different waveforms. the complex waveforms that can occur ν_τ event suggest that the waveform can play a substantial role in the particle identification.

- Orientation: The pulse shape depends to some extent on the orientation of a cascade.

Reconstruction methods that exploit this rich information are yet to be developed. However, based on the above simulations, we conclude that the characteristics of the pulse shapes show a strong correlation with fundamental physical parameters. It should therefore be a goal to record the pulse shapes with a precision sufficient to extract the important features.

It should be noted that the sampling depth of 4 μs can be exceeded in very rare cases (e.g., time profiles of tau events). Also, the dynamic range of existing large area PMTs will be exceeded if either the energy of the event is very high or the PMT is very close to the event. An increased dynamic range remains desirable. However, one should keep in mind that the detection volume at larger distances from the event is very large in these cases. For example, in case of 100 PeV energy cascades or higher, the PMTs will be saturated up to distances of more than 200 m. However there remains a very large shell of detector volume where hundreds of PMT will sample waveforms. This will compensate to a large extent the limited signal quality at closer distances.

5.7 Lower Energy Phenomena and Exotica

5.7.1 Muon Neutrinos from WIMP annihilation

If Weakly Interacting Massive Particles (WIMPs) make up the dark matter of the universe, they would also populate the galactic halo of our own Galaxy. They would get captured by the Earth or the Sun where they would annihilate pairwise, producing high-energy muon neutrinos that can be searched for by neutrino telescopes. A favorite WIMP candidate is the lightest neutralino which arises in the Minimal Supersymmetric Model (MSSM).

The typical energy of the neutrino-induced muons would be of the order of $\leq 25\%$ of the neutralino mass. Since the muon threshold for IceCube is expected to be fairly high (~ 100 GeV), we expect IceCube to be sensitive mainly to neutralinos heavier than about 400 GeV.

In [121] the performance of IceCube was studied for two configurations, a 9 string $\times$ 9 string pattern with 125 m string spacing and a detector consisting of eight sub-modules of 10 strings each, with string spacing of 70 – 90 m within the sub-detectors (see fig. 47).

The effective area for WIMP detection depends on the WIMP mass as well as on the typical decay channel ("soft" channels from WIMP decays into many secondaries, "hard" channels from decays into a few secondaries only). Figure 48 shows effective volumes and effective areas for the rectangular pattern ("standard" geometry, left) and the modular pattern (right), separately for neutrinos from the Sun and the center of the Earth, and for soft and hard spectra, respectively.

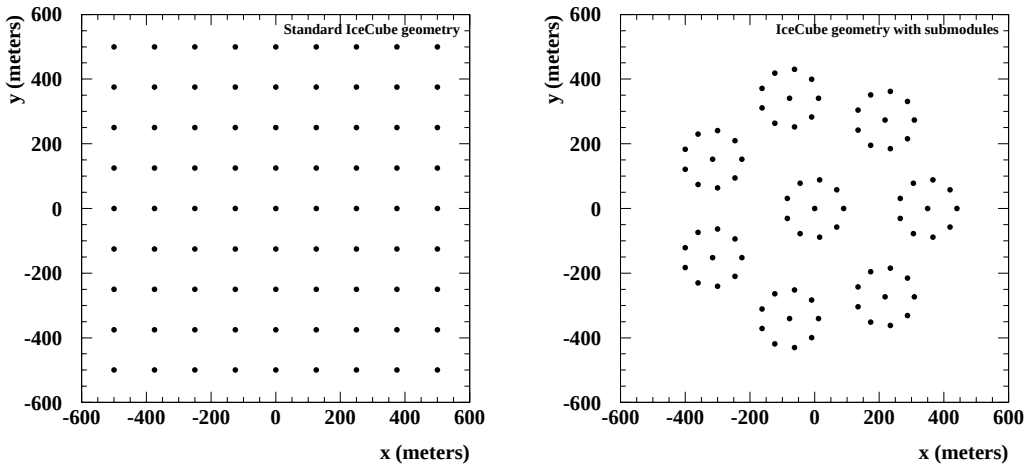

Figure 47: Configurations studied in [121]

The standard geometry gives about 0.7 square kilometer area for both solar and terrestrial WIMPs, provided the decay channels are preferentially hard. For soft channels, the area drops down to less than 200 000 m^2 for WIMP masses of 200 GeV. Compared to the standard geometry, the modular geometry gives somewhat worse results for hard decay channels and slightly better results for soft channels.

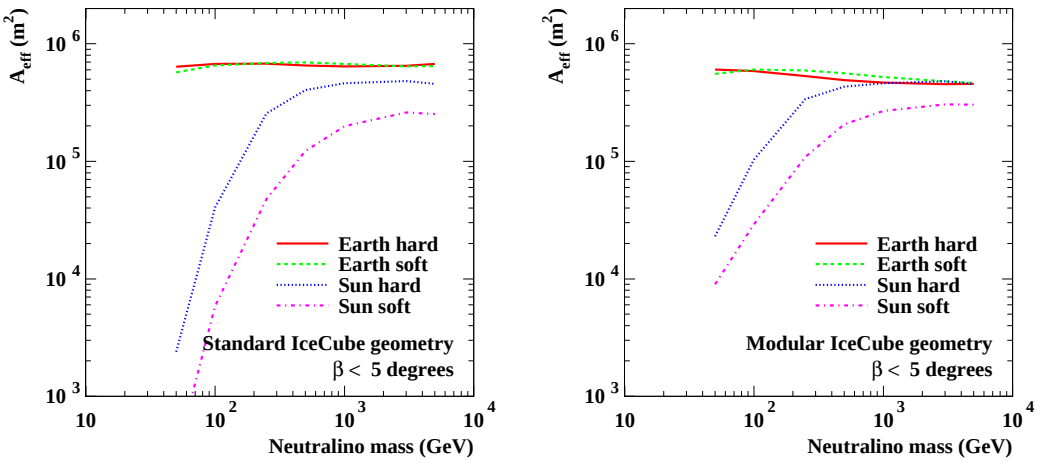

Figure 48: Effective area after a 10-degree cut on the angle between the reconstructed muon and the angle of the source, for different annihilation places, annihilation channels and WIMP masses. Results for the standard geometry to the left and for the modular geometry to the right.

Figure 49 shows the predicted muon rates from WIMPs annihilating in the Earth and the Sun as a function of the WIMP mass. Shown are results for the standard configuration with simple quality cuts after reconstruction. Each symbol in the plot corresponds to one particular combination of MSSM parameters (with the WIMP mass being one of them). Lines indicate the limits which could be achieved with IceCube after 5 years observation. Different symbols mark MSSM versions which are currently ruled out by direct detection experiments, which could be seen by direct detection experiments if the sensitivity is increased by a factor of ten, and which could not be seen by present direct detection experiments even after tenfold increase in sensitivity, respectively. All values are normalized to 10 GeV threshold for reasons of comparison[6]. It has been shown in [121] that IceCube could play a complementary role to future direct detection experiments (like CRESST or GENIUS) for annihilation in the Earth, and even has

[6]For certain directions the IceCube energy threshold indeed might be reduced below 20 GeV. If the track of the secondary muon is close to the vertical and close to an individual string (say less than ∼7 m), PMT amplitudes will be high, scattering effects will be small, and consequently arrival time jitters will be small. Under these conditions not only the muon energy can be determined with an accuracy of a few GeV from its track length, but also the vertex cascade may be identified and its energy determined. Taken all strings together, one obtains a detection volume of 10 Megatons at a threshold of 20 GeV.

a slight advantage over direct detection experiments for certain low-mass WIMP models and annihilation in the Sun.

5.7.2 Neutrino oscillations

With a 10 Megaton detector of 20 GeV threshold, IceCube may also play a role in confirming the compelling indications that atmospheric neutrinos oscillate. Studies of systematics and backgrounds have revealed that significant progress requires much smaller spacing of OMs along a string than presently planned (namely 4-6 meters). For reduction of the threshold toward the horizon also a considerably smaller string spacing would be necessary. Such specialized effort is only warranted if ongoing experiments fail to conclusively prove the oscillation hypothesis. In that case one would consider to create a densely equipped region for detection of low-energy contained events as one part of IceCube. This region would be nested in the full array which acts as veto against through-going tracks. A possible solution would be to fill AMANDA-II with additional strings with small OM spacing. Note that interpretation of the feeble angular dependent oscillation effects at high neutrino energies require an extremely good understanding of the detector systematics.

In recent papers [122], the possibility is discussed to direct a neutrino beam to IceCube - either a WBB beam or a beam from a neutrino factory. The short duty time of an accelerator would allow to relax the cuts for background suppression since during the short spill times the detector is nearly free of background. The aim would be to measure mixing angle θ_{13} and the sign of Δm^2_{31}, even though it is not possible to discriminate between charges. However, it has has to be investigated how well discrimination between muon tracks and ccascades at low energies would work.

5.7.3 MeV Neutrinos from Supernovae

Although the MeV-level energies of supernova neutrinos are far below the AMANDA/IceCube trigger threshold, a supernova could be detected by observing higher counting rates of individual PMTs over a time window of 5-10 s. The enhancement in rate of *one* PMT will be buried in dark noise signals of that PMT. However, summing the signals from *all* PMTs over 10 s, significant excesses can be observed. With background rates more than 10 times lower than ocean experiments, AMANDA and IceCube have the potential to see a supernova and to generate an alarm signal.

IceCube, with low-potassium glass spheres (^{40}K decays in the glass sphere are the main source of external noise), might barely reach the the Large Magellanic Cloud.

AMANDA is officially, and will actively be in the near future, a member of the Supernova Early Warning System (SNEWS) [154]. The role of AMANDA will be to yield one of several coincident alarm signals from different detectors like Super-K, LVD and SNO (Macro being shut down in the mean time). On top of that, IceCube might participate in the goal to estimate the supernova direction by triangulation [153].

Figure 50 shows the increase in counting rate as seen in AMANDA-II and IceCube. Given

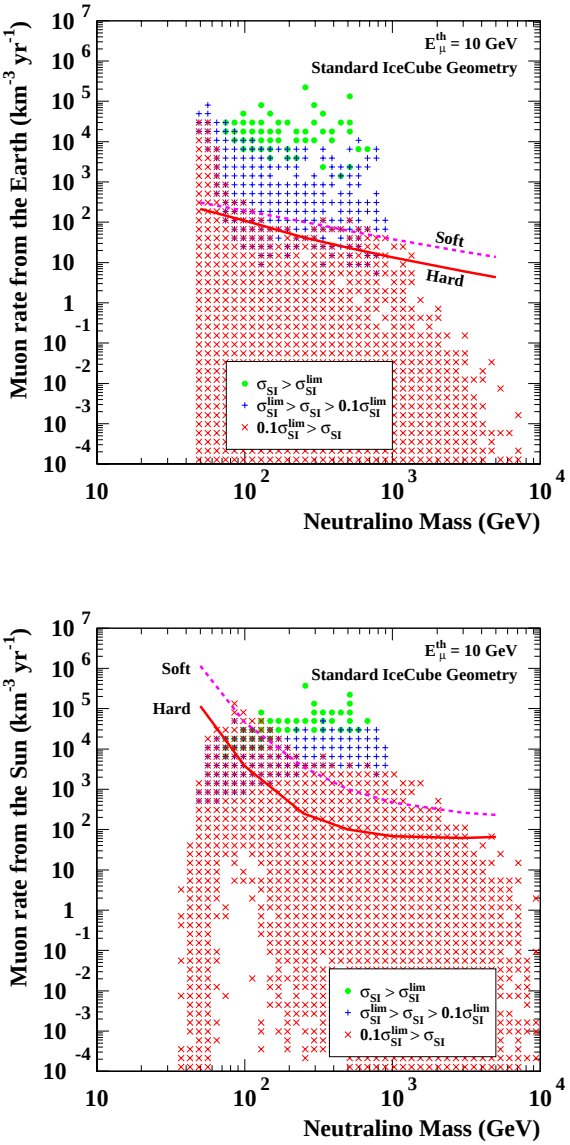

Figure 49: The predicted muon rates from WIMPs annihilating in the Earth (left) and the Sun (right) as a function of the WIMP mass. Each symbol in the plot corresponds to one particular combination of MSSM parameters. Lines indicate the limits which could be achieved with IceCube after 5 years observation. Different symbols mark MSSM versions which are currently ruled out by direct detection experiments (dots), which can be seen by direct detection experiments if the sensitivity is increased by a factor of ten (+), and which could not be seen by present direct detection experiments even after tenfold increase in sensitivity (×), respectively.

a known template for time evolution of the pulse, the resulting accuracy in timing could be 14 ms for AMANDA-II and as good as 1-3 ms for IceCube. The resulting angular resolution depends on the orientation of the triangulation grid with respect to the supernova. For the three detectors Super-K, SNO and IceCube it would between typical values of 5 to 20 degrees. Figure 51 shows the χ^2-contours of reconstructed supernova direction for a randomly choosen supernova event.

With dedicated detectors like Super-K, one can determine the neutrino direction from electron direction measurement in νe^- interaction with an accuracy of about 5°.

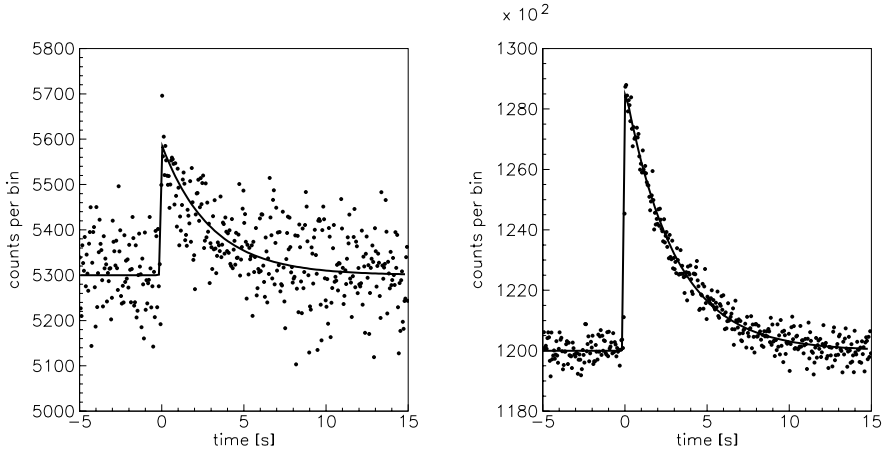

Figure 50: Simulated count rate data for a supernova at the center of the Galaxy, for AMANDA-II (left) and IceCube (right). The lines correspond to the simulation input.

5.7.4 Relativistic magnetic monopoles

Several theories predict the existence of magnetic monopoles with a magnetic charge which obeys the Dirac quantization rule $g = n \cdot e/(2\alpha)$ with $n = 1, 2, 3, ...$ and $\alpha = 1/137$. A magnetic monopole with unit magnetic Dirac charge $g = 137/2 \cdot e$ and a velocity β close to 1 would emit Čerenkov radiation along its path, exceeding that of a bare relativistic muon by a factor of 8300 for $\beta = 1$. The value 8300 is obtained from $(137/2)^2$ multiplied with n_r^2, with $n_r = 1.33$ being the refractive index of water. This is a rather unique signature. Figure 52 shows the light emission from a monopole as a function of β. Note that due to the production of δ electrons, the monopole produces light even below its own Čerenkov threshold.

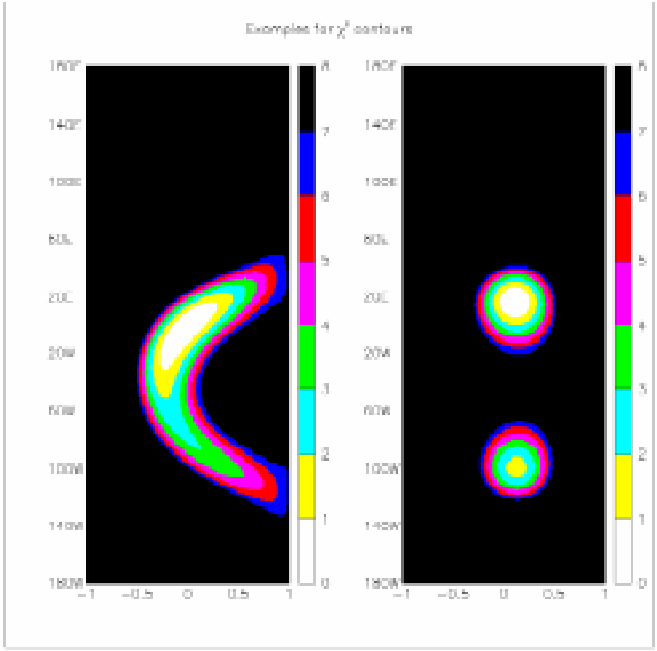

Figure 51: χ^2-contours of reconstructed supernova direction for a randomly choosen supernova event. It was assumed, that timing data from a detector at the South Pole are combined with data from SuperKamiokande and SNO. In the left figure, a time resolution of 14 ms (AMANDA-II) was assumed, in the right figure, a time resolution of 3 ms (IceCube). The nominal supernova direction was $\cos\theta = 0.1$, $\phi = 2.98$. Note the twofold ambiguity which even for IceCube necessarily remains if only three sites contribute.

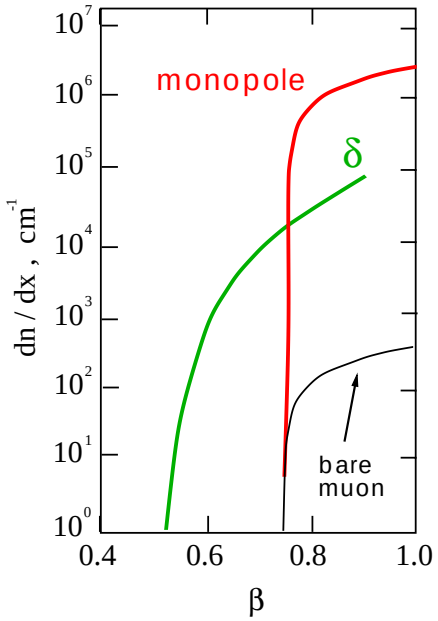

Figure 52: Čerenkov light emission from magnetic monopoles in water (in photons per cm) as a function of velocity. The curve labeled "δ" represents the light produced by delta electrons which are generated by the monopole below its Čerenkov threshold.

Any early Universe phase transition occuring after inflation has the potential to populate the Universe with a flux of magnetic monopoles. Observations of galactic magnetic fields, as well as observations matched with models for extragalactical field lead to the conlcusion that monopoles of masses below 10^{15} GeV can be accelerated in these fields to relativistic velocities [147]. Figure 53 summarizes the limits obtained until now. Note that these limits are below the so-called Parker bound (10^{15} cm^{-2} s^{-1} sr^{-1}). This bound is is derived from the very existence of galactic magnetic fields which would be destroyed by a too high flux of magnetic monopoles.

A cube kilometer detector could improve the sensitivity of this search by about two orders of magnitude compared to the present AMANDA limit. As mentioned above, the search could be extended to down to velocities $\beta \sim 0.5$ by detecting the δ electrons generated along the monopole path.

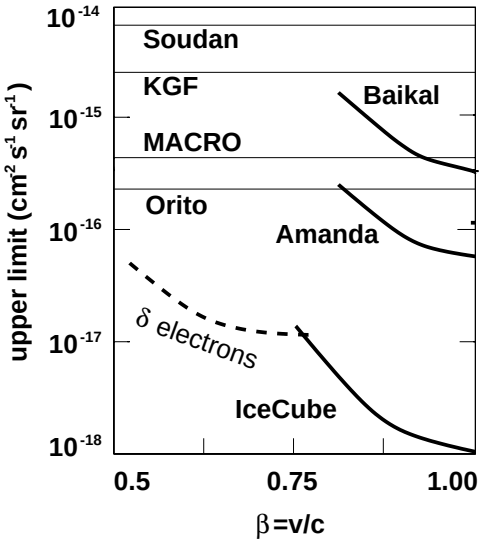

Figure 53: Limits on the flux of relativistic monopoles achievable with IceCube compared to existing limits.

5.7.5 Slowly moving, bright particles

The passage of a particle with a velocity significantly below c yields a very distinct time pattern.

Candidates for particles with a velocity $\beta < 0.1\,c$ and with strong light emission are GUT magnetic monopoles or nuclearities [120, 148]. GUT monopoles may induce protons decays. Therefore one would expect Čerenkov light signals generated by the nucleon decay products along the path of the monopoles. For certain regions of the parameter space in monopole velocity and catalysis cross section, these signals would cause sequential hits in individual PMTs within time windows of 10^{-5} – 10^{-3} s.

Nuclearities (strange quark matter) should be aggregates of u, d and s quarks in equal proportions, and of electrons, to ensure their electrical neutrality. They should be stable for

all baryon numbers in the range between ordinary nuclei and neutron stars ($A \sim 10^{57}$). They could have been produced in the primordial Universe or in violent astrophysical processes. See for recent reviews [148, 149].

The most relevant upper limits on the flux of these particles come from track etch experiments or liquid scintillator experiments (both e.g. represented by MACRO). The Baikal experiment has searched for enhanced counting rates over time intervals of 500 μs and deduced upper limits on the flux of GUT monopoles and strange quark matter [120]. The search technique relies on detectors with a low counting rate. In the Baikal case a rate as low as 100 Hz is achieved by local coincidences. With a counting rate per OM of 300 Hz (compared to typically 1 kHz for AMANDA), also IceCube may look for corresponding phenomena.

5.8 IceCube Configuration Flexibility

The default IceCube configuration is optimized for the TeV–PeV neutrino energy region. In the scenario where a potential signal is seen at PeV energies or above, but the IceCube array has not yet been fully deployed, the IceCube design permits considerable flexibility. String deployments can be modified to increase subsequent interstring spacings, expanding the geometrical area at little added financial expense. Since muons at these energies are brighter, one crossing the array would experience no "blind" corridors. Of course, performance at lower energies would suffer with increasing interstring spacing. Conversely, if a signal is detected at the lower end of the TeV–PeV energy scale, the detector can be "backfilled" using as-yet-undeployed DOMs to increase the overall pixel density. This would enhance sensitivity to lower energy neutrinos.

5.9 Calibration of High-Level Detector Response Variables

Detector geometry, angular response, vertex resolution and energy response can be calibrated using *in situ* light sources, IceTop-tagged or untagged downgoing cosmic-ray muons, and atmospheric neutrinos. Examples of *in situ* light sources include blue and UV LEDs, lasers buried in the ice or placed on the surface and connected via optical fiber to diffusing elements placed in the ice, buried DC light sources, etc. Lower-level parameters like cable lengths will be calibrated online by the DAQ system and can be verified by adapting some of the techniques described below.

5.9.1 Geometry Calibration

IceCube simulations indicate that downgoing muons can be used to determine the relative positions of the OMs to an accuracy of less than 1 m, which is sufficient for accurate reconstruction of neutrino-induced muons and cascades. The algorithm entails using fitted downgoing cosmic-ray muon tracks and calculating the probability for a photon from the track to arrive at each of a number of imaginary spatial grid points surrounding the putative OM position. Averaging over many tracks, each set of grid points around each OM describes a paraboloid whose maximum can be used to estimate the true OM position. Using these new position estimates for each OM we can then repeat the entire procedure until the iterative procedure converges.

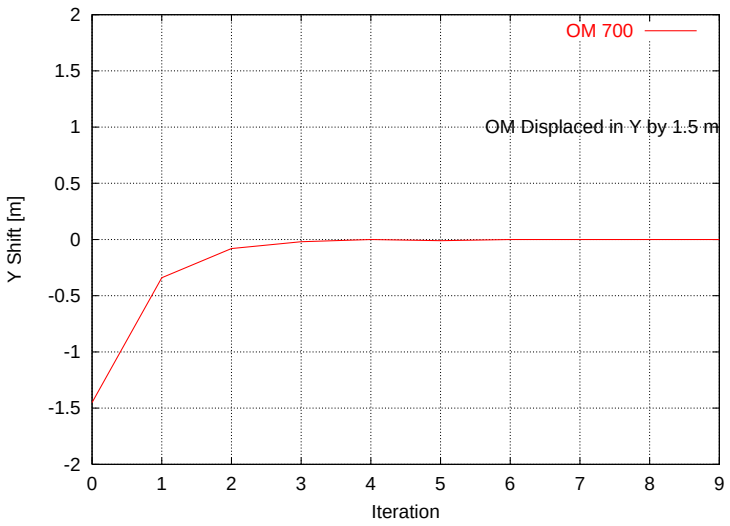

Figure 54: Calculated correct position of a single OM. The OM was intentionally displaced from its true position by 1.5 m The procedure demonstrates that convergence occurs in three iterations.

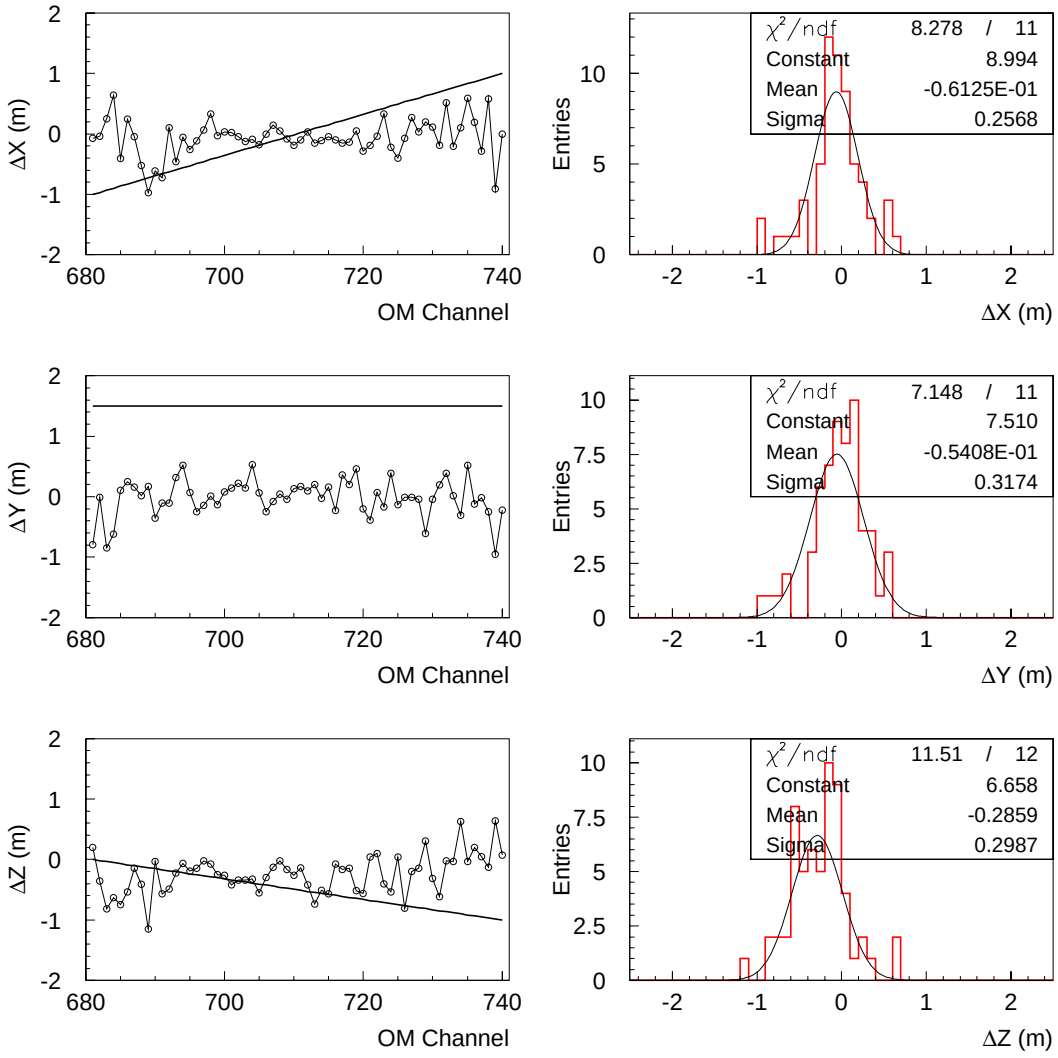

Figure 55: Left plots: Intentional displacements of OMs (straight lines), all applied at the same time, and their calibrated positions (dots connected by lines). Right plots: Calibrated OM positions relative to original correct values. The left plots demonstrate that the calibration procedure can cope with string displacements which are larger than what the IceCube drill is designed to deliver. The right plots show that the resolution of the calibration is roughly 30 cm. The offset in ΔZ is believed to be an artifact of inaccuracies in the Monte Carlo parameterization of the photon arrival times.

Tests using simulated data have shown that the procedure converges quickly enough that it can be used to determine geometry positions of OMs almost immediately after deployment. A plot showing the convergence of the procedure for a single OM, whose position was intentionally displaced from its correct position by 1.5 m, is shown in fig. 54. Figure 55 shows how well the procedure calibrates the correct OM positions after intentional three-dimensional displacements of a string's position. This procedure will be a useful high-level test of the success of the deployment at the full-string level, and will permit the running of subsequent calibrations which require detector geometry as input. More computationally intensive refinements of the technique can be used to fine-tune the positions for use by the online filters and downstream data analyses. (Bright *in situ* light sources may also be useful for geometry calibrations, and indeed this is how the AMANDA geometry has been calibrated. However, IceCube's larger interstring spacing may limit the effectiveness of this techinque.)

5.9.2 Calibration of Angular Response

Events simultaneously triggering IceTop and IceCube constitute a data sample which can be used to calibrate IceCube's angular response. A similar technique has been used successfully by AMANDA with SPASE-2 triggers, where only a limited solid angle was available for study. With substantially larger solid angle coverage, IceTop should enable IceCube to calibrate its angular response more completely and accurately.

Over a smaller solid angle, IceTop can provide a tagged *single* muon beam for calibration of IceCube response to single muons and their direction reconstruction. This will require a denser subarray component, either in the center or perhaps also at one or more other locations on the surface, that triggers at a much lower threshold for showers with energies of roughly 10 TeV that are most likely to have only zero or one high energy muon capable of reaching IceCube.

5.9.3 Calibration of Vertex Resolution

The vertex resolution for cascades can be studied with pulsed *in situ* light sources located at known positions in the ice. Varying the intensity of these sources provides a way to study the vertex resolution as a function of energy. In AMANDA, sources have been determined to produce light outputs equivalent to a cascade event with several hundred TeV of energy.

5.9.4 Energy Calibration

The IceCube energy response can be calibrated using a number of independent techniques. Atmospheric neutrinos provide a test-beam with a known energy spectrum against which IceCube can be calibrated. Downgoing muons may also be of use here, although often such events are composed of mulitple muons. (This may be addressed by IceTop, as discussed below.) Bremsstrahlung events from downgoing muons provide an energy calibration for cascades at the lower end of the energy scale, up to several hundred GeV. *In situ* light sources, preferably with precisely controllable output intensities, offer a way to calibrate IceCube energy response to cascades at higher energies, up to roughly 500 TeV.

5.10 IceTop

The solid surface above IceCube allows the possibility of a surface air shower array that can be used for calibration (by providing a set of tagged muon bundles), for veto of certain backgrounds generated by large air showers and for cosmic-ray studies. A square kilometer array of suitably designed detectors on a 125 m grid has full efficiency for air showers from 10^{15} eV to 10^{18} eV. Thus it covers an important energy range from below the knee of the primary spectrum to an energy where we may expect at least the beginning of a transition from galactic cosmic-rays to cosmic-rays of extragalactic origin.

5.10.1 Tagged Muon Bundles

Figure 56 summarizes the characteristics of IceTop events in IceCube. Bundles range from ~ 10 muons at the top of IceCube from 10^{15} eV protons to $\sim 10^4$ muons in the core of a shower generated by an iron nucleus of 10^{18} eV. Most of the muons are concentrated in a core with typical size less than the spacing between IceCube strings, and about half the muons in the bundle range out inside IceCube. The high energy events contain muons with sufficient energy to produce bursts of radiation in IceCube. There will be about 100 tagged air showers per day with multi-TeV muons in IceCube. Since a muon that goes through IceCube deposits about 200 GeV or more of energy, one sees from the diagram that there will be of order ten thousand tagged events per year in IceCube in which more than 100 TeV of energy is deposited by the muons. The ability to identify and measure such coincident events readily is a unique feature of a deep neutrino detector under a solid overburden.

The surface detectors are modelled on the water Čerenkov tanks pioneered by the Haverah Park air shower experiment [89] and currently used in the Auger detector now under construction in Argentina [155]. At the South Pole the water freezes, but the Čerenkov light generated by relativistic charged particles is essentially the same as in water. This has been verified by a small test tank deployed inside the current South Pole Air Shower Experiment (SPASE) [156] during the 00/01 Antarctic season. Design and layout of the tanks is described in 6.9.

We have adapted Auger tank simulation tools and used them to simulate IceTop tanks in order to simulate waveforms expected in showers with energies in the PeV–EeV energy range. Figure 57 shows a sample IceTop waveform generated in this manner.

Most of the showers that trigger the detector will be near the threshold energy of approximately 200 TeV. Air showers with this energy typically contain 1 to 10 muons with sufficient energy to reach the deep detectors within a radius of 20-30 m of the shower trajectory. A fraction of these events will be used for calibration of the angular response and reconstruction algorithms of IceCube, as mentioned above.

5.10.2 IceTop as a Veto

In addition to providing a sample of events for calibration and for study of air-shower-induced backgrounds in IceCube, the surface array will act as a partial veto. All events generated by showers with $E > 10^{15}$ eV can be vetoed when the shower passes through the surface array. In

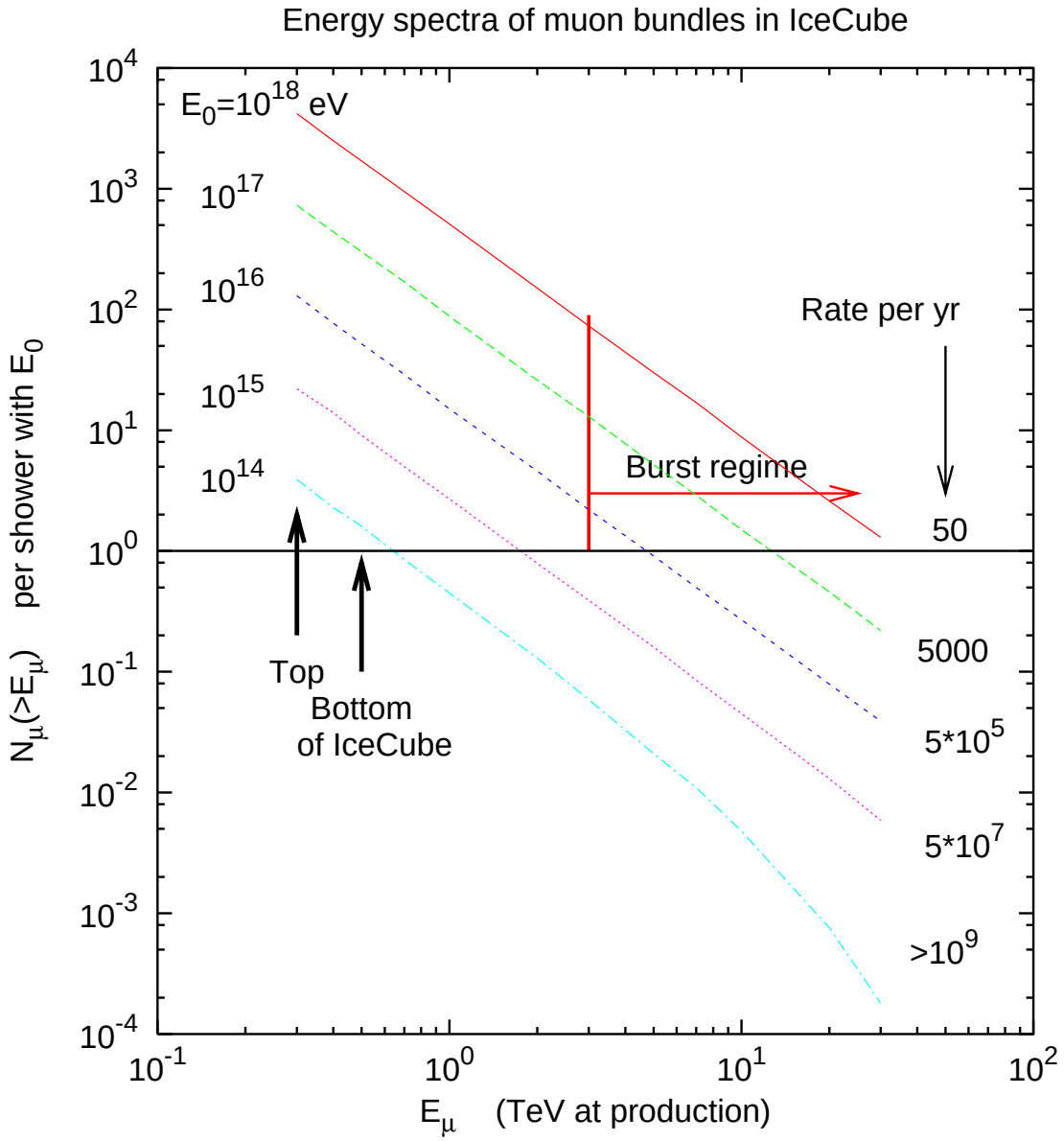

Figure 56: Diagram showing the energy spectra of muon bundles in IceCube associated with air showers (proton primaries) that can be measured with IceTop. Each curve is labelled at the left by the primary energy of the associated shower and on the right by the number of events per logarithmic energy interval that strike the surface array within the solid angle determined by IceTop and IceCube. The surface array is fully efficient for showers above 10^{15} eV. The arrows indicate muon energy at production in the atmosphere needed to reach the top and the bottom of IceCube. Muons above $\sim$ 3 TeV will tend to produce bursts of radiation in IceCube.

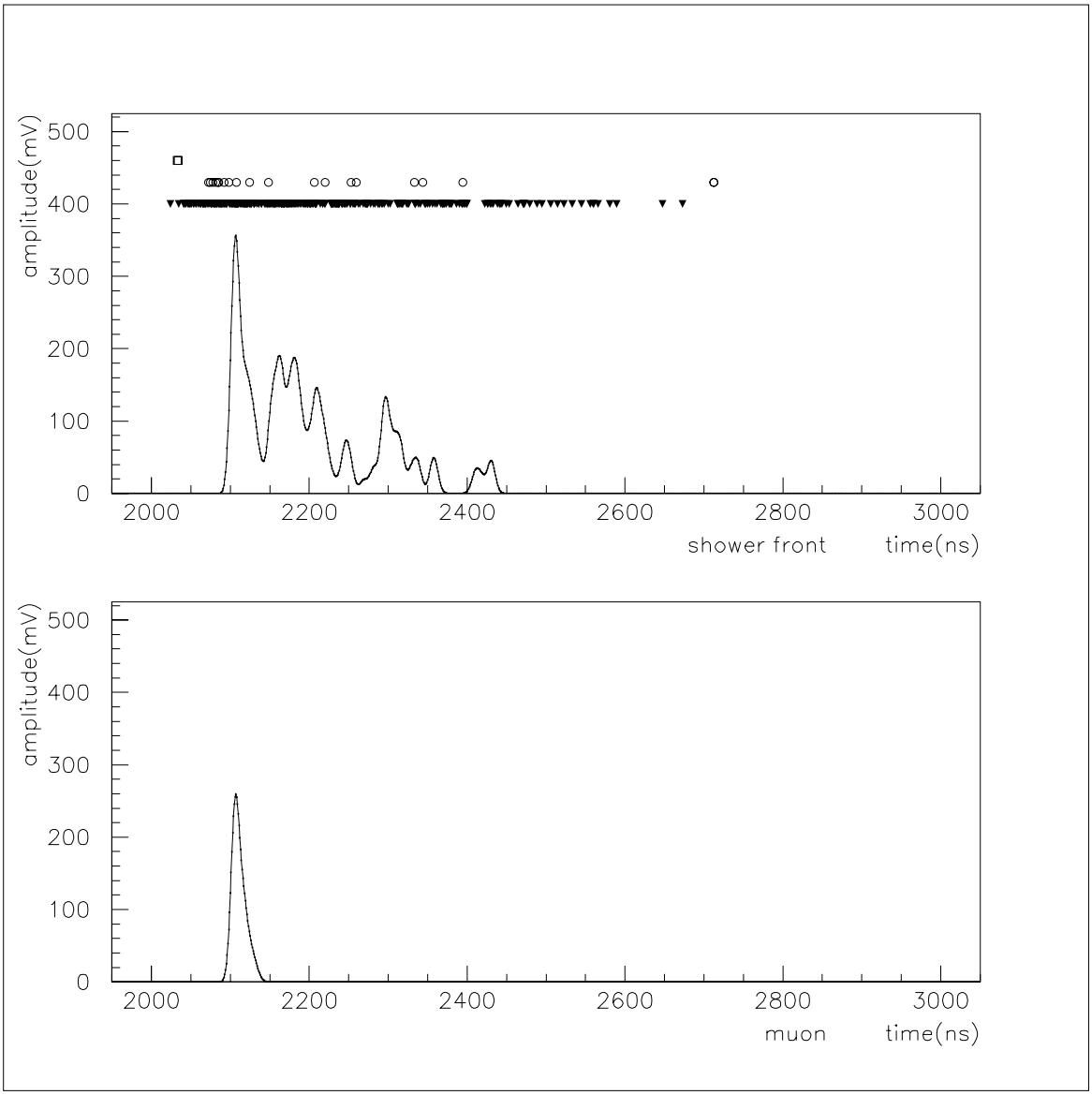

Figure 57: The upper panel shows the waveform of the signal at 300 m from the shower core for a proton-initiated shower of 100 PeV. The simulation is for an 8 in PMT at the center of the tank viewing photons reflected from the bottom and sides of the ice tank. The lining of the cover is black. The marks at the top of the figure indicate the arrival time at the top of the ice of muons (top set of marks), electrons (middle set of marks) and γ-rays (bottom set of marks). The lower panel shows the the muon contribution to the waveform. In both panels the amplitude is plotted as a function of time at the output of the base of the PMT. Most of the delay is due to the drift time of electrons in the PMT.

addition, higher energy events, which are a potential source of background for neutrino-induced cascades, can be vetoed even by showers passing a long distance outside the array. In particular, showers with $E > 10^{17}$ eV and cores a km outside the array will produce a minimal trigger near the boundary of the array.

5.10.3 Cosmic-ray Physics

The IceCube-IceTop coincidence data will cover the energy range from below the knee of the cosmic-ray spectrum to $> 10^{18}$ eV. Each event will contain a measure of the shower size at the surface and a signal from the deep detector produced by muons with $E_\mu > 300$ GeV at production. At the high elevation of the South Pole, showers will be observed near maximum so that shower size will give a relatively good measure of primary energy. The ratio of the muon-induced signal in IceCube as a function of primary energy (as determined by shower size at the surface) will give a new measure of primary composition over three orders of magnitude in energy. In particular, if the knee is due to a steepening of the rigidity spectrum, a steepening of the spectrum of protons around 3×10^{15} eV should be followed by a break in the spectrum of iron at 8×10^{16} eV.

6 Experimental Requirements

In this section we discuss the requirements on IceCube technologies dictated by science. The most important requirements can be summarized as follows:

- time resolution of ≤ 5 ns rms,
- waveform digitization with ≥ 200 Msps (first 400 ns) and ≥ 33 Msps (thereafter),
- waveform sampling depth of 4 μs,
- dynamic range of ≥ 200 PE/15 ns,
- dead time of $\leq 1\%$,
- gain variation of $\leq 2\%$ per week,
- OM noise rate ≤ 500 Hz,
- overall permanent channel failure rate of $< 5\%$.

While extensive simulations of the IceCube detector and its performance have been done, ongoing studies of improved analysis techniques using the operating AMANDA-II detector may still suggest changes in these requirements.

6.1 Time Resolution

From operation and Monte Carlo simulations of the AMANDA detector we have learned that event rates and angular resolution of atmospheric neutrinos, as well as the efficiency for rejecting the background of atmospheric muons, do not depend on the accuracy of time calibration (t_0) and on time resolution (σ_t) provided they do not exceed 10 ns. Deterioration of the detector performance becomes apparent only above 15 ns because below this scale scattering in the bulk ice is the dominant effect. For the higher energy PeV–EeV neutrino signals in IceCube, the requirement may even be looser because the average distances over which photons are collected are increased and so are the effects of scattering. For electromagnetic showers, waveform digitization will be important, but a timing accuracy similar to the one required for muon tracks should be adequate.

A resolution of ≤ 5 ns is a well-motivated requirement. Better resolution results in better performance in rare cases. For instance, science requiring low thresholds, or the detection of short muon tracks very close to strings, may benefit from better time resolution because the effect of scattering is suppressed. Examples are the detection of neutrinos from the annihilation of dark matter particles in the center of the Earth (producing short, nearly vertical muons) and the detection of oscillating beams from an accelerator at a northern site. One may also be able to argue for improved time resolution on the basis of better reconstruction of the direction of electromagnetic showers induced by electron-neutrinos, or to separate close showers from the production and decay of tau-neutrinos (double bang events). One should keep in mind that time resolution is ultimately limited by the PMT at 1–2 ns for multi-PE signals.

6.2 Waveforms

Experience with the AMANDA detector for observing electromagnetic showers and high-energy showering muons has demonstrated the significant advantages of using the presently available "reduced" waveform information, like amplitude and time-over-threshold (TOT) rather than amplitude alone. Light scattering results in strong signal dispersion over large distances. This effect dilutes information (namely the precise arrival time of the first photon), but also adds information: The length of the light signal recorded by a single PMT indicates the distance to the light source. Therefore the combination of amplitude and time structure allows one to distinguish between close, dim light sources and distant, bright light sources. The reconstruction of distant tracks and very large high energy showers will therefore require full waveform digitization. For instance, simulations based on TOT alone have demonstrated very poor angular resolution for electromagnetic showers.

Waveforms should be recorded at a rate of ≥ 200 Msps for the first 400 ns in order to obtain good timing and double pulse resolution. For longer times, a lower sampling rate of ≥ 33 Msps is sufficient to tease out structure due to secondary light pulses such as those due to double bangs from ν_τ events.

The waveform sampling depth should be roughly 4 μs, long enough to capture full waveform information from most (but not all) double bang events.

6.3 Dynamic Range and Linearity

The basic requirement is a dynamic range of 200 PEs per 15 ns. The interval 15 ns represents the typical time duration of a single PE pulse. This requirement is mostly driven by the reconstruction of energy and direction of very high-energy showers, typically 1 PeV. These produce measurable light over times of several hundreds of nsec. The amplitude and the waveform of the light pulses at the OM carry information on the position, the directionality and the energy of the shower. Figure 58 shows AMANDA-II PMT pulses from an *in situ* N_2 laser pulse with a light output equivalent to a 1 PeV shower. The oscilloscope pulses shown are from OMs at three distances between 45 and 167 m.

Because of scattering of the photons in the ice, the shape of the photon pulse broadens with increasing distance from the point of emission. For example, at a distance of 60 m (about half the string spacing in IceCube) a 1 PeV shower will generate a PMT pulse of 1000 (200) PEs with a FWHM of 100 ns (150 ns) in forward (backward) direction of the shower. The example illustrates the directionality information contained in these data. Such an event will be observed by hundreds of OMs up to distances of more than 250 m from the interaction. The maximum current in this event reaches 12 PE/ns, or 180 PE/15 ns. Because of the greatly enhanced cross-section at 6.4 PeV (Glashow resonance), events at this energy may be preferentially observed, despite a falling spectrum. For these events, the peak input signal is more than 1000 PE/15 ns (at a distance of 60 m).

The non-spherical shape of the initial light pattern can be exploited for good directional and energy reconstruction. While the number of PMTs that saturate increases with higher

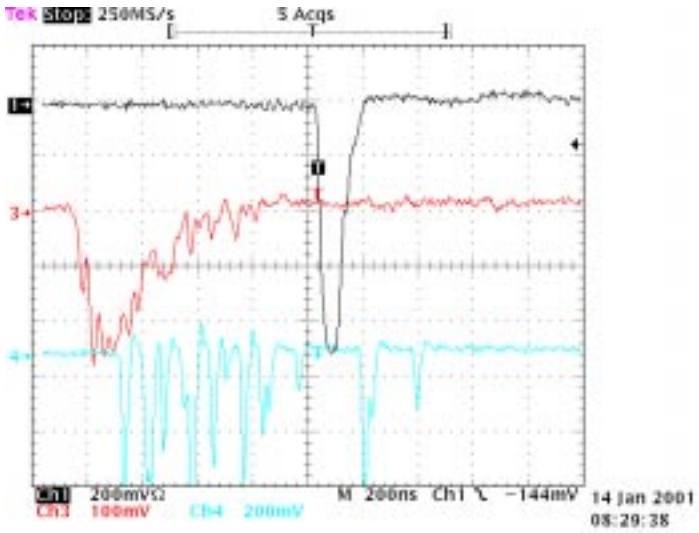

Figure 58: PMT signals from a 335 nm nitrogen laser signal simulating a 1 PeV shower (about 10^10 photons). The light is detected by AMANDA-II optical modules with fiber-optic readout at distances of approximately 45 m (black trace), 115 m (red trace), and 167 m (cyan trace).

energies (10 PeV and higher), the total number of PMT that observe a signal grows by an even larger number. Based on evaluations of simulated waveforms, we conclude that a dynamic range of about 15 PE/ns would be sufficient for an accurate reconstruction of the relevant event parameters (energy, direction), even though OMs nearest the shower will saturate.

PMTs that are very close to the shower core will saturate at the maximum anode current that a PMT is able to sustain. In the case of the Hamamatsu 10 in PMT, which is a prime candidate for IceCube, the anode current is limited to 80 mA, which sets an upper limit on the dynamic range in PE that depends on the gain. The operating conditions of IceCube suggest a gain of $\sim 10^7$, corresponding to a theoretical peak of 500 PE/15 ns. It seems reasonable to expect that the PMT can sustain anode currents of 200 PE per 15 ns for intervals of about 100–200 ns. Recognizing the limitations on the dynamic range set by the PMT, and accepting a saturation of the 10% of the OMs near the shower core, we set the physics requirement for the dynamic range to 200 PE/15 nsec.

6.4 Absolute Amplitude Calibration and Stability

The absolute calibration of OMs should be known to better than 5%. The absolute calibration and measurement of the angular acceptance of the instrument will be performed by observing known signals from LEDs and from cosmic ray muon tracks. The measurement of shower profiles requires good calibration of individual OMs; see above. The dependence of the muon effective area of the operating AMANDA-B10 detector is close to, but less than linear.

6.5 Dead time

We aim for a deadtime for muon triggers as low as 1%, assuming a trigger rate of 100 Hz. Actually, one might consider to lower certain thresholds of the hardware triggers, e.g. in order to cover low energy tracks. This might increase the trigger rate and finally lead to a slightly higher deadtime.

6.6 Sensitivity of optical modules

Maximum light collection is of highest importance. In particular, it helps to lower the detection threshold for low energy muons and increases the detection sensitivity for supernovae. For high energy muons or cascades, it might allow for an increase in the string spacing. Compared to Amanda-II, the light collection will be improved by the use of PMTs with diameter 10 in or larger, giving about 40% better light collection than the present 8 in PMTs. If a sound technological solution is found, wavelength shifter coatings should be applied to the glass spheres. Present results indicate that this may result in a 20–35% better light conversion.

6.7 Noise Rate and Noise Rate Stability

Ice is a very low noise medium; the noise is dominated by radioactivity introduced by the OM itself. The noise rate in individual OMs is required to be less than 0.5 kHz (compared to typically

1 kHz in the present AMANDA array). For that aim, glass spheres with very low radioactivity content ($< 0.05\%$ potassium content) should be chosen. Rates for all OMs should be recorded for optimal sensitivity and detector monitoring.

For the muon trigger, this level of noise is readily eliminated by the use of local coincidences (a pair of OMs that are adjacent or separated by no more than one OM report).

Supernova detection is based on the identification of rate excesses over a few seconds. It is made possible by the low noise rates and becomes impossible if the rates are as high as 2 kHz. With 300 Hz noise rates, IceCube could monitor not only our own Galaxy, but also the Magellanic cloud.

Rates have to be recorded every ms with 10 bit dynamic range, with the possibility to adjust artificial dead time between 0 and 1 ms in 10μs steps.

6.8 Failure Rate

IceCube Monte Carlo studies have shown that the quality of muon and cascade reconstructions are rather resilient to permanent channel failure rates as high as 10%. (A permanent channel failure is one which cannot be repaired, e.g., a broken in-ice connector.) For muons, only the difference between the true and reconstructed space angle shows some degradation, but only by roughly 3%; for cascades there is essentially no degradation at all. These results can be extended qualitatively to tau events as well.

The main impact of such failures would be to reduce the detector sensitivity. This reduction is energy-dependent and is more pronounced at lower energies. For example, a 10% failure rate results in the loss at trigger level of 40% of muons with energies between 400 and 500 GeV, but only 5% of muons with energies between 8 and 10 TeV. Above about 30 TeV there is no loss. A 10% loss would therefore not dramatically affect ultrahigh energy muon neutrino physics, but it would adversely impact IceCube atmospheric muon neutrino physics, and the usefulness of these neutrinos as an IceCube calibration tool.

Under the reasonable assumption that sensitivity loss varies roughly linearly with the permanent failure rate, requiring the permanent channel failure rate to be below 5% reduces the impact of such losses on atmospheric muon neutrino physics. At the same time, a 5% failure rate is a realistic goal.

6.9 IceTop

The IceTop array should trigger at near the 90% level for air showers above 500 TeV, which will require stations of roughly 7 m^2 area located near the top of each string. The tanks should have a dynamic range of $\sim 10^4$ to cover the PeV–EeV energy range without saturation over the full lateral extent of the showers. This will likely require using separate low gain and high gain modules within each tank.

To reduce the background rate each station should consist of two tanks, each roughly 3.5 m^2 in area. A local coincidence should be implemented between neighboring tanks to eliminate single muon events as well as reduce the likelihood of triggering on random electron and photon

hits not associated with larger air showers. The separation of these individual tanks should be large enough to keep the number of local triggers to a level that can be handled by the DOM communications, perhaps several meters.

A denser subarray within IceTop should consist of smaller tanks on the order of 1 m^2 area separated by 10 m so that they will have a much lower threshold near 10 TeV to trigger on showers most likely to contain only one high energy muon. This subarray could be composed of the present SPASE array with an embedded standard IceTop station. The subarray should record only a fraction of the data that triggers depending on what is needed for calibration and most acceptable for the DAQ.

In addition, it is possible that we will decide to record as much of this low energy data as DOM communications will allow, storing several days of data in a disk cache at the Pole. This cache should be accessed when interesting IceCube events come in over that same time, when all low energy surface array data from a wide time window on each side of the interesting events should be separated out and stored for later investigations.

7 Design and Description of IceCube

7.1 Overview

In the IceCube baseline design, 80 strings are regularly spaced by 125 m over an area of approximately one square kilometer, with OMs at depths of 1.4 to 2.4 km below the surface, as shown in fig. 59. In sections 5 and 6 the performance criteria and experimental requirements for this device have been distilled from the scientific goals. In addition to explicit technical requirements, however, the instrumental design concept must incorporate many additional factors such as system cost, software/hardware integration issues, engineering risks, lowest practical power dissipation, noise rejection, noise generation, thermal and physical shock, data flow, Mean Time Before Failure (MTBF) of components, production Quality Assurance (QA), deployment, constraints on commissioning personnel, remote intervention capabilities, calibration, cost of operations, as well as disparate factors such as safety and educational values. The process of optimization involving all these disparate issues has led to an innovative approach, with many attractive features. Nevertheless, no exotic, high speed, brute force, or unproven elements are needed in this concept.

There are three fundamental elements in this architecture, common to both IceCube and IceTop:

- The **Digital Optical Module** (DOM), which captures the signals induced by physical processes and preserves the information quality through immediate conversion to a digital format using an innovative ASIC, the Analog Transient Waveform Digitizer (ATWD);
- A **Network**, which connects the highly dispersed array of optical modules to the surface data acquisition system (DAQ) and provides power to them;
- A **Surface DAQ**, which maintains a master clock time-base and provides all messaging, data flow, filtering, monitoring, calibration, and control functions. Many design features have been realized in the AMANDA string 18, as discussed below.

The instrument design is based on a decentralized digital architecture [157]. The motivation for this approach arises primarily from the need to acquire, from a km-scale instrument, quite complex information in the presence of substantial backgrounds.

Roughly 1.5 kHz of downgoing cosmic ray muons penetrate the geometric volume of IceCube, about six orders of magnitude more than muons induced by neutrinos. The Čerenkov radiation cones generate complex optical signals that are further complicated by scattering in the ice before detection. Parent directionality is not uniquely determined by simple time differences – a horizontal muon generates equal quantities of upgoing and downgoing light. In most cases, neutrino-induced upgoing muons are distinguishable from backgrounds only with sophisticated fits using global space-time correlations.

Given the high background/signal ratio and event complexity, it would be imprudent to filter out the atmospheric muons with tight trigger logic at an early stage. In addition, the downgoing muons offer an ever-present and copious calibration source, as well as a potential arena for the

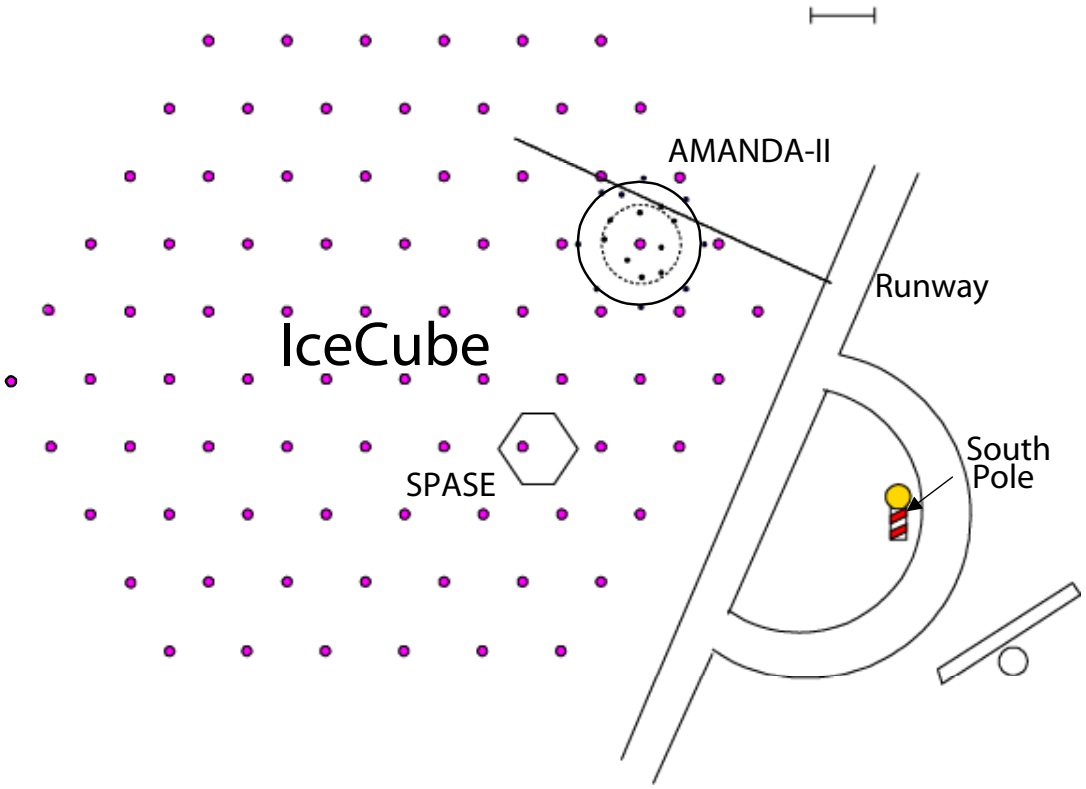

Figure 59: A top view of the IceCube detector, showing the locations of the 80 IceCube strings as well as the AMANDA-II array, the SPASE array, the airplane runway and the South Pole.

detection of subtle astrophysical processes, or possibly even signatures of extreme energy release events in the cosmos.

As noted in section 5, data and simulations show that, for both neutrino-induced and background events, the information content at the photomultiplier (PMT) ranges from single photons arriving over a span of about 1 μs to many hundreds (even thousands) of photons arriving within 15 ns. Extremely high-energy events may generate many thousands of photoelectrons in a continuum of complex patterns lasting several microseconds.

Figure 60 shows a fairly typical raw waveform obtained from a DOM operated in coincidence mode to capture signals induced by a down-going muon. In this figure, the first photon to be detected appears in the ATWD record at about sample 20. Somewhat later, a larger number of detected photons appears, possibly the result of a shower process at some distance from the direct path of Čerenkov light, or possibly the result of multiple muons passing nearby. From a study of these waveforms it is clear that the arriving signals are frequently complex, in the range of 15% for muon-induced signals. Because of the optical scattering, all photons must be included in the analysis to determine the nature of the event.

A measure of the parent muon neutrino energy comes primarily from the capability to record very large energy losses producing electromagnetic showers along a muon trajectory. For electron neutrinos, the showers occur in isolation, requiring for identification that no muon trajectory is present. Tau neutrinos at extreme energies can produce two showers separated by a short distance. The earlier parts of the shower-induced waveforms vary most rapidly and reach the highest amplitudes. The most useful information about shower direction is found here, imposing challenging technical requirements.

Time measurement of these signals over the km-scale volume must be established and maintained with a resolution and accuracy of $\leq$5 ns. The capture of this highly variable complex information requires high-speed ($\geq$200 Msps), high dynamic range ($\geq$14 bits) waveform recording. These technically challenging *desiderata* provide the impetus for an innovative instrument design.

The architecture makes use of modern ideas that rely on time-stamps applied very early to each datum. This approach reduces the amount of real-time circuitry to a remarkably small level relative to traditional DAQ concepts. Correspondingly, data flow is built on conventional networking techniques using messages that may contain either data or control content. Advantages of the architecture based on the DOM include:

- **High dynamic range and signal purity** since PMT signals are captured and digitized in proximity and isolation.
- **Low system power consumption** due to an innovative custom ASIC, the Analog Transient Waveform Digitizer (ATWD).
- **Fully automated remote commissioning and calibration procedures**, minimizing South Pole personnel, an extremely important consideration during South Pole modernization .

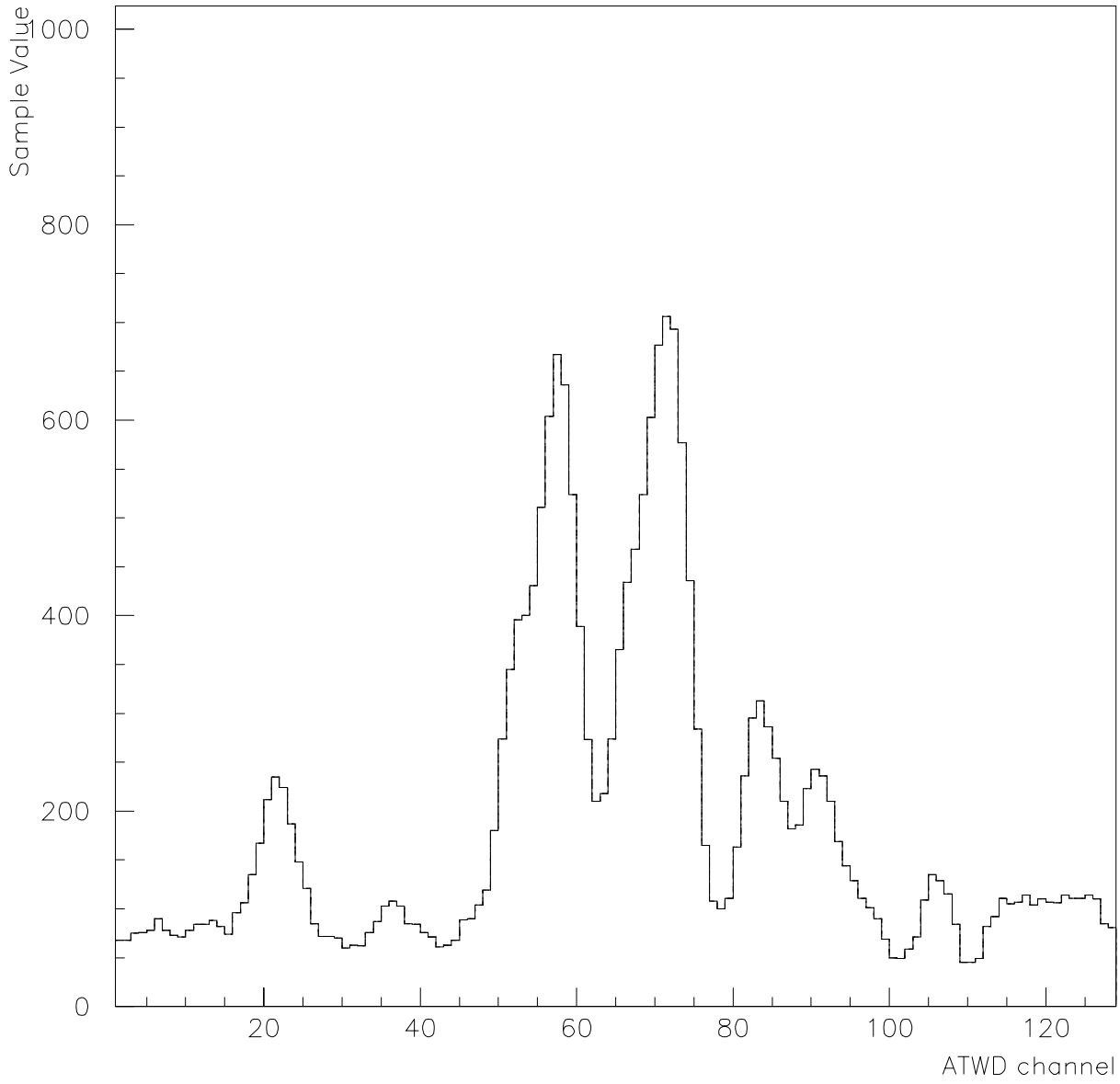

Figure 60: An observed waveform due to muon(s) passing near a DOM pair, operated in coincidence.

- **No low-level analog signal processing in the counting house** offers more predictable large-scale system behavior.
- **Absence of optical fibers** in the system reduces system cost substantially, eliminates $\sim$ 30 plane flights, simplifies and shortens deployment procedures, and maximizes reliability since all connectivity is carried by copper wire pairs.
- **Minimal real-time circuitry within the DAQ**, made possible by time-stamped data and message-based architecture.
- **Network-based DAQ organization** requires only one custom hardware design (the DOM Hub).
- **Use of commercial off-the-shelf components** reduces costs, shortens development time, and enhances test facility realization.
- **Year-round regular operation** provided by robustness against noise at surface due to drilling and pole operations, even during commissioning of new strings.
- **Operational flexibility** is provided by programmable logic and CPU located within DOM, permitting changes stimulated by data or new ideas.

The discussion of the Instrument Design elaborated below will benefit from a brief description of the performance obtained with a string of 41 Digital Optical Module (DOM) prototypes deployed in January 2000 by the AMANDA Collaboration. These DOMs were intended to serve two purposes:

1. Contribute to the regular AMANDA data stream by delivering real-time analog PMT signals via optical fibers to the AMANDA counting room. Because these signals appear identical to the signals of other strings, string 18 contributes to the scientific goals of AMANDA without compromise.
2. Demonstrate the advantages and feasibility of a purely digital technical approach, in which PMT signals are captured and digitized locally, within the optical module. The digital data were transmitted to the surface using the twisted pair copper conductors that also bring power and control signals to the DOMs.

Both of these purposes were achieved, despite challenging schedule and financial constraints. The DOM prototypes of AMANDA string 18 were designed, built, and deployed in about 14 months, and strong support throughout the collaboration during this period was essential for the ultimate success of the effort. Because schedule pressures were so severe, little attention could be given to the issues of reliability and QA. Nevertheless, most of the DOMs of string 18 have delivered extremely stable performance throughout the nearly two year period of operation. One DOM board seems to have developed an internal problem; PMT HV can still be set so that this module continues to contribute to AMANDA data. Two PMT HV bases appear to have failed,

indicating that re-engineering to enhance QA for this subsystem may be needed. There appears to be an intermittent electrical connection in the main cable for another DOM. The remainder of the 41 DOMs have operated continuously with no glitches, crashes, or other indications of instability.

During CY 2000, the DOMs were equipped with a simple surface DAQ that could control PMT HV, set other operating parameters, and return housekeeping data and occasional waveforms to the surface. In January 2001, a subset of four DOMs was equipped with a more complete surface DAQ based on single-channel *Test-Boards*, designed initially for commissioning of DOM boards. With the four-channel Test-Board DAQ, time synchronization is possible, permitting data from different DOMs to be correlated to a few nanoseconds, and even demonstrating the detection of downgoing muons. Most of the technical results described in this section come from an analysis of data obtained with the Test-Board DAQ.

The successful operation of AMANDA string 18 has proven not only the feasibility of the digital system architecture, it has also shown that the associated software is both straightforward to design and stable in operation. Much of the software framework that has enabled these technical results will serve as a springboard for subsequent IceCube efforts.

The block diagram of the Test-Board DAQ is shown in figure 61. For reference, the various approaches used by AMANDA are described in section 7.5.

7.2 Digital Optical Module

The **Digital Optical Module** (DOM) is a self-contained data acquisition platform that is capable of capturing and digitizing real-time PMT pulses, storing data internally, and, when requested, transmitting them to a surface data acquisition (DAQ) system. It contains its own processor, memory, flash file system, and real-time operating system (RTOS). The DOM is capable of scheduling background communications tasks while acquiring data from a local waveform digitizer. All calibration functions needed to interpret data for physical content may be invoked under software control; some operate as scheduled tasks without interfering with data acquisition, and others require dedicated control of state.

A Field-Programmable Gate Array (FPGA) is used to implement most low-level logical functions of the DOM, facilitating fully programmable and flexible implementation of performance features. The FPGA is programmed automatically from a configuration file that the CPU retrieves from flash memory in the DOM after power-up and self-boot has occurred. The FPGA design and CPU programs can be replaced at will subsequent to deployment to enhance functionality. This capability has been exploited already in the AMANDA string 18 (DOMs only), using the satellite link to the south pole from the northern hemisphere.

The basic elements of the DOM are the optical sensor for Čerenkov light, an electronic circuit board for processing signals, a HV generator for the optical sensor, an optical beacon for calibration purposes, and the glass pressure housing. The general physical layout of a generic DOM is shown in fig. 62.

Test DAQ Board Layout

Main Components Diagram
Deployed for Time Calibrations, 2001.

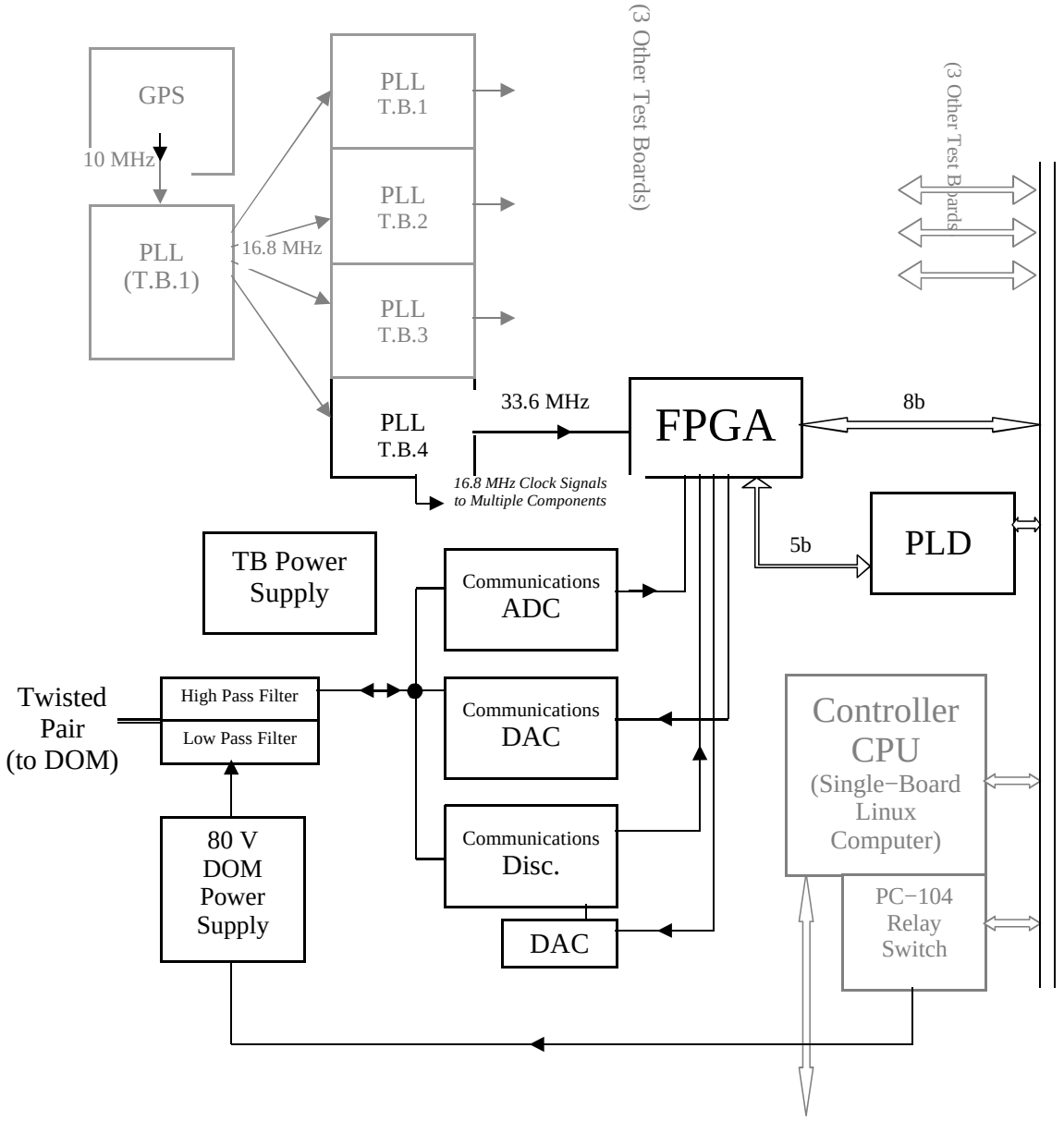

Figure 61: Block diagram of the "Test-Board" used in the AMANDA DOM string DAQ system.

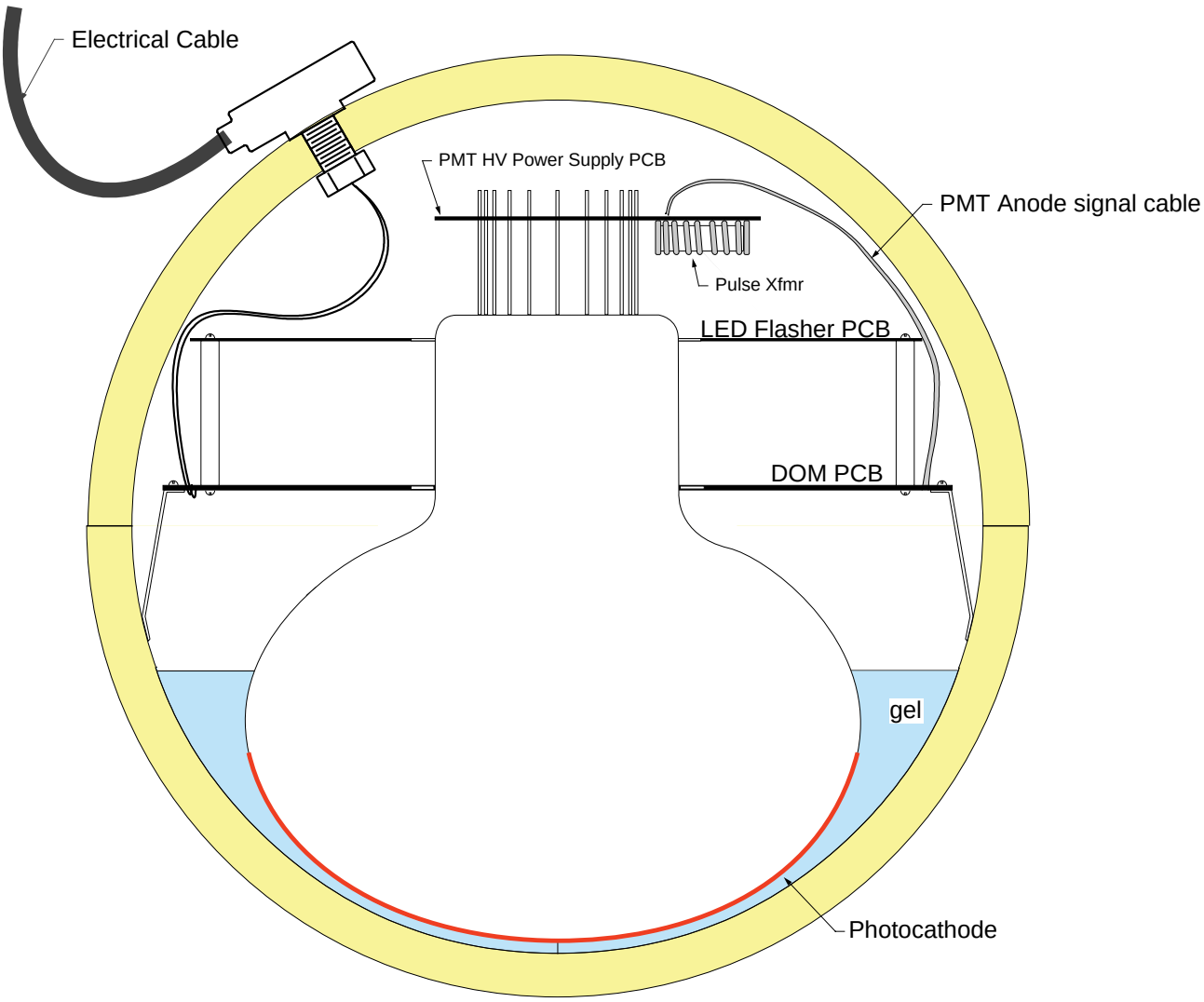

Figure 62: Schematic profile view of a generic Digital Optical Module, showing pressure sphere, optical coupling gel, PMT, signal processing electronics board, LED flasher board, PMT base, and electrical penetrator.

7.2.1 Pressure Housing

The spherical glass pressure housings are standard, well-proven items of commerce, used in numerous oceanographic and maritime applications. For IceCube, the most important qualities are mechanical reliability, cost, optical transmission, and potassium content. Commonly known in the US as Benthospheres, a trade-name of Benthos, Inc., the dominant US supplier, these simple devices have an excellent record for reliability. Over 700 of these, from both Billings and Benthos, in various implementations and sizes, have been deployed in AMANDA without evidence of a single implosive failure. To ensure reliability against implosion, care must be taken not to chip either the surfaces of the hemispherical rims that form the equatorial ground-glass seal, or the holes that permit penetrators to carry signals and power across the boundary. Costs for standard pressure-tested Benthospheres are modest, in the range of $350.

For IceCube, a 13 in diameter sphere is the optimum size. While larger spheres are available that could a accommodate larger optical sensor, the costs for drilling larger diameter holes (with an appropriate margin of safety during deployment) rise very quickly, making larger sizes a poor overall trade-off.

Because the Čerenkov radiation mechanism produces the greatest intensity at ever-smaller wavelengths, limited ultimately by self-absorption, it is of interest to push the optical transmission limit of the glass to a value below the quantum efficiency limit of the PMT. For processing and mechanical strength, the manufacturers use a borosilicate glass that limits transmission to about 350 nm, well above the expected ∼220 nm limit for deep polar ice. It is conceivable that an exterior surface layer of an appropriate wavelength shifter for the component shorter than 350 nm could increase the effective light yield, and this is being explored.

The potassium content of the typical borosilicate glass includes a naturally occurring fraction of ^{40}K. The β particle from the decay of this isotope produces Čerenkov radiation at a level that dominates the observed PMT noise rate, unless steps are taken to reduce the overall potassium content of the glass. At the request of IceCube collaborators, manufacturers have been able to produce glass with substantially lowered potassium content without compromise to important processing, mechanical, or optical qualities. It is anticipated that IceCube optical modules will display noise rates very close to those of isolated dark-adapted PMTs.

7.2.2 Optical Sensor

The optical sensor is a medium-size (∼10 inch diameter) hemispherical 10-stage photomultiplier tube (PMT), made by Hamamatsu. PMTs very similar to the intended device have been deployed within AMANDA with generally excellent experience. These large PMTs offer surprisingly good time-resolution, as indicated by a transit-time-spread (TTS) for single photo-electron (SPE) pulses of about 2.5 ns rms. Despite their large photocathode area, these PMTs, in total equilibrated darkness, generate only ∼300 Hz or less of spontaneous noise pulses at temperatures less than 0°. Photocathode sensitivity extends well into the UV, limited by the optical transmission of the glass pressure sphere at 350 nm. For each detected photon, the PMT produces SPE pulses that have characteristic rise (fall) times of 7 (11) ns.

Due to the stochastic nature of the electron multiplication process, SPE pulses display significant variations in pulse shape and amplitude. The measured pulse area distribution of DOM #1 (the deepest), acquired over a period of 10 days, is shown in fig. 63. The histogram is formed by adding together consecutive ATWD samples for the pulses that rise above a digital threshold, and subtracting a measured pedestal. This simple method works well enough if the discriminator threshold that launches the ATWD is sufficiently low that nearly all SPE pulses result in a trigger. It should be noted that a fair fraction of the PMTs in string 18 do not have such good peak to valley ratios, and the spectrum shown in fig. 63 is better than most.

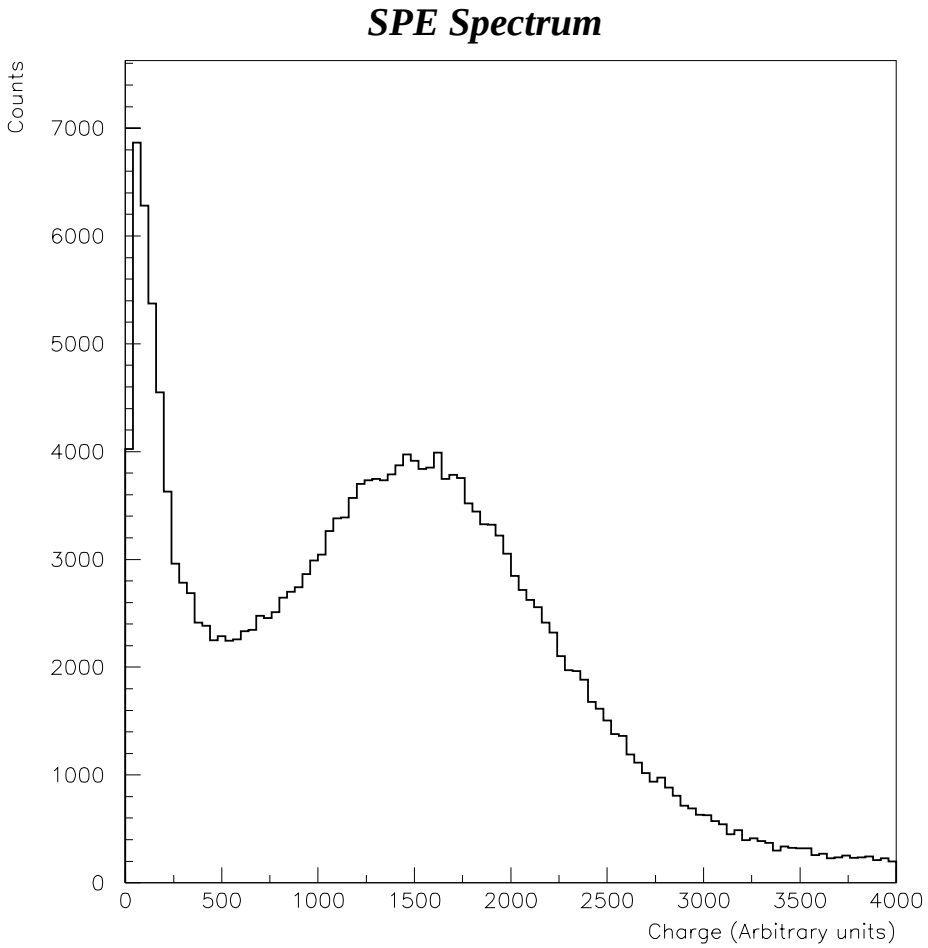

Figure 63: Measured pulse area distribution of DOM #1 measured over a period of 10 days in CY 2001. Most of the histogram is SPE noise pulses. The stochastic nature of the electron amplification process leads to a very broad distribution such that some SPE signals fall below threshold.

To define a measure of gain, the peak region of spectra such as that shown in fig. 63 are

fit to a simple a Gaussian form. From the fit parameters, an average gain can be extracted. Repeated measurements taken over 180 days in CY 2000 have demonstrated that the combined PMT + DOM signal processing electronics provide excellent gain stability. These results are shown in fig. 64. Because PMT gains were set to optimize the optical signal paths, which had wide variations, and because some PMTs displayed poor peak-to-valley ratios, high quality fits could be obtained for less than half of the deployed ensemble of DOMs. The mean of the distribution, $\sim -2.8\%$ per year corresponds to drifts of 0.05% per week, far below the experimental requirement of 2% per week; none of this subset comes close to 2% per week.

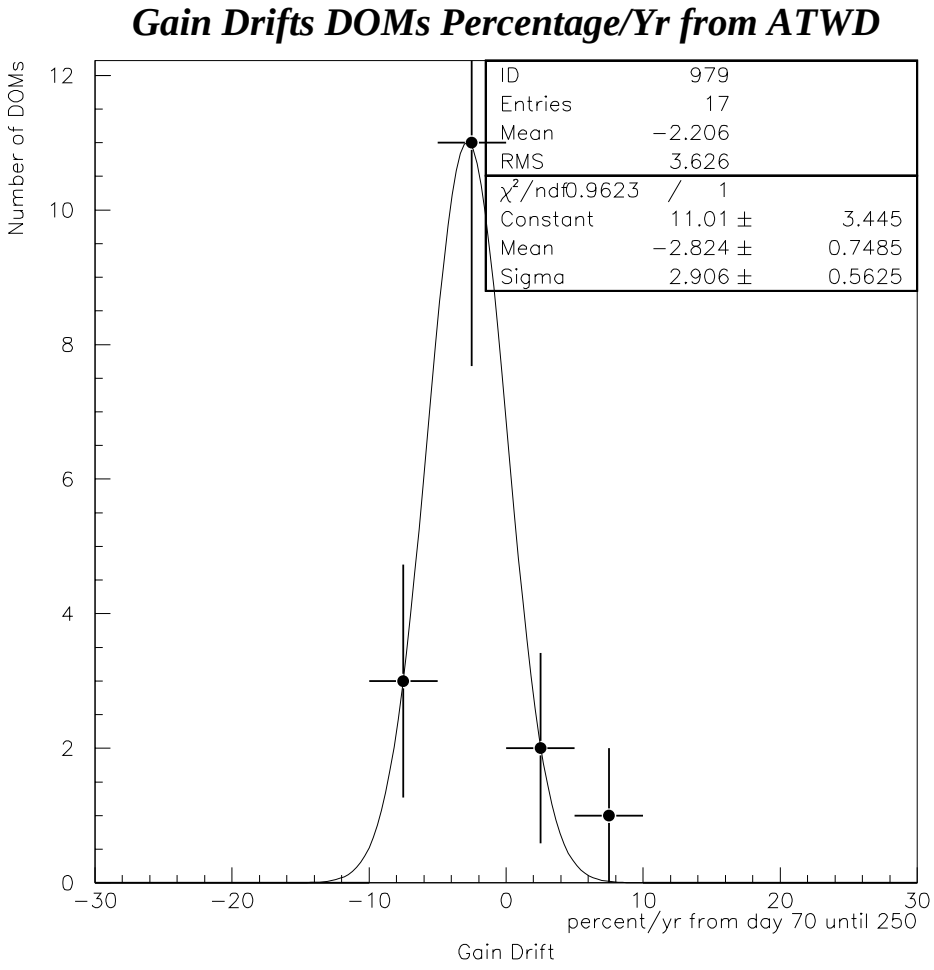

Figure 64: Measured distribution of a subset of DOM gains, recorded over a period of 250 days in CY 2000. The mean in this ensemble is less than 3% per year, with none approaching the experimental requirement of $\leq$2%/week.

At a gain of 10^7, a typical SPE pulse will have an amplitude of $\sim$8 mV into a 50 Ω load.

Under these conditions, the signal displays some nonlinearity at around 2 V, reaching complete saturation at ∼4 V. The effective dynamic range under these conditions is approximately 500 PE. The PMT maximum output current at the anode is limited by space charge effects in the dynode chain. As signal size increases, the space charge effects appear first at the last dynode, then at the next to last, and so forth. Not only does the pulse amplitude display a non-linear relationship to the input photon signal, but the pulse shape begins to stretch out considerably. The effective dynamic range may, in principle, be increased by lowering the PMT gain below 10^7. At some point in the range of a few millivolts, intrinsic electronic noise will degrade performance at the SPE level.

With careful circuit design and layout, however, ultimate performance may exceed 500 PE significantly. It seems feasible to utilize a dynode tap to obtain a signal that could extend the dynamic range at least another order of magnitude beyond what can be practically achieved from the anode signal. This general idea has been used in many past experiments, and should be practical for IceCube. This possibility is being explored actively.

7.2.3 PMT HV Generator

The PMT HV generator, known familiarly as the PMT base, is a multi-stage voltage multiplier, or Cockroft-Walton circuit, with an oscillator running at a few tens of kHz. The base must meet a number of important requirements, in particular, high reliability, high stability and low induced noise. A voltage multiplier has certain potential advantages since the voltage steps are smaller than that of a single stage multiplier. If arranged correctly, the base will naturally supply the most current to the dynode stages near the anode, where the pulse loading occurs. This produces an attractive low power design. On the other hand, there are more parts, which could affect MTBF.

The IceCube PMT base will have two separate sections. One section, supplying the potential difference between the photocathode and the first dynode, will be fixed at a voltage near the manufacturer's indicated maximum. This produces a uniform transit-time among the DOMs, and produces the best peak-to-valley ratio for the SPE pulse-height spectrum. The second section will be variable under software control, to obtain the desired 1×10^7 gain. Experience with AMANDA string 18 shows that reliability is an issue, as two bases appear to have failed. All HV designs involving semiconductors must be based on conservative design practices, since even extremely rare discharge mechanisms can be fatal. Induced noise also appears to be present, at least in the timing measurements, which give better results with the PMT HV off. The re-engineering of the PMT base to improve reliability is recognized as an important task.

7.2.4 Optical Beacon

The string 18 DOMs are each equipped with six GaN LEDs, which emit predominantly in the near-UV at 380 nm. The luminous intensity and the pulsing rate may be varied over a wide range under software control. At their brightest, these beacons can be seen by OMs 200 m distant. Due to their high intrinsic capacitance, LEDs are not easy to pulse at ns speeds; the

pulse width is ∼5 ns. The LEDs are broad angular emitters, spaced at 60° around a vertical axis, and are canted over to produce a roughly hemispherical source. Some AMANDA analog OMs have been equipped with similar optical beacon boards using GaN LEDs emitting at 450 nm; these have also proved to be useful for test purposes. The PMT HV must be turned down at the emitting DOM to avoid potentially harmful pulses.

The optical beacons can be used to knit together a highly over-constrained measure of relative DOM positions within the array. They can also be used to study optical properties of the ice at these wavelengths.

7.2.5 Signal Processing Circuitry

The block diagram of the DOM signal processing circuitry is shown in fig. 65. The principal logical and functional elements are:

- State control;
- Waveform capture and digitization;
- Local time generation;
- Local/master clock time transformation;
- Cable length measurement for timing offsets;
- Data flow;
- Local coincidence capability;
- Control and glue logic, provided by an FPGA;
- A low-power 32-bit ARM CPU for higher level operations;
- Power conversion and filtering;
- Monitoring and calibration;
- Message handling - send/receive .

State Control The DOM is operated as a slave in a master/slave relationship with the surface DAQ. Upon power-up, it enters a *wait state* for an interval of a few seconds, to permit down-loading of new firmware or software. If no messages are received before time-out, the DOM will boot from Flash memory and await commands. Normal operation of the DOM is dominated by a data-taking state.

In addition, a local-time calibration process is periodically invoked, so that the local DOM time may be ultimately transformed to master clock time with nanosecond accuracy. The time calibration process appears as separately scheduled thread, with no deleterious impact upon

Digital Optical Module

Main Components Diagram

First Prototype, Deployed 2000.

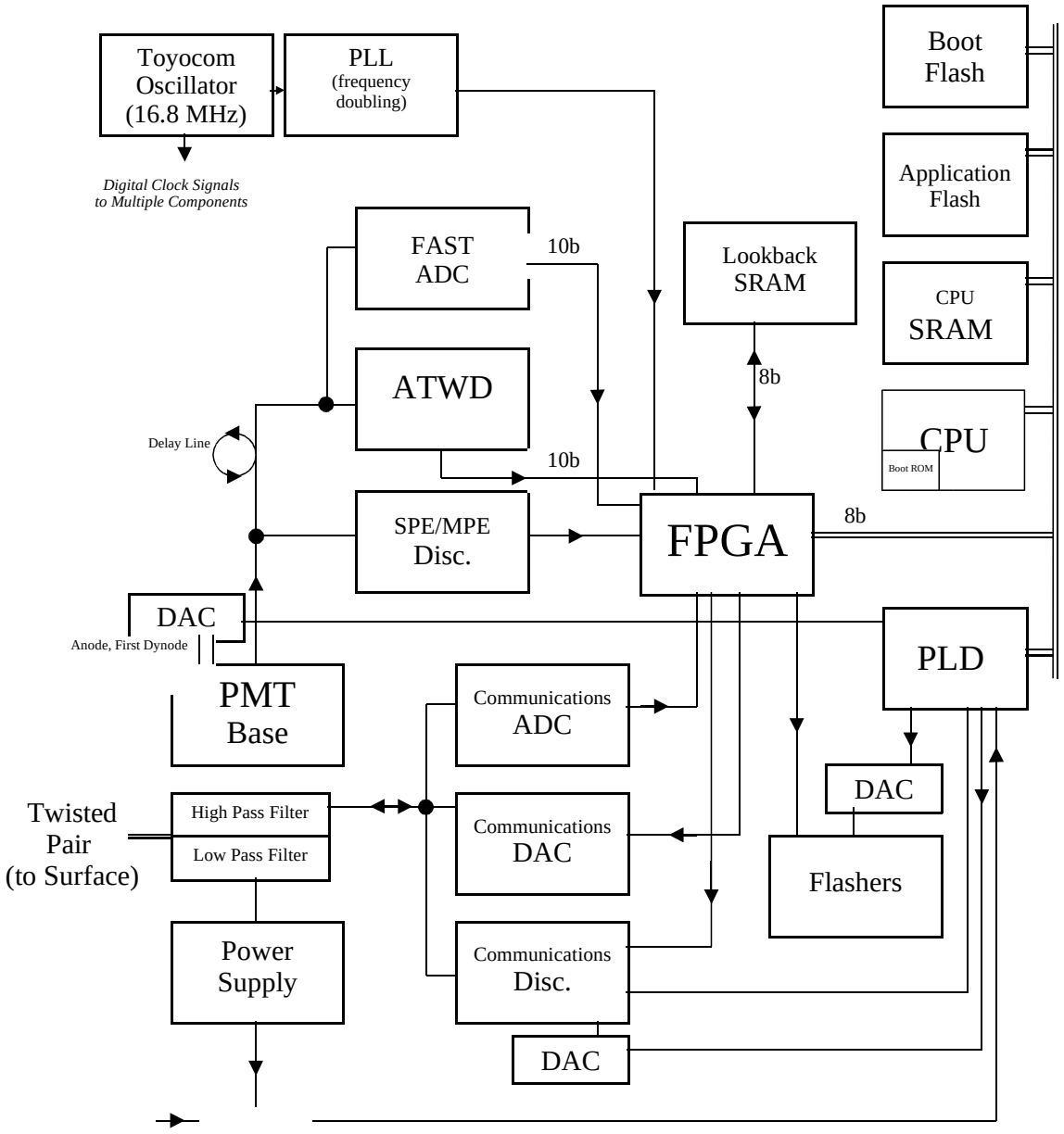

Figure 65: Block diagram of the digital optical module signal processing circuitry.

the data-taking state. Other active threads are message receive/send and data transmission, also invisible to the data-taking process. There are several calibration modes, such as running optical beacons, cable length measurement, etc., during which normal data-taking is presumably inactive.

Information Capture The DOM is equipped with innovative circuitry that is well-matched to the PMT pulse characteristics and dynamic range. The capture of waveforms with ∼300 MHz 14 bit resolution is a daunting technical challenge if only conventional flash ADCs are considered. Power dissipation for the ensemble of FADCs would be several watts, imposing an undesirable operating condition; noise due to the large amount of digital activity and data flow presents an inhospitable engineering environment. Instead, the DOM concept takes advantage of the fact that, most of the time, nothing is happening: Δt between pulses is more than 10^6 ns. Circuit activity need occur only when pulses appear.

The waveform capture capability is realized through a custom Application Specific Integrated Circuit (ASIC) designed at Lawrence Berkeley National Laboratory (LBNL), the Analog Transient Waveform Digitizer (ATWD). The ATWD has four channels, each with 128 samples, that synchronously record different input waveforms. For IceCube, three of the channels will capture the PMT signal presented at three different gain settings. This arrangement provides an elegant multi-range linear PMT signal capture method. With three channels operating at $\times$15, $\times$3, and $\times$0.5 gains, the ATWD provides the rough equivalent of a $\geq$14 bit 200–800 MHz ADC. Due to schedule pressures, the DOM prototypes in string 18 were equipped with only $\times$10 and $\times$2 gain channels. The third channel was, instead, routed to an analog multiplexer that could connect to various internal signals for diagnostic purposes.

The fourth ATWD channel in string 18 DOMs is permanently connected to the DOM internal clock, to calibrate/monitor ATWD sampling speed. Experience with string 18 has shown that the ATWD sample speed is extremely stable. In IceCube, the fourth channel will be connected to an analog multiplexer to permit that channel to share more than one function. The ATWD sampling speed needs to be calibrated and monitored, but only rarely after initial calibrations are completed and the system is stable. As noted above, some other internal signals that have diagnostic value also need only infrequent interrogation. Most of the time, $\geq$99.9%, the fourth channel is available to capture a dynode tap signal that could increase the PMT signal effective dynamic range by at least another order of magnitude. The goal is to reach at least 5000 PE, a capability that will enhance the reconstruction of EHE events, should they occur within the volume of IceCube.

The capture process is initiated by a "launch" signal derived from a discriminator connected to the high-gain signal path. The capture process stores waveforms as analog voltages on four internal linear capacitor arrays. The sampling action is generated by an active delay line within the ATWD, with "look-ahead" to create a sampling gate of width sufficient to obtain adequate settling on a capacitor before the gate switch opens, effectively closing that sampling window.

With the ATWD, waveform capture occurs at sampling speeds that may be varied at will from ∼200 Msps to more than 1 Gsps, corresponding to capture intervals of 640–128 ns. It

appears that capture at ∼300 MHz (3.3 ns/sample) is appropriate for our scientific goals. The higher speed capture is useful for characterizing PMT signal shape and other diagnostic purposes, but is not needed to extract timing information from a typical waveform. A single DC current controls the sampling speed. All channels within an ATWD sample synchronously, with aperture variations between channels measured to be less than 10 ps.

The ATWD performance combination of ∼GHz sampling and very low power dissipation, ≤100 mW is unmatched by any single commercial device for transient waveform capture. The sampling action is controlled by an active delay line internal to the ATWD. No ultra-high speed logic/clocks are needed in the DOM, a highly desirable engineering situation. The maximum frequency in the string 18 DOMs is the local clock frequency, a very comfortable 33.6 MHz. For IceCube, this frequency may be higher, but will likely not exceed 40 MHz.

Two ATWDs, arranged with alternate selection logic, permit capture of longer waveforms, and also serve to reduce dead-time. For waveforms exceeding the ATWD capture interval, sampling at a lower frequency is sufficient to capture relevant information at later times. For this purpose, The DOM is equipped with a 10-bit low-power FADC, operating at the DOM local clock frequency. The PMT signal in this path is reshaped to match the lower sampling rate.

The ATWD has two distinct functions–transient waveform capture, and digitization of captured signal. These two functions are separately controlled, so that a captured signal subsequently judged uninteresting may be ignored. This feature minimizes dead-time, and also facilitates a true local coincidence capability (see sec. 7.2.9) between neighboring DOMs, in which only time- and space-associated signals are digitized. The immediate conversion to a digital format preserves data quality during subsequent DAQ data flow processes.

For interesting events, waveform capture in the ATWD is followed by 10-bit simultaneous conversion of all 128 samples/channel by an internal common-ramp Wilkinson ADC. The internal scalers count on both positive and negative clock transitions. At 33.6 MHz, complete digitization requires about 15 μs. Because of natural CMOS manufacturing variations that create offsets in the internal comparators, there exists fluctuations in the baseline, or pedestal, of the captured waveform. These pedestal variations are in the range of 5–15 counts; they are quite stable and are easily subtracted away during data processing.

A single ATWD digitizing waveforms at the nominal noise trigger rate of 300 Hz, will introduce deadtime of ∼0.5%. To this, an additional deadtime of about 0.1% must be included for readout of data via a 10-bit parallel bus. With two ATWDs operating in ping-pong mode, deadtime due to random noise hits is less than 1×10^{-4}.

The ATWD is currently designed for a 1.2 μm CMOS process with double polysilicon capacitors. This manufacturing process may not be available indefinitely, as new CMOS processes with ever-smaller feature size and other characteristics supplant older ones. The ATWD should be updated by not only choosing an appropriate one of these processes, but by increasing sample depth to perhaps 256 instead of 128, and adding new features such as a built-in DAC to reduce ADC pedestal offsets to an insignificant level. For IceCube, no aggressive design steps would be contemplated, only those for which substantial experience already exists in other ASICs.

Local Time Generation Each PMT hit must be time-stamped such that correlated hits throughout IceCube meet the relative timing accuracy requirement of 5 ns rms. This is accomplished within the DOM using a two-stage method that produces a *coarse time-stamp* and a *fine time-stamp*, both in local time units. Once data reach the surface, the local time units are transformed to master clock units, and ultimately linked to GPS.

Although timing accuracy and resolution are in the few nanosecond range, no high-speed clocks are needed anywhere in the system for the time measurement process. The current string 18 DOM design maintains a 54-bit local clock running at the DOM 33.6 MHz clock frequency. The 33.6 MHz is obtained by frequency-doubling a free-running Toyocom 16.8 MHz quartz oscillator. For IceCube, as noted earlier, the local clock frequency may be higher.

This oscillator product displays exceptionally stable behavior: measured drifts (Allan variance) taken in the laboratory are typically δt $\sim$ 0.06 ns/s, *i.e.* $\delta f/f \sim 60 \times 10^{-12}$, as shown by the histogram of 46 of 49 tested oscillators in fig. 66. The three oscillators not included in the histogram were markedly worse, but still within the manufacturer's specifications. A test program will select the best 90–95% of the devices. Each point in the histogram represents the analysis of 720 measurements taken consecutively over an hour (5 s intervals). The samples in this histogram were taken after a stabilization period of a few days, as it is well known that quartz oscillators will display asymptotically better stability after an initial run-in to shake off dust, relieve strain, etc. This extraordinary stability obviates the need (and perhaps even the practical possibility!) for a phase-locked loop connecting the local and master clocks. Such short-term stability is only an order of magnitude or so worse than that of high quality commercial rubidium stabilized clocks. The cost of the Toyocom oscillator is $\sim$\$25.

The coarse time-stamp process begins as a PMT signal triggers the discriminator. The discriminator pulse is then resynchronized to the next DOM clock transition edge. The resynchronized pulse provides the ATWD "launch" signal. In other words, the synchronous launching of the ATWD causes the PMT signal to arrive within a one-cycle wide region of the ATWD capture window. The clock value at the instant of ATWD launch is recorded in an appropriate FPGA register. *The "coarse time-stamp" is defined as the clock value recorded in this register.* At 33.6 MHz, this coarse time-stamp provides a time quantization $\Delta\tau$ of $\sim$29.76 ns (at 40 MHz, $\Delta\tau$ is 25 ns). Because the register is loaded by the same signal that launches the ATWD, the connection between coarse-time stamp and ATWD launch is robust.

Clearly, the coarse time-stamp does not provide the desired $\sim$5 ns resolution. However, the leading edge of the PMT signal waveform within the ATWD record will occur somewhere within this particular 29.76 ns interval. *The "fine time-stamp" is defined as the waveform position within the ATWD record.* The measure of the fine time-stamp must be extracted from the ATWD record by an algorithmic method. A simple extrapolation to baseline of the waveform leading edge can serve as the measure of the fine time-stamp, although more sophisticated methods can be easily envisaged. Even with the small SPE signals, the contribution to timing resolution due to all electronic noise sources and digitization is expected to be less than 1 ns rms, smaller than the PMT transit time jitter of 2.5 ns rms.

For all this to work, the PMT signal must be delayed sufficiently such that the leading edge of the signal always appears well after the ATWD sampling action has begun. An overall delay

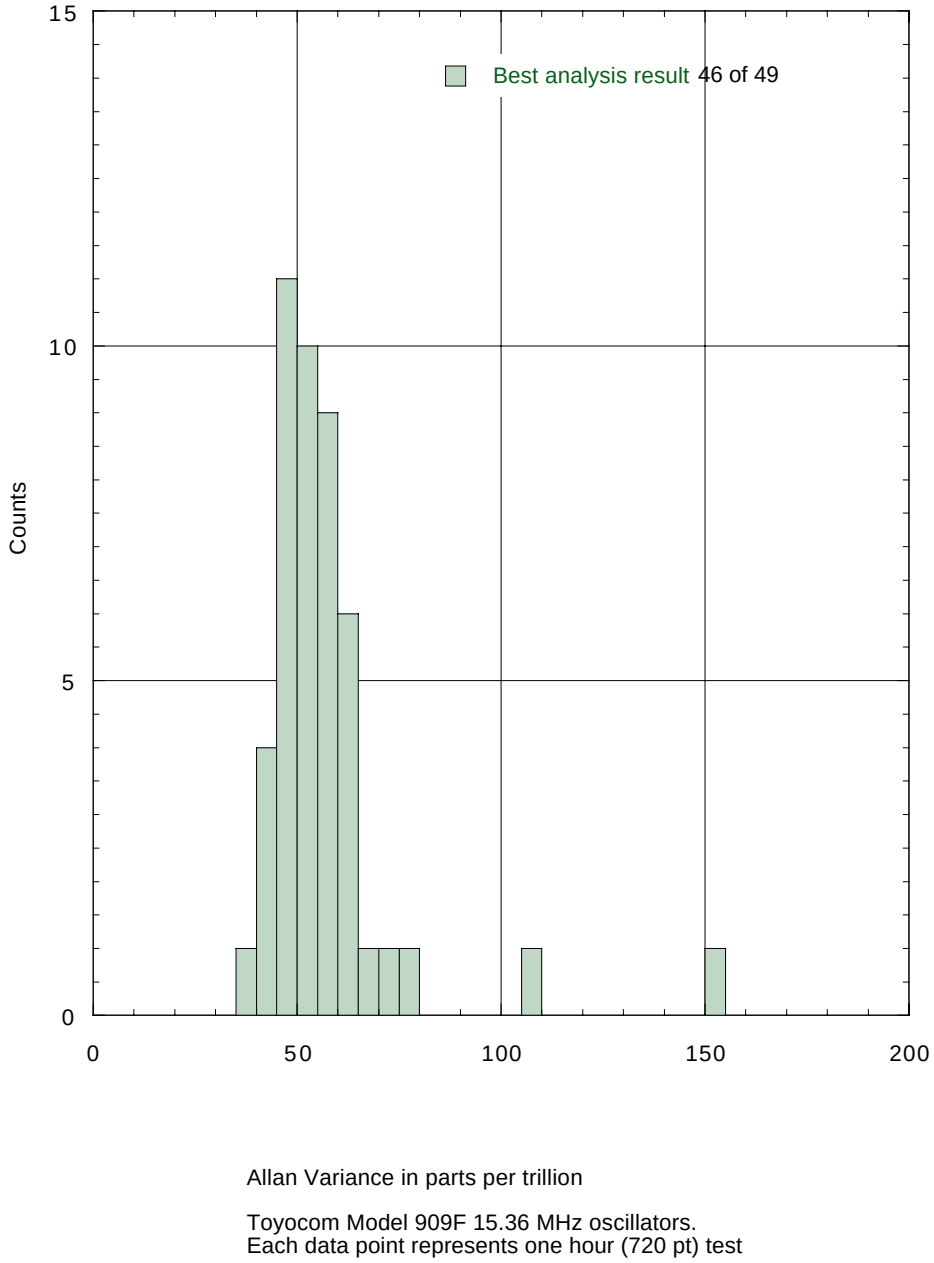

Figure 66: Histogram of measured Allen variance for 46 Toyocom oscillators, measured at 5 s intervals relative to a good frequency standard. Some of the outliers above 100 ppt later stabilized to fall within the trend.

of about 75 ns is needed to accommodate both the coarse time-stamp $\Delta\tau$ random delay and the propagation delay of the circuitry. In string 18 DOM prototypes, a coil of coaxial cable ($\sim$50 ft) was employed for this purpose, an effective but bulky solution. For IceCube DOMs, a lumped delay line may be chosen. These provide adequate performance and offer an attractively compact solution; of course, reliability of this device (as well as all other parts) at low temperatures must be demonstrated.

Our observations confirm that standard commercial GPS clocks are subject to much larger short-term drifts than the Toyocom devices themselves. Figure 67 shows measured drifts of one DOM local clock (in the ice) showing a 3.5 ns short-term variance between measurements taken at 2.6 s intervals relative to GPS. In comparison, the Toyocom oscillators displayed about 50 times better stability than this during laboratory measurements taken relative to a good frequency standard (a Stanford Research Systems Loran system). Clearly, standard commercial rubidium clocks, which typically offer $\delta f/f \leq 2 \text{ x } 10^{-12}$ per 100 s, are a much superior choice for the master clock. The link from master clock to GPS can be easily made once per second with standard hardware and software.

7.2.6 Local/Global Time Transformation

All DOM data, recorded in association with the free-running local clocks, must be transformed to IceCube master clock units in order to reconstruct events. Because drift is negligibly small over a period of seconds, a simple linear transformation between local and master time is sufficient. This could be performed within the DOM or, more likely, at the surface within the DAQ. In either case, this transformation requires continuously updated knowledge of local clock frequency and phase, relative to the master clock. Because the Toyocom oscillators are so stable, the local/master clock calibration process needs to be invoked only a few times/min per DOM. Consequently, this vital function requires only a tiny fraction of the network bandwidth.

The master clock units are linked to GPS time once per second in the online DAQ to permit the connection of IceCube events with other detectors, and offline comparison with potentially interesting astrophysical occurrences. Interpolation within the one second interval is expected to be better than $\pm$1 ns rms. Synchronization of event time with other laboratory detectors, terrestrial or non-terrestrial, will require detailed accounting of delays throughout the as-installed IceCube DAQ and master clock system. The ultimate accuracy for inter-laboratory timing cannot now be specified but may reasonably be expected to fall in the range of $\pm$10 ns.

The calibration process involves a periodic transmission to a DOM by the surface DAQ of a simple bipolar *time-mark* signal, perhaps 5 μs between edges, synchronized precisely to the master clock. These time-mark signals, however sharply defined at the moment of generation, experience degradation while propagating down the twisted pair cables due to dispersion and attenuation. Propagation over 2–3 km of cable results in rise-times of roughly 1.8–2.4 μs. These values depend somewhat on the definition of rise-time, since the 1/t asymptotic approach is very slow. The propagation of signals such as step functions over cables such as these is very well understood. In most respects, they can be modeled as delay lines with $\sim$10:1 ratio for delay/rise-time. This is schematically illustrated in figure 68.

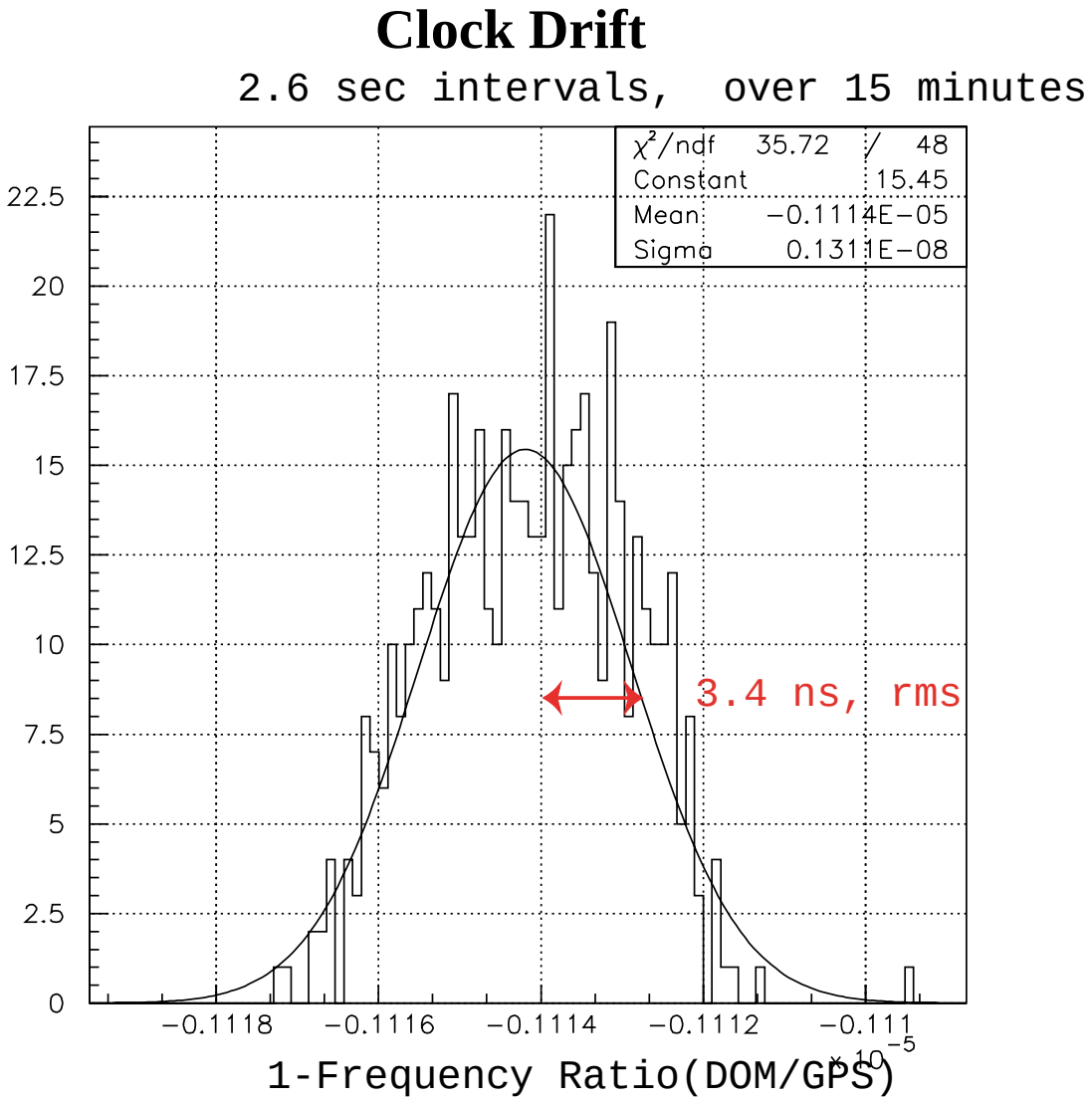

Figure 67: Measurement of Toyocom/GPS frequency ratio at 2.6 second intervals for 15 minutes. The ~3.4 ns rms is the product of the distribution sigma value times the measurement interval, *i.e., 1.3 x 10^{-9} x 2.6 seconds* dominated by short term drifts in the GPS unit.

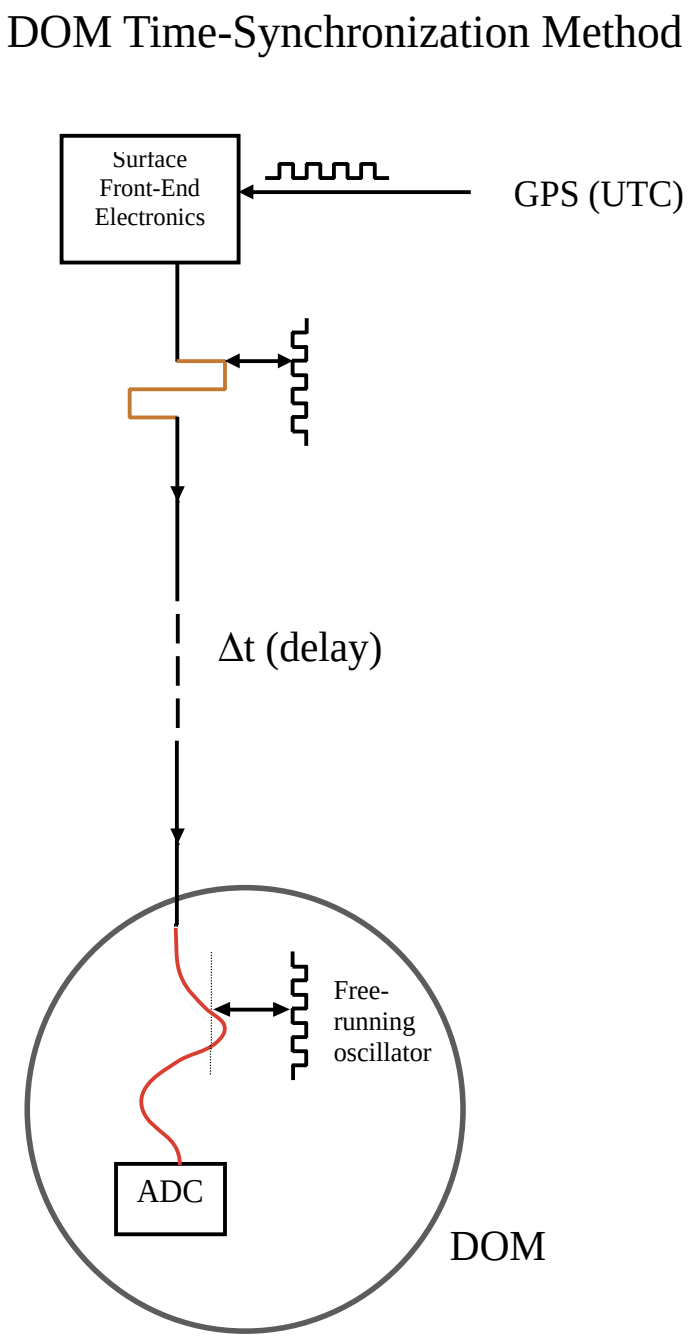

Figure 68: Transmission of a bipolar time-mark signal synchronized to the master clock by the surface DAQ to the DOM provides the connection between local and master clock time.

The challenge is to exploit the very stable behavior of the cables and clocks to extract a timing measure with a *relative accuracy* not exceeding 5 ns. The term "relative" is essential, since an offset due to method, common to all DOMs within the required resolution, is irrelevant. The other essential conceptual element is a simple relationship between voltage noise during measurement and time resolution:

$$\delta \mathrm{t} = \delta V/(dV/dt) \tag{5}$$

The dV/dt of signals arriving at the DOM fall in the range of $\sim 10^6$ V/s. If voltage measurement noise is on the order of 1 mV, then timing resolution will be in the range of 1 ns. Clearly, environmental noise can significantly degrade time resolution, and must be controlled for this to work well. In the laboratory, using a simple discriminator and filter, resolutions less than 1 ns are easily achieved. However, this simple approach contains an undesirable flaw due to random errors in device thresholds, which may be several millivolts. According to the above equation, shifts of several nanoseconds may occur among an ensemble of DOMs because of unknown threshold offsets. The threshold offsets can in principle be measured by pulse injection, but questions linger as to validity of method due to concerns such as the integrative behavior of the discriminator coupling pulse rise-time and width to effective threshold.

On the other hand, it is completely straightforward to employ a conventional FADC and measure the entire waveform of interest, including baseline just before the pulse arrives. Digital offsets from one FADC to another become irrelevant. Most noise sources are very effectively suppressed because the baseline is measured just before the pulse appears. Defective or distorted waveforms, for whatever reason, may be recognized and rejected. A 10-bit FADC running at the local clock frequency samples the leading edge and the immediately preceding baseline, as well as subsequent features such as the zero-crossing point. About 16 samples of each feature is more than sufficient. Figure 69 shows the actual received waveform after ≥ 2 km of cable.

The measure of timing may be chosen in various ways by focussing on various parts (or perhaps all) of the waveform, with differing systematic impact. The two most illustrative approaches focus on the leading edge or the zero-crossing point of the received bipolar time-mark waveform. Although dV/dt is higher for the zero-crossing point, this measure is prone to greater error since the extrapolation to baseline is less immediate, and the instant of zero-crossing depends on circuit component values and on the risetime of the pulse, which depends on cable length. The zero-crossing method, although offering somewhat better precision for tracking oscillator frequency, is not as suitable for establishing the local-master time transformation, which also includes phase. A leading-edge method is a simpler and more appropriate choice.

The presently used leading-edge algorithm simply extrapolates to baseline using a few samples above a threshold. Benefits from using more sophisticated fitting to the waveforms surely exist, but remain to be explored. The leading edge measurement algorithm, in whatever form it takes, must be sophisticated enough to avoid excursions into the very first part of the waveform during which the first and second derivatives have the same sign, or it must permit a sufficiently complex spline form that spans accurately the somewhat asymmetric point of inflection. In any case, the results show that the desired time resolution can be obtained, even with the most simple approach.

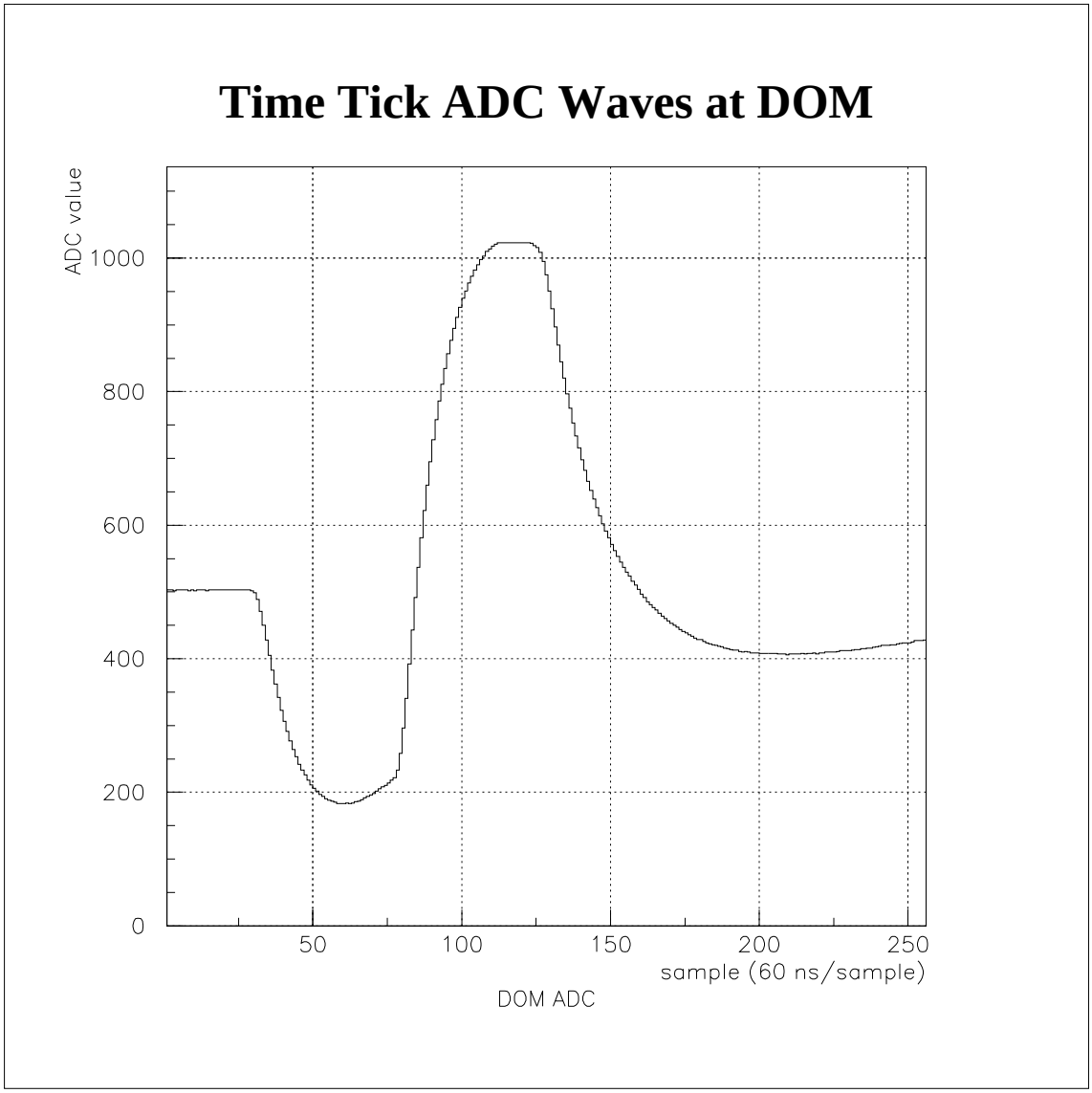

Figure 69: Time-mark waveforms measured at the digital optical module, after traveling through 2+km of twisted pair.

The extrapolation-to-baseline algorithm defines the instant that the waveform was received, in local DOM time units. At the surface, the moment of transmission is precisely defined by the master clock time distribution subsystem. Repeated measurements of this type serve to measure the frequency and phase of the DOM local clock very accurately. The stability of the Toyocom oscillators will permit, with beneficial effect, fits that include measurements made over several minutes.

Figure 70 presents the results obtained with DOMs deployed in the ice. This figure needs some explanation to extract the intrinsic resolutions of the DOM and Test-Board DAQ. Each point in the one-way histograms is based on two consecutive measurements; the rms of each measurement is $1/\sqrt{2}$ smaller. The differences between up-going resolution (7.8 ns) and down-going resolution (4.5 ns) is thought to be due to a noisier environment in the counting room (where the Test-Board DAQ is located) than in the DOM. The round trip resolution involves one up-going and one down-going measurement, and is observed to be approximately the sum of the individual resolutions taken in quadrature. In the future, resolutions should be better, since a GPS clock would not be used directly as a master clock, and steps would be taken to reduce or eliminate environmental noise in IceCube. The time resolution measured in the laboratory using a Toyocom oscillator as reference was indeed significantly better, $\sim$3 ns rms, supporting this hypothesis.

The measurement of the local clock *phase*, however, contains an *Offset* due to the differing physical lengths of the twisted quads throughout the detector. The differing physical lengths, twists, and stretches introduce differences in the propagation time for signals to pass from one end of a cable to the other. The signal propagation time, or *cable electrical length*, can vary by a large amount, up to $\sim$5000 ns from the top of the IceCube string to the bottom.

The traditional way to measure cable electrical lengths is known as Time Domain Reflectometry (TDR). Simply put, the TDR method sends a short pulse into a cable and measures the time between input and a return signal from the end of the cable; however, the TDR method requires either an unterminated or a shorted end point to reflect electrical energy. Neither condition is permitted in our case, since the cable must serve as a fairly high-bandwidth network and deliver power as well. In addition, the return pulse shape is very different due to dispersion and attenuation in the cable during the round trip, complicating the definition of time measurement at the level of accuracy that we require. More relevant than the electrical lengths themselves, however, are the *differences* in these electrical lengths. The cable electrical lengths must be measured in a way that provides accurate *relative values* of the cable lengths. There is an easy way to do this, known as the *Reciprocal Active Pulsing (RAP)* method (see next section) [158].

Since our approach is novel, we present in some detail how timing precision and accuracy of $\sim$3–5 ns is obtained throughout a simple copper-based km-scale network. We emphasize that every critical functionality regarding time-base integrity has already been demonstrated in the AMANDA string 18 DOM ensemble.

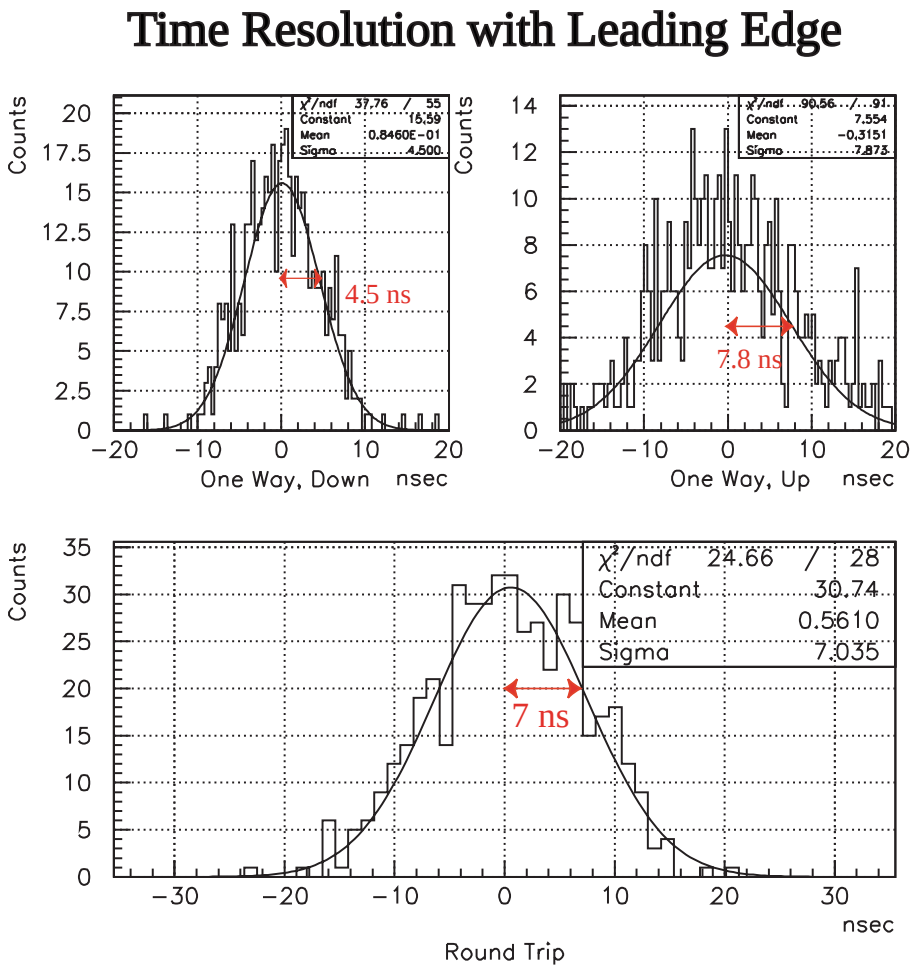

Figure 70: Time resolution results obtained with the digital optical modules currently deployed in the ice. The resolutions displayed here are $\sim \sqrt{2}$ larger than the individual resolutions because two consecutive measurements are used to generate each point in the histograms. GPS clock drift, digitization noise, and environmental noise in the counting house dominate the resolutions.

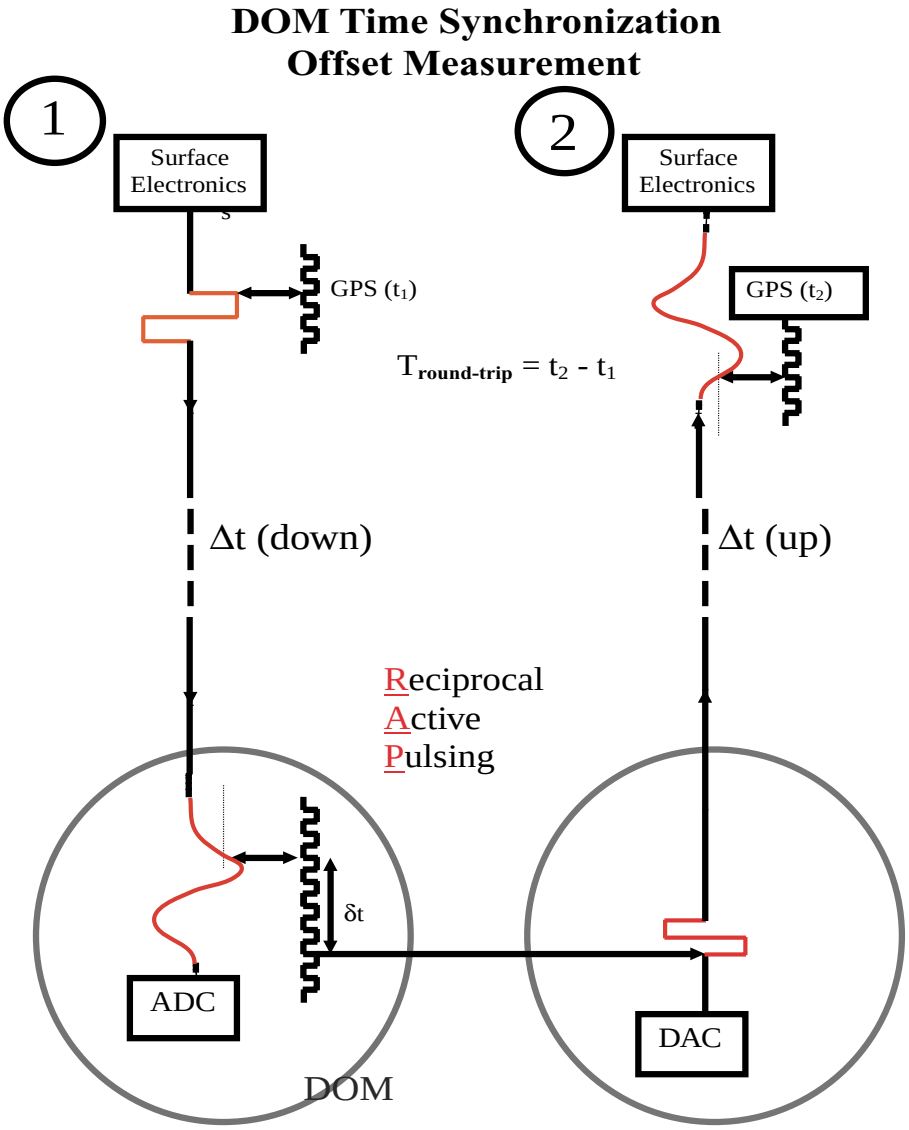

Figure 71: General concept of the RAP method for measurement of the electrical length of the twisted quads.

7.2.7 Cable Electrical Length Measurement

The RAP method employs a timing strategy identical to the local/master clock time-base calibration, but adds symmetric round-trip measurement with identical bipolar time-mark pulses that are sent/received in both directions. The return pulse is separated by a known, programmable *wait interval*. The *wait interval* is chosen to allow the pulse energy in the cable to dissipate, so that the first pulse has a negligible impact on measurement of the second. By using circuitry, firmware, and software identical to that used for local time calibration in both DOM and Surface DAQ, the measurement of cable length provides high relative accuracy in cable length measurements, even though the rise-times vary somewhat due to differing cable lengths. The RAP method may be used with either the DOM or the DAQ as the initiator of the first pulse; consistent results are obtained in either case. The RAP method is, of course, invoked by software, with no need for manual intervention. The general idea is illustrated in fig. 71.

The definition of cable length is simply one half of the total delay between initiating pulse and received responding pulse, minus one half of the *wait interval*. Although a common offset exists in this method, taking the relative differences among the ensemble of cable lengths reduces this source of error to a negligible level.

Measurements of the deployed AMANDA string 18 cables were made from the northern hemisphere using the satellite link to the South Pole to download relevant code and commands. The results, shown in fig. 72, are completely consistent with expectations. The statistical error bars, $\leq$1 ns, are much smaller than the points. The RAP process may be invoked repeatedly, leading to a measurement value for each DOM with negligible statistical errors; it may also be invoked automatically at periodic intervals, to monitor system stability, without interfering with normal data acquisition.

7.2.8 Data Flow and Feature Extraction

The raw representation of a digitized waveform would include 128 10-bit samples and the 54-bit time stamp, requiring at least 170 bytes in an unreduced format. Waveforms exceeding the maximum digitization value of 1023 would initiate digitization of the next (lower) gain channel, resulting in additional 1280 bits of data, etc. Without filtering or compression, a DOM with 300 Hz noise would generate 50 kB/s, or more, most of which is uninteresting noise hits with long pedestals. Such a data rate would overtax the network capacity.

Feature extraction, local coincidence, and zero-suppression offer useful methods to reduce the bandwidth burden on the network. Feature extraction offers a powerful means to reduce transmission rate since most of the hits, perhaps more than 95%, are simple SPE pulses. The feature extraction process for SPE events reduces the waveform information to amplitude and timing information only. After extraction, an SPE hit should require only 8 bytes to characterize, including coarse and fine time-stamps. What is critical is that the algorithmic procedure that makes the determination whether a given waveform is an SPE or not be robust, since detailed information is permanently lost after extraction. It seems reasonable to set the cut such that typical SPE waveforms pass occasionally to the surface.

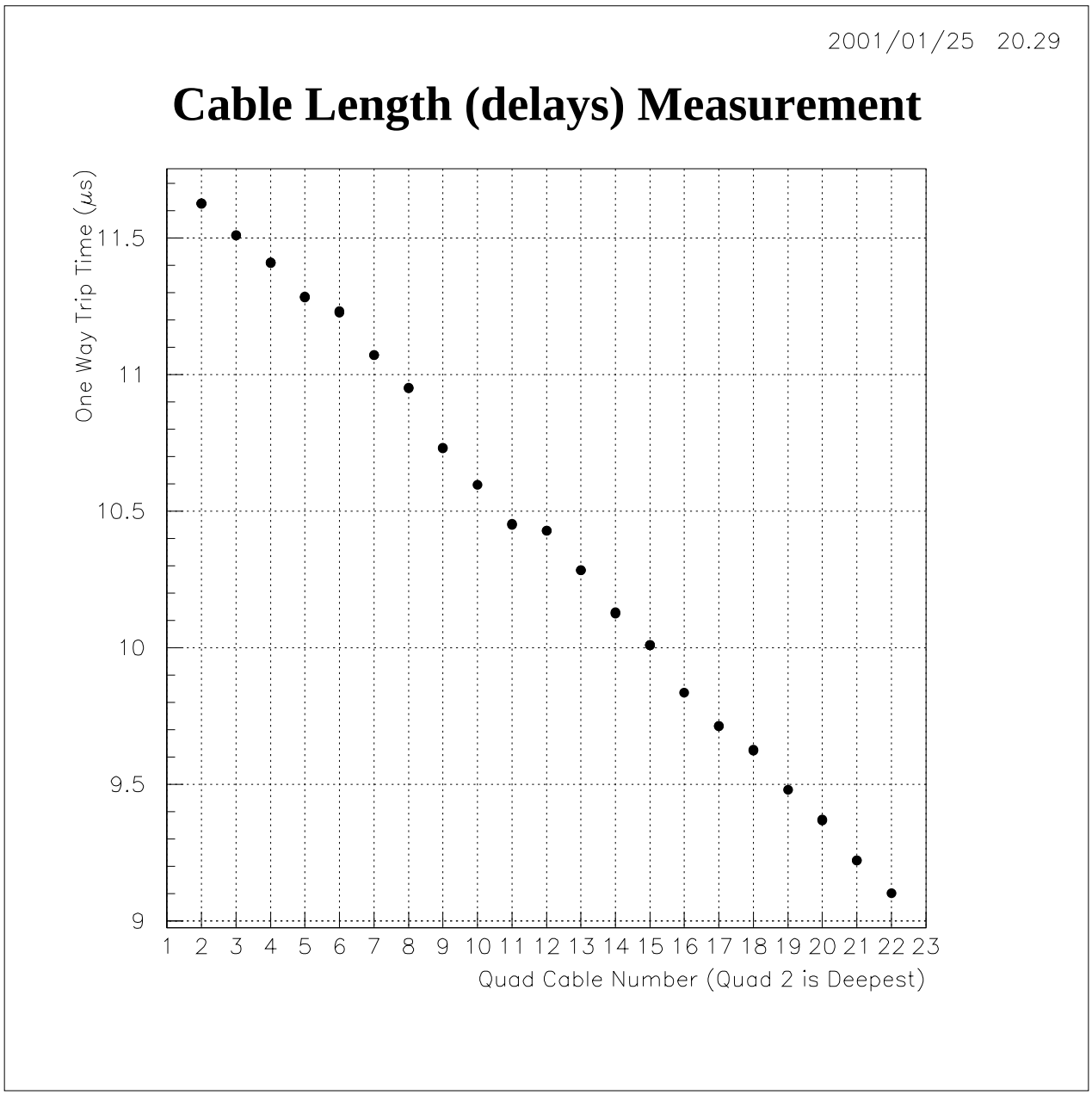

Figure 72: Measured electrical lengths of twisted quad cables in string 18 using the RAP method.

In any case, the bandwidth requirement for SPE waveforms will drop by a factor of 20 with feature extraction. This leads to a data rate/DOM for SPE pulses of ∼2.3 kB/s, assuming a 300 Hz noise rate. Feature extraction is included in the baseline DOM capabilities because it provides such a large data compression factor.

For multiple photoelectron events, the "non-SPE" waveforms, perhaps the full 170 bytes/event are needed. Assuming 5% of the 300 Hz hit rate fall into this category, another 2.5 kB/s are generated. While zero-suppression can reduce the unneeded pedestal data for this category, the factor of reduction here may be only a factor of ∼2. Zero-suppression may also complicate event formatting, and its role in DOM data transmission may not be prominent.

7.2.9 Local Coincidence

Conventional experimental design traditions bring all real-time signals to the counting-house, within which various trigger logic arrays impose filters to retain only events of interest. For IceCube, the architecture is quite different, and real-time functions play a limited role in the DAQ. Information arrives at the "counting house" in the form of time-stamped data packets. Since the vast majority of PMT pulses are noise hits, it is reasonable to ask what is the impact of noise on system design and cost, and on physics.

The noise rates of the PMTs are interesting for scientific purposes such as SN/GRB searches and for diagnostic purposes such as PMT gain stability. However, the DOM noise rate is approximately 100 times greater than the rate induced by high-energy particles. The question naturally arises whether it is necessary to transmit all the noise pulses individually to the surface DAQ. Unlike hits due to high energy particles, noise hits appear randomly, primarily as *isolated hits*, with no correlation to neighboring or nearby DOMs. *Isolated hits* are defined as those hits falling within a loose timing window, ∼1 μs, but separated by two or more unhit DOMs between. In AMANDA, such isolated hits have been relentlessly "cleaned out" during an early stage of analysis. From the standpoint of event fitting, an isolated hit is more than 100 times more likely to be noise than signal.

Given that ∼5% of the PMT hits are non-SPE events, and that feature extraction is in operation for the remainder, the data rate per DOM is ∼5 kB/s, without local coincidence. Evidence from string 18 suggests that ∼15% of the coincidence events are non-SPE in character. The expected coincidence rate is ∼5 Hz, including random coincidences. At this rate, each DOM would generate only ∼500 bytes/s, about one order of magnitude lower than without coincidence. With local coincidence, data processing resources needed at the surface become smaller by a comparable factor as well.

The question turns next to whether some simple local coincidence requirement, imposed in the ice, selects essentially all interesting hits for transmission to surface. Early work on this topic, including both analytical and Monte Carlo studies based on an IceCube-like geometry, but using an AMANDA-like trigger criterion, suggest that a local coincidence requirement does eliminate a small fraction, ∼1–3%, of real events [159, 160, 161], depending on the tightness of timing cuts. These isolated hits may add some useful information about energy, but likely add very little to tracking precision.

It should be noted that event filtering in IceCube is likely to be quite different than that of AMANDA. The digital system architecture permits much greater flexibility in the design of filters, due to software implementation rather than hardware. Studies have not yet been made to determine whether IceCube would or would not suffer a loss of efficiency, and hence whether the instrument would be operated with some form of local coincidence. If the conclusion is yes, local coincidence will be used, then *isolated* hits would not be present in the output data, except as they contribute to the noise rate histograms for SN/GRB searches. In either case, the DOM design will include the local coincidence capability. IceTop, discussed elsewhere, will employ local coincidence operation to mitigate the uninteresting but copious flux of low-energy muons at the surface. For IceCube, the use of local coincidence is an option that can be turned on or off.

Each DOM communicates with its nearest neighbors by means of a dedicated copper wire pair about 20 m in length. This link is thus capable of propagating short pulses, $\sim$50 ns, with good edge characteristics. The DOM is capable of sending and receiving these short signals in a full duplex mode. It is therefore straightforward to arrange logic within the FPGA such that digitization occurs only when some coincidence requirement has been met. Once a DOM has triggered an ATWD, it sends signals to each of its neighbors and also starts a count-down from a predetermined number of clock cycles. While the count-down is active, a DOM is receptive to pulses from either or both of its neighbors. Should this occur, the DOM will digitize, store, and subsequently transmit the time-stamped data to surface. Meanwhile, the neighboring DOM will have started a count-down period to initiate a period of receptivity, even if it has not yet been triggered. If the neighboring DOM had been triggered prior to receiving a pulse, it will initiate digitization as well. This logic ensures that the local coincidence will capture events independent of which DOM is hit first.

In this way, a local coincidence requirement of programmable width has been implemented in AMANDA string 18 and has worked flawlessly. For the future, it is intended to augment this capability such that a DOM which receives pulses from each of its neighbors during the programmed interval, which itself has not yet been triggered, will transmit pulses back to both so that they will initiate digitization. This will realize next-to-nearest neighbor coincidence.

A somewhat more sophisticated approach is also possible, in which a triggered DOM transmits a pulse to each of its neighbors, as before, but which is now a pulse of predetermined length, say three clock cycles. A neighboring DOM that has not triggered will observe this pulse and transmit it onward but with only two cycles in length; each untriggered DOM in this chain will transmit the pulse onward, shortening it until it reaches zero length. In this manner, a correlation length for the local coincidence requirement can be introduced that extends beyond next-to-nearest neighbor. It remains to be determined whether such a scheme adds to physical content.

The cost for implementation is fairly modest, as a minimal amount of circuitry is needed to generate and receive these pulses, in any scenario. The penetrator must have six pins, rather than two. The cable connecting DOMs is more complicated since it must support six wires. However, by using a short cable to connect four DOMs to just one main cable breakout, a simplification has been achieved in the main cable construction; costs for the main cable are

reduced significantly.

The PMT noise rate can be recorded properly by the DOM, and transmitted periodically to the surface DAQ as time-ordered histograms, so that the supernova/GRB search capability is retained. Programmable dead-time for the histogramming scalers can be included to alleviate statistical degradation due to after-pulsing; this requires only a small amount of FPGA logic to implement. Assuming that the histogramming intervals for detection are 10 ms, the average count is only 3. Allocating 8-bit (maximum count: 255) scalers for the GRB/SN search adds only 100 bytes/s, an insignificant burden. These 10 ms, 8-bit, scalers are unlikely to overflow, even for a very nearby SN.

In addition, however, the DOM can maintain a circular buffer of many seconds (even minutes, if needed) depth, filled with the stream of coarse time-stamps, rounded off to $\sim$0.1 ms. This provides a detailed record of any anomalous rate development, should a nearby SN occur. The interval of interest could be requested in the event that a global sum of the 10 ms data indicates the onset of a significant upward rate fluctuation.

7.2.10 System Design Aspects

Control Logic An Altera 10K50 FPGA provides the glue logic between circuit elements and handles all real-time activities, *i.e.,* those operations for which nanosecond timing is required. The FPGA handles the synchronized launch of the ATWD, loads data into memory, receives messages from the surface and transmits the requested response message. The FPGA will be the site for the SPE feature extraction process. For an FPGA implementation, algorithms involving only integer arithmetic are desirable; this does not appear to impose a limitation for accuracy, robustness or execution speed.

ARM CPU The string 18 DOM state is controlled by a low-power Cirrus logic 32-bit CPU targeted toward the hand-held market. The choice of an ARM device was deliberate, in the reasonable hope that this general architecture would remain viable in the market-place at least for the duration of the IceCube production phase. The particular CPU employed in AMANDA string 18 is certain to be replaced by similar but more powerful devices on a yearly time-scale; nevertheless, software compatibility is expected to be high. A product from another vendor may be chosen for IceCube.

The CPU runs a Real-Time Executive, a thin version of a Real-Time Operating System (RTOS). This facilitates interrupt response and message handling. The CPU boots from flash memory upon power-up, and runs at 16.8 MHz in string 18. It offers the rough performance equivalent of a 31 MHz 486, with a power dissipation of only 50 mW. Higher level functions requiring code unsuitable for FPGA implementation will be realized in the ARM CPU. Since the string 18 DOMs were designed, new FPGA products that offer embedded ARM CPUs (hard or soft) have become available. Such integrated devices may provide an attractive simplification through the elimination of one complex component.

Slow Control, Calibration, and Self-Test Features Each DOM is responsible for controlling critical data taking parameters. These include setting local PMT high voltage levels, discriminator threshold levels, ATWD digitizer control voltages, and even selection and loading of appropriate FPGA programs. Since none of these operations is performed during actual data acquisition, they are deemed part of the slow control system. All adjustments capable of affecting the quality and quantity of data produced by the DOM are controlled from within the DOM itself. Therefore, all slow control requests, regardless of their origin (user interface, automated experiment control sequences, etc.) are finally serviced within the DOM and its resident software.

Each DOM is also capable of carrying out extensive self-test sequences. In addition to verifying correct operation of the digital platform and peripherals within the DOM, these programs can test analog electronics for the presence of increased noise, or spurious discriminator or ATWD behavior. Upon initiation, these tests are carried out under the control of the local DOM processor and results are reported back to surface electronics upon their completion.

One of the most important of these self-test features is *uniqueness*. Each DOM has its own serial number, most likely and elegantly implemented via a preprogrammed serial memory chip on the PC board. Upon booting up, this identification number is transmitted to surface DAQ, which can then verify that the channel number in the DAQ corresponds correctly to the deployed sequence along the string. Thus, cockpit errors that can easily lead to reversed connections or misplaced channels are instantly located.

There are many DOM parameters, measurable either with scheduled tasks in the DOM CPU, or via command messages from anywhere, that must be included in the calibration database. The primary scheduled task is the local-master clock transformation calibration process. Other tasks that should not require frequent activation are the ATWD capture speed calibration, the ATWD trigger discriminator threshold scan, the PMT SPE pulse-height distribution/average, and ATWD transfer characteristics such as sample pedestal values, gain and linearity. The transit time of photoelectrons through the PMT can be measured using a built-in triggerable weak light source (not the optical beacon board).

7.3 Network

The km-scale network supporting the signal detection elements must be robust, cost-effective, and transparent, in the sense that data quality and operational flexibility are not compromised. Despite the challenging technical requirements for data quality, a simple all-copper network can suffice.

7.3.1 Copper Links

All timing calibration, control, and communications signals between a given DOM and the surface DAQ are provided by one conventional twisted pair of $\sim$1 mm diameter copper conductors insulated with PVC. The impedance is in the range of 100 Ω. This pair also supplies power to the DOM. The resulting network is both cost-effective and robust, since the number of connections

(i.e., two) needed for all functionality is minimal. The twisted pairs are assembled first in double pairs, as "twisted quads," and enclosed in a common sheath. The required number of twisted quads are then wrapped around a Kevlar strength member and covered with a protective sleeve. Breakouts of individual quads to facilitate connections to the DOMs are periodically introduced at the appropriate positions.

Cable bulk and cost are reduced by planned operation of two DOMs per twisted pair. This means that two neighboring DOMs are ganged together at depth, with a simple network at the junction point to distribute power and transmit impedance-matched signals. DOM operation employs alternate interrogation of each member of the DOM pair to obtain unambiguous and unconflicted data flow. The data rates per DOM are anticipated to be $\sim$5 kB/s. Even with two DOMs/twisted pair, the bandwidth of the copper links is sufficient to support easily the expected traffic level of 10 kB/s, or equivalently, 80 kbits/s. Fast base-band communication over twisted pair links of 2–3 km can reach 400 kbits/s or significantly higher, depending on protocol. Nevertheless, it should be noted that the margins here are only a factor of $\sim$4, and any action that would increase the PMT noise rate or data/hit will reduce the margin of safety against network saturation, increasing the motivation to utilize the local coincidence feature.

Data transmission to the surface DAQ occurs by alternate interrogation of the DOMs sharing a twisted pair. Differential send/receive results in very low levels of cross-talk for these digital signals, measured to be less than 1% using the deployed AMANDA string 18 cables. Deployment operations are also simplified substantially, since only a single electrical connector needs to be mated and verified.

The use of an all-copper wire network eliminates the need for the optical fibers that have been used in AMANDA. Optical fibers are obviously capable of transporting analog information at the bandwidth needed, but the copper network can meet this goal with digital transport of information. In the rather unorthodox AMANDA mode of optical fiber use, *i.e.,* being frozen in while supporting large vertical gravitational forces and freeze-in force gradients, failure or degradation of signal was commonly observed, typically in the range of 5–15% of channels. This pattern presents an unacceptable level of loss for an instrument of the scale of IceCube. The actual causes of failure or degradation have remained a subject of speculation, since realistic testing of ideas and possible remedies does not appear feasible. Combined with the goals to save costs, eliminate dozens of plane flights, simplify and shorten deployment procedures, the history of reliability problems generates ample motivation to develop an instrument design based on an all-copper network.

7.3.2 Time-Base Distribution

While the all-copper network plausibly meets the goals of robustness and cost-effectiveness, it may seem less apparent that such a network could meet the goal of a distributed time base at the few nanosecond level. As noted earlier, dispersion and attenuation lead to a substantial degradation of pulse rise-time in copper links of this length ($\sim 2\mu$s for 2.5 km). Nevertheless, the realization of local $\Rightarrow$ master clock time transformation with a relative accuracy of 3 ns over a km-scale array is remarkably straightforward, requiring only a tiny fraction of bandwidth and

minimal circuitry for this purpose. The exceptional stability of the DOM local oscillators facilitates this process. Preliminary results with the four DOMs in string 18 in AMANDA operated by the Test-Board DAQ give values for time "synchronization" of ∼5 ns rms, in agreement with expectations, and with clear prospects for further improvement by algorithmic modifications.

The measurement and calibration of timing offsets introduced by differences in twisted-pair cable lengths has been performed automatically and remotely via satellite links by system operators in the Northern Hemisphere. No manual interventions by pole personnel are necessary at any time for this purpose. The *Reciprocal Active Pulse* (RAP) technique exploits the capabilities of the DOM to measure offsets with a statistical precision of ∼1 ns as discussed in section 7.2.7.

7.4 Surface DAQ

7.4.1 Overview

The general concept for the surface system DAQ is shown in fig. 73. The proposed DAQ design revolves around three separate phases of event creation:

1. Within a string, the collection of hits into "string coincidence events."
2. The collection of string coincidences and the decision to form a global event trigger.
3. The gathering of hits on all strings which belong to global events, and the recording of the complete event information on disk and tape.

These tasks can be laid out in more detail by enumerating the messages that are exchanged on the various networks of the DAQ. The following items are also summarized in the figure. Since 100BaseT networking is assumed, bandwidth requirements are shown to be comfortably less than 8 MB/sec in each case.

One notable feature about this design is the prevalence of off-the-shelf computing and networking hardware from the earliest possible point in the data flow diagram. It should be further noted that the focus is on commercial hardware and software found in the world of e-commerce and Web services industry as opposed to process control. Furthermore, there is a clear emphasis on the use of commercial Ethernet networking protocols and hardware in place of more traditional bus-based architectures such as VME or CPCI. Both of these features are intentional and represent our belief that, given both the expected data rates and the difficult maintenance environment at the South Pole, these choices represent the best solutions for both system performance and stability. A corollary of the emphasis on off-the-shelf hardware products is that most of the effort in DAQ is software.

The system consists of an interconnected set of hardware components and software tasks. While this design does allow for a great deal of flexibility in how these components are grouped together and mapped onto various networks and processors, the overall system performance goals dictate that certain aspects of this grouping are fixed. In the following discussion, the distinction between system software processes and actual CPUs within the system should be noted. For

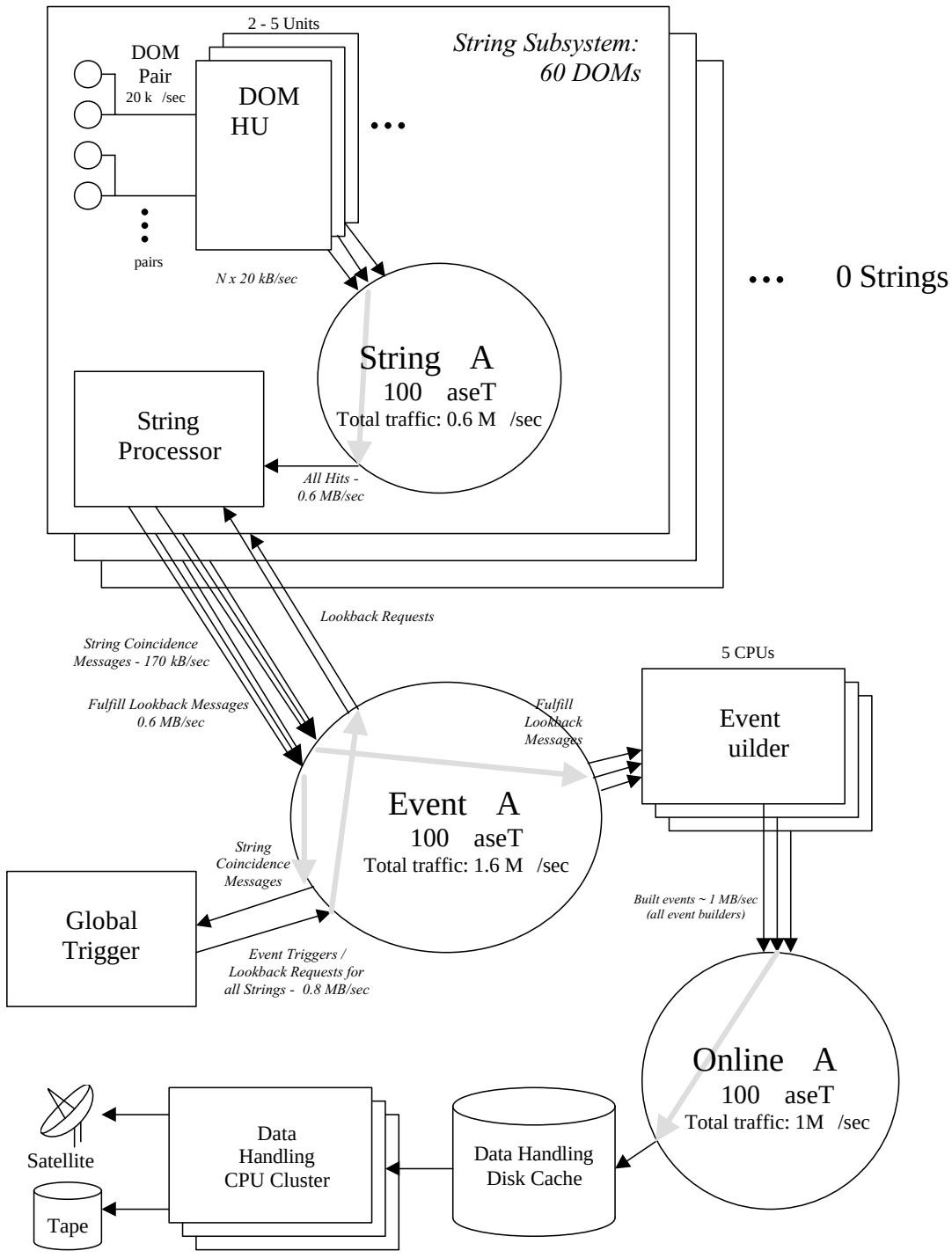

Figure 73: Conceptual illustration of DAQ system organization.

example, a complete string of optical modules is said to terminate in a single processor, called the string processor.

For the purposes of system design, it has been important to decide that, since an optical module string represents a logical grouping of data for triggering purposes, all data from one string will always flow to a single processor and will not be distributed across multiple CPU's. While, for the purposes of this document, it is easiest to discuss the string processing program as executing on a single processor, namely the string processor, the system design does not require that each string be handled by a separate processor. It does, however, require that all data from all DOMs in a string are routed to a single system process that can deal with them in an efficient and complete manner.

7.4.2 DOM Hub

At the surface, the twisted pairs from DOM pairs on a string are connected to a DOM Hub. Each twisted pair connected to the DOM Hub is defined as a *channel*. It is appropriate to design the Hub such that the number of channels per Hub is a factor of the number of DOM pairs on a string, *i.e.* 30. For example, if the DOM Hub accommodates six channels, five DOM Hubs are needed to service an entire string. If the DOM Hub accommodates ten channels, then only three DOM Hubs are needed (similarly, two DOM Hubs will suffice if a Hub has 15 channels).

The functions of the DOM Hub include power distribution and control for each DOM pair, message control, data flow management from the DOMs, downloading of software, firmware, and operating parameters, and generation of time calibration signals. The DOM Hub design is derived from the single-channel *Test-Board* used to read out string 18, and is the only significant piece of custom hardware awaiting realization. It is conceivable (and likely) that the design and layout of the DOM Hub will accommodate more than six channels. In what follows, however, we assume a conservative default of six channels per DOM Hub (12 DOMs).

The DOM Hub design is centered on an embedded processor that provides low level communications services between the surface and the DOM and provides high level communications services (i.e. TCP/IP) to the string processor. The DOM Hub will consist of 1U rack-mounted chassis with front-end electronics including FPGAs and FADCs for 12 DOMs, an embedded CPU daughter card for processing and communications functions, and a power supply capable of providing power for all attached DOMs. The back panel of the chassis contains connectors for direct attachment to DOM deployment cables, master clock distribution, and a standard 10/100BT network connector. The embedded processor is a credit-card-sized 200 MHz StrongARM CPU running Linux.

The DOM Hub will support TCP/IP protocol and will deliver data streams for each DOM to the string processor using the standard socket programming model. Furthermore, the DOM Hub will provide transparent web-based communications with individual DOMs so that maintenance and minimal testing functions may be performed remotely without the need of the full data acquisition system.

All real-time functions in the surface DAQ that depend on nanosecond-level timing are contained within the DOM Hub. Data transferred from the DOM Hub to downstream elements in

the surface DAQ are time-stamped messages; subsequent processing needs only to ensure adequate data flow. The latencies of network operation do not introduce synchronization problems.

The DOM Hub receives a carefully distributed 40 MHz master clock. This master clock will be linked ultimately to GPS, providing a universal time reference to other GPS-linked data sets to $\leq$ 40 ns. The DOM Hub maintains a register capable of assigning a unique time-stamp for at least one day (44 bits). Although runs will likely not extend more than one day, it is straightforward to track time perhaps for as much as a year (51 bits). Test functions will be incorporated to ensure that every DOM Hub has exactly the same master time. These test functions will operate as separate, scheduled threads that will not interfere with normal data acquisition.

Assuming a PMT noise rate of 300 Hz, 60 DOMs per string, a fraction of 5% of hits needing full waveforms, 170 bytes per waveform and 8 bytes per non-waveform hit, one obtains a DOM data rate of about 5 kb/s and 0.3 MB/s per string. Because these data flow rates are modest, the surface DAQ can be network-based rather than a more traditional crate/backplane/bus implementation. Of course, with local coincidence, these rates would drop an order of magnitude further.

Data from each DOM is requested periodically, at a rate of $\sim$10 Hz. This provides adequately small latency for data streaming purposes, and maintains a reasonable transmission burst of 0.5–1 kb/request. Each request for data includes the time-mark signal as the first pulse. The DOM will ignore most of these, using them only as frequently as local clock drift characteristics require.

DOM data packets with local time-stamps are locally buffered in the DOM Hub. For each string, hits from DOMs connected to five DOM Hubs are sent over a String LAN (one 100BaseT network switch) to a String Processor (SP).

7.4.3 String Processor

Data buffered in the DOM Hub is block-transferred periodically, $\sim$10 Hz, to the *String Processor (SP)*. The SP is expected to be a standard PC CPU running a Linux OS. Here, data is converted to master time units. The desired space-time correlations characteristic of physics, traditionally defined with real-time electronic trigger systems and called "triggers," are found in our case through software algorithms in the SP. Simulations have shown that only about 5% of available CPU cycles of a 1 GHz PC are needed to perform typical coincidence algorithms for a 60-DOM string.

Each String Processor is also connected to a global Event LAN. String coincidences are reported by each String Processor to the Global Event Trigger on the Event LAN. The Global Event Trigger is envisioned as a single processor on the Event LAN, which is also connected to a set of processors that serve as Event Builders. Assuming a string coincidence rate of 60 Hz per string, an average of 4 hits per coincidence event, and 60 DOMs per string, one obtains a total data rate for all 80 strings of less than 0.2 MB/s for these messages.

When trigger conditions for a particular event type are fulfilled, the global event trigger informs the String Processor to tag all hits that occurred near enough in time to the global trigger time. If one assumes a global aggregate trigger rate for all trigger types of 1 kHz,

10 bytes per message, and 80 string processors, these "Look-back Requests" require an average bandwidth of 0.8 MB/s.

The String Processor sends the data for the tagged hits to one of a set of Event Builder CPUs. This also occurs over the Event LAN. Assuming 20 random noise hits per event, 12 muon hits per event, and the above values for the average number of bytes per hit and for the global event rate, one obtains an average bandwidth of 0.6 MB/s. This brings the total bandwidth usage on the Event LAN to about 1.6 MB/s, well within the capabilities of 100BaseT switches.

It may turn out that the waveform data retrieval task for the look-back requests may be just as easily handled by sending all waveform data associated with the string coincidence trigger messages, since the amount of data arriving at the SP is roughly the same as the look-back request traffic. This software architecture would eliminate the look-back process, yielding a data flow diagram without loops at this level. In this scenario, however, the destination of the waveform data needs to be considered carefully to ensure arrival at the appropriate Event Builder target CPU.

The Event Builder CPUs send fully constructed events to a disk server over the Online LAN. The disk server will write events to disk. Since the bulk of the event data is in the hits, the bandwidth on this network will be not significantly more than 0.6 MB/s. 1 MB/sec is a safe number to assume, well within the 100BaseT limits. In addition to the Event Builder processors and the disk server, the Online LAN also is connected to the processors that constitute the online filtering and data archiving system. Events are still represented in master clock time units, but also have the associated GPS times linked to each.

This design is attractive, in part, due to its high degree of modularity and flexibility. Thus to create a minimal test stand for DOM production and quality control, one can simply work with a single DOM Hub attached to one or more DOMs (or DOM pairs). Functionality for a whole string can be achieved by networking the DOM Hubs to an off-the-shelf String Processor CPU and installing the requisite software. In an international collaboration where hardware production, software development, testing and deployment will be carried out on multiple continents, this is a key advantage. Finally, with the proposed "network-heavy" scheme, IceCube will benefit from a tremendous amount of community experience and publicly-available tools for TCP and UDP-based networking, which far outstrips the resources available for bus-based architectures such as VME or Compact PCI.

7.4.4 IceCube and IceTop System Integration

The DOM and its associated DOM Hub design will accommodate the technical requirements of both IceTop and IceCube, with differences confined to firmware, software, and operating conditions. Within the counting house, the differences would be apparent only in the network configuration.

Each IceCube string requires 15 quads for the 60 DOMs. Unlike IceCube, the IceTop DOMs will not share a twisted quad with a neighboring DOM since the expected rates are higher than those of IceCube. The four IceTop DOMs thus require two quads, for a total number of 17 DOM twisted quads/string. In addition, there will be ancillary devices added to the string, such as

pressure sensors used during deployment and freeze-back, so the expected total number of quads will be at least 18 per string, perhaps more. The fraction of counting house resources needed for IceTop is $\sim$15% relative to IceCube.

IceCube The 80 strings of IceCube will require 400 (240, 160) DOM Hubs in the counting house under the assumptions that a DOM Hub has 6 (10, 15) channels (two DOMs per channel in IceCube) and is housed in 1U mechanics. The DOM Hubs and 80 (perhaps less) associated String Processors will require something like 10 (6, 4) floor-to-ceiling racks. The space-saving that would be obtained with the 10- or 15-channel version is substantial, and provides ample motivation for high design density.

IceTop IceTop, described in detail elsewhere in this document, will consist of an ensemble of frozen water tanks situated just below the surface, and located near each of the 80 strings. Each string will have two tanks separated by a few meters to suppress single muon events, yielding a total of 160 tanks. To extend the dynamic range, each tank will be viewed by two DOMs operated at substantially different gain settings. This facilitates the capture of extremely high-energy air showers. The local coincidence requirement will be operational between the high-gain DOMs in the two tanks. The coincidence requirement will reduce to an acceptable level the rate induced by the relatively copious flux of uninteresting single muons penetrating the tank volume.

With 160 tanks and two DOMs/tank, IceTop's 320 DOMs will bring 320 twisted pairs (in 160 twisted quads) into the IceCube/IceTop counting house. These IceTop quads will plug into 54 (32, 22) DOM Hubs dedicated to IceTop, if the DOM Hub supports 6 (10, 15) channels. The IceTop DOM Hubs will connect to a dedicated IceTop Global Trigger CPU and Event Builder, with a LAN architecture analogous to IceCube. The output data stream will be linked to IceCube by both master clock times and GPS time units for online and offline analysis.

7.4.5 Experiment and Configuration Control

The system design described in this document is based on a loosely-coupled collection of sub-systems whose operations are, for the most part, decoupled. One advantage of such a design is that it allows some independence in the design and implementation of individual sub-systems. However, in order to co-ordinate these elements into a single, coherent system, some degree of overall control is required. This function is provided by the experiment control system.

The IceCube detector can, at any given moment, be described as being in one of several operational states. These states serve as short, meaningful descriptions of just what operations are being performed by the detector. By enumerating which operations are allowed in which detector states, this state model also serve as a mechanism to control and co-ordinate operations of separate detector sub-systems.

Scope of Experiment Control The detector, as a whole, can be though of as being in one of the following states: "idle," "entering data-taking state," "running," "paused," "exiting data-taking state," "calibrating" or in one of several "testing" states. Each of these states has certain implications for the operations of each sub-system. For example, if the detector is taking data, the DOM string control sub-system should not be able to alter PMT high voltage settings on an active OM. Similarly, although it is permissible to alter individual settings for an inactive DOM (i.e. an DOM not included in the global trigger's list of active DOMs), it should not be possible to initiate LED beacons on this particular DOM since resulting light would affect data taking activities. Therefore, all sub-systems refer to experiment control as the single indicator of the system's current aggregate operational state. Each sub-system is responsible for designing its internal operations and states to be consistent with the overall detector behavior described by experiment control's current state.

Common Component Control Model In addition to providing all sub-systems with a consistent indication of the detector's overall state, experiment control must, in order to initiate and control data taking, be able to request sub-systems to perform certain actions. Depending on a particular sub-system's role in the detector's operation, these actions can be relatively simple or fairly complex. For example, when beginning data taking, DOM string control will be required to log current DOM parameter settings to a local database and change its state from "idle" to "data taking." The fact that the DOM string control sub-system is in the "data taking" mode implies that it will be unresponsive to user requests to reset critical DOM parameters. Other sub-systems may require more complex responses to experiment control commands.

To the extent that the complexity of these operations is only of concern to the sub-system itself, the details of these operations should remain concealed within the sub-system's operation. Each sub-system should be able to accept a high-level request from experiment control to move into a new state. Following this request, each sub-system will respond with its new state and status. Successful transitions of each sub-system into the appropriate state will lead experiment control to indicate that the detector has taken on the desired final state (e.g. "running"). The failure of any sub-system to appropriately move to the desired target state will indicate a system problem and will cause experiment control to bring all sub-systems back to a consistent and safe state.

It should be noted that with the loosely-coupled system described here, individual control operations are best handled directly by those sub-systems involved. That is, commands and requests for monitoring and status information will be processed by the sub-systems themselves, not by some single intervening agent (e.g. experiment control). The advantage of such a design is that additions and alterations to sub-system controls and interfaces need only be implemented in one place -the sub-system itself. They do not have to be further integrated into additional supervisory programs or levels.

However, it should be pointed out that, with this implementation model, it is possible for there to be a wide and confusing variety of user interfaces for each sub-system. Even with experiment control properly playing its detector-wide coordinating role, it will be possible to

implement sub-system user interfaces in many different and potentially awkward styles. A certain degree of discipline in design and implementation of individual sub-system user interfaces will be required in order to produce a consistent overall look and feel. Given the breadth of functions requiring user interfaces and the necessity for effective remote (albeit secure) access, the adoption of a web-based user interface model is preferred.

DAQ Configuration Database The DOM string control sub-system will be responsible for keeping an accurate database of DOM-related parameters for each data taking session. While this list of DOM parameters and operational settings is not yet complete, it is safe to assume that, during any given data taking session, each DOM participating in the detector array will have 50 to 100 parameters that describe its intended operation. These will include static fiducial information such as serial number, string and position location, firmware version number, etc. It will also include per session information such as PMT high voltage, trigger threshold level, and, if some level of waveform capture is included in the DOM, parameters that describe operation of waveform capture and feature extraction algorithms.

This same database will also be used to control which DOMs are actually participating in data acquisition operations for detector array and, if required, insure that unused DOMs are powered down and/or not contributing unwanted triggers to string processor trigger processors. This same database will be used by the Global Trigger and Event Builder sub-system to control operations of the String Trigger processor algorithm.

Component Discovery and Self Configuration The IceCube detector will be deployed over a period of several years. Furthermore, during the summer deployment season, optical module strings will be deployed, tested and integrated at rates far in excess of that experienced by the current collaboration. While the physical logistics for drilling, deploying and cabling detector strings are critical to the success of this timetable, the speed with which the data acquisition system can adapt and re-configure to the addition or deletion of new optical module strings will be of equal importance.

Each sub-system located at the South Pole must be aware of its environment and capable of determining whether needed hardware and software components are available. This operation can be performed automatically when individual sub-systems are started or can be the result of an explicit re-configuration command. The most basic example of such an operation is enabling the experiment control sub-system to locate, via a set well-defined network operations, and establish communications with all other operating sub-systems. A more complex, but conceptually similar, configuration operation enables the DOM string control sub-system to determine which strings are present and which optical modules are in an operable state. This resource discovery scheme can be extended to on-line sub-systems as well by enabling the filter farm manager to discover which individual processors are available to participate in its operation.

If this technique is consistently applied across all sub-systems and is combined with accurate and complete documentation of the experiment cable plant, it becomes relatively simple to incorporate both additional DOM strings and computing resources as they are installed. The

presence or absence of portions of the hardware and software system become apparent to operators as each sub-system reports its success or failure during a "configure" operation. In addition to speeding integration of new portions of the detector, this capability allows fast and effective resolution of complex system-wide equipment problems. This capability can also provide critical equipment status information when recovering from an unscheduled power loss.

Just as it is critical to be able to automatically incorporate new DOM strings and computing components as they are installed, it is also important to be able, under computer control, to mark portions of the system as off-line or "non-participating." The most obvious need for such a facility is during system debugging. It is often useful to remove elements from the system in order to investigate their role in generating specific error conditions. Unfortunately, it is not always convenient or possible to electrically disconnect or power down suspected hardware or software components. Some data acquisition problems may require this sort of system de-population for correct diagnosis and repair. If these problems occur during the winter season, the ability to remove some components from the system, via remote access, will be of great advantage.

7.4.6 Security Environment

"Security" can cover a wide range of capabilities and protections. It is worth reviewing the current use of the term in computing and communications systems. In current computing usage, the term security is based on four principles: authentication, authorization, privacy, and non-repudiation. Briefly, authentication involves the verification that a user has the identity they claim to have, authorization verifies that a given user has the authorization or privilege to perform a requested operation, privacy assures users that messages and data exchanged with another user will be private to only those two parties, and non-repudiation stipulates that requests received from a user cannot be repudiated at a later date (e.g. electronic transfer of funds). Each of these principal functions can be implemented separately and each with varying degrees of completeness. Furthermore, several different technologies can be used to achieve some or all of this functionality. While simple open password schemes are not considered to provide any real level of security, suitable software mechanisms, such as DES, Kerberos, and PKI (Public Key Infrastructure), exist and are readily available.

An exact statement of IceCube security requirements does not, as yet, exist. However, based on past AMANDA experience and reasonable projections of IceCube operations, several needs are obvious. Regardless of what network access level protections may be implemented upstream, such as screening of requestor IP addresses, it is important that all control commands be verified and screened by a security service at the South Pole site. This service should provide, at a minimum, strong authentication and authorization functions. These would basically regulate who would have access to data acquisition and on-line control and monitoring information and which specific capabilities would be allowed on an individual basis. While privacy and non-repudiation functions do not appear to have any role in experiment control and monitoring at present, any suitable security service will allow their implementation at a later date. In discussing security in the context of experiment control, it is assumed that a certain level of robust security is provided by the underlying operating system and network environment. It is

assumed, for example that unauthorized access to system accounts has been eliminated and that network routers and their control ports have been made suitably safe. The following discussion centers on the application design decisions that will enhance this low-level security and protect the resulting system from unauthorized or inadvertent use.

One mechanism used in designing secure control systems is to create a finite number of "roles" that users can take on when logged onto a system. These roles are typically descriptive in nature (e.g. "operator," "implementers," "maintenance technician," "super-user"). Users requesting access to the data acquisition or on-line sub-systems at the South Pole will present their name, security credentials, and intended operational role to the security service. After authenticating user identity, the security service determines whether a user is authorized to take on the requested operational role. If these security checks are successful, the user then has all the privileges associated with that operational role.

One of the advantages of this scheme is that it creates a clean partition between security services and system operations. Security mechanisms can be centralized into a single point of access. Individual sub-systems are then able to treat all commands as having been issued by authenticated users acting in an authorized capacity (i.e. role). In addition to these implementation efficiencies, this scheme also clarifies overall system design and operation. Although commands to sub-systems will carry the identity, as well as the acting role, of the requestor, the design becomes one primarily driven by the requestor's role. The act of describing the set of all possible user operational roles implicitly describes all possible modes of system operation. For example, since each sub-system differentiates between normal operations allowed by an "operator" and those privileged commands reserved for "implementers," lists of permissible "operator" and "implementer" functions take on detector-wide meaning and significance. Furthermore, since, at the sub-system implementation level, every command must be checked against the role of the requestor, sub-system behavior becomes both well-organized, easily described and, hopefully, documented.

7.4.7 DAQ Components

Slow Control The DOM string control sub-system will consist of a central control program and co-operating tasks executing on each string's dedicated control processor. Since the detector will grow by the addition of DOMs organized as strings and since the only electrical and logical path for communicating with a particular OM is through its string processor and cable, this design is a natural fit for the detector's topology.

The central slow control program will be responsible for all user and experiment control interface functions to the optical modules and will be responsible for all DOM-related interactions with the detector configuration database. These database interactions will include queries of DOMs currently active in the detector, setting and recording of internal DOM parameters for data taking, and recording of individual DOM calibration information acquired during low level calibration operations. Most DOM string control operations will be synchronous command or monitoring requests.

At present, there are only a small number of possible states for the DOM string control sub-

system. These states should be sufficient to indicate the following DOM string control activities: off-line or idle, performing self-configuration and string discovery, performing one or more local DOM calibration functions, on-line and able to accept operator commands, and on-line but only accepting monitoring requests (as during normal data taking). Additional states can be added as needs arise. It should be noted that these states, as well as those of other sub-systems, will not correspond exactly to those of the experiment control program. They do, however, represent a list of possible sub-system behaviors that are consistent with the overall detector operation.

The central control program will also be responsible for discovering via their associated string processors, all DOMs presently in the detector. Once connected to the local area network, newly added strings will be incorporated into the central control program through a single "reconfigure" command. This same operation will allow strings temporarily removed from the detector for purposes of test or electronics repair to be marked as "non participating strings" and their respective DOMs recorded as "off line."

String Data Handling Each DOM in a string produces a stream of hits and waveforms that, via the String LAN, ultimately reaches the string processor. All operations surrounding data transfer, sorting and interactions with other system components (e.g. the global trigger) are the responsibility of the string data handling process. The first phase of its operations center on the delivery of string level hit information to the global trigger process. Upon reception of data from one or more DOMs, its initial task to sort this data into structures that allow quick, efficient determination of local coincidence during a sliding time window (typically 8 μs). When all coincidences for a given time period have been found, they are properly formatted and passed on to the global trigger process.

The second phase begins when the global trigger process responds with a list of time intervals of interest. It is then the string data handler's task to collect raw data from all DOMs for each of the time intervals of interest and forward the resulting data set to the appropriate Event Builder. In practice, these two phases will overlap and provision must be made to have several such operations in progress at any one time.

There are only a small number of possible states for the string handler process. These states should be sufficient to indicate the following activities: off-line or idle, performing self-configuration and DOM discovery, processing normal data triggers, paused due to operator request or error condition, and performing string specific tests. Additional states can be added as needs arise.

Global Trigger As described above, the global trigger is responsible for generating lists indicating the occurrence of detector-wide events of interest. It consumes the list of hits as determined by the string data handling process in each string processor and emits a list of UTC-based times that bracket hits considered to be possible events. The global trigger behaves synchronously with the aggregate collection of on-line string processors. That is, the global trigger waits until all string processors that are configured and active to report their contributions for a given time interval. Only when all string contributions are present, can the global trigger

begin the process of determining what events might have occurred. Once this determination is complete, the Global Trigger selects an Event Builder for the current data sequence and passes a list of UTC time intervals to both the selected Event Builder and all string handling processes.

During normal operation, all 80 string processors will remain synchronized within the reporting period specified when data taking was initiated. This period can range from as low as $\sim$100 ms to perhaps a few seconds, without degradation of system performance or compromise of data integrity. Several global triggers may be found within one reporting period. As described above, for each reporting period, ALL string processors must forward string-level local coincidences, or their absence, to the global trigger in order to initiate the global triggering process. In the absence of such a report, the global trigger will re-synchronize all string processors and forward, to the Event Builder an indication of what reporting periods were discarded. Persistent failure of a string processor program or CPU will cause the global trigger manager to enter a non-operating error state. Experiment control will detect, during periodic system scans, this state change and force an abnormal end of run sequence for all data acquisition sub-systems. Co-ordination activities and generation of global triggers are performed by a single global trigger process executing on a dedicated processor. Since this activity requires the exchange of multiple messages between this process and each string's data handling process during each reporting period, high speed, low latency network connections between these processors is of great importance.

There are only a small number of possible states for the global trigger sub-system. These states should be sufficient to indicate the following activities: off-line or idle, performing self-configuration and string processor discovery, processing normal data triggers, paused due to operator request or error condition, and performing global trigger specific tests. Additional states can be added as needs arise. As with other sub-systems, it should be noted that these states need not correspond exactly to those of the experiment control program. They do, however, represent a list of possible sub-system behaviors that are consistent with the overall detector operation.

Event Builder The I/O requirements for IceCube are not very demanding, opening up many possible approaches to event building. We opt for a simple yet flexible approach based on commercial hardware. Its main elements are a farm of the order of five "event worker" PCs connected via a switched ethernet network and a control PC that manages the farm and distributes the work. This asynchronous approach offers a redundant, fault-tolerant, reliable and scalable solution that should work with minimal maintenance effort. The amount of CPU time needed for event building has not yet been studied in detail but is estimated not to be the defining factor for the size of the farm. The number of PCs is rather determined by the requirement of redundancy. To exploit the CPU capacity, several tasks will be incorporated in addition. We currently envision the following set of tasks:

- Asynchronous merging of data from 80 string-wise sources (event building);
- Low level monitoring, data consistency checks and online calibration;

- Feature extraction from digitized pulse shapes.

A special control PC is used to control event building by selecting specific event worker PCs that are ready to accept data, usually in a round-robin way. In addition it will be used for configuration, system and data supervision and will host a graphical user interface. If a PC has crashed, the load is taken over by the other PCs in a dynamic way and the PC is question is automatically rebooted. All event working PCs 's have identical functionality. Their number is completely scalable and can be adjusted according to needs. The buffered string-wise data will be "pushed" to an idle event worker PCs roughly every 10–100 s. The Control PC also provides a list of links to data belonging to the same trigger time stamp. In this way only pointers are modified and the PCs are running in an "I/O-free" mode. The data are actually only moved in the last step before writing the data to disk. Such a farm can be built based on today's standard networking equipment.

7.4.8 Calibration Operations

Calibrations serve a crucial and central role in the operation of the IceCube detector. They must, to the greatest extent possible, be automated. The present digital design allows calibrations to be carried out without any physical intervention to the data acquisition system. That is, all calibrations can be performed without disconnecting cables or physically re-configuring DOM electrical data paths. However, while this is a necessary condition for fully automated, unattended calibration operations, it is not a sufficient one. Further design and detailed descriptions of operational sequences are still required for automated operations to become a reality. While the following framework should allow such operations to take place, further discussions are needed in order to insure their successful operations within the current design.

DAQ Calibration Operations The primary calibration operation carried out within the DAQ system is that of synchronizing time bases for all DOMs with the GPS clock. This operation will take place automatically once every 5 to 10 seconds. The actual nanosecond-level signaling operations are performed by the DOM Hub and DOMs themselves. The DAQ's only role is in enabling such operations and supervising the dissemination of the calculated clock offsets for each DOM to both the DAQ configuration data base and, through an as yet unspecified mechanism, the Online system. The primary DAQ component involved at the supervisory level is the string processor. Since all data leaving the string processor is corrected to UTC, this is the rational point at which to control and implement needed time base corrections. All other calibration IceCube calibration operations are based on analysis of data collected by a carefully configured, but normally operating DAQ. Therefore, these calibration operations fall outside the scope and capability of the DAQ and are, more properly, Online functions.

Online Calibration Operations In addition to the time base synchronization calibration performed by the DAQ system, additional calibration operations are required for successful detector operation. These include, but are not limited to, determination of individual PMT

high voltage settings, determination of proper PMT trigger thresholds and measurement of cable delays for all DOMs. As noted above, all of these calibration tasks are based on specific data analysis applied to the detector data stream. Therefore, these calibration operations are primarily operating in the Online domain. In fact, they can all be considered to be part of a special subset of normal data taking operations. It should be noted that some of these Online calibration operations will produce data required for correct operations within the DAQ system. In these cases, mechanisms must be in place for inserting these calibration values into the DAQ configuration data base.

In practice, these operations can be automated and orchestrated by the main supervisory program, experiment control. Experiment control can select a particular DAQ configuration and instruct DAQ to begin operations. It can then select a particular Online configuration and instruct Online to begin operation. With a suitable level of flexibility at the experiment control level, fairly complex sequences of calibrations can be carried out in an automated manner.

7.4.9 DAQ and Online Monitoring

Operations and Error Logging The design described in this document partitions system behavior into a number of low-level tasks and assigns them to individual sub-systems. Furthermore, these sub-systems are organized together through a single experiment control sub-system that is able to orchestrate their operations into a single co-ordinated activity. While such a design has been proven to be both flexible and reliable, when problems do occur, the relatively "loose" connection between subsystems can make proper diagnosis difficult. A well-designed operations log is a key tool in allowing rapid discovery and correction of individual sub-system problems.

All sub-systems will be able to log messages to a single, system wide operations log. Each message will be tagged with the name of the sub-system as well as the time of entry. Each message will also include numerical and text fields to describe error conditions as well as global state information such as experiment control run number and state. While there will be provision for one or more free form text areas, the format will include mandatory fixed format fields to facilitate automated searching in one of several modes. At a minimum, the log will be searchable by sub-system, time and global run number. In practice, this operations log may be built on existing open-source or commercial database technology.

DAQ and Operations Monitoring It is anticipated that, at least for purposes of detector and data acquisition system monitoring, there will be a number of groups interested in having independent and uncoordinated access to one or more software sub-systems at the South Pole. As described earlier, design distinctions between monitoring requests and control commands will allow the use of robust, commercial-grade web server programs for a large portion of these user interactions. Routing requests for monitoring data through a web server concentrates most of the interactive data flow through a well-debugged program that acts as a buffer between off-site data requests and data acquisition and on-line sub-system programs. Unfortunately, this mechanism is still subject to periodic and occasionally unscheduled communications outages

between the northern hemisphere and the South Pole. Given the wide distribution of local time zones within the IceCube collaboration, this can create limited or, at a minimum, inconvenient access to monitoring data.

With the interposition of a northern hemisphere server/cache gateway system, much of the data acquisition and on-line sub-system monitoring data can be made available to collaboration members at their home institutions during reasonable day-time hours. This gateway system would be configured to refresh its cache from sources at the south pole during times of expected communications availability and serve these monitoring data files in response to browser and client requests. During times of communications blackout between the south pole and northern hemisphere, collaboration members would be able to direct their browsers and client programs to the gateway system and obtain current, within 24 hr, detector and sub-system status. Furthermore, if it were deemed necessary to restrict general collaboration access to South Pole systems, this architecture would provide a straight forward mechanism for distributing detector monitoring information. Thus, up-to-date detector and data acquisition system performance data is made available collaboration-wide on a best-effort basis.

Portions of the monitoring and operational information will be needed for correct interpretation of data during later analysis. This can include current and cumulative trigger rates for all trigger types as well as Event Builder statistics and gross DOM data rates on a string by string basis. There must be a mechanism for identifying and passing monitoring data from the DAQ system to the Online system. This may consist of a separate data stream, or even the periodic inclusion of monitoring data in normal data streams.

Online Components The Online system is essentially a carefully organized portion of the Offline environment that has been targeted for execution at the data acquisition site under the control of the experiment control sub system. It has three primary responsibilities. First, it is the sole component responsible for copying the DAQ event stream from the shared disk system, located on the Online LAN, to both archive storage (i.e. tape) and, via satellite, to the northern hemisphere. As such, it is capable of reformatting and repackaging data from the Event Builder into those forms best consumed by offline analysis tasks. Secondly, it provides the framework and control mechanisms for executing any online filter operations used to analyze, reduce or reject data from any of the data streams emitted by event builders. And thirdly, as described above, the Online system contains filters and or programs that perform all calibration functions beyond those of DOM time base synchronization performed by the DAQ system

7.4.10 DAQ Computing Environment

COTS Hardware and Software Components There has been a real effort, during the design of both the DAQ and Online systems, to maximize the potential for using commercial, off the shelf (COTS) hardware and software components. At a minimum, this includes use of open source operating systems (namely, Linux), standards-based network and communications software and PC-based computing platforms. Of course, we feel it also should allow for the purchase of standards-based components as required. This can, for example, include purchase

of PC clusters that have well engineered cooling and maintenance features or disk systems that have extensive space management and diagnostic software packages.

String LAN Components As noted earlier, each string terminates in its own private network. In practice, this network consists of a set of DOM Hubs and a single processor connected to an off-the-shelf switched Ethernet hub. This design nicely encapsulates the entire string behind each string processor, which serves as the complete interface to the string. Based on system performance, we may choose to have two or more strings share the same string processor. If so, we need only increase the number of Ethernet attachments required for the commercial switched hub.

String, Global Trigger, and Event Builder Processors Depending upon the degree to which multiple OM strings can be accommodated on a single string LAN and processor, the IceCube DAQ, when fully implemented, may have on the order of 50 to 100 processors. By any measure, this is a substantial number of systems to house and maintain. When designing a system with such a large number of processors, several factors besides basic unit processor cost must be considered, such as operation in a low humidity and low pressure environment with an occasionally unreliable power source. Many vendors have addressed the ancillary issues involved in configuring, operating, and maintaining large clusters of PC-based Linux systems-most notably for use in the e-commerce industry. For these markets, vendors have addressed such issues as increased packing density (e.g. one processor per 1U rack space), improved ventilation and temperature monitoring, improved, tool-free, modular repair capabilities, and network-based remote diagnosis and control of individual processors. These systems typically have a full, but limited set of disk, communications, and PCI resources. In determining the functionality and interconnections needed to implement both the DAQ and Online systems, care has been taken to stay within the physical and logical constraints presented by these PC cluster implementations.

Event LAN The data rates presently anticipated indicate that the communications network used to connect all OM string processors with the single global trigger processor and multiple Event Builder processors can be adequately serviced by conventional data network (100BT or Gigabit Ethernet). As with the String LANs, this network is well bounded and only requires a local switch-based infrastructure.

If these data rate projections grow beyond the capabilities of either 100BT or Gigabit Ethernet technologies, alternate, off-the-shelf solutions can be inserted into this architecture without major perturbations to the system design. In particular, we have investigated the Myricom switched fabric inter-processor network as a potential solution.

Storage Systems and Online LAN As with network infrastructure, storage systems represent an area where system data rates dictate the technical solution. The primary storage facility shown in this design is that which provides the flexible data buffer between the DAQ

and Online system partitions. This system design effectively increases performance by providing parallel computing resources for those paths with the highest data throughput rates. At the juncture of the DAQ and Online systems, this implies a shared network-based storage system with multiple access paths to both Event Builder and online processors. The current aggregate data rates indicate that a 100BT based commercial SAN (Storage Area Network) system will meet the necessary storage and throughput requirements. As with the selection of processors, storage system selection should not be based solely on hardware costs. Most modern commercial systems include system level features such as automatic mirroring, local automated backup and remote fault diagnosis and configuration tools. These facilities should receive high consideration in vendor and system selection.

As with the Event Builder LAN, the technical solutions are sensitive to the ultimate data rates expected within the system. If the current projected data rates prove inadequate, consideration will be given to their effect on the I/O bandwidth requirements of the shared disk system. Alternate solutions with substantially higher throughput rates do exist - most notably fiber channel based SAN arrays. Since these storage systems use individual PCI interfaces and a separate switched fabric interconnect for all disk related data, the costs - as well as the data throughput - increase dramatically.

7.5 AMANDA Data Transmission Techniques

For historical reference, we present here the data transmission techniques used in the past by the AMANDA detector. The present AMANDA II detector has been deployed over several seasons, with a stepwise implementation of detectors with improved data transmission techniques. An array of four strings (AMANDA-B4) was installed in 1995/96, with the OMs connected to the surface by an electrical coaxial cable that transmits both the HV and the analog anode signal; see fig. 74, left. PMTs are operated at a gain of 10^9 to drive the pulses over 2 km of coaxial cable without in-situ amplification. Hamamatsu R5912-2 PMTs with 14 dynodes are used to achieve the high gain; they require positive high voltage (HV) at the anode. The signal at the surface is picked up via a DC blocking high-pass filter. The time-offset t_0 is measured by sending a laser-generated light pulse through an optical fiber from the surface to a diffuser ball close to the OM. The anode signal is considerably attenuated and dispersed by the 2 km cable, with typical time over threshold of 550 ns and rise time of 180 ns. A correction for the amplitude-dependent offset of the time when the signal exceeds a fixed threshold (time slewing correction) is applied off-line, resulting in a time jitter of roughly 5 ns. Coaxial cables have been replaced by twisted-pair cables for the 216 OMs deployed on six strings (strings 5-10) in 1996/97. Both attenuation and dispersion were significantly reduced compared to coaxial cables. The rise time decreased from 180 ns to 100 ns. Some test-OMs were instrumented to transmit analog optical signals through the laser calibration fibers.

In 1997/98 the array was expanded by 3 test strings (strings 11-13) that used optical fibers on all OMs, both for calibration and for analog transmission of the PMT pulses. The main goal was to evaluate this technology under realistic conditions and to compare various optical fibers and optical connectors. Electrical transmission was installed as a backup. The PMTs were operated

at a gain near 10^9. Figure 74 shows the functionality of these OMs. The fiber transmitting the calibration signal from the surface penetrates the OM. The light is directed to the diffuser ball via an optical splitter. The PMT anode current is converted into an infrared signal by an LED operating at 1300 nm, which is transmitted to the surface where it arrives essentially without dispersion. Optical fibers, connectors and penetrators are more vulnerable to the high pressures when the hole refreezes than their electrical counterparts. For electrical connectors, the losses were close to 10% for string 1-4 but, after using penetrators with an appropriate shape, this value was reduced to 3% for strings 5-10. The failures of the optical connections have been, and still are, about 10%, although half of these operate satisfactorily with attenuated amplitudes.

The advantages of the optical analog transmission compared to the electrical analog technique are:

- High bandwidth (rise time of 5 ns);
- Good double pulse resolution;
- Higher dynamic range due to lower HV;
- No correction for amplitude-dependent time slewing needed and, therefore, easier calibration;
- No pickup of electromagnetic noise, no cross-talk;
- Operation during drilling operations is possible.

The analog fiber optic signal transmission became the default technology for the expansion to AMANDA II.

Experience with AMANDA II has shown that before establishing analog fiber optical transmission as an adequate technology for IceCube, the following improvements are required: 1) the light transmitter, whether LED or laser diode, has to be operated with an independent and adjustable bias current, and local electronics in the OM must provide that function, and 2) a higher current-to-light conversion factor must be achieved. This resulted in the dAOM (digitally controlled Analog Optical Module) concept. An alternate technical approach is the DOM (Digital Optical Module), which represents a departure from traditional AMANDA techniques because the digitization of the PMT signal is performed under ice. The right part of fig. 74 gives a functional description of both. Both technologies were deployed and tested with the 1999/00 completion of AMANDA II.

The dAOM concept is depicted as second from right. A DC/DC converter in the OM converts the 60V-supply voltage to the low voltage required to operate a microprocessor and other integrated circuits. The HV is generated by a Cockcroft-Walton generator, which is implemented in the PMT base. Voltages between the cathode and the first dynode, and between the first dynode and the anode, can be set separately. Slow control and reply signals are exchanged over the electrical cable. Also, an electrical analog signal is transmitted as a backup to prevent a complete loss of signal in case of damage to the optical fiber.

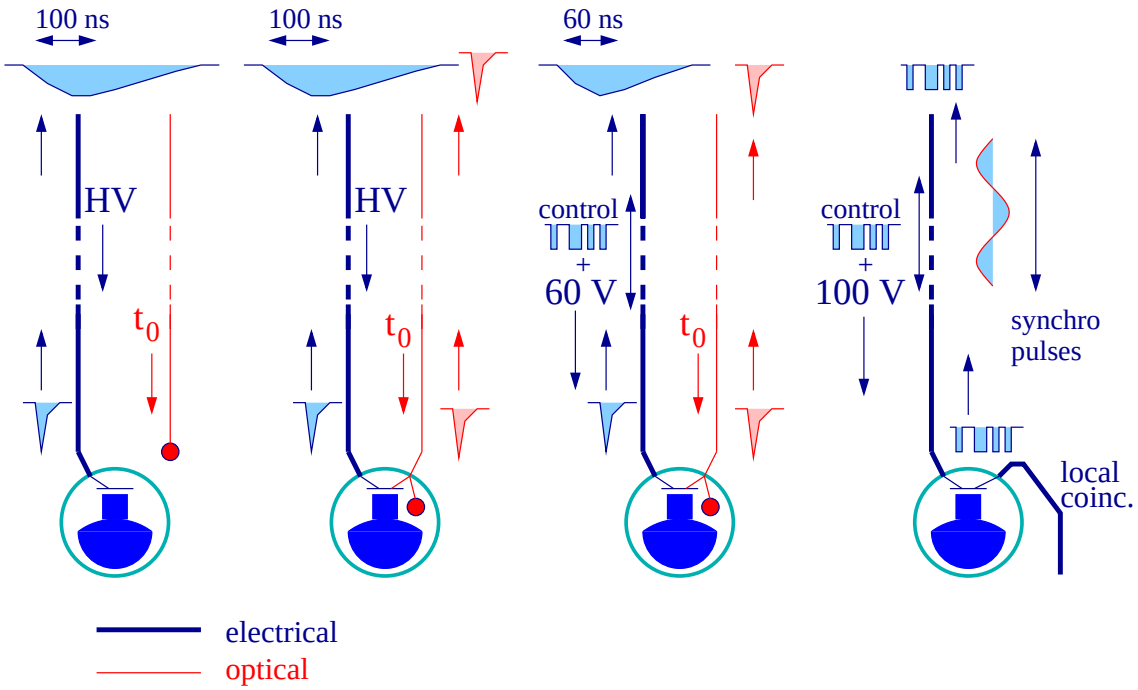

Figure 74: AMANDA OMs (from left to right): electrical signal transmission, passive optical signal transmission, active optical signal transmission (dAOM) and digital signal transmission (DOM).

Rightmost, the DOM is shown, which makes use of the same HV generator as the dAOM. The waveforms are digitized in the OM and transmitted to the surface via the electrical cable. Determination of the t0 offset and the synchronization between clocks at the surface and the OM are done using the electrical cable. There is no need for a fiber cable, which results in a savings of approximately \$1.8k hardware costs per channel; other significant but less direct savings, such as $\sim$30 fewer plane flights, deployment simplifications, etc., are also realized.

In the 1999/2000 season six strings (strings 14-19) with 42 (41) OMs each were deployed. Of the 251 OMs, 189 use an improved passive, analog optical transmission system (with electrical back-up). The PMT anode current that drives the LEDs is now amplified in the OM by a transformer circuit. The HV is supplied from the surface. The rest of the OMs use DC/DC conversion inside the OM. Twenty-three OMs were of the dAOM type, with 10 using LED transmitters and 13 using Laser Diode (LD) transmitters. Forty-one modules are of the DOM type. The DOM modules have been equipped with LEDs and fiber optic read-out for implementation in the AMANDA II DAQ. Both the dAOM and the DOM are operated at considerably lower voltages than the standard analog OMs. They did not show any significant gain loss during the year 2000.

8 Data Handling

Data from the IceCube sensors will be selected, reconstructed, filtered and analyzed to achieve the scientific goals of the project. The software used in this endeavor extends from firmware deep in the ice, through the DAQ, to the Data Handling, and finally into the analysis. In this section, we describe the Data Handling software and associated computing hardware.

The location of IceCube at the South Pole places special demands on what would otherwise be a straightforward software system. First, the Data Handling software must provide robust, fast and accurate filtering of the data in an essentially online environment. This is because IceCube's high data rate from downgoing muons results in a large data volume in spite of a small individual event size, and the satellite bandwidth for uploading data to the northern hemisphere is much too small to permit full raw data transfers. Second, the harsh environment of the South Pole and its inaccessibility for about nearly 3/4 of the year mean that "winter-overs" must be employed to maintain the detector. Since winter-overs will often not have expertise in all aspects of the detector, the interfaces used to control and monitor the Data Handling system at the Pole must be simple, user friendly, and battle-tested, and the associated computing hardware systems must be reliable and fault-tolerant. Third, in the absence of a centralized laboratory facility, and since the collaboration cannot meet as frequently as one might wish, it is crucial that interfaces between various subsystems are very well defined to allow for independent software development.

In sec. 8.1 we describe the general features of a Data Handling software system for the IceCube detector, and demonstrate that these features are available in existing software packages, or require no special techniques to custom build. Offline data flow is covered in sec. 8.2. The various streams into which we divide the data are discussed in sec. 8.3, and the way it is organized in sec. 8.4. Data latency requirements are described in sec. 8.5, and sec. 8.6 gives an outline of the schedule for implementation of the Data Handling system.

8.1 System Elements

IceCube data is similar to that of other high-energy and astrophysics experiments. In particular, the concept of uncorrelated triggered events allows us to reuse many of the tools and concepts of other projects. More generally, the IceCube data handling system can be built with current technology. The main elements of the Data Handling system are:

- software management;
- system engineering;
- development environment;
- analysis framework;
- database;
- visualization;

- development interface;
- integration at the Pole;
- hardware;
- data distribution.

These elements are discussed in the following subsections.

8.1.1 Software Management

The complexity of IceCube software and the dispersed nature of the IceCube collaboration strongly suggest the use of standard software management practices to organize communication, manpower, money, and project reviews. Industry software project management practices will be followed to implement the IceCube software.

Project-wide software management has several broad areas including oversight of:

- the DAQ real-time system,
- the Data Handling framework and database tools,
- the development of simulation, trigger and filter algorithms.

A common development environment and software architecture will be most efficient for both implementation and long-term maintenance.

Interfaces will be defined between subsystems and testing procedures established. Software professionals will be employed to build the database and network programs. Physicists will likely implement many of the procedures. To ensure robust operation, software consultants will be involved at every stage–the design phase, a construction or development phase, and finally a maintenance phase–and perform regular reviews of the code. The data will be stored for many years, and the analysis is anticipated to continue for up to 15 years. Long-term software maintenance must be considered.

8.1.2 System Engineering

System engineering involves identifying the most logical set of subsystems and specifying completely all interfaces between them. In broad strokes this defines the structure of the software project. Subsystem specification will then occur in parallel by people with appropriate software skills. The specifications will be reviewed to ensure overall system integrity.

A unified architecture minimizes the number of people needed for development and more importantly, long term maintenance. The main cost of architecture is in the initial stage of system engineering. Common interfaces will be used by all subsystems. Single implementations are easier to maintain and more flexible to replacement. In long-term projects, flexible application program interfaces (APIs) can be re-implemented as commercial products become old and better options become available.

8.1.3 Development Environment

A development environment is used to support the software development. Design tools, debuggers, etc. are needed in all stages of software development. In addition, both code and documentation need to be added, removed, and modified in an organized fashion by all developers. It is especially important for developers in different subsystems to be able to discuss the meaning of the specification and modify it as needed in a rational system. To save in overhead a common development environment will be used to implement IceCube software.

Design packages such as *Rational Rose* [162] or *SourceForge* [163] provide visual modeling tools which are useful for creating a blueprint of the software architecture, a critical first step in the design of a complex software system. We will evaluate such tools to determine which, if any, might suit our needs. If we opt for a tool that the collaboration is not familiar with, it will be important to provide training in its use. The freeware GNU debugger GDB, the GNU compilers for FORTRAN, C and C++, the source code manager CVS and the release management and distribution system based on RPMs are all standard in the physics community, currently in use in AMANDA, and meet our requirements for ease of use and effectiveness. Tracking and distribution of important design and technical documents can be accomplished with existing packages, such as the commercial EDMS system used at CERN [164].

8.1.4 Analysis Framework

The framework is used to define how users interact with pieces of data. It is a set of rules and methods for selecting data, applying algorithms and adding new information to the dataset. Several frameworks are under consideration including the CERN packages Gaudi, LHC++ and Root [165]. Importantly, these packages will be supported over the lifetime of IceCube.

Implementation of the framework for IceCube will include a flexible API to event, calibration and monitor data. Time correlation of these types of data will also be provided by the framework. For example, this allows an analyzer to correlate measurements of the South Pole environment with physics data. Data objects are stored in memory so that all algorithms act on the same data. The input data is protected from corruption by making copies of it as deemed necessary.

The framework also supports an arbitrary number of modular algorithms through a standard API. Algorithms may add or remove data from the data stream. A standard set of options is made available to select needed operational modes.

A users manual including documentation to the APIs is provided to ensure optimal user access to the data. Except for visualization components, all components support execution via batch mode.

8.1.5 Database

Organizational elements in the data sample are supported by one or several databases. Calibration, file/stream organization, and possibly event data are organized using database tools. The calibration and monitoring database contains all the information needed for reconstruction, simulation and analysis (like geometry, PMT gain, and OM status) but also slow control

information, hardware configuration, trigger status, and an electronic logbook. This database requires and is optimized for fast access through APIs by the software on the basis of the event time stamp. Quantities needed, for instance to define an OM status and calibration, are defined by a starting time and a validity time range. Its size, which depends on system stability and our chosen time granularity, is small enough to work on local copies regularly distributed to slave nodes. Access to the master copy is, of course, write-restricted. Multiple calibrations can be performed and checked with possibility for rollback.

A similar approach has been successfully developed and implemented for AMANDA-II using *MySQL*. Relational databases are well-suited for this kind of conditional (temporal) database. Many database managers using SQL exist and are well-tested. Commercial products like Oracle provide in addition a high level of security, advanced developing and managing tools and permit object-oriented interfaces to user software.

The file/stream organization database contains the complex data sample/stream organization. The large number of chunks into which data are sliced requires a database (most probably relational) to speed up random access of events. Placing the full sample of events in a large database is under consideration. For this kind of application, object oriented database management systems (ODBMS) like Objectivity are probably best suited and are used by large HEP experiments in the US (Babar) and Europe (the current choice of all LHC experiments at CERN). However, one must keep in mind that IceCube has a large number of events of small size and a simple event and detector structure. As a consequence, requirements are quite different from those needed for accelerator/general purpose detectors. ANTARES, which is quite similar to IceCube, uses Oracle, a relational database management system (RDBMS), instead of Objectivity. Yet another possible option is one of the object-relational database management systems (ORDBMS), like Oracle 9i.

The strong points of the ODBMS approach are: the database mirrors the structure of events and objects in the software, links and relations between objects are easier to modify, a lot of tools have already been developed by the HEP community, the user does not need to know where the data are physically located, and physics is done by event tagging instead of the usual miniDST/Ntuple strategy. On the other hand, there are also strong drawbacks to an approach that relies heavily on network performance and introduces large overheads which do not scale with the database size. Large-scale realistic tests are necessary to check that for IceCube where simple, well-tested solutions exist for event handling, this kind of ODBMS solution would confer a true benefit.

The database is designed so that it can be interfaced to and used for online, offline and Monte Carlo reconstruction and analysis. In any case, the physical organization of the database (internal tables, physical location on disk/tape) is designed to optimize data access. Graphical user interfaces and histogramming facilities to display and study database contents are provided. An adapter layer of software is used to plug the database into the analysis framework. Improvements in commercial databases and the support of a few carefully chosen file formats are expected to result in several database implementations and adapters. The framework and user interface are isolated from changes in the details of the database implementation via the adapters.

Benchmark tests were performed (using Linux on a 700 MHz PII and using TrueUnix on a 500 MHz Alpha) using a simple relational data base manager like MySQL with a 300 MB conditional (temporal) data base (corresponding to about six years of IceCube calibration/monitoring). Mean access time, based on a user key like "instant of validity" ranged from 0.5 to 5 ms for random search on randomly generated data depending on the cache state, demonstrating the feasibility of this approach. If it is decided that the full event sample is also stored in a database, the size of the sample may reach many terabytes (even after selection of a given physics stream). Even if careful organization of the data structure can keep the space overhead small, time overhead and data transfer time can become very large. Since database managers like Objectivity do not scale simply with the size of the data sample, large scale tests have to be performed before adopting such a solution.

Projected sizes of the individual database components are as follows:

- Calibration: 4800 OMs $\times$ 200 bytes $\times$ 5 calibration types $\times$ 5 times/year: 25 Mbytes/year.
- Monitoring: About 10 of AMANDA's 700 OMs change status each day. Extrapolating to IceCube with 4800 OMs, conservatively assuming that OM stability does not improve, about 50 will change status each day. Assuming a status change is described by 60 bytes: 2 MB/year.
- Slow control, configuration, trigger status: 1MB/year.
- Electronic logbook: 10 MB/year.
- File handling management: 200 bytes to describe file $\times$ 160 files $\times$ 360 days: 11 MB/year.

8.1.6 Visualization

Software tools will be provided to display the data in several forms:

- Dump events to screen in text format.
- Plot statistical distributions (PAW style).
- 3-D event visualization.
- Monitor plots showing trends in time.

8.1.7 Development Interfaces

Collaborators are anticipated to interact with the software at some level either as algorithm/filter developers or as users of the visualization packages. Developer physicists will have access to user manuals and local experts to aid in their work. Visualization packages will have user manuals, and commercial products will be used whenever possible to minimize the amount of specialized knowledge needed to work with the data.

8.1.8 Integration at Pole

Operation of the detector at the pole requires all processes be directed by an experimental control process. The online filters, trigger, disk, tape and satellite bandwidth need to be implemented within this system. Embedding the framework modules and data access (not necessarily natively) into the South Pole system is crucial to the smooth operation of the detector.

8.1.9 Hardware

Computers and storage are needed both at the Pole and in the northern hemisphere. A cluster of roughly 50 CPUs (with 1 GHz processors) is needed to satisfy the peak demand for quick turnaround post-deployment calibrations, and the steady-state demand for reconstructing and filtering 1.5 kHz of events. This cluster provides sufficient peak processing power to keep pace with deployments, and allows an ample 33 ms/event of processing to reduce the data by a factor of 30 down to 50 Hz. Several additional machines are needed at the Pole for satellite transfer, tape backup and disk cleanup. Four terabytes of disk is needed at the Pole for storage of thirty days' worth of raw files. A total of 500 tapes (at 100 GB/tape) is needed to store the full raw data sample each year, and 50 additional tapes for backing up the filtered data. In the northern hemisphere, the filtered and raw data are stored for > 15 years at 2 TB/year and 50 TB/year, respectively. A disk archive of 60 TB will be needed to cache 15 years' worth of filtered and simulated data. Several clusters totaling 300 CPUs (with 1 GHz processors) are needed to support the offline analysis. This cluster is used for data reorganization for the archive long-term access, additional reconstructions and filters, and simulations of background and signals.

The data from the Digital Optical Modules (DOMs) is transferred to standard 100BaseT network hardware once reaching the surface. From this point on requirements for computing, networking, and storage can be met by commercial hardware. The design of data flow in the hardware is modular, allowing for scalability and maximizing robustness. It is possible to make estimates of upper limits on data flow rates, and it is found that presently available commercial hardware will be adequate.

Once the data signals from the OMs are being transferred to a standard network, a cascading design of switches with redundant paths will be used. At 10 Tb/day transfer rate current 1 Gb Ethernet has orders of magnitude higher capacity than what we anticipate IceCube will require on average (tested using the NFS protocol).

The operating conditions at the South Pole dictate that certain measures are taken to ensure performance equal to a more standard working environment. The IceCube system is operated on UPS (Uninteruptable Power Supply) systems. This protects against transient power anomalies, and provides a grace period for controlled system shutdown if a power outage lasts longer than a user-specified period of time. Due to the high altitude at the South Pole, the effectiveness of air cooling systems is reduced. Most computer components are not specified to operate at this altitude. Also the very dry environment results in large static build up. Experience has shown that by using more aggressive cooling systems, careful anti-static handling techniques,

and routine discharging by numerous grounding strips, the same level of performance can be achieved as in a normal working environment.

Because of the physical isolation of South Pole for almost 3/4 of the year, and the limited personnel available during this period, the standardization of hardware with the support contractor to NSF is essential to obtaining the maximum level of mutual technical support, and efficiency in stocking spare components. This attitude has already been adopted by AMANDA and has been shown to provide many advantages not only to the science project, but South Pole support crew.

Storage The choices for large data storage are expanding rapidly with options such as Snap file servers, IDE RAID, FireWire disks arrays, and the more traditional SCSI RAID disk arrays. The system most suitable for IceCube is the SCSI RAID array. This system provides adequate storage size, reliability, and transfer speeds. A major advantage is that the main components, the SCSI disks, are standard throughout the whole systems. With the introduction of the Ultra 160 72 GB disks, arrays of 8 disks giving an overall size of 500 GB (access rates greater than 10 MB per sec through an NFS mount), or 4 days of uncompressed raw data. Two such arrays would be adequate for storage of raw and filtered data. Arrays such as these are highly reliable with hot swappable disks and power supplies resulting in operation being continuous even through hardware failures. Another advantage of using SCSI is that the tape drives have access to the data on the same bus, resulting in very high data transfer rates. Similar units are used as caches along the data flow chain to guard against data loss if the data flow is interrupted. All Data Handling hardware, including CPU, disk and tapedrives, fits into three standard-size racks.

Due to the unreliable nature of the satellites available for use at the South Pole, all *filtered* data is backed up on tape in the unlikely event that this data will need to be physically transferred north. Also, to guard against the possibility that a future technique requires re-filtering, tape copies of the raw data are made. Currently available tape technology such as SDLT (Quantum SDLT, 110 GB raw data at 22 MB/sec) is adequate for the maximum expected data rate of 130 GB per day. Using an array of 4 tape drives gives roughly one week between operator interventions. The filtered data and raw data are stored on separate tapes.

CPU Cluster Once built events are on disk storage they need to be filtered. This requires large amounts of CPU power and a means of controlling the priority of the filtering and other important tasks. This is a problem that the High Performance Computing community has been addressing for many years and a number of batching and load equalization systems are available. A system that is widely used, and which suits this situation well, is PBS (Portable Batch System). This is a very flexible system with a very large user base. It will give priority control over jobs, as tasks such as post-deployment calibrations and monitoring are given high priority, and ensures optimal use of the CPU resources. A large cluster such as this is accessed via one control node, with the rest of the system being easily expanded as required by the expansion of the detector, and or the use of more advanced filtering techniques. Very powerful, compact and inexpensive clusters are now available using dual CPU 1U rack mount machines.

The long period over which IceCube is installed and operated means the consequences of technology advances need to be considered. Such advances in the past have resulted in increased system performance at reduced cost, and size. More recently there has been a strong focus on increased energy efficiency and robustness. Thus, all future advances in technology work in the favor of IceCube, and restraints imposed by current hardware specification will only be relaxed and limited resources such as power and space will not be greater than what is estimated now. By standardizing on specific vendors early, upgrading hardware will be feasible and as straightforward as possible.

Hardware Monitoring Monitoring of the performance of the detector can be divided into two sections, the hardware health, and the state of physical characteristics of each device. The hardware layout of the detector is very modular, with only a few basic units being used. The characteristics of these basic units depends on their function. Disk storage has characteristics such as total storage used and available, and rate of change. The performance of networking devices can be measured by connectivity and response times. CPU nodes have characteristics of both a storage and a network device.

Modern hardware has the ability to monitor the physical health of a device, usually through a system monitoring bus. The Linux OS has software written to access this information, making it possible to quickly monitor CPU loads, temperatures, cooling systems, and power supply voltages. Other devices such as network switches use messaging protocols such as the traditional UNIX syslog system to make this information available.

As with other monitor information, the hardware status information will be entered into the data stream. A hardware monitoring process, as part of the overall monitoring package for the detector, will extract these packets of monitoring information from the data stream and display them in a graphical manner. Many such graphical systems already exist with features such as visual highlighting of system states and problems. During the hours of network connectivity to the South Pole, users will be able to examine the state of the detector as a function of time. This information will be regularly synchronized with a server which is always available for detailed examination both at the Pole and elsewhere. On-site users will be immediately notified of problems through an email pager system.

With the implementation of IceCube being over a period of years, it will be possible to test performance estimates of the system as it is scaled up. This will allow for adjustments and corrections before full operational mode is reached.

8.1.10 Data Distribution

Filtered data is transferred via satellite to a single location in the northern hemisphere. From there it is automaticaly copied via the internet to a designated IceCube institution in the US, where one or more backup copies are made and a standard set of data quality checks are performed. Checks are made to ensure that all the data from the Pole has been transferred completely and correctly, e.g., through use of checksums. Further tests investigate the quality of the data itself. Some of these tests are exactly the same as those performed at the Pole

to further check the integrity of the filtered data transfer. Other more detailed tests are also performed (these tests have not yet been defined).

The data is then copied via the internet to a few designated distribution centers in the US and Europe and additional tape backup copies are made. Ultimately, all the filtered data, at 2 TB/yr, reside on disk at each institution (or at centralized facilities shared by a small group of institutions).

The tapes of raw data are shipped north from the Pole at the beginning of each season to a location where at least one full copy is made. Each copy is stored at a different locations in Europe or the US for added safety.

8.2 Offline Data Flow

The DAQ system depicted in fig. 73 deposits data of several different origins into a disk cache at the South Pole. Triggered events with a size of about 1.0 kB are collected at roughly 1.5 kHz and are intermingled with monitor and calibration data. Triggered events are dominated by downgoing atmospheric muons. These figures can be used to estimate the total data from the detector: 130 GB/day or 50 TB/year. Since the satellite bandwidth is 12 GB/day, we must reduce the data volume by roughly an order of magnitude at the Pole. This reduction will be accomplished with specialized filters. The hardware required to implement these filters is described in sec. 8.1.9. In addition to the filtered data, we will also send monitor data and calibration data over the satellite. A sketch of the Data Handling system is provided in fig. 75.

Note that during the six-string first year, all raw data will be delivered to the northern hemisphere over the satellite for analysis and filter development, and taping at the Pole will only be used for data backup. The required bandwidth is estimated from the fraction of strings relative to the full IceCube detector and the estimated IceCube unfiltered raw data rate: $6/80 \times 130 \simeq 10$ GB/day. (AMANDA-II will also require satellite bandwidth of about 2 GB/day; the total required bandwidth remains below 12 GB/day.) Transferring the entire unfiltered raw data the first year gives the software developers additional time to develop a coherent system, and in particular to develop the robust online filters which will be required in all subsequent years.

A pre-filter raw data cache will hold 2 days' data so that correlations with GRBs and other external triggers can be studied. The post-filter cache needs to hold at least a week of data to handle failed transfers and satellite down times smoothly. We will avoid continuously saturating the bandwidth every day to further ensure that the transfer process can catch up with the data taking in a reasonable amount of time. Prioritizing data for transfer may be useful during recovery period.

After transfer, the filtered data will be cached for the indefinite future in a mass archive. Expected data size is 2 TB/year plus a comparable amount of simulated data. Additional processing will be provided as necessary to support the analysis working groups' access needs and use of the data. The CPU requirements for IceCube simulations are estimated from the desire to simulate a reasonable fraction of the background (e.g., 20%), and from an estimated 1 s/event IceCube simulation time. Table 11 lists bandwidth, CPU and diskspace requirements for IceCube. Data which is not transferred over the satellite will take over a year to receive

Process	approx. output bandwidth	1-GHz CPU requirements
event builder	1.0 MB/s	1
Pole filter	50 kB/s	45
online calibration	25 MB/yr	5
satellite transfer	12 GB/day	1
simulation	n/a	300
offline processing	< 50 kB/s	50

Cache (cache type)	cache size
30-day raw (FIFO)	4 TB
30-day filtered (FIFO)	330 GB
filtered data archive (permanent)	2 TB/year
simulated data archive (permanent)	2 TB/year

Table 11: Bandwidth, cache and CPU requirements for IceCube data handling. Note that the online calibration uses 5 CPUs only for the deployment period.

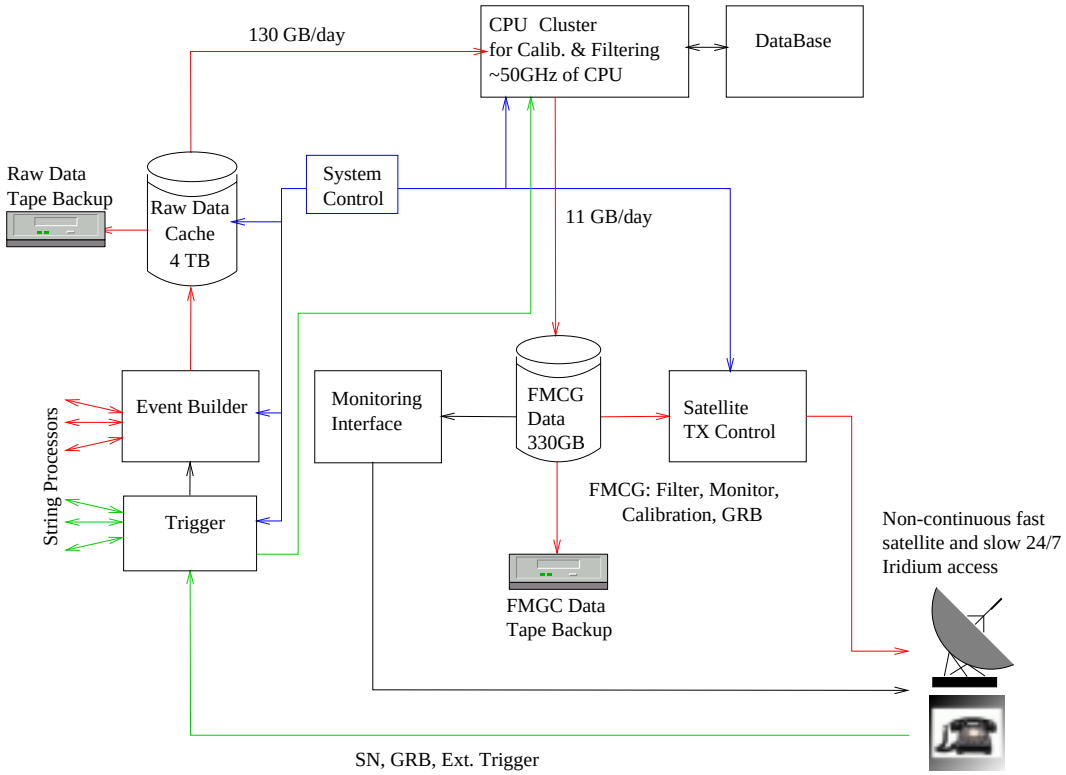

Figure 75: Diagram of the IceCube Data Handling system at the Pole. Arrows indicate direction of primary data flow, with data flow volume as indicated. The raw data is cached for filter processing and to permit extraction of raw data coincident with GRB (and other external) triggers. External triggers may arrive at any time if Iridium access is available. Raw data is permanently recorded to tape. Filter, monitor, GRB and calibration (FMGC) data are buffered to a small disk cache and transferred via satellite link to the northern hemisphere. With Iridium access, monitor data can also be uploaded to the northern hemisphere. FMGC data is also backed up to tape at the Pole. (See fig. 73 for a diagram of the upstream DAQ system.)

from the Pole, archive and filter. Since it is highly desirable and certainly feasible to perform filtering at the Pole, we are concentrating our efforts on such a system. There are several benefits which accrue from this decision. First, the data analysis can begin essentially right after data is taken, more than a year sooner than otherwise. Second, priority is placed on looking at the data immediately so that problems are detected and fixed promptly. Finally, we are concentrating our efforts on a single system from the start. To avoid having to refilter this data, it is imperative that this system works reliably. Note that the scenario in which filtering occurs only in the northern hemisphere has its own serious downside beyond its inherently longer latency: computing needs grow overwhelmingly large if we demand reasonably fast filtering turnaround times.

Tapes are used at the Pole to backup filtered data in order to deal with possible long-term satellite outages. Tapes are also used at the Pole to make copies of all the unfiltered raw data. All data written to tape is checksummed to help ensure data integrity.

In the northern hemisphere, the computing constraints are similar to those for any large computing project. Data samples of about 2 TB/yr are archived in a mass storage system for access. Distributed data needs to fit on user's facilities at their home institutions. Processing power needs to be somewhat centralized for big projects and otherwise distributed for accessibility to the analysis. Expensive software tools or licenses need to be purchased in such a way that all collaborating institutions can participate fully in the data analysis.

8.3 Data Model

The signal data will be separated with good efficiency from the downgoing muons using just a few selection criteria. These criteria are desiged to include overlaps between the filtered data sets to ensure that no valid data is lost. Table 12 lists a set of tagged data samples that are to be extracted at high efficiency from the downgoing muon background and the approximate satellite bandwidth required for each one. A short description of these samples follows in order to give correspondence between the data samples and the analysis topics. The purpose of describing the samples is not to solidify their description, but rather to indicate the level of background reduction we believe is necessary for this data model to work. Final available satellite bandwidth will not be known precisely for some time, and event size and event rate can only be estimated at this stage, but table 12 is sufficiently accurate to guide design work.

8.3.1 High Multiplicity

The IceCube trigger system will probably include some sort of majority trigger in which some number N of time-coincident hits fire the trigger. For some $M > N$, the trigger rate is sufficiently low to fit within the satellite budget. This sample is otherwise unfiltered. It supports the search for new physics at the highest energies accessible to IceCube. The other physics samples are devoted to the lower-energy analyses.

Data Samples	Required Tape Bandwidth (GB/day)	Required Satellite Bandwidth (GB/day)
Full Raw	130	
High Multiplicity	4.0	4.0
Upgoing Tracks	1.5	1.5
Cascade/tau	3.0	3.0
GRB downgoing Muons	1.0	1.0
Icetop	2	0.1
Supernova	0.1	0.1
Prescaled Raw Data	0.5	0.5
Monitor	0.1	0.1
Calibration (from *in situ* light sources)	0.1	0.1
Full-sky Summary Histograms	0.5	0.5
Total	$130 + 13 = 143$	11

Table 12: Summary of IceCube Data Samples designed to support the science goals. The two right columns indicate the tape and satellite bandwidths budgeted to each sample at this very preliminary stage.

8.3.2 Upgoing Tracks

Upgoing tracks are typically muons originating from neutrino interactions in or below the instrumented volume. Upgoing tracks can be selected by zenith angle after a quick reconstruction. Tracks may be triggered via either a global multiplicity trigger or a string multiplicity trigger.

Candidate upgoing muon tracks need further requirements imposed, such as a minimum path length that is greater than the string spacing, and a zenith angle $> 80^\circ$. The "line fit" angular resolution for short tracks is not good enough to reduce the misreconstructed background sufficiently. However, recent improvements in the speed of the likelihood reconstruction make it possible to include it in the Pole Filter. With a resolution online of roughly 2 degrees, misreconstructed background is eliminated much more efficiently. A similar cut on AMANDA data reduces the data by a factor of 100: (130 GB/day)/100 results in < 1.5 GB/day.

Events triggered by a string multiplicity trigger select nearly vertical tracks at lower energy than the previous selection. Additional selection criteria are a veto on activity elsewhere in the detector and timing profiles near the speed of light.

8.3.3 Cascades/Taus

Cascades are the result of electron-neutrino interactions and neutrino neutral-current interactions. IceCube triggers on them using some type of multiplicity trigger. Evidence that the events contain a core of light due to the large number of charged particles in the shower is required to separate them from the downgoing muons. Cascade energies need to be sufficient to light up several strings for analysis purposes.

Cuts on the spatial extent of the charged core may be used provided tau detection efficiency remains high. The high energy cascades, one of which is displayed in fig. 24, are of sufficient energy to be included in the high multiplicity sample. This sample is dedicated to the lower-energy cascade analysis.

8.3.4 GRB Downgoing Muons

To study Southern Hemisphere GRBs, one needs to keep all downgoing muons for a 10 min period around the GRB time. At the South Pole it takes a day or two to receive the GRB trigger times from other experiments, so the raw data needs to be cached for a minimum of 2 days. One external GRB trigger per day and saving 10 min of raw IceCube centered around the external trigger time corresponds to 1 GB/day required bandwidth out of the Pole.

It will be some time before another satellite is launched to provide these data as frequently as once per day. The next generation experiment may have a higher GRB notification rate. For the first few years, therefore, we expect the IceCube GRB bandwidth requirements to be much less than 1 GB/day.

A recent paper by Waxmann suggests that once every 40 years a supernova is close enough to produce about 100 muons in IceCube shortly after the event. Presumably this event would be very bright and we could search for it in the same way that we search for GRB.

8.3.5 Icetop

The IceTop array detects high energy cosmic ray shower events. These events typically have high multiplicity and are expected to include waveforms. Their estimated raw data rate is 1–2 GB/day, reduced to 0.1 GB/day after filtering.

8.3.6 Supernova

Supernova are expected to produce a large number of low energy neutrinos. The experimental signal is an increase in all the PMTs of about 100 photons over a 10 s period. This analysis requires us to record the PMT noise rates in 10 s bins for the duration of the experiment. This adds up to about 0.1 GB/day.

8.3.7 Prescaled Raw Data

A minimum bias sample of prescaled downgoing muons can be used for geometry and timing calibrations, to monitor detector stability, and as a test of background rejection algorithms used in other analyses. Taking this data at 4 Hz yields a data sample of 0.5 GB/day.

8.3.8 Monitor

Monitor data is used to measure the quality of the data and verify the stability of the detector over the lifetime of the experiment. Types of monitor data that we considered are: trigger, filter,

and reconstruction rates, temperature sensors, DOM RAP jitter, PMT gain, risetime, peak-to-valley, occupancies and noise rates, network activities, system deadtime, building power, UPS status, local weather conditions, and station parameters such as satellite status, drilling, and airplane landings. Measuring the DAQ related quantities once every 10 min seemed sufficient and contributes about 1.5 MB/day for each item monitored on 4800 PMTs. The 1 GB/day bandwidth allows us to measure 600 such quantities. Many quantities are recorded much less often, and some have fewer than 4800 channels.

There is no reason to limit the monitor data to activities at the Pole. The software is also designed to include monitor data from any post-processing filters as well. We will build on the AMANDA experience to implement a web-based monitoring interface and electronic logbook for IceCube.

8.3.9 Calibration

This sample consists of data from *in situ* light sources. This kind of data is triggered event data, although several different triggers may contribute. Triggering either from the light pulse or with coincident hits is possible. Our other calibration source is downgoing muons which will be available in the prescaled raw data.

Other calibrations, such as PMT gain and efficiency, may be generated in real time in the DOM firmware, and as such will already exist in the data stream. These calibrations need to be extracted and analyzed offline.

From various sources, calibration constants are compiled and stored for use by the reconstruction. Since constants may be modified as the analysis improves, a database implementation is the obvious preferred choice with version numbers to keep track of what has been done.

8.3.10 Full-Sky Summary Histograms

High energy photons are predicted to send showers deep into the ice, triggering the IceCube detector. Since this analysis requires sifting through every downgoing muon that triggers the detector, it would be too cumbersome to achieve without a predefined histogramming of the data. Full-sky summary histograms are therefore created every few minutes, resulting in 0.5 GB/day. From these histograms energetic point sources in the Southern Hemisphere may be discovered.

8.3.11 Unfiltered Raw

After the first year, all unfiltered raw data is written to tape at the Pole, hand-carried out of the Pole at station re-opening each November, copied and stored in at least two locations in the northern hemisphere. The limitations on the use of the raw data are described in sec. 8.4.

8.4 Data Sample Organization

Several tagged samples will be bundled into one "physics" stream. The physics stream includes the monitor, high multiplicity, upgoing tracks and cascade/tau data. They are distinguished

from one another by virtue of, for example, a set of bits in each data record's header. An actual data event, for example, may have both the bits corresponding to the high multiplicity and cascade/tau tags set. Monitor information has the monitor bit set, etc. It is a requirement that data from one of the above streams can be time-correlated with data from any other of the above streams. One possible way to implement this is to have all the data time-ordered and resident in one file, but other implementations are certainly possible. Time slicing may prove valuable as well. In this scenario, the data are sliced into chunks representing a short length of time (something like 10 s or 10 min). A database can then catalog the chunks, speeding up random access to the events.

Several obvious advantages accrue from this "bundled data" scenario:

- Monitor data is available at analysis time from within the same program used to analyze data, so one can imagine plotting not only (say) zenith angle of selected events, but also noise rates measured at roughly the same time the event occurred in the detector.
- There are not multiple types of files which need to be transferred from pole; the system is simpler overall.
- Prescaled raw data is also available at analysis time, making background estimation and monitoring detector performance with downgoing muons easier.

The size of the files is dominated by tagged physics events, so the additional data volume of the monitor data, prescaled raw data, etc. does not substantially increase overall file size.

An important point here is that we are saving the full raw data stream. In the six-string first year, the raw data are transferred over satellite for analysis and filter checkout. After that it grows too large for the satellite bandwidth, and we plan to copy it at the Pole onto tape. The estimated size of this sample is 50 TB/yr. The tapes are mainly envisioned as an insurance policy and we are only allocating resources for their archiving and no additional resources for their use. If a collaborator comes up with a compelling new analysis idea which requires data not present in the various filtered data sets, the first step will be to develop a new filter and install it at the Pole. In this way, current data is used to validate the new idea. After the new idea passes this test, the collaboration may decide to obtain the significant additional resources needed to refilter all the raw tapes.

8.5 Latency

Latency is defined as the time between when an event is triggered and when it arrives on an analyzer's disk. Data from the main analysis tags (high multiplicity, upgoing track, cascade/tau) should have a 1-2 week latency, which includes possible further processing/filtering in the north. Monitor data should have a latency of less than 24 hrs. Supernova data should have as close to zero latency as possible. One way to implement a very short latency time is to use the Iridium system (if it remains available). Data volumes for supernova triggers are small enough to make this feasible. IceCube can then be a full-fledged participant in SNEWS, the Supernova Early Warning System [48].

Possible uses of 24/7 low-bandwidth coverage beyond SNEWS include IceCube monitor data. This would have the clear advantage of allowing us to keep close track of detector performance, including during times when the winter-overs would be sleeping. This coverage would also be very handy for small system maintenance tasks and for sending alarms to to the winterovers. Obviously, the South Pole becomes much less remote with this kind of coverage.

After the first six-string year, the full raw data has a latency of at least a year, corresponding to the movement of tapes from the Pole to the north. For IceCube design purposes, the latency of this data sample should be considered infinite since the resources needed to use it are not in the current budget.

Another latency issue arises due to calibration constants (e.g., geometry) which will be needed by the Pole filters. We envision three categories of constants:

- initial constants: Within 2 days of deployment, crude constants should be available for the operation of the string. An example of this would be OM locations from drill logs.
- on-line constants: Within a week or two of deployment, the results of *in situ* light sources and downgoing muons need to be included for stable data taking.
- offline constants: As the analysis requires, constants need to be included in the database. Multiple sets can be supported with the use of version numbers.

8.6 Schedule

IceCube construction will take a number of years. A simplified first-light data model is used consisting of only a multiplicity stream, calibration and monitor data. The multi-sample modes and full online filtering machinery are realized in the second year of operation as more strings are deployed and the unfiltered raw data rate outstrips the available satellite bandwidth.

Software subsystem development must be prioritized, so that the first year's data is handled without having to deviate dramatically from the overall system design. We need to develop much of the infrastructure in the first year. Defining APIs completely enables us to produce needed subsystems without recoding later.

8.7 Summary

The IceCube Data Handling software system, though far from trivial, can be constructed using existing software tools and methods, and it can be realized using existing commercial hardware. To fully design and implement a reliable and robust system in time to analyze the data from the first six IceCube strings will require a substantial software design effort which is best managed by professional software engineers with experience in large scale projects like IceCube.

9 Data Analysis

9.1 Introduction

The main goal of the IceCube data analysis organization is to bring analyses to publication as quickly as possible while maintaining the highest possible scientific standards. To achieve this goal, the organization strives to ensure the infrastructure needed for analysis is provided and maintained, to use analysis manpower resources in an efficient and fair manner, and to oversee and streamline a rigorous internal analysis review process. Analysis infrastructure includes the three broad areas of detector calibration and data quality, signal and background simulation, and event reconstruction, and three working groups are formed to oversee these areas. Analysis infrastructure also includes computational resources, and large and small computer clusters are employed for data distribution, analysis and simulation purposes. Analysis manpower is organized into five separate working groups, each of which contains several separate but related analyses, so that ideas and methods can be shared easily among similar analyses. An Analysis Coordinator oversees the activities of all the working groups. The internal review process is managed by the Analysis Coordinator who, in consultation with the Collaboration Board, appoints a small committee responsible for bringing an analysis from the first draft stage to publication readiness and collaboration-wide approval.

9.2 Analysis Infrastructure

The analysis infrastructure is designed, constructed and maintained by three working groups, each led by its own Working Group Coordinator (WGC). The coordinators are responsible for ensuring that his/her group's responsibilities are fulfilled and for maintaining communications with one another and with the Analysis Coordinator. These working groups are as follows:

- The detector calibration and data quality working group;
- The simulation working group;
- The event reconstruction working group.

Given the vital importance of these tasks, both for performing viable analyses and for engendering a deep understanding of the IceCube detector, the associated workload is shared across the collaboration, and each institution is obliged to contribute manpower to one or more of these groups.

9.2.1 Calibration Analysis and Data Quality Working Group

The responsibility of this group is to collect, validate and install all detector-related constants needed for data analysis, and to continuously measure and help maintain data quality. This work includes, for example, the generation of detector geometry constants, measurement of ice parameters, and studies of detector response using *in situ* light sources, followed by installation of the resulting constants into the database. This work also includes the measurement and

analysis of quantities which track and improve data quality, such as the number of hot or dead PMTs, PMT noise rates, possible drifts in various online calibrations, and checks of overall data quality using downgoing muons.

Much of the output of this group is in the form of entries to the database. This database, described in sec. 8.1.5, is accessed by both the reconstruction and the simulation codes, and this group provides the appropriate software to make such access straightforward.

9.2.2 Simulation Working Group

The simulation working group is responsible for writing, supporting and documenting all required simulation programs. The group develops the software which simulates the response of the detector to charged particles emitting Čerenkov light, including but not limited to the simulation of ice parameters, photons passing through the ice, the PMT response, the DOM electronics, and the trigger. The simulation package is compared to data whenever possible to ensure that it is as close an approximation to reality as possible. This group also provides Monte Carlo generators for the basic science topics covered by the Physics Working Groups (see below).

9.2.3 Reconstruction Working Group

The reconstruction working group is responsible for writing, supporting and documenting the reconstruction programs for single muon tracks, multimuons, cascades, taus, contained events and the energy reconstruction. The reconstruction programs are created within the software framework provided by the Data Handling group.

9.3 Computing Infrastructure

Computing resources are needed for data distribution, data analysis and simulation. Two copies of all filtered data reside on disk in two post-filter clusters, one in the US and the other in Europe. This data amounts to roughly 2 TB/yr. In addition to the servers needed to control these disk caches, permitting ready access to all members of the collaboration, each cache also has an associated $\sim$50 GHz of CPU to perform additional filtering and/or reconstruction tasks. This cluster is built up in stages to match the rate at which data is acquired and to minimize the total expense.

Each FTE in data analysis is provided with a small "local" computing cluster (on the order of four machines with ample disk space and some peripherals, replaced every three years) for use in analyzing data. These clusters reside at each user's home institution, and are probably ganged together when multiple FTEs in data analysis are at the same institution.

Acquisition of a large cluster for simulating IceCube and IceTop data is also planned. The cluster also filters and caches this data. The nominal goal is to keep pace with the actual data rate. Assuming roughly 0.5 s/event/GHz-CPU for generation and simulation, this translates to a need for 800 GHz CPU power for the full detector. As with the post-filter cluster, this cluster is also built up in stages.

9.4 Physics Analysis

There are five physics data analysis working groups focussing on the scientific topics listed below. The divisions between the different working groups are not absolute and it will almost certainly be necessary to have collaboration between different groups. Each of these working groups is led by a Working Group Coordinator (WGC). The WGC is responsible for organizing the analysis work within his/her group, for scheduling and leading regular intra-group discussions, for overseeing the internal review of analyses, and for communicating regularly with the Analysis Coordinator.

- Physics Working Group 1
  - Atmospheric muons
  - Icetop

  This group develops the tools and the filters for analyzing muons coming from cosmic-ray interactions in the atmosphere. The use of the IceTop detector is very important for geometry and efficiency calibration of the IceCube detector. In addition IceTop is used as a veto detector for downgoing atmospheric muons. The group also does general air shower physics analyses.

- Physics Working Group 2
  - Atmospheric neutrinos
  - Neutrino oscillations
  - WIMPs

  This group analyzes the low energy charged-current muon neutrino interactions, including the atmospheric neutrinos, neutrino oscillations, and neutrinos from WIMP annihilations in the Sun and the Earth.

- Physics Working Group 3
  - High energy muon neutrinos (diffuse)
  - High energy muon neutrinos (point sources)
  - GRB muon neutrinos
  - Relativistic monopoles

  This group concentrates on analyzing the high energy charged-current muon neutrino interactions inside and outside the detector. It searches for high energy neutrinos from diffuse sources, point sources, GRBs and relativistic monopoles.

- Physics Working Group 4
  - Isolated cascades

  - Electron neutrinos
  - GRB electron neutrinos
  - NC events
  - Tau neutrinos

  This group analyzes high energy cascade events which could be due to electron neutrino interactions, neutral current neutrino interactions or tau neutrino interactions.

- Physics Working Group 5

  - Supernova
  - Seasonal muon rate variations

  This working group analyzes the Supernova data and Seasonal muon rate variations.

Certain general rules are followed to reduce experimenter bias in the analysis of data. Manpower permitting, analyses are done in parallel and independently by two or more groups. The collaboration may decide to insist that a particularly important analysis be done in this manner. Each analysis uses only a fraction of the available data to tune selection criteria, and only looks at the full data set when all selection criteria have been finalized. Certain analyses should also be "blind" such that the analyzer cannot tune selection criteria to enhance known source directions or times. For example, in a point source search one could alter reconstructed directions in a deterministic but hidden way, and only after the analysis is finalized are the true directions used.

The Analysis Coordinator presents a report at each collaboration meeting giving an overview of the status of each working group and its analysis work. Working Group Coordinators may also be requested to give reports depending on the circumstances.

9.5 Internal Review Procedure

9.5.1 Introduction

Analysis results produced in the different working groups should be approved for submission to refereed journals and presentation at conferences with a minimum of administrative delays, while at the same time rigorously checked to ensure the highest possible quality. The Analysis Coordinator has the primary responsibility for this important task.

9.5.2 Procedure

The first venue in which a data analysis is discussed is within the appropriate Working Group. This discussion is led by the WGC, and eventually results in the production of a document detailing all aspects of the analysis. The level of detail should be such as to enable anyone in the collaboration to repeat the analysis, with all systematic studies described and presented in

detail. All documentation produced in the Working Groups is made available to everyone in the collaboration.

For parallel analyses where disagreement arises, or in other instances of disagreement, the WGC attempts to resolve the issue. If the WGC cannot, the Analysis Coordinator tries to do so. Ultimately, the Collaboration Board may be asked to intervene.

The next step is production of a first draft for publication. At this point, the Analysis Coordinator appoints a paper committee. This committee consists of a small number of collaborators, preferably including some from outside the Working Group in question, to conduct the internal review of the analysis and to shepherd it from first draft to publication readiness. The Analysis Coordinator also appoints one or more primary authors if there is no obvious person for the task.

Once the paper committee is satisfied with the quality of the analysis and paper draft, the draft is submitted to the collaboration for criticism and, eventually, approval for submission to a refereed journal. Final approval for submission to a refereed journal is given by the Collaboration Board.

9.6 Prerequisites and Schedule

IceCube data analysis obviously requires filtered data, which depends on numerous aspects of the data handling machinery to be in place, and on geometry and other low level constants placed into a functioning database. The analysis framework software must be functioning. The post-filter clusters must be operating. The simulation framework and generation software must be capable of simulating background and signal events, and the simulation cluster must be operating. Basic monitoring information is required to permit verification of data quality. The data analysis management structure should be in place.

Initial analysis efforts will focus on verifying overall detector performance in order to demonstrate clearly that IceCube is a functioning neutrino telescope. With this in mind, analysis of atmospheric muons, especially in conjunction with IceTop, and analyses of atmospheric electron and muon neutrinos, would all be a high priority.

Subsequent effort will focus on those analysis topics that do not require substantial numbers of strings to get started, such as searches for WIMPs, monopoles, supernovae, and extremely high energy cascades. Analysis topics relying on more strings, like searches for ultrahigh energy muons and cascades from point sources and diffuse sources, searches for ultrahigh energy tau neutrino interactions, and IceTop composition studies would follow.

10 Drilling, Deployment and Logistics

10.1 Drilling

10.1.1 Introduction

For decades glaciologists have used hot water drilling for rapid access to the inner workings of glaciers. Though both hardware and energy intensive, hot water drilling provides the fastest and most efficient way to access the deep ice. Water is also the ideal drilling fluid for the IceCube application. It is readily available, the hole is self-healing since the ice returns to essentially its original condition after the deployment of the detectors, and its optical properties meet the experimental requirements. Importantly, this technique is the only drilling method capable of meeting the hole straightness requirement. Finally, components used to operate the system are standard, reliable, and readily available from industrial outlets.

IceCube holes will be drilled with the Enhanced Hot Water Drill (EHWD). The EHWD represents an evolution of the AMANDA drill, which was a research tool, to a production drill capable of drilling 16 holes per season with 60 cm diameter to a depth of 2450 m. We have used data gathered from drilling 23 holes for the AMANDA project to depths varying from 1000 to 2400 m to design a drill enabling us to drill and instrument a hole every 3.5 days.

Conceptually, hot-water drilling is as simple as it sounds. Water is pumped at high pressure through a heating system and heated to near boiling temperature. The water is then forced through a drill nozzle that directs a high-velocity stream of hot water against the ice in the hole, melting it. The drill is steered by gravity.

Hot-water drilling is energy intensive because of the large amount of energy associated with the ice-to-water phase change. This distinguishes hot-water drilling from the more energy-efficient, but much slower ice-coring method.

A hole with a 60 cm diameter and, for instance, a 1 m depth has a volume of 78 gallons. With South Pole ice at -40°C, an equal volume of 100°C water is required to melt this volume of ice. To achieve this in one minute, or drill at a rate of 1 m/min, requires 2 MW of heat. After accounting for heat losses to the ice surrounding the hole, we conclude that a 5 MW system is required to drill at an average rate of 1.5 m per minute. With this rate the EWHD can deliver IceCube holes to 2400 m depth in 40 hours with 7000 gallons of fuel. This can be seen as follows:

- One gallon of fuel can produce enough heat to produce about 80 gals of hot water at 100°C. When burner efficiencies of 80% and the efficiency of conversion to electrical power are included, this the number reduces to 50 gal of water per gallon of fuel.

- A 2450 m deep hole contains 190,000 gallons of water. To melt this amount of ice at 50 gallons of water per gallon of fuel requires about 4000 gallons of fuel. Since the overall efficiency of the drilling process is 35% (half of the heat escapes into the surrounding ice without melting it), we calculate that a hole will require 7000 gallons of fuel to drill. The drilling time is 40 hours.

The relevant drilling parameters are pressure, flow and temperature. The heat delivered is the product of flow and temperature. For constant pressures this flow varies as (hose diameter)$^8/3$ and therefore this important parameter drives the performance of the EHWD system.

The conclusions presented above are buttressed by the wealth of data acquired with experimental AMANDA drills.

While hot-water drilling is conceptually simple, meeting the power requirements for safe and reliable drilling operations can be quite challenging. Drilling holes at the rate proposed to 2400 m depth requires the design, construction and operation of a major industrial complex in a hostile environment. We list below the salient features of a hot-water drill system meeting our requirements.

10.1.2 Evolution of AMANDA Drills

Initially, the AMANDA drill was designed to provide holes to 1000 m depth for the deployment of 10 in bathyspheres and the 1.5 in diameter cable connecting them to the surface. This was accomplished with 1 MW of heat delivered through the largest commercial synthetic hose available (1.25 in). Drilling time was about 70 hr using 4500 gallons of fuel per hole.

The current AMANDA drill was designed to drill to 2000 m. It requires three hose reels to hold hose reaching this depth. The heat input to this drill was increased to 2 MW. While drilling in the upper portion of the hole with only one reel of hose connected into the system, high flow rates and rapid drilling rates were achieved. Even though the ice is about 25°C warmer near the bottom of the hole, the flow rate decreases significantly due to friction with the hose wall. With reduced flow rate, most of the heat is lost through the hose wall before reaching the drill head. Thus, in the lower part of the hole, drilling is very slow as a result of the delivery of low-pressure cool water to the drill nozzle. To drill efficiently, the heat delivery to the drill head at 2450-m depth should be comparable to the heat delivered by the drill at the top of the hole. Three holes were drilled to 2450 m with substantially increased fuel consumption and drilling times. Drilling to 2400 m required 120 hours and 13,000 gallons of fuel, demonstrating that the drill had reached a practical limit. In summary, the current AMANDA drill system is capable of drilling only four of these holes per season at these fuel consumption rates and would require 150 hours of drilling time per hole. The current drill also requires several weeks to build-up and build-down each season, limiting actual drilling to about six weeks per season.

10.1.3 Performance Criteria and Design of the EHWD

Requiring that the heat input achieved with the AMANDA drill is doubled and a constant water flow is maintained through the entire drilling process, both of which are possible only with a single-reel design, one can extrapolate from drill data collected during the first 1000 m of AMANDA drilling. This extrapolation indicates that drilling to a depth of 2400 m can be achieved in 40 hrs while consuming about 7000 gallons of fuel per hole, corresponding to a savings of about 400,000 gallons of fuel for IceCube's planned 80 holes. Note that faster drilling is inherently more efficient because less time is spent warming surrounding ice. This

extrapolation matches our earlier estimate based on the thermodynamics of the problem.

To deliver the required heat without increasing pressure, the hose size must be increased from 1.5 in to 2.5 in diameter. The hose must be mounted on a single large hose reel to eliminate the 8 hr hose reel changes currently required for each hole during drilling and drill extraction. The drill components are housed in mobile drilling structures that can be quickly towed into place and integrated, so that the drill build-up and build-down time must be reduced to a total of about three weeks, permitting the drilling of 16 holes during an approximately 75 day field season.

To improve fuel consumption we need to drill the holes quickly, particularly in cold ice. This requires more heat at the drill nozzle. The amount of heat delivered to the drill nozzle is a function of the hose diameter (given the desire to avoid hose pressures greater than 1000 psi). The velocity of the water in the hose must be kept above 10 ft/s to avoid losing too much heat through the hose wall.

The discussion of the requirements above shows that, relative to the present AMANDA drill system, the general design criteria of the EHWD are:

- Higher efficiency
- Higher heat generating capacity
- Greater heat delivery capability

Additional design criteria are set by the need to:

- Drill 16 holes per season (IceCube proposal requirement)
- Reduce fuel consumption to 7000 gallons or less per hole

Other objectives are:

- Increase efficiency to minimize fuel consumption
- Increased reliability
- Decrease the work load for the drill crew
- Decrease the time to set up and take the drill apart
- Improve mobility to cover the square kilometer array
- Maintain a high degree of safety

To achieve a drill design that meets these requirements, each major subsystem must be designed accordingly. The major subsystems of the drill are:

- Power Generation Subsystem
- Preheating Subsystem

- Main Heating Subsystem
- High-Pressure Pumps Subsystem
- Heat Delivery Subsystem
- Drill Head

The ways in which these drill subsystems will meet the various efficiency, speed, and heating generation and delivery requirements are detailed below.

Power Generation Subsystem

- Efficiency: Two efficient (12 kWh per gallon of JP-8) 400 kW generators (one on line, one in standby) will provide all electric power for the drill during drilling and deployment operations; two 60 kW generators will provide all electrical power during non-drilling operations. By comparison, the AMANDA generators produce only about 7 kWh per gallon of fuel. Thus, the new generators are about 54% higher in efficiency. Waste heat recovery for supplementing preheating plant and Rodriguez well heat requirements are included in the design. Waste heat recovery is expected to save eight gallons of fuel per hour.
- Faster Build-up and Build-Down: The generators will be sled-mounted and will have fuel, water and electrical quick-connects for rapid integration during build-up and reduced build-down time.
- Greater heat generating capability: Waste heat recovery will recover about eight gallons of JP-8 equivalent per hour of drill time.
- Greater heat delivery capability: not directly applicable. However, the main generators are sized to provide the additional power required to electrically drive two new high-pressure pumps added to the high-pressure pumps subsystem, as well as replace the two diesel drives on the two current AMANDA high-pressure pumps. This more than doubles the generator output requirements of AMANDA.

Preheating Subsystem

- Efficiency: The Preheating plant provides about 25% of the total heat generation of the drill. Waste-heat recovery heat will supplement the heat generated by high efficiency (80%) fuel-fired heaters.
- Faster Build-Up and Build-Down: The Preheating subsystem will be located in sled-mounted Mobile Drilling Structures having fuel, water and electrical quick-connects for rapid integration during build-up and reduced build-down time.

- Greater heat generating capability: The Preheating Plant will provide enough heat generating capability to increase the 200 gallons/min return and makeup water from near-freezing to approximately 70°F. This is approximately double the AMANDA capability.
- Heat Delivery: The pumping capacity of circulator and transfer pumps will move about twice as much water per minute as in the AMANDA drill. About 200 gallons/min of 70°F water will be supplied to the suction side of the high-pressure pumps.

Main Heating Subsystem

- Efficiency: The design requirement is 80% minimum. Reusable AMANDA heaters will be refurbished as necessary to achieve this design efficiency.
- Faster Build-Up and Build-Down: The Main Heating subsystem will be located in four sled-mounted Mobile Drilling Structures having fuel, water and electrical quick-connects for rapid integration during build-up and reduced build-down time.
- Greater heat generating capability: The EHWD must heat 200 gallons of 70°F water to 190°F per minute, twice as much as the AMANDA drill. The EHWD has twice as many heaters as AMANDA's main heating plant.
- Heat delivery: The inlet and outlet plumbing has been increased from 1.5 in to 2.5 in to accommodate the increased flow.

High Pressure Pumps Subsystem

- Efficiency:The high-pressure pumps are the same as AMANDA's, but four will be required instead of two for AMANDA. However, the inefficient diesel drives (about 7 kWh per gallon of fuel) will be replaced with electric drives. Since the new generators will deliver about 12 kWh per gallon of fuel and assuming an electric drive efficiency of 90%, the efficiency is expected to improve by about 54%.
- Faster Build-Up and Build-Down: The High-Pressure Pumps subsystem will be located in a sled-mounted Mobile Drilling Structure having water and electrical quick-connects for rapid integration during build-up and reduced build-down time.
- Heat delivery: The number of pumps will be doubled and the inlet and outlet plumbing must be increased from 1.5 in to 2.5 in to accommodate the increased flow.

Heat Delivery Subsystem The Heat Delivery Subsystem includes the high-pressure hose and the hose reel.

- Efficiency: The hose is increased from 1.5 in inside diameter to 2.5 in to accommodate the increased flow and decrease the heat loss through the hose wall.

- Faster Build-Up and Build-Down: a single hose reel will hold the hose between the drill head and hose reel (about 10,000 ft) instead of three for AMANDA. This reduces the number of sled-mounted components by two.
- Heat delivery: The hose is increased from 1.5 in to 2.5 in to accommodate the increased flow.

Drill Head

- Faster Build-Up and Build-Down: housing to be constructed of aluminum for lighter weight and easier handling.
- Heat delivery: The nozzle size is increased to accommodate the increased flow.

10.2 Deployment

10.2.1 Overview

The installation of optical modules (OMs) in the ice is referred to as string deployment. In a wider sense the string deployment includes the preparation of the string hardware at the South Pole and the termination of the string in the IceCube counting house. Once the borehole of approximately 50 cm diameter is drilled (melted) into the ice, the drill is removed from the hole and the site is available for the string deployment. From that moment on, the water column of 2400 m depth begins to refreeze. The refreeze process is complete after about 5 days. However, already after about 24 hrs the diameter of the water column shrinks to a diameter comparable to the size of the OMs. The OMs must reach their final position before the water column becomes too narrow. Figure 76 shows an image taken with a TV camera, which was deployed with an AMANDA string. The glass sphere shown in the figure was deployed for demonstration purposes only. Its diameter was 10 in, which is less than the 13 in spheres used for the OMs. Nonetheless, it can be seen that in this case the water column was much larger than needed, and therefore that more fuel was used to drill the hole than necessary. An engineering project called *Smart Drill* is underway to optimize the drilling by maintaining an adequate hole diameter while minimizing fuel consumption.

The deployment coordinator must decide how much time is needed for the deployment. The drill team must provide a hole that meets certain requirements. These requirements and the protocol of the hand-over are discussed later. Once the hole is released for deployment the countdown starts. After this moment the time constraints for the string deployments are absolute and unforgiving. In the worst case scenario a string can get stuck in the ice at a shallow depth where it is of little or no scientific value.

10.2.2 AMANDA Experience

AMANDA deployed a total of 23 strings to depths between 1000 and 2350 m. The chronology of deployments is listed in table 13. The importance of the experience and expertise obtained in

Figure 76: Video image taken during deployment of string 13.

Year	Mission	Strings	OMs/string	Depth (m)	Duration (h)
93/94	AMANDA-A	4	20	1000	13-18
95/96	AMANDA-B4	4	20	2000	15
96/97	AMANDA-B10	6	36	1950	12-15
97/98	AMANDA-II	3	42	2350	18-21
99/00	AMANDA-II	6	42	2020	10-15

Table 13: Chronology of AMANDA string deployments.

Figure 77: Installation of an OM.

five AMANDA expeditions with string deployments cannot be overestimated for future IceCube deployments. The first deployments of strings to a depth of 1000 m were of an exploratory nature. Over time, the number of OMs per string increased from 20 to 42. In addition, the complexity of the OMs themselves increased. Optical modules on strings 11 to 19 of AMANDA-II use both electrical cable and optical fibers for signal transmission. For the DOM string (string 18) a more complex connectorization scheme was used. A total of 3 winches were operated simultaneously for all AMANDA-II deployments. During the 99/00 field season the installation time was as little as 8 min per OM, despite the enhanced complexity. In fact, the overall deployment time for the strings remained approximately constant for all strings while the number of OMs per string and OM complexity increased. This was accomplished due to a steady improvement in the deployment procedure.

10.2.3 AMANDA Deployment

The basic components of a string are the main cable and the OMs. The OMs are attached to the cable for the first time at the South Pole. There are no test installations prior to the shipment of these components to the South Pole, so precise specification and quality assurance procedures of all components are critical for a successful deployment.

Figures 77-79 illustrate the important components of the deployment sequence. Three people work on the actual installation of the OM on the main cable. In total, a minimum of 7 people are needed for a deployment. For each OM the tension on the main cable is temporarily transferred to the tower winch cable. Then the OM is integrated in the main cable and the tension is transferred back to the main cable. The OM is now integrated into the main cable.

Figure 78: An OM ready to be lowered into the drill hole.

Figure 79: An OM being lowered into the drill hole.

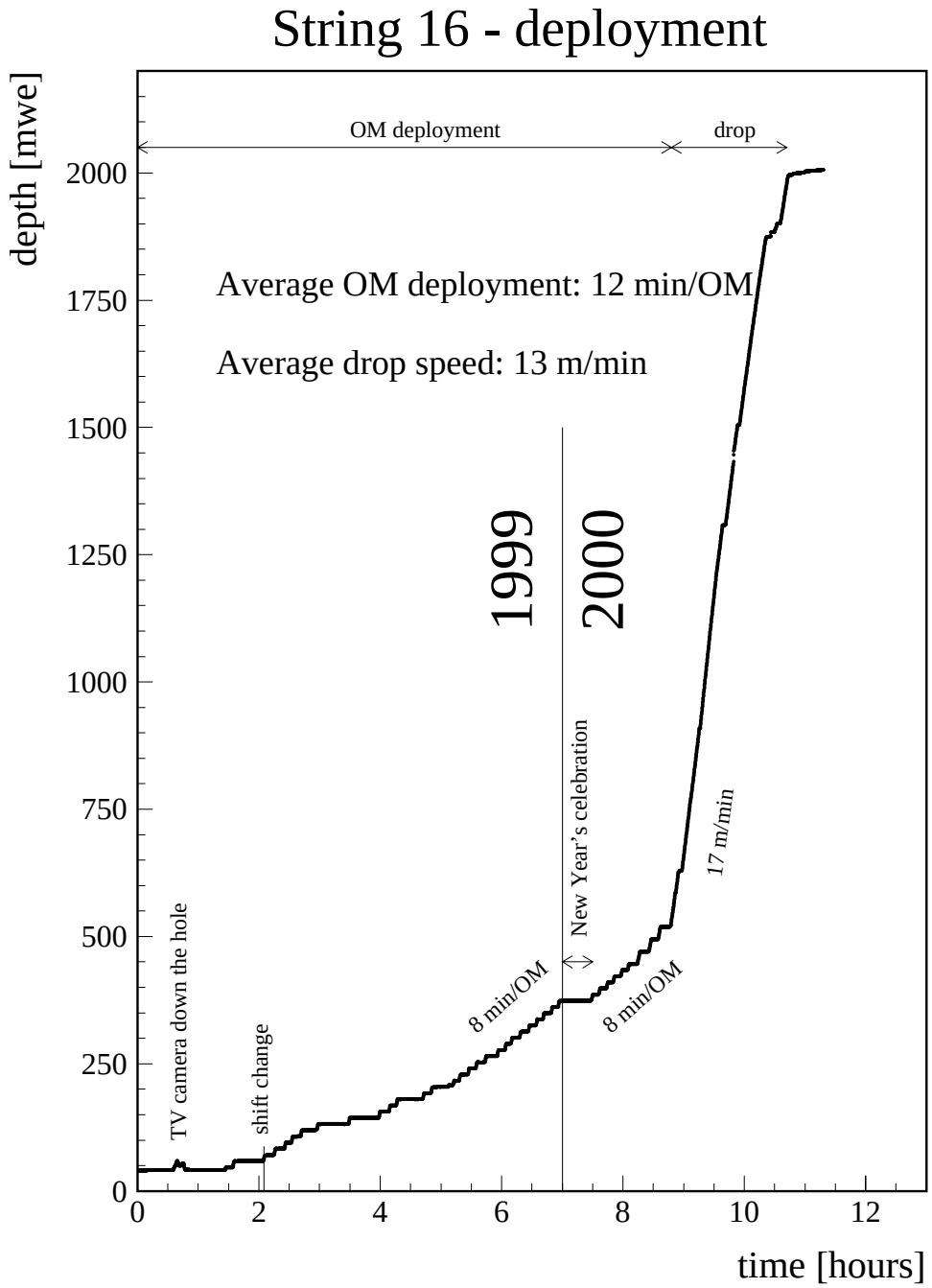

Figure 80: Deployment of AMANDA string 16. The depth, as measured by a pressure sensor, is plotted versus time. For this string the OM installation time was less than 10 hrs. The drop takes about 2 hrs.

Figure 80 shows the progress of the deployment with time. A pressure sensor mounted to the bottom of the string monitors the depth of the string. The drill hole is filled with water up to a level of about 50 m below the snow surface. The pressure begins to increase strongly after the sensor reaches the water level. The pressure sensor is the primary measure of the absolute depth of the string. Other measures are cable marks and possibly a secondary pressure sensor. Each stop corresponds to the installation of on OM. The deployment reached speeds of 8 min per OM. Once all OMs are installed the pressure corresponds to about 350 m water equivalent pressure (the length of the instrumented portion of the string minus 50 m at the top). Now the "drop" begins. The string is lowered to its target depth at a speed of approximately 15 m/min.

10.2.4 IceCube Deployment Overview

A diagram of the full IceCube deployment setup, depicting the counting house, the surface cable, an IceTop detector module and the down-hole cable, is shown in fig. 81.

The mechanical installation of the OM is illustrated in fig. 82. The OMs are attached to the main cable below and above as shown. A chain with a shortening clutch allows adjusting the length to a precision of 1 in. This design is identical to that used on AMANDA strings 14 to 19 and is well understood.

Each OM is connected electrically to the cable via twisted quad cable breakouts at every fourth OM position as shown in fig. 83. Each twisted quad cable consists of 2 twisted pairs. Each twisted pair provides 2 OMs with power and communication from the surface. Figure 84 illustrates how 4 OMs are connected to the main cable. The OMs are spaced by 17 m. Thus, there will be a breakout of a quad cable every 68 m. A wiring harness will be used as an interface between the twisted quad breakout on the main cable and the OM.

10.2.5 IceCube String Deployment Procedure

The requirement to deploy 16 strings with 60 OMs each in a single season, particularly in view of South Pole population constraints, requires a further improvement of the deployment operation. During the AMANDA deployments, the shortest time between the start of two subsequent deployments was 120 hr. For IceCube the average deployment cycle time will be 84 hr for a period of about 60 days, excluding 5 days of down time. The increase in the efficiency is possible by optimizing every single element of the deployment procedures, in particular in the pre- and post-deployment activities.

The digital signal transmission based on the design of the DOM allows a significant change and simplification of the deployment procedure of IceCube strings. No optical fiber cables will be required. Thirty twisted pair cables will provide power and signal transmission for 60 OMs. The absence of optical fibers reduces the cargo by about 9000 lb per string, and simplifies test procedures prior to and during the deployment. (During deployments of AMANDA strings 11-13, problems were encountered when the breakouts of fiber cables and electrical cables did not match up. These phasing problems were one of the reasons why the deployment times were

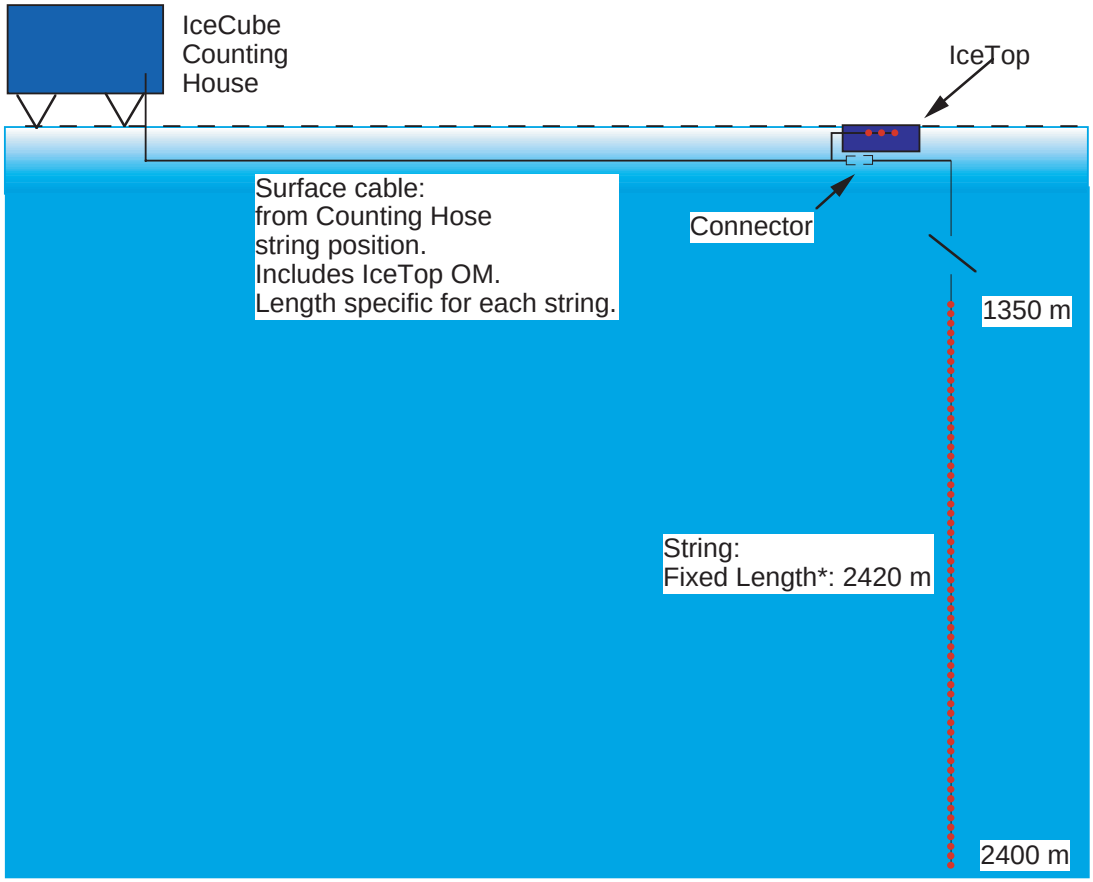

Figure 81: Schematic view of the string, the surface cable and an IceTop detector.

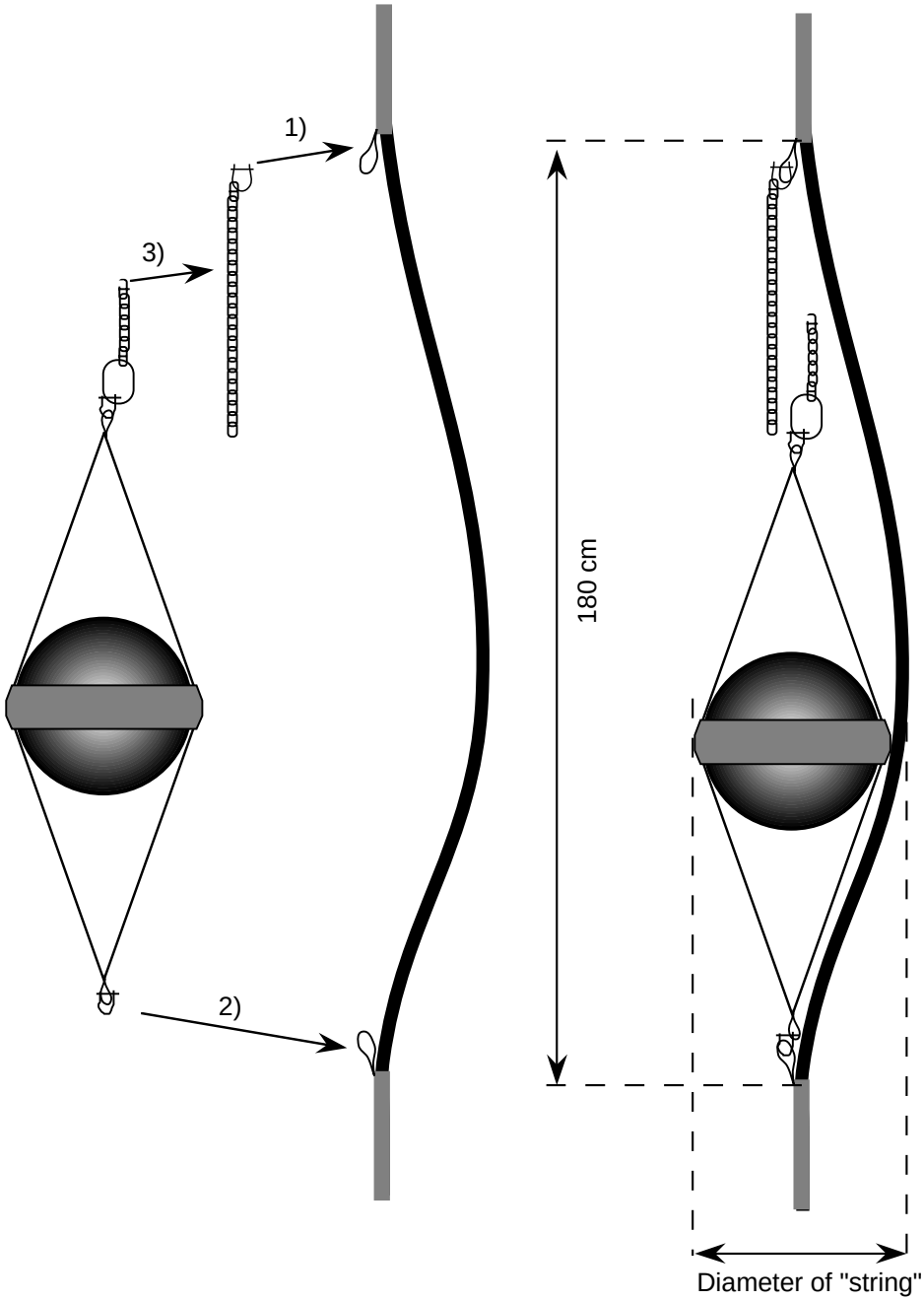

Figure 82: Mechanical integration of OM into the main cable.

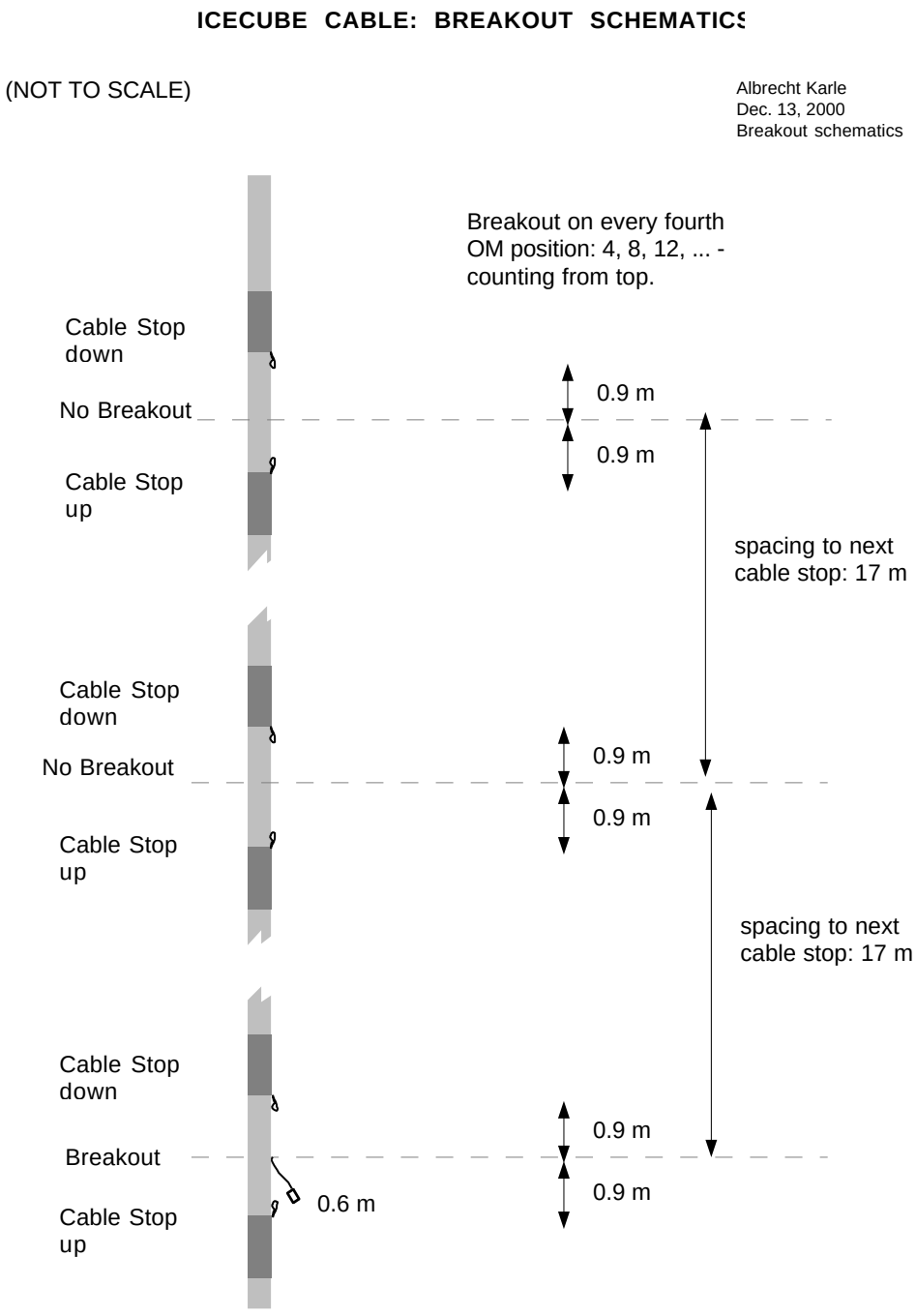

Figure 83: Breakout schematics on main cable. Pre-installed cable stops are used to mount the OMs. A twisted quad is broken out at every fourth OM position.

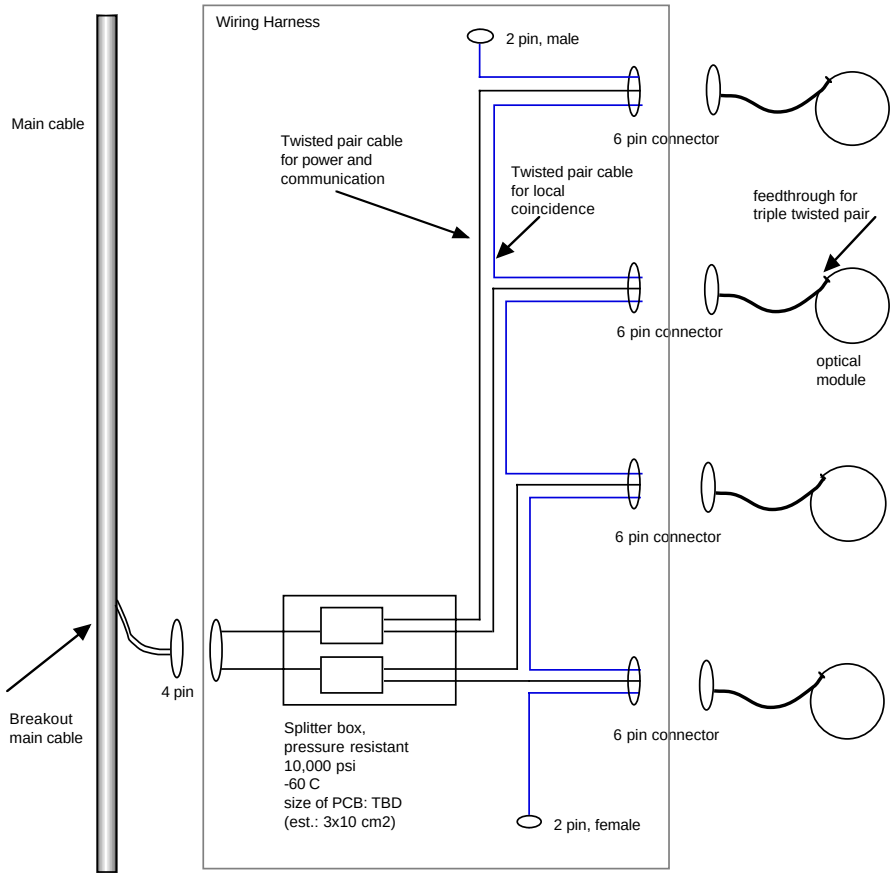

Figure 84: A group of four OMs is operated through a single twisted quad.

particularly high for strings 11-13. The phasing problems were solved in the 99/00 campaign. The deployment with a single cable, of course, means such phasing problems cannot occur.)

The phases of string deployment are as follows:

1. Install weights (600 lb);
2. Install 60 OMs;
3. Lower string to its target position at 2403 m.

Several pressure sensors on the string are used to monitor the correct motion of the string. Communications and power to the pressure sensors and to the newly connected OM is provided through a slip ring mounted at the cable winch. The actual payout of cable will be measured at the surface. The measured payout at the surface and the pressure increase at the bottom of the string will be monitored for consistency. The correct electrical connection of each OM is verified at time of installation. A short electronic test sequence of no more than a few minutes is performed at this time. Additional communication tests to the recently installed OMs can continue for a few more minutes.

10.2.6 IceCube Indoor Deployment

The shelter at the deployment site is very important for high quality OM installation at a rate of 2 strings per week. In the past, these shelters consisted of simple wind shields or a tent structure. Figures 85 and 86 show the dome structure that was used for AMANDA string 14-19 deployments.

For IceCube a heated building (see figs. 87–90) coupled to the drilling apparatus will be used as a deployment facility. This approach will improve the work conditions for the deployers substantially. All deployers work indoors. The electronics control room is inside this building but separated by a wall with large windows. The building is large enough to bring all or at least most of the OMs inside prior to the deployment. A furnace will replace noisy bullet heaters and eliminate exhaust near the work site. The ceiling may be partially transparent to take advantage of solar power and light. This building will also serve as a drilling shelter during the drill operation.

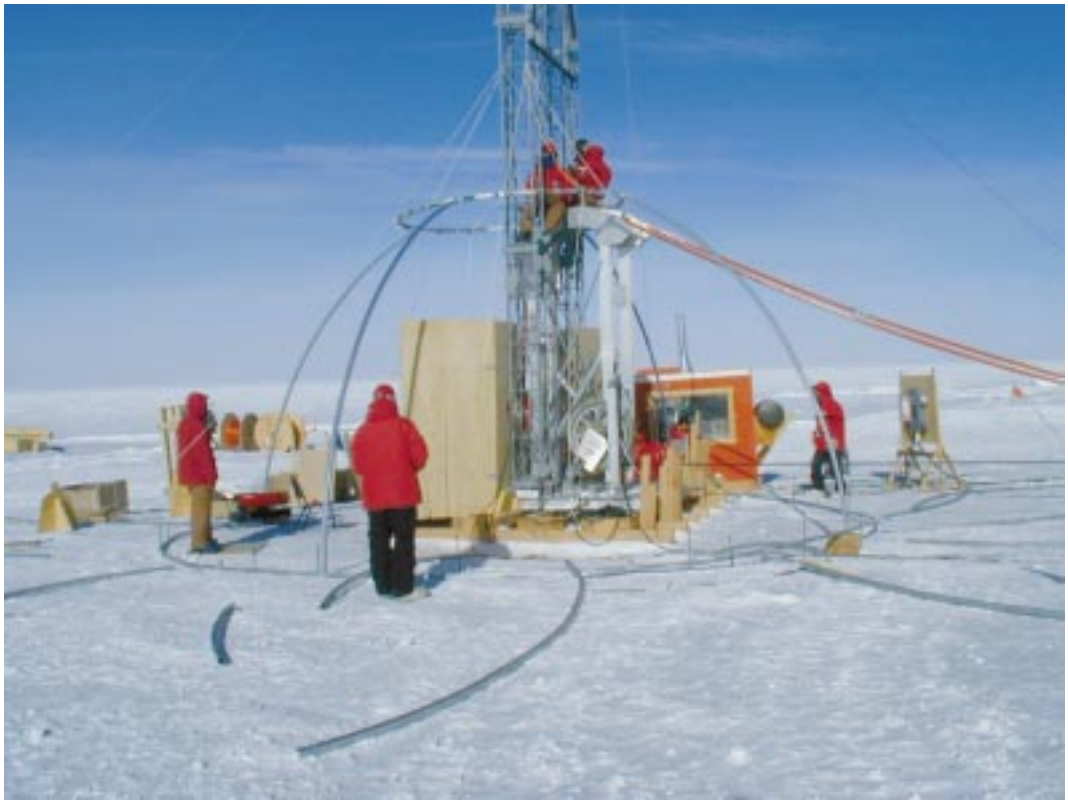

Figure 85: Setting up a shelter for AMANDA deployments. The setup time of 3 hours is too long for IceCube.

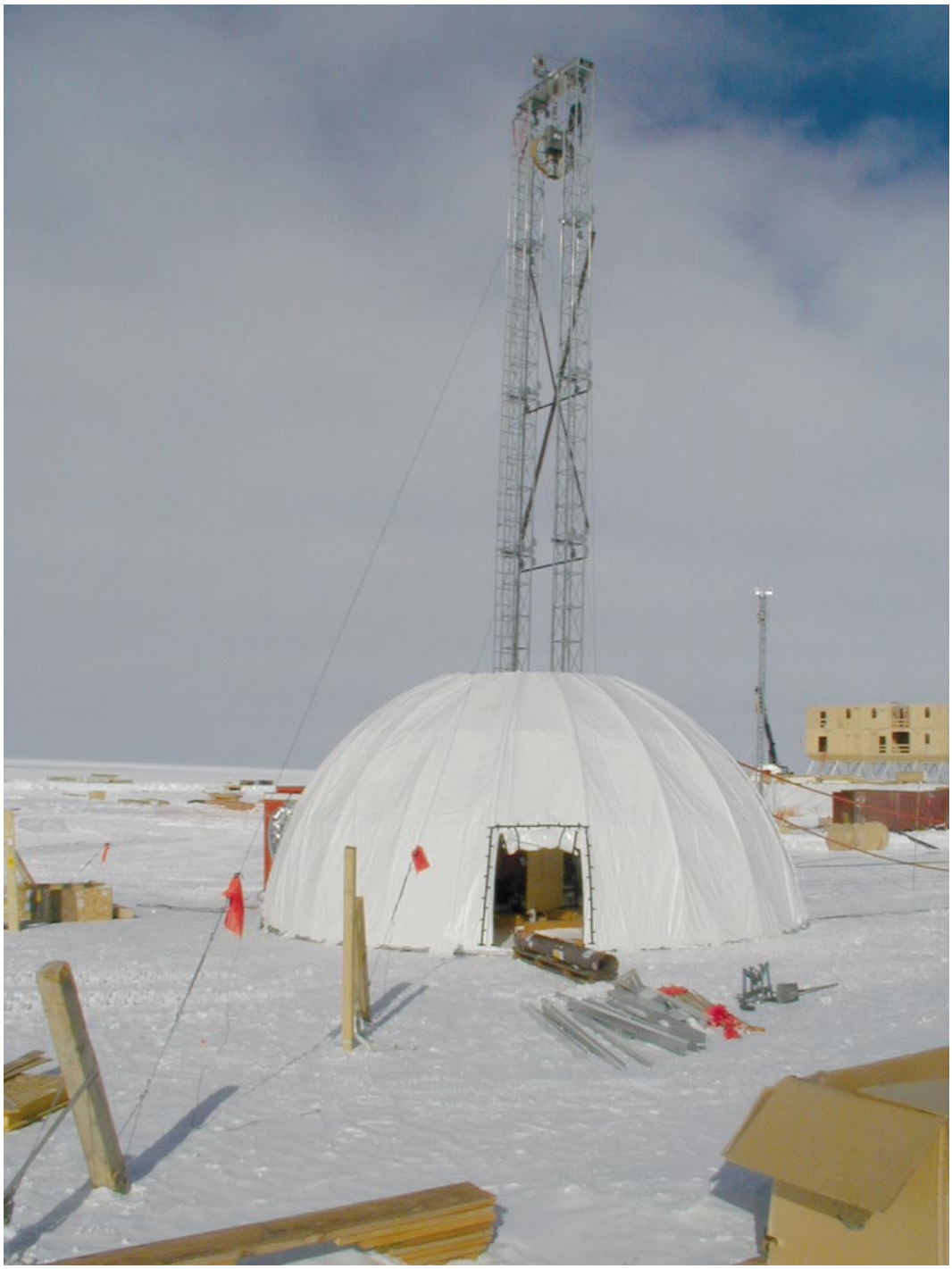

Figure 86: Completed shelter used for AMANDA deployments. This is type of shelter is not adequate for IceCube.

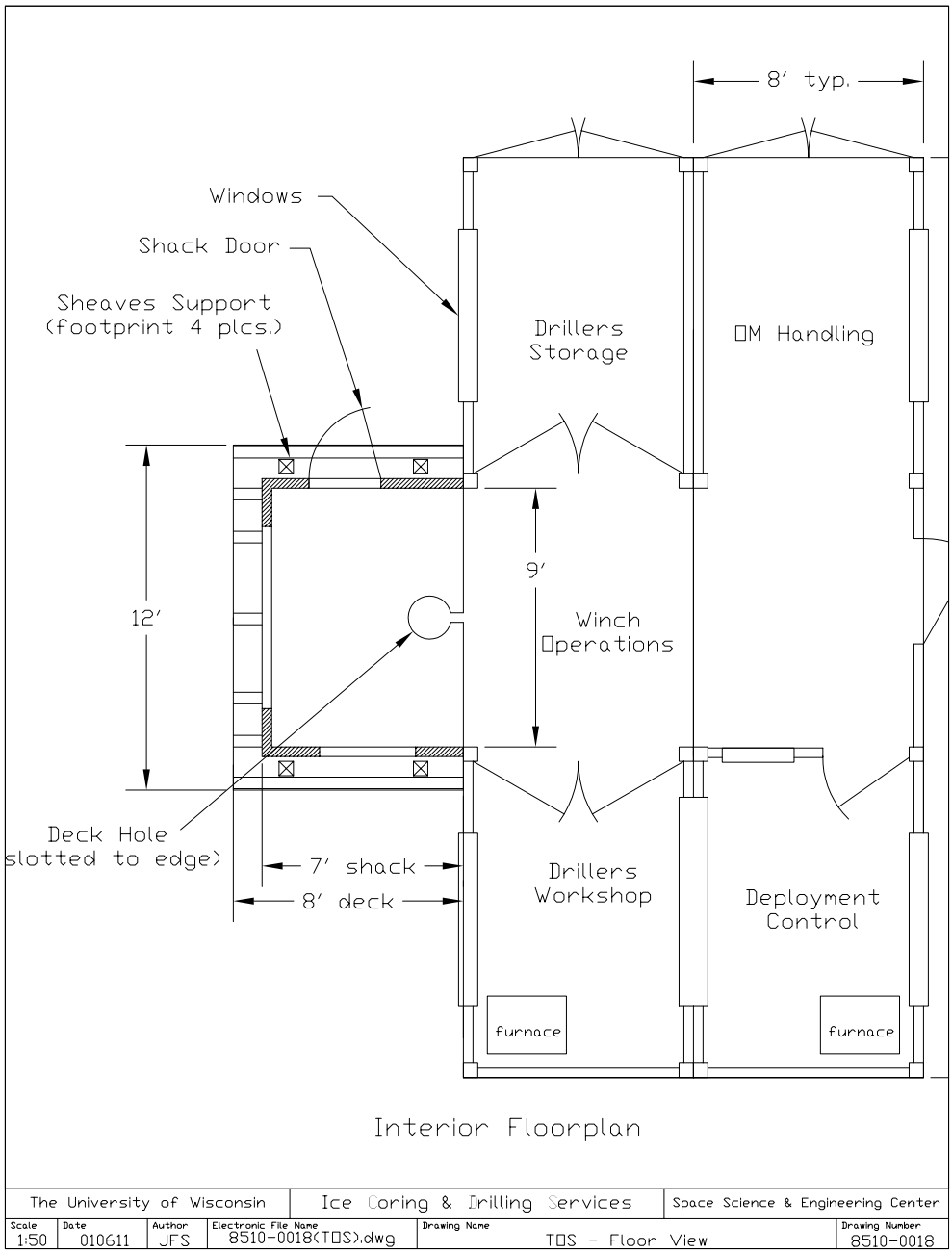

Figure 87: Floor plan of the tower operations structure (TOS). The building is used for drilling and deployment. The heated building provides power and network access.

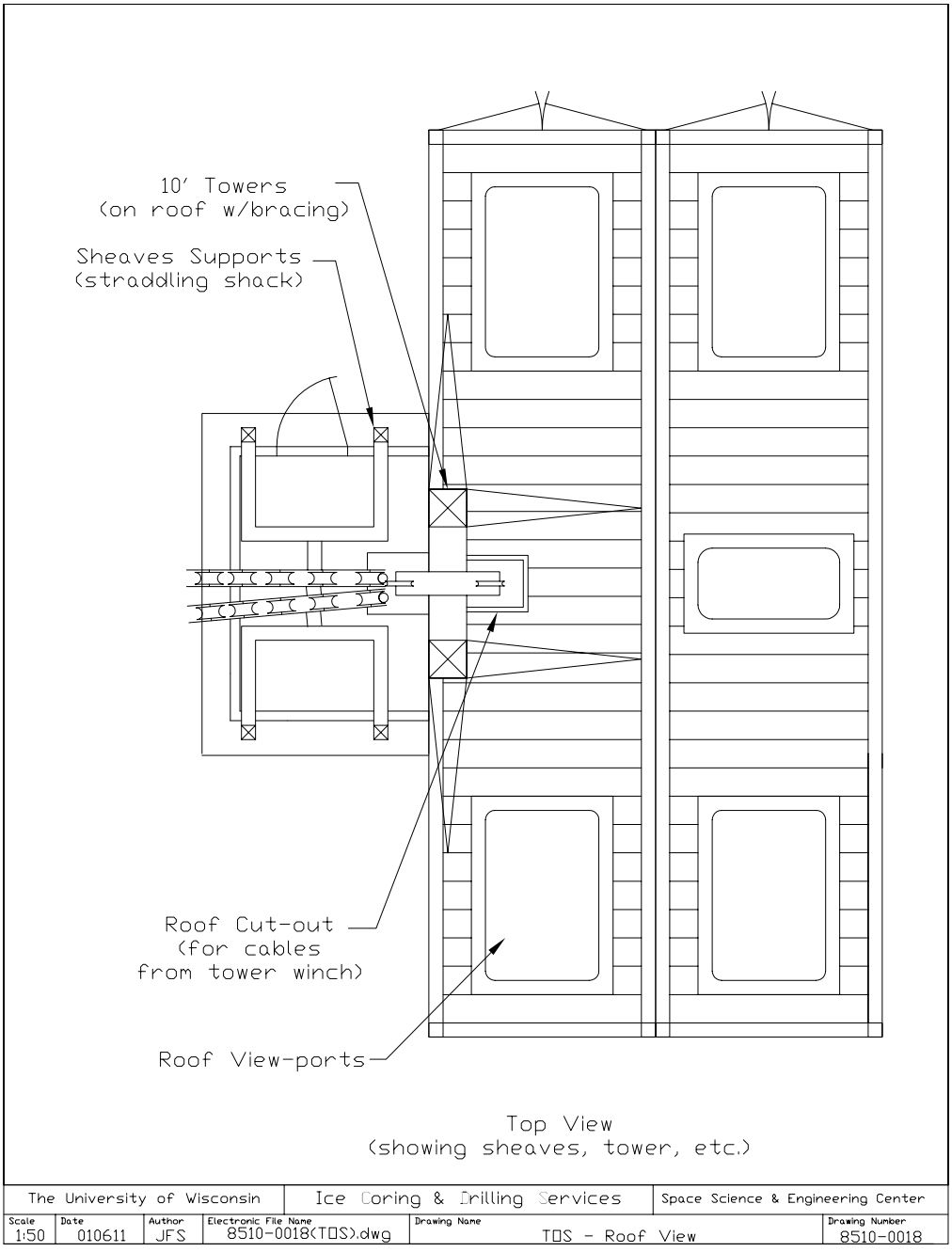

Figure 88: Roof plan of the tower operations structure (TOS).

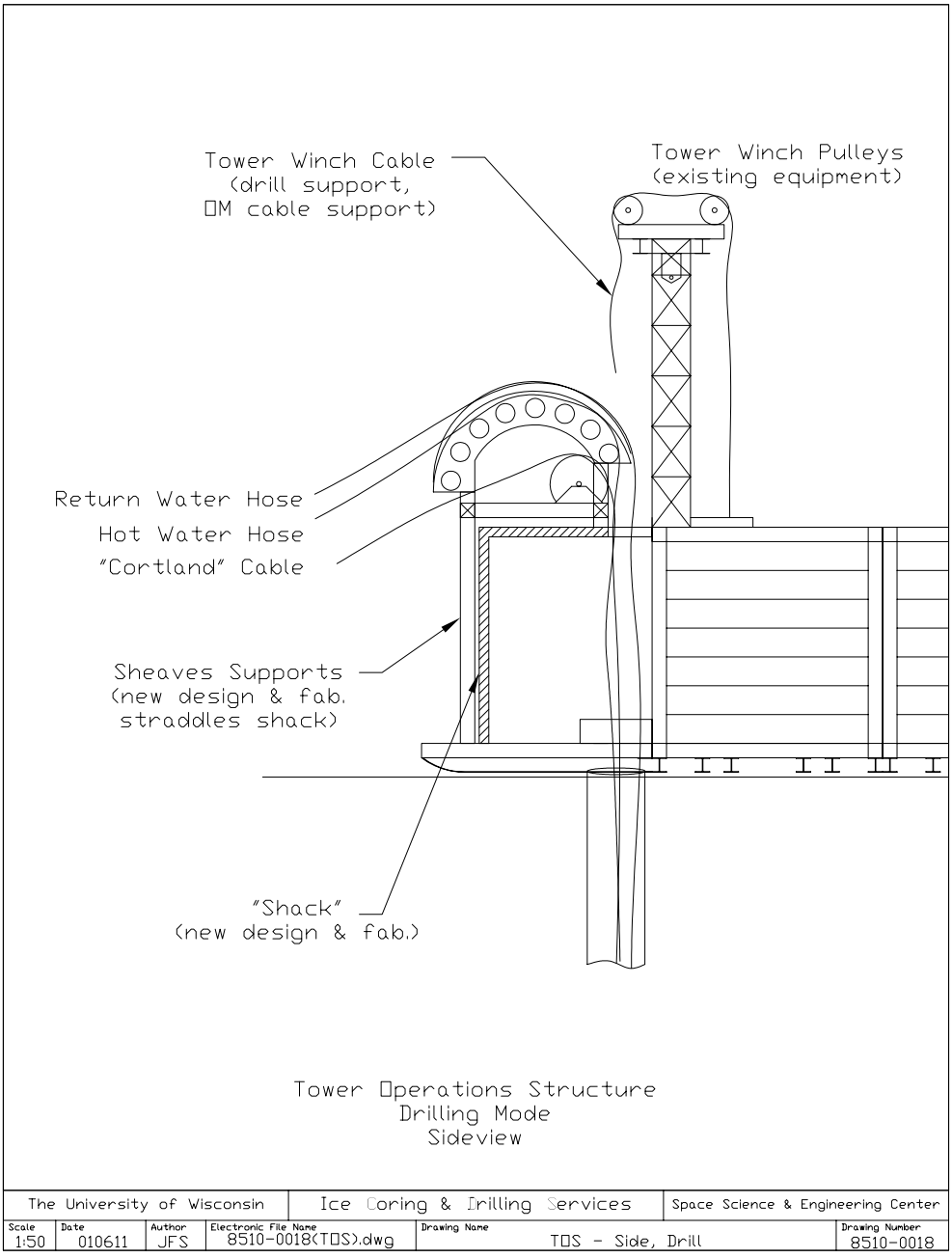

Figure 89: Side view of the TOS. The tower is at the top of the building to allow optimal conditions at the drill hole.

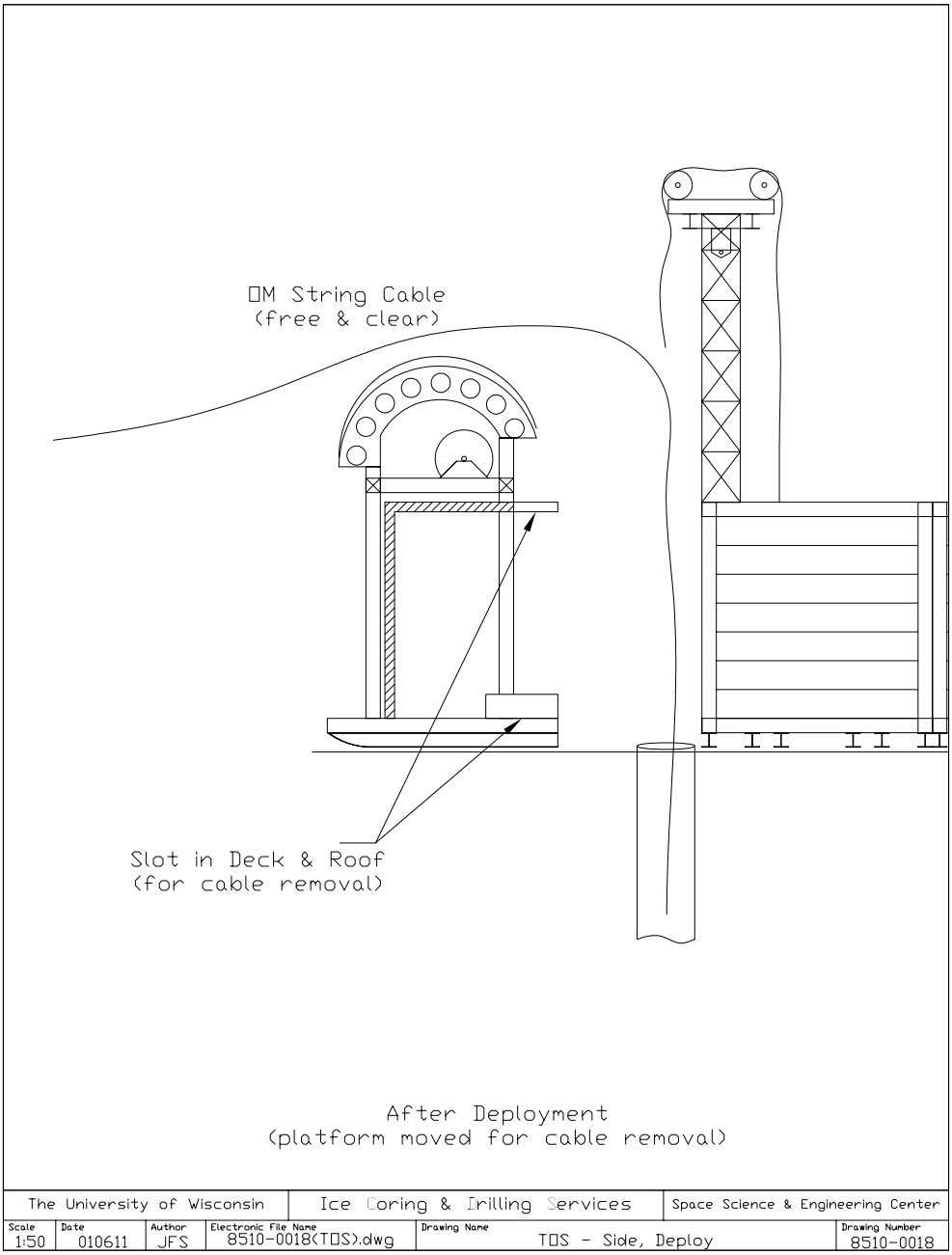

Figure 90: The sheave is detachable from the main structure for transportation purposes.

Diameter	43.0 cm
Depth	2410 m
Lifespan of 1st hole per season	32:00 hr
Lifespan of subsequent holes	29:30 hr

Table 14: Requirements which the drill hole must meet at the time of handover to the deployment team.

Deployment phase	Allocated Time (hr)		
	Nominal	Contingency	Total
Preparation	1:00	1:00	2:00
Weights, pressure sensor	0:40	0:20	1:00
OM installation	14:00	6:00	20:00
Drop	2:30	2:00	4:30
Finish and secure string	1:00	1:00	2:00
Total	19:10	10:20	29:30

Table 15: Breakdown of deployment phases and allocated times.

10.2.7 IceCube Drill Hole Requirements

The drill hole needs to be of a minimum diameter and depth for at least the time required for the string deployment. The minimal diameter is determined by the size of the OM (36 cm, including the harness) plus the cable (4 cm). The tolerances on the OM size are 0.8 cm. The tolerance on the cable diameter is 0.7 cm. We add an additional 1.5 cm for tapes and cable ties. *The maximum diameter of the string is 43.0 cm.* The drill hole requirements are listed in table 14. The specified duration contains contingency time for the deployment operation. The nominal total deployment time is estimated to 19 hr. This allows for more than 10 hr of contingency. The nominal depth is 2403 m. We allocate 7 m of contingency.

The deployment operation begins when the drill hole is accessible for the deployers. At this time the drill and the downhole pump have been removed from the hole. In addition it is required that the area behind the tower be accessible to position the winch with the IceCube cable. Once these conditions are met the hole is handed over from the drilling to the deployment command. A breakdown of the different phases of the string deployment operation and the estimated time for each phase is given in table 15. Contingency times are based on experience and possible failure mechanisms. Possible failure scenarios include power, winch control, winch drive, tower winch, computer and unexpected situations.

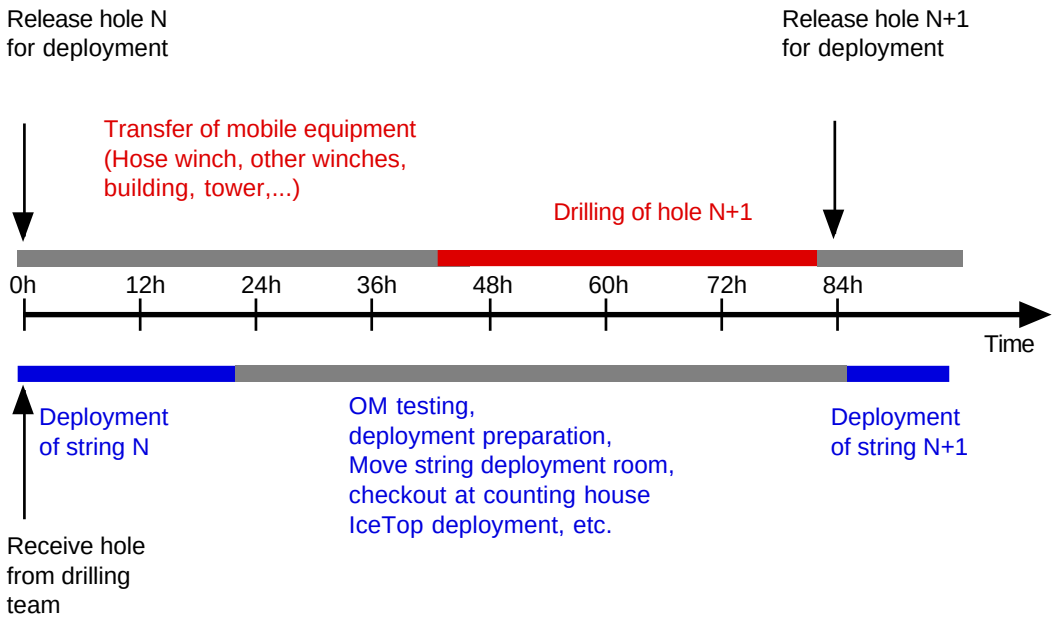

Figure 91: Time schedule of a single drilling and deployment sequence. The projected time for a single cycle is 84 hours.

Figure 91 gives an overview of the major operations during a single drilling and deployment cycle of 84 hr, and fig. 92 shows a schematic view of arrangement of drilling and deployment infrastructure in the course of drilling five holes.

10.2.8 Quality Assurance

Optical modules and associated components are all tested at various stages leading up to and including deployment. Tests which are done at McMurdo and the South Pole are described below.

McMurdo Test Stand All OMs undergo a detailed test procedure and burn-in operation before they are shipped to the South Pole. OM tests concern the integrity of the hardware after the transportation. Most OMs will be shipped by vessel. They arrive in January in McMurdo and stay there until about October of the same year. From here they are sent by air to the South Pole. The infrastructure at McMurdo permits extensive testing of OMs there. Therefore, only a very brief test sequence will be required at the Pole. (The details of the tests will be described elsewhere.) It is a fundamental concept of the test procedures that they do not require unpacking the OMs from the shipping crates. The crates are therefore light-tight. It is planned to wire the OMs inside the crate to a patch panel, which is accessible from the outside.

Only in the first season (FY04) will all OMs be shipped by air to McMurdo. In the following seasons an increasing fraction of OMs will be shipped by vessel. This requires that up to 1000

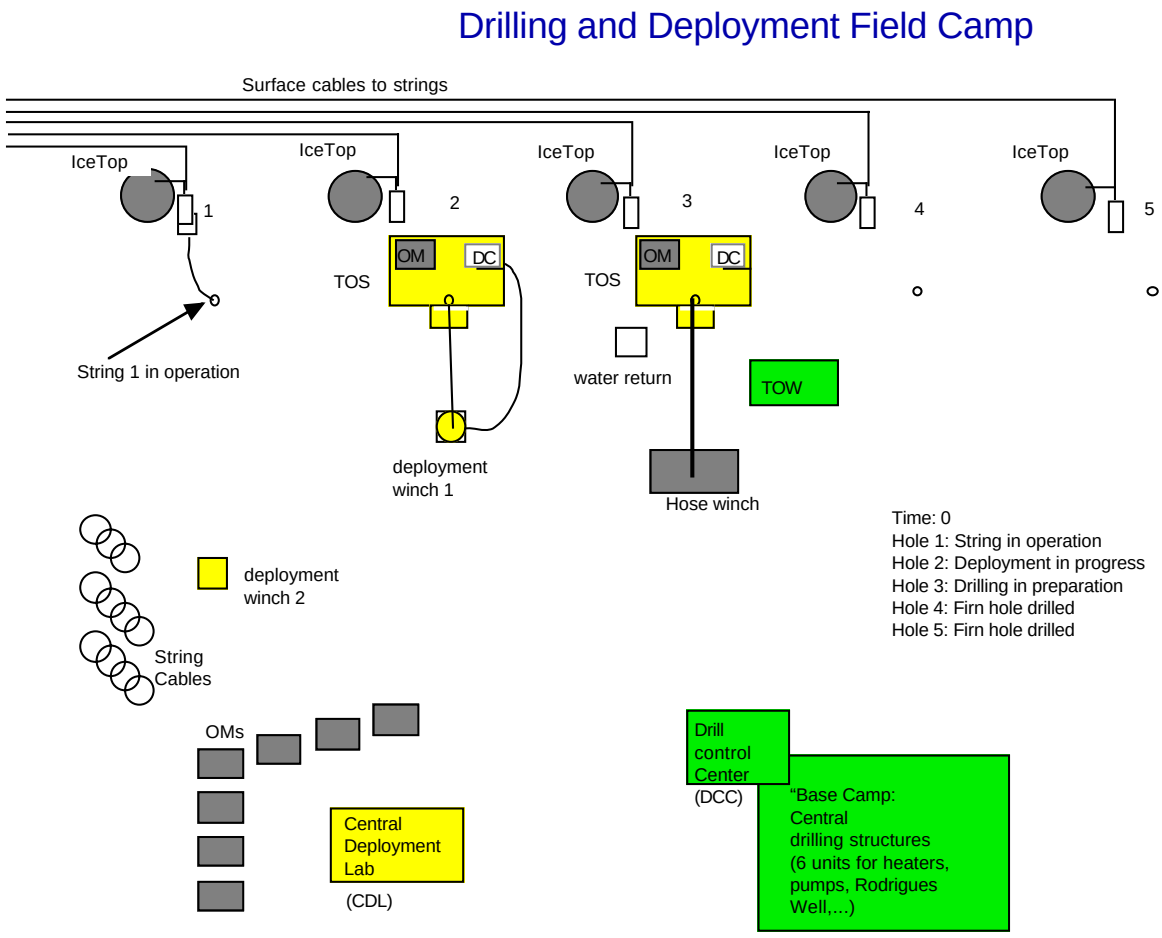

Figure 92: A schematic view of the drilling and deployment infrastructure with five drill holes is given.

OMs be stored in McMurdo, and hence a similar number need to be tested there each season. This is done with a DAQ system with 500 channels to test the all the OMs in two batches. The duration of the tests is 2–3 months. The DAQ hardware can be shipped to the pole with the last batch of OMs in the last year of string deployments and used for the main DAQ.

South Pole Test Stand The deployment infrastructure at the pole can be divided in three categories:

1. The central deployment lab;
2. The string deployment room;
3. A room allocated for deployment support in the IceCube counting house.

All OMs are delivered to the central deployment lab. Here they undergo a final test sequence of not more than 60 min per OM. Again, the OMs are tested in the crates. The crates must be light-tight such that the OM can be powered up and noise pulses and cosmic-rays observed.

A test DAQ is available to operate up to 100 OMs at a time. The test DAQ is very similar to systems used at various locations during the OM production and shipping. The tests are short in duration, ranging from 10 min to not more than 60 min. The tests are pass/fail and executed in software. OMs that fail the Q/A procedure are rejected for deployment and sent back. Only minor mechanical problems are fixed at the South Pole. OMs that show electronic problems are not opened for repair at the Pole, instead they are sent back to McMurdo.

About 60 OMs will be tested at a time. Fifteen twisted quad cables (or 30 twisted pairs) need to be connected to the crates waiting for tests. The time to wire up all the crates is estimated to be 1–2 hr. While the test runs no longer than one hour, the time for debugging and evaluation may take several hours. In total we allocate 24 hr of labor per string at the central deployment lab.

After this test the OMs are powered off and the crates are opened for the first time since shipment from the northern hemisphere. The content of the crates is checked for completeness of all mechanical components. At this time the pressure inside the OMs is checked to make sure there are no leaks. Once the OMs are certified the crates will be marked and sent the next deployment site.

Once the OMs are certified for deployment they can be moved to the string deployment site. Sixty OMs plus about eight spares are loaded into the deployment room and partially unpacked. During the deployment a final continuity and communications test is performed. This test requires at most a few minutes and can be performed in parallel with the mechanical installation. The OMs are connected in groups of four. Once connected the deployment DAQ verifies the continuity and runs some basic electronic and communications tests.

10.2.9 Practice Deployments

Experience has shown that the first string deployment in each season is particularly challenging due to lack of experience of most of the team members. Two strategies are planned to optimize

Year	FY04	FY05	FY06	FY07	FY08	FY09
baseline schedule	6	12	16	16	16	14
possible range	3-6	8-14	15-17	15-18	15-18	14-18

Table 16: Schedule for string deployments. The numbers indicate the how many strings are to be deployed in each season in the baseline schedule and the possible range in the number of strings deployed each year, as described in the text.

the performance during the first deployment. A pre-deployment workshop of about two weeks is planned and budgeted for all deployers. This is an opportunity to familiarize the team with the procedure and the instruments used. Unexpected situations can be discussed. Particular responsibilities can be defined. A test stand will be available to practice the actual OM installation. The full deployment team must be at the South Pole two weeks prior to the first deployment to begin with the preparations, test procedures, and the setup of the instruments and labs. A practice hole of about 50 m depth together with the full deployment infrastructure (tower, string deployment shelter, etc.) will allow deployers to practice the deployment on the site. A subset of the deployment team needs to arrive at least three weeks prior to the first IceCube deployment to prepare the new infrastructure.

10.2.10 Surface Cable Installation

Deployment Sequence and Cable Plan Table 16 shows the deployment sequence during the IceCube construction period, and fig. 93 illustrates this sequence. The baseline schedule calls for six strings to be installed in FY04, followed by 12 in FY05, then 16 for FY06–FY08 and finally 14 strings in FY09. In FY04, the chief goal is to achieve an end-to-end test of all detector systems, a goal which is best achieved with a minimum of three strings, as indicated by the first number in the "possible range" row in Table 16. Similarly, in subsequent years the first number represents the minimum number of strings to be deployed, and the second number the maximum, subject to the constraint that the sum over all years equals 80. Experience gained in earlier years may permit even larger numbers of strings to be deployed in later years than indicated in the table. For any year in which the number of strings deployed exceeds the baseline schedule, there are production, logistics, and schedule implications which have not yet been addressed. It is possible that an accelerated schedule, using contingency funds in earlier years, will result in an overall savings to the project.

The addition of 12 strings in FY05 will embed the AMANDA array in IceCube strings. The SPASE-2 array will be embedded only in FY09. A few SPASE-2 stations will have to be relocated then, assuming that it is still in full operation. Trenches are used to bury the cables at depths which will keep them secure for $\sim$ 15 yr.

Cable Trenches The separation of the main cable in a surface cable and an in-ice cable allows for a very flexible cable management. The surface cables will be laid and trenched independent

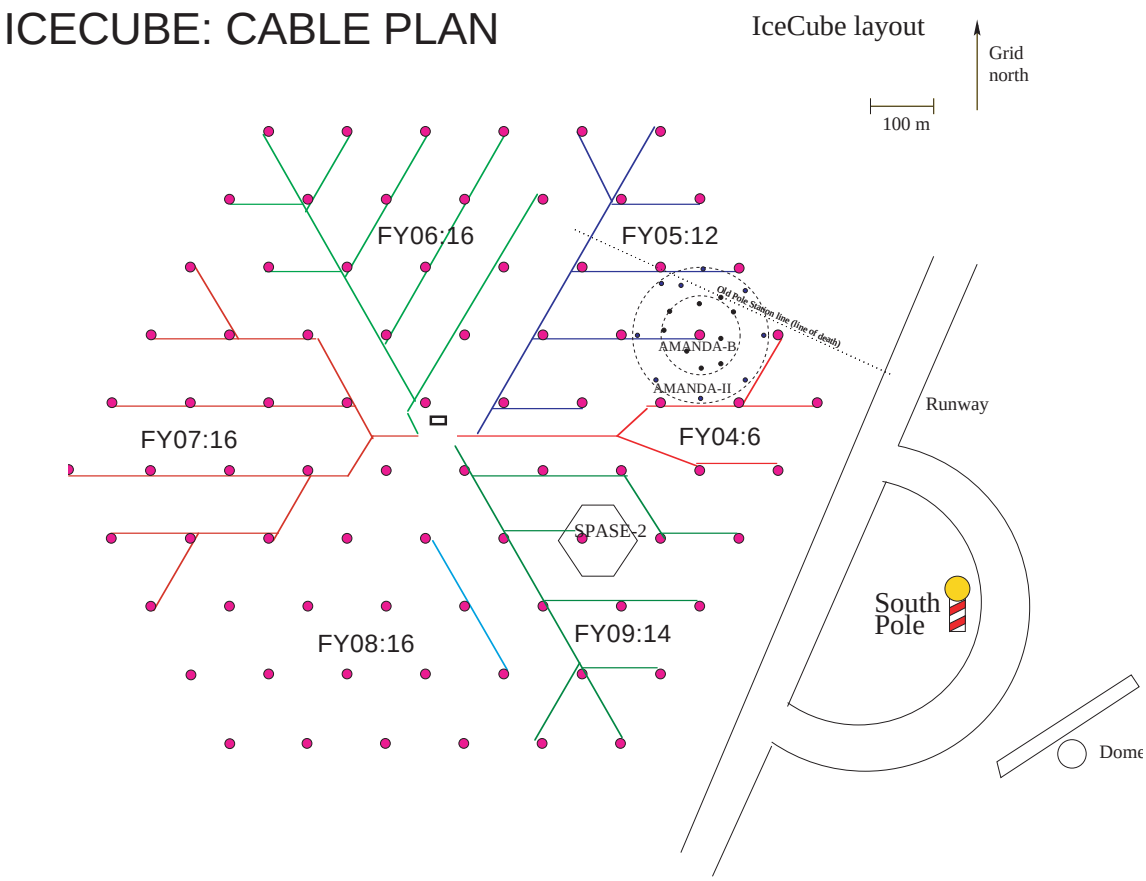

Figure 93: The deployment sequence.

of the exact timing of the drilling and deployment. In this design, the surface cable will be trenched before the drilling starts. Ideally the surface cable is already wired up in the counting house by the time the string is deployed. As soon as the string is deployed it will be connected to the surface cable and the string will be operated from the counting house hours after the deployment is completed. Another advantage is that the valuable time during November will be used to do the cable trenching. There is no need to wait for the strings to be deployed first. The cables will be trenched starting from the counting house. This avoids the pile-up of excess cable in its vicinity. The small amount of excess cable, a few tens of meters, will be buried together with the IceTop tank in the snow. This is where the connection between the in-ice cable and the surface cable will be located. Cable trenching is done by the NSF contractor.

10.3 Logistics

10.3.1 Introduction

A South Pole Experimental Deployment is a highly detailed operation requiring the efforts of many groups at the NSF and the Support Contractor as well as detailed planning of the experimental group. This planning starts with the Operational Research Worksheet (ORW) which describes the full long-term requirements of the experiment. It is supplemented each year with the Support Information Package (SIP), and later with direct meetings between the experimenters, the NSF, and the Support Contractors so that all can agree on the exact level of field-support the experimenters can plan on being delivered by the NSF and the Contractor.

10.3.2 Documentation

The ORW is submitted along with the experimental proposal to the NSF, and it is reviewed by the contractor to assess whether the experimental proposal can be adequately supported to meet the needs of the experimenters. This document serves to outline the annual support an experiment will require during the entire lifetime of the experiment.

The type of information required for both the ORW and SIP is listed below.

- PI and co-PI Contacts
- Project Description: Locations and Scientific Opjectives
- Personnel: Proposed time period at the pole and specific job-tasking, medical/dental examinations and clearances. Travel arrangements.
- Safety Environment and Health Issues: Ice coring, use of heavy equipment, placement of probes. use of radioactive materials, hazardous waste, etc.
- Cargo: A complete listing of all of the cargo items one expects to ship.
- Construction and Fabrication Required
- Computers and Communications: Connectivity, system maintenance, on-site support

- Laboratory/Observatory Requirements
- Aircraft Support
- Vehicle Support
- Global Positioning (GPS) Support

Experience with AMANDA has shown us that the best way to keep the NSF and Contractor up to date concerning South Pole population levels and personnel medical/dental and travel status is to maintain a Deployment WWW-page. Both personnel and cargo movement information is presented in spreadsheet formats (presently using EXCEL). These formatted personnel and cargo spread-sheets are also forwarded electronically to the contractor.

10.3.3 Personnel and Taskings

South Pole population levels are highly restricted, mainly due to station size limitations. In the past AMANDA has been forced to cap its population to about 12-15 people at any time. The field-season generally runs from November 1st to about February 15th each year. This 15 week period is generally divided into 3-4 project periods of 4-5 weeks duration. This generally matches with the period of time that people spend on the pole so that in any season we may have as many as 35-45 people working at the pole during some period. Generally a task will involve 3-4 people and we generally schedule in 3-4 parallel tasks at any one period. This generally means that anywhere from 12-15 specific tasks invoving 3-4 people for 3-5 weeks will get done during a field-season

The labor hours required for the deployment of a single string and the associated IceTop detector is given in table 17. The total population required to perform these tasks follows from the labor required per string. Almost 40% of the deployment time is required for the actual string deployment operation.

The basic string deployment operation requires 7 people during the core deployment operation. 24 hours are allocated for the deployment operation. This is almost 5 hours more than the nominal deployment time to ensure the readiness of the team at the time of the hand-over from drilling. Including the IceTop deployment, we plan on a total population of 16 people during times of full capacity string deployments. Three people are allocated for the IceTop deployment. The IceTop deployment personnel requirements are the most difficult to estimate due to lack of experience.

As shown in table 18, the projected population reaches a maximum of 44 in all years. The drilling population is higher in the first year, due to the drill construction. The AMANDA and SPASE population is higher in the first 4 weeks of FY04. The "Science" population is the personnel required for the installations of the electronics and software in the counting house and in the B2 science lab. This group will commission and operate the detector during the summer. As soon as the deployment operation is phased down by the end of January, the science population is increased to accelerate the commissioning of the last strings and to increase the efforts on data handling operations.

Operation	Time allocated (h)
Cable drag	52
Deployment (24*7)	168
Site. Preparation	16
Cable unpack and prep	20
OM Testing	24
Documentation	10
PTS prep	15
Logistical and other support	20
IceTop	84
General assistance	20
Total: String	429
Total: Week	858
Number of 54 hour shifts/week	15.9

Table 17: Labor hours required for a single string.

	Person days: Total/season			Population during deployment periods: (Maximum/day)		
Year	FY 04	FY 05	FY 06 - 09	FY 04	FY 05	FY 06 - 09
Drilling	1509	1308	1307	18	15	15
Deployment	796	1334	1316	15	16	16
Science	676	905	1032	8	10	11
A-II/S-2	611	392	238	3	3	2
Sum	3592	3939	3893	44	44	44

Table 18: Population required for the fiscal years FY04 to FY09. The population is broken down in drilling personnel, deployment personnel, science personnel for IceCube and science personnel for the subsystems AMANDA-II and SPASE-2. The total number of person days during a South Pole summer is given on the left. On the right the number of people is given during the periods of highest population.

Item	Weight (lb)	Volume (ft^3)
Cable	10560[a]	307[a]
60 OM	3300[b]	270[b]
Mechanical	400[c]	4[c]
Weights	600[c]	6[c]
IceTop unit	1200[c]	120[c]
Total: single string	16060	7070
Total: 16 strings	25690	11310

Table 19: Breakdown of weights and cubes per string and total for a single string and 16 strings. (Quantities come from RK quotes (a), Hoffman (b) and Karle (c).)

10.3.4 Medical/Dental Examinations

All personnel deploying to the South Pole have to pass a medical and dental examination. This can be complicated and time consuming so the process is started in the May-June time period. The contractor sends out the medical/dental packets and they also view the results of the tests and make the decision if a South Pole candidate is medically qualified. Differences in European and American dental standards have caused problems in the past. Medical qualification is a precondition to Antarctic travel.

10.3.5 Airline Travel

All U.S. experimenters have their airline tickets purchased by the contractor. These tickets provide travel between their university location and Christchurch, New Zealand. Foreign participants have to provide transportation at their own costs to Christchurch. At that point all participants are provided transportation at no cost to them, from Christchurch to Antarctica.

The experimenters are expected to pay for their lodging and food from their research contracts. Once in Antarctica there are no costs, since both food and lodging is provided.

10.3.6 Weights and Cubes

The main elements of a string are the cable and the OMs. Smaller mechanical components are needed for the installation of the sensors. Weights are used at the bottom to keep the string under tension. The weights and cubes for each string are listed in table 19. We group the cargo in three categories: Cables, OMs, and miscellaneous, where miscellaneous stands for mechanical components, the weights and for the IceTop tank for each string. The following cargo movements are required:

1. All incoming cargo is delivered to the central deployment lab as it arrives.

2. The equipment used for each string is transported to the exact location near the deployment site of a given string. The equipment is requested at the deployment site before the drilling starts. This will be approximately 48 hours before the deployment begins.

3. Remaining packing materials are transferred to South Pole waste management.

10.3.7 Cargo Transport

Estimates of total mass and volume of material ("weights and cubes") required by IceCube over its lifetime are given in the tables below. There are three ways that cargo can get to the South Pole site, by "vessel," "Comm-Air" and "Kilo-Air."

The vessel is the cheapest means of transport, but requires the most advance planning. Cargo leaves Port Hueneme, CA by vessel on about December 15 and arrives in McMurdo, Antarctica about 6 weeks later on January 25. The cargo is then flown in C-130 Hercules aircraft to the pole or it winters in McMurdo and is is flown at the beginning of the next season. Either way the cargo is only available for use at the pole the following season. The vessel requires that equipment be ready one year before it will be needed at the pole.

Kilo-Air is the most common way to ship items. Under this plan, items are shipped from Port Hueneme to Christchurch NZ by vessel about September 15. From Christchurch they are flown down to McMurdo, and then from McMurdo to the pole. This means that cargo usually has to be ready about 60-70 days before it is needed at South Pole.

Comm-Air is the fastest and most expensive way to ship cargo to the pole and it requires NSF approval. Items travel from Port Hueneme to Christchurch by commercial air-cargo. From Christchurch to Antarctica they travel the same way as Kilo-Air.

All Antarctic cargo orginating in the U.S. is shipped from the NSF facility in Port Hueneme, CA. Cargo originating in Europe is generally shipped to the NSF facility in Christchurch, NZ. During the course of the IceCube deployment it is expected that about 1300K lbs of detector components and 650K lbs of drilling equipment will be shipped to the South Pole via vessel. We also plan to ship about 100K lbs of detector components and 100K lbs of drilling equipment via Kilo-Air.

The tables 20 10.3.7 10.3.7 10.3.7 10.3.7 list the cargo to be shipped by the various means listed above. In these tables, "ROS" stands for "Required On Site" and "N" is the current year's string count minus one. The cargo is given in two categories that describe the mode of transportation: Kilo-Air and Vessel. The cargo is broken down further in 3 categories of string equipment: Optical Modules (OM), Cables, Miscellaneous.

FY	Strings	Weight (lbs)	Cubes (ft^3)	ROS
04	6+1	23100	1890	12-13-03+N×5 days
05	6	19800	1620	11-20-04+N×3 days
06	4	13200	1080	11-16-05+N×3 days
07	0	0	0	0
08	0	0	0	0
09	0	0	0	0

Table 20: Optical Modules to be shipped by "Kilo Air."

FY	Weight (lbs)	Cubes (ft^3)	ROS
04	4000	1890	12-15-03
05	6000	1620	12-15-04
06	4000	1080	12-15-05
07	4000	0	12-15-06
08	1000	0	12-15-07
09	1000	0	12-15-08

Table 21: Miscellaneous hardware to be shipped by "Kilo Air."

FY	Strings	Weight (lbs)	Cubes (ft^3)	ROS
04	0	0	0	12-13-03+N×5 days
05	6+2	26,400	2160	11-20-04+N×3 days
06	12+2	46,200	3780	11-16-05+N×3 days
07	16+1	56,100	4590	11-16-06+N×3 days
08	16+1	56,100	4590	11-16-07+N×3 days
09	14	46,200	3780	11-16-08+N×3 days

Table 22: Optical modules to be shipped by vessel.

FY	Strings	Weight (lbs)	Cubes (ft^3)	ROS
04	6	13200	720	12-13-03+N×5 days
05	12+2	30800	1680	11-20-04+N×3 days
06	16+2	39600	2160	11-16-05+N×3 days
07	16+1	37400	2040	11-16-05+N×3 days
08	16+1	37400	2040	11-16-05+N×3 days
09	14	30800	1680	11-16-05+N×3 days

Table 23: Miscellaneous hardware to be shipped by vessel.

FY	Strings	Weight (lbs)	Cubes (ft^3)	ROS
04	6	63,350	1842	12-13-03
05	12	126,700	3685	11-20-04+N×3 days
06	16	168,900	4913	11-16-05+N×3 days
07	16	168,900	4913	11-16-05+N×3 days
08	16	168,900	4913	11-16-05+N×3 days
09	14	147,800	4299	11-16-05+N×3 days

Table 24: Cables to be shipped by vessel.

11 Quality Assurance

The IceCube project office will implement a quality plan meeting the requirements of ANSI/ISO/ASQC Q9001-2000 (ISO 9000). The UW Space Science and Engineering Center (SSEC) is in the process of implementing a Quality Management System (QMS) meeting the requirements of ISO 9000 and eventual registration.

The IceCube Quality Plan will define the overall project policy, the processes to be controlled and how they interact, and the procedures to be used. The plan will include, but not be limited to, addressing the following areas:

1. The overall scope of the Quality Plan, the standards (ISO 9000, etc.) it is designed to meet, and the management commitment to the plan. Exclusions, if any, will be listed. The plan will make it clear how each element of the program is affected by the quality plan, who is responsible, how each requirement is to be met, and how we verify the effectiveness of the plan.

2. Control of documents: who approves, how released and distributed, lists of documents, change procedures, how users are assured they have the latest documentation, and how obsolete documentation is removed from the system. The document control system will use on-line databases with web access to simplify the process, reduce paper handling and the time and effort needed to make changes, and make the latest information available to all project elements without delay.

3. Control of customer and supplier documentation: How such documentation is received, logged, and stored. The process for assuring such documentation is the latest and correct version is also described.

4. Procurement controls: how requirements are passed to suppliers and collaborators, what information and documentation is required, how material is verified upon receipt, what records are generated and kept. The nature of the quality requirements that are to passed on to suppliers and collaborators will be described.

5. How the quality system is planned, maintained, improved, and verified. Management review process, internal audits, corrective and preventive actions will be included and will follow the ISO 9000 standard model. The essence of the system is to make our processes clear and understandable so they can be reliably executed. The processes must be sufficiently clear and verifiable so that deficiencies can be readily identified and corrected, ideally before problems arise.

6. The quality organization: who is responsible for what. Internal communication processes, management roles and responsibilities, the nature of the management reviews, internal audits, and how these processes are carried out.

7. Awareness and training, certification, assuring personnel have the appropriate skills and experience, the records required for these elements, the process for verifying the effectiveness of training, and how deficiencies are corrected.

8. Design and development process: inputs and outputs, design reviews, design documents required by phase, the purpose of the reviews, who is involved, the specific items needed for the review, the process for documenting review actions and closeout, the points of the project where reviews are required, major and minor reviews (formal and informal)

9. Reliabilility guidelines: assembly standards, parts program (standards, testing, screening), parts derating guidelines, traceability requirements, vendor documentation, receiving inspection, certifications, parts documentation and how tied to assembled items. Spares logistics and parts guidelines relating to spares.

10. Manufacturing planning: How manufacturing and assembly processes are planned, controlled, and verified. How in-process material is identified and what records are kept. This includes the traceability documentation (parts lists, lot numbers, serial numbers, etc.), how inspections are handled, by whom, the process for documenting non-conformances, how the documentation and actual hardware are processed, test procedures, how test data is kept, and what happens to the final records after the item is complete.

11. Verification: Inspection and tests: standards, records, test procedures, integration processes, calibration of test equipment and associated records, integration logbooks, record retention, configuration identification lists, and test procedures.

12. Non-conformance control: Identification of non-conforming articles, disposition processes, rework, repair, MRB, and associated records. How repairs are planned and documented, rework vs repair and how each are handled, Who determines what levels of disposition of non conforming articles and why.

13. Service, field support, logistics: spares, records of failures and malfunctions, configuration management, configuration records, maintaining configuration records of items deployed, maintaining spares and support for deployed items and items subject to configuration control that are changed.

14. Internal audit plans and procedures, management reviews, schedules, personnel, training for audits, audit follow up

15. Analysis of data for determining status and trends of product quality, customer satisfaction, supplier performance, areas needing attention for continual improvement and/or corrective and preventive action and how this all relates to the management review process.

The details of the plan will resemble plans appropriate for spacecraft instrumentation because IceCube must operate reliably in a remote and harsh environment, is a large and complex system,

once deployed cannot be returned for repair, and represents a major investment. The quality plan must therefore be rigorous and fully integrated in the management and development process.

The ISO 9000 standard is process based using a "plan, do, check, act" model. The plan begins with identification of the processes necessary to control quality. The definition and documentation of those processes are done to the extent required to achieve the desired results. The QMS emphasizes the process of continuous improvement via internal audits, corrective and preventive action, and management review. The system is based on the heritage of assurance programs meeting NASA requirements for spacecraft instrument development projects which SSEC has implemented within a university based research and development organization. The quality aspects of the project are designed and built-in from the beginning, rather than "tested in" after the fact. This approach makes quality assurance part of the management and engineering process thereby increasing efficiency, improving results, and minimizing errors.

The key documents defining the IceCube Quality Plan are:

1. American National Standard ANSI/ISO/ASA Q9001-2000 (and referenced documents). These define the standards we are intending to meet.

2. The SSEC Quality Management System (QMS) Plan (in development). This describes the UW-Madison SSEC Quality Management System policies and procedures.

3. The IceCube Quality Plan. This plan will detail the quality plan for the IceCube project. The application of the SSEC QMS for this project and any special needs of IceCube will be described in this document

4. Supporting Procedures, Specifications, and Instructions. Some of these will be created for the project, others will documents used by other projects.

12 Relationship of AMANDA and IceCube

The AMANDA-II detector will continue to take data during the construction phase of IceCube. During and after this period, members of the AMANDA-II (and IceCube) collaborations will be writing theses and publications based on analyses of AMANDA-II data. Since some members of the AMANDA-II collaboration are not members of IceCube, AMANDA-II will continue to produce an independent data stream. Also, since AMANDA-II needs to digitize its PMT signals within a few microseconds, it must be running and triggering independent of IceCube.

During the 2001/2002 and 2002/2003 seasons the AMANDA-II detector will be upgraded with waveform recording of its channels with optical readout. The DAQ system will in the same period be upgraded in order to increase data capacity and reduce dead time. No significant further upgrades of AMANDA-II are foreseen after the 2002/2003 season. Thereafter, the AMANDA-II detector will mainly need maintenance and calibration, and as such it will take data with minimal investment in personnel.

The AMANDA-II detector will be surrounded by IceCube strings (see fig. 59), permitting the two detectors to be run in coincidence. As the number of deployed IceCube strings increases, data taken from a combination of the two detectors will provide a useful testing ground for IceCube software, an important calibration tool for IceCube, and accelerate the ability of IceCube to produce scientific results.

Coincident triggering of AMANDA-II and IceCube is feasible at several levels. One could treat AMANDA-II and IceCube as completely independent entities at trigger level and write out the triggered data in two independent output streams. Selecting coincidence events can then be done offline, or in the IceCube event builder, using each detector's GPS timestamps. This scheme is simple, but it has the (perhaps unimportant) drawback that it will miss parts of those events which are below trigger threshold in one detector but not the other. It will also miss coincident events which are below threshold in both detectors.

It is possible to correlate events earlier in the data stream. The global trigger in the IceCube DAQ system receives hit information via ethernet and the global trigger software runs on a standard computer (see Sec. 7 for details). By sending similar information from AMANDA-II to the IceCube global trigger, a search for correlations between the two detector systems can easily be done, without the need for any new hardware. The timestamps for AMANDA-II hits would have to be corrected by the measured signal delays due to the down-hole optical fibers, but this can be accomplished with a straightforward look-up table in the global trigger software.

The information that both detectors have correlated hits can be sent to both systems and flagged in their respective data structures. This will make offline analysis easier. It is also possible to write out a data stream with fully combined data information from AMANDA-II and IceCube.

The information coming from AMANDA-II will differ in format and content from IceCube data (with the partial exception of the DOMs in AMANDA-II string 18). The channels in AMANDA-II which have only electrical read out will have no waveform information, only time, TOT and ADC information. The AMANDA-II channels with optical readout will have waveform information, but with different sampling frequency than that of IceCube. Data format trans-

lation and the ability of the IceCube offline analysis software to handle disparate information content are therefore required.

The tasks outlined above require some IceCube software effort, but that effort should not be substantial in the context of a well-designed IceCube software system. Further effort to maintain and calibrate AMANDA-II is also needed, and will be part of the winter-over responsibilities, with oversight and calibration analysis work done by IceCube and AMANDA-II physicists. Overall, the effort to integrate AMANDA-II and IceCube is not large, and the returns on the effort will substantially outweigh the investment.

References

[1] M. Nagano *et al.* J. Phys. G10 (1984) 1295.

[2] Yu. A. Fomin *et al.*, Proc. 22nd Int. Cosmic Ray Conf. (Dublin) vol. 2 (1991) 85.

[3] M. Takeda *et al.*, Phys. Rev. Lett. 81 (1998) 1163.

[4] M.A. Lawrence, R.J.O. Reid & A.A. Watson, J. Phys. G17 (1991) 733.

[5] M.I. Pravdin *et al.*, Proc. 26th Int. Cosmic Ray Conf. (Salt Lake City, 1999) vol. 3, p. 292.

[6] D.J. Bird *et al.*, Astrophys. J. 424 (1994) 491.

[7] D.J. Bird *et al.*, Phys. Rev. Letters 71 (1993) 3401.

[8] E. Waxman & J. Bahcall, Phys. Rev. D 59 (1999) 023002.

[9] J. Bahcall & E. Waxman, Phys. Rev. D 64 (2001) 023002.

[10] G.R. Farrar & T. Piran, Phys. Rev. Letters 84 (2000) 3527.

[11] K. Griesen, Phys. Rev. Lett. 16 (1966) 748; G.T. Zatsepin and V.A. Kuzmin, JETPh Lett. 4 (1966) 78.

[12] A. Achterberg in *High Energy Gamma-Ray Astronomy*, (A.I.P. Conf. Proc. 558, ed. Felix A. Aharonian & Heinz J. Völk, γ2000) 392.

[13] J. Bednarz & M. Ostrowski, Phys. Rev. Letters 80 (1998) 3911.

[14] J.G. Kirk, A.W. Guthmann, Y.A. Gallant & A. Achterberg, Ap.J. 542 (2000) 235.

[15] T. K. Gaisser, in *Observing Ultra-high energy Cosmic Rays from Space and Earth* (A.I.P. Conf. Proc. 566, ed. Humberto Salazar, Luis Villaseñor & Arnulfo Zepeda, Metepec, Puebla, Mexico, August 9-12, 2000), p. 238.

[16] R. Gandhi, C. Quigg, M.H. Reno & I. Sarcevic, Astropart. Phys. 5 (1996) 81.

[17] T.K. Gaisser, astro-ph/9707283.

[18] Mannheim, Protheroe & Rachen, astro-ph/9812398; J.P. Rachen, R.J. Protheroe & K. Mannheim, astro-ph/9908031.

[19] J. Learned & K. Mannheim, Ann. Revs. Nuclear and Particle Physics.

[20] C. Schuster, M. Pohl & R. Schlickeiser, submitted to Astronomy and Astrophysics.

[21] M. Pohl & R. Schlickeiser, Astron. & Astrophys. 354 (2000) 395.

[22] F.A. Aharonian *et al.*, Astron. Astrophys. 349 (1999) 11.

[23] F.W. Samuelson *et al.*, Ap.J. 501 (1998) L17.

[24] A. Djannati-Atai *et al.* Astron. Astrophys. 350 (1999) 17.

[25] Eli Waxman & John Bahcall, Phys. Rev. Letters 78 (1997) 2292.

[26] J. Rachen & P. Mészáros, Phys. Rev. D58 (1998) 123005.

[27] P. Mészáros & E. Waxman, astro-ph/0103275.

[28] A.K. Konopelko, J.G. Kirk, F.W. Stecker & A. Mastichiadis, Ap.J. 518 (1999) L13.

[29] W. Bednarek & R.J. Protheroe, Phys. Rev. Letters 79 (1997) 2616.

[30] R.J. Protheroe and T. Stanev, Phys. Rev. Lett. **77**, 3708 (1996) and Erratum **78**, 3420 (1997).

[31] G. Gelmini and A. Kusenko, Phys. Rev. Lett. **84**, 1378 (2000).

[32] M. Birkel and S. Sarkar, Astropart. Phys. **9**, 297 (1998).

[33] T. Weiler, Astropart. Phys. **11**, 303 (1999); D. Fargion, B. Mele and A. Salis, Astrophys. J. **517**, 725 (1999).

[34] D. Cline and F.W. Stecker, contributed to OWL/AW Neutrino Workshop on Observing Ultrahigh Energy Neutrinos, Los Angeles, California, Nov. 1999, astro-ph/0003459.

[35] V. Berezinsky, M. Kachelreiß and A. Vilenkin, Phys. Rev. Lett. **79**, 4302 (1997).

[36] J. Alvarez-Muñiz and F. Halzen, Phys. Rev. D **63**, 037302 (2001).

[37] F.W. Stecker et al., Phys. Rev. Lett., **66**, 2697 (1991).

[38] J. Alvarez-Muñiz and F. Halzen, First International Workshop on Radio Detection of High-Energy Particles (RADHEP 2000), Los Angeles, California, astro-ph/0102106

[39] Super-Kamiokande Collaboration, Y. Fukuda *et al.*, Phys. Rev. Lett. 81 (1998) 1562.

[40] Sudbury Neutrino Observatory (SNO) Collaboration, Q.R. Ahmad *et al.*, submitted to Phys. Rev. Lett. (nucl-ex/0106015).

[41] J.G. Learned and S. Pakvasa, Astrop. Phys. 3 (1995) pp 267-274.

[42] F. Halzen & D. Saltzberg, Phys. Rev. Letters 81 (1998) 4305.

[43] H. Athar, G. Parente & E. Zas, Phys. Rev. D62 (2000) 093010.

[44] A.P. Szabo & R.J. Protheroe, Astropart. Phys. 2 (1994) 375.

[45] J. Edsjo, WIMP searches with IceCube, Amanda Internal report, Jan.7, 2000.

[46] J. Bahcall and P. Meszaros, hep-ph/0004019.

[47] AMANDA supernova search paper, A. Bouchta et al.

[48] see K.Scholberg, Nucl.Phys.Proc.Suppl. 91 (2000) 331-337.

[49] A. Loeb and E. Waxman, astro-ph/0007049.

[50] T.K. Gaisser, F. Halzen, T. Stanev, Phys. Rep. 258 (1995) 173.

[51] F.W. Stecker, O.C. de Jager, Astron. Astrophys. **334**, L85 (1998).

[52] E.N. Parker, Astrophys. J. **160** (1970) 383.

[53] E. Andrés *et al.* (AMANDA Collaboration), Astropart. Phys. 13 (2000) 1–20.

[54] E. Andrés et al. (The AMANDA Collaboration), *Nature* **410** (2001) 441.

[55] Bai et al., Proceedings of 27th Int. Conf. on Cosmic Rays, Hamburg 2001.

[56] T. R. DeYoung, Observation of atmospheric neutrinos with AMANDA, Dissertation, University of Wisconsin-Madison, April 2001

[57] Ch. Wiebusch, Muon Reconstruction with AMANDA, DESY-PROC 1999-01, July 1999

[58] G. C. Hill, proceedings of the XXXVIth Recontres de Moriond, Electroweak Interactions and Unified Theories, March 2001.

[59] V. Agrawal, T. Gaisser, P. Lipari, and T. Stanev, Phys. Rev. D53 (1996) 1314.

[60] Nellen, L., Mannheim, K., & Biermann, P.L. Neutrino Production through Hadronic Cascades in AGN Accretion Disks. Phys. Rev. D47, 5270-5274 (1993).

[61] W. Bednarek and R. J. Protheroe, Mon. Not. Roy. Astro. Soc. 287(1997) 560.

[62] S. Colafrancesco, and P. Blasi, Astropart. Physics 9 (1998) 219

[63] Stecker, F.W. & Salamon, M.H. High-Energy Neutrinos from Quasars. Space Sci. Rev. 75, 341-355 (1996).

[64] T.K. Gaisser, R.J. Protheroe, and T. Stanev, Ap. J. 492 (1998) 219.

[65] E. Andrés et al. (The AMANDA Collaboration), Proceedings of Neutrino 2000 Conference, Sudbury, e-print: astro-ph/0009242.

[66] Bolesta J.W. et al., Proc. 25-th ICRC, Durban South Africa, 7:29 (1997)

[67] Porrata et al., Proc. 25-th ICRC, Durban South Africa, 7:9 (1997)

[68] Rhode W. et al. (Frejus-Coll.), AstroPart. Phys. 4:217 (1996)

[69] Protheroe RJ, astro-ph/9809144 (1998)

[70] C.Spiering, Nucl.Phys.Proc.Suppl. 91 (2000) 445-452.

[71] Balkanov,V.A. et al., Astropart. Phys. 14, 61-67 (2000). See also http://www-zeuthen.desy.de/baikal/baikalhome.html.

[72] Nucl.Phys.Proc.Suppl. **87** (2000) 436-438. See also http://antares.in2p3.fr/.

[73] G.V.Domogatsky (for BAIKAL Collaboration), Nucl. Phys. Proc. Suppl. **91** (2000) 438-444.

[74] See http://www.nestor.org.gr/.

[75] Zh.-A. Dzhilkibaev (for BAIKAL Collaboration), these proceedings, Int. Conf. on Neutrino Telesopes, Venice, 2001, astro-ph/0105269.

[76] Waxman, E. & Bahcall, J.N. High-Energy Neutrinos from Cosmological Gamma Ray Burst Fireballs. Phys. Rev. Lett. 78, 2292-2295 (1997).

[77] Waxman, E. & Bahcall, J.N. High Energy Neutrinos from Astrophysical Sources: An Upper Bound. Phys. Rev. D59, 023002 (1999).

[78] E. Waxman and J.N. Bahcall, Phys. Rev. Lett. **78**, 2292 (1997).

[79] AMANDA Collaboration (Bai et al.), Sep 2000. 7pp. Contrib. to the proc. of 3rd Int. Workshop on the Identification of Dark Matter (IDM2000), York, England, 18-22 Sep 2000. e-Print: astro-ph/0012285

[80] Paper in preparation.

[81] Ahrens et al. (AMANDA collaboration), Search for Supernova Neutrino Bursts with the AMANDA detector, accepted for publication, AstroParticle Physics, April 2001.

[82] http://www-zeuthen.desy.de/nuastro/publications/others/proposal.shtml

[83] http://www.ssec.wisc.edu/a3ri/icecube/proposal/

[84] http://www-zeuthen.desy.de/nuastro/

[85] *The Origin of Cosmic Rays*, V.L. Ginzburg & S.I. Syrovatskii (Pergamon Press, 1964).

[86] M. Nagano *et al.* J. Phys. G10 (1984) 1295.

[87] Yu. A. Fomin *et al.*, Proc. 22nd Int. Cosmic Ray Conf. (Dublin) vol. 2 (1991) 85.

[88] M. Takeda *et al.*, Phys. Rev. Lett. 81 (1998) 1163.

[89] M.A. Lawrence, R.J.O. Reid & A.A. Watson, J. Phys. G17 (1991) 733.

[90] M.I. Pravdin *et al.*, Proc. 26th Int. Cosmic Ray Conf. (Salt Lake City, 1999) vol. 3, p. 292.

[91] D.J. Bird *et al.*, Astrophys. J. 424 (1994) 491.

[92] E.G. Berezhko & H.J. Völk, Astroparticle Phys. 7 (1997) 183.

[93] T.K. Gaisser, F. Halzen, T. Stanev, Phys. Rep. 258 (1995) 173.

[94] E. Waxman & J. Bahcall, Phys. Rev. D 59 (1999) 023002.

[95] P.Lipari, Astropart. Phys. 1 (1993) 195-227.

[96] G.R. Farrar & T. Piran, Phys. Rev. Letters 84 (2000) 3527.

[97] T. K. Gaisser, to be published in Proceedings of the International Workshop on Observing Ultra-high energy Cosmic Rays from Space and Earth (Metepec, Puebla, Mexico, August 9-12, 2000), astro-ph/0011525.

[98] T.K. Gaisser, Talk given at the OECD Megascience Forum Workshop, Taormina, Sicily, 22/23 May, 1997, astro-ph/9707283.

[99] Mannheim, Protheroe & Rachen, Phys.Rev. D63 (2001) 023003, astro-ph/9812398; J.P. Rachen, R.J. Protheroe & K. Mannheim, Comment presented at the 19th Texas Symposium, Paris, December 1998, astro-ph/9908031.

[100] J. Alvarez-Muñiz and F. Halzen, Phys. Rev. D **63**, 037302 (2001).

[101] L.V. Volkova, Yad. Fiz. **31**, 1510 (1980) [Sov. J. Nucl. Phys. **31**, 784 (1980)].
(1999).

[102] D. Cline and F.W. Stecker, science white paper from UCLA Workshop on High Energy Neutrino Astrophysics, astro-ph/0003459.

[103] R.J. Protheroe and T. Stanev, Phys. Rev. Lett. **77**, 3708 (1996) and Erratum **78**, 3420 (1997).

[104] G. Gelmini and A. Kusenko, Phys. Rev. Lett. **84**, 1378 (2000).

[105] *The Detection of Faint Light in Deep Underwater Neutrino Telescopes*, C. Wiebusch, Ph.D. Thesis, PITHA 95/37, RWTH Aachen, Dec. 1995.

[106] M. Birkel and S. Sarkar, Astropart. Phys. **9**, 297 (1998).

[107] Supernova Neutrino-Burst Detection with the AMANDA Detector, to be published.

[108] F. Halzen, J.E. Jacobsen: Possibility that High Energy Neutrinos Telescopes could detect Supernovae, Phys. Rev. D49, 1758 (1994).

[109] K. Scholberg, SNEWS: the Supernova Early Warning System, Conference proceedings paper of the 3rd Amaldi Conference on Gravitational Waves, astro-ph/9911359.

[110] Christian Weinheimer and Lutz Köpke, AMANDA internal note 20000203.

[111] Marc Hellwig et al., AMANDA internal note 20010301.

[112] T. Neunhöffer for the AMANDA Collaboration, contributed paper to ICRC 2001.

[113] P. Bauleo et al., UV-enhancement of photomultiplier response, a study of wavelength shifters for the AMANDA/IceCube detector, August 99.

[114] J.F. Beacom and P. Vogel, Phys. Rev. D60, 33007 (1999).

[115] T. Weiler, Astropart. Phys. **11**, 303 (1999); D. Fargion, B. Mele and A. Salis, Astrophys. J. **517**, 725 (1999).

[116] V. Berezinsky, M. Kachelreiß and A. Vilenkin, Phys. Rev. Lett. **79**, 4302 (1997).

[117] F.W. Stecker et al., Phys. Rev. Lett., **66**, 2697 (1991).

[118] J.G. Learned and S. Pakvasa, Astrop. Phys. 3 (1995) pp 267-274.

[119] H. Athar, G. Parente and E. Zas, in preparation.

[120] I.Belolaptikov et al., Astropart.Phys. 7 (1997) 263.

[121] J.Edsjo, WIMP searches with IceCube, Amanda Internal report, Jan.7, 2000.

[122] K.Dick et al., Nucl.Phys. B588 (2000) 101-109 and Nucl.Phys. B598 (2001) 543-553.

[123] J.G.Learned, K.Mannheim, High Energy Neutrino Astrophysics, Ann.Rev.Nucl.Phys. (2000).

[124] M.Leuthold, Proc.Simulation and Analysis Methods for Large Neutrino Telescopes, DESY Zeuthen, 1998, DESY-PROC-1999-01 (ed. C.Spiering), 484.

[125] M.Leuthold, IceCube Performance Studies, Amanda Internal Report, Nov.1999.

[126] J.Krabi, C.Spiering et al., preprint PHE 91-03, Zeuthen 1991.

[127] E. Waxman & J. Bahcall, Phys. Rev. Lett. 78 (1997) 2292.

[128] E. Waxman & J. Bahcall, Phys. Rev. D 59 (1999) 023002.

[129] C.Hettlage and K.Mannheim, to appear in the Proceedings of the XXIst Moriond Workshop *Very High Energy Phenomena in the Universe*, Les Arcs, France, January 20-27 2001, astro-ph/0103499

[130] T.Gaisser, to be published in Proceedings of the International Workshop on Observing Ultra-high energy Cosmic Rays from Space and Earth (Metepec, Puebla, Mexico, August 9-12, 2000), astro-ph/0011525.

[131] P. L. Biermann *et al.*, Nucl. Phys. Proc. Suppl. 87 (2000) 417, astro-ph/0008063

[132] G.C. Hill, K. Rawlins, Amanda Internal Report

[133] G.C. Hill Astropart. Phys. 6 (1997) 215.

[134] G.C. Hill. *PhD thesis, University of Adelaide* (1996)

[135] G.C. Hill &. K. Rawlins *Presentation at NSF Hartill Icecube Review*, June 2000

[136] A.Hillas et al., Astrophys.J. 503, 744.

[137] T.Weekes, to be included in proceedings of the International Symposium on High Energy Gamma-Ray Astronomy, Heidelberg, June 2000, astrop-ph/0010431.

[138] K.Wang et al., A survey of the Northern sky for TeV point sources, astro-ph/0103353

[139] M.Leuthold, C.Spiering, H.Wissing, Amanda Internal Report.

[140] G.Feldman, J.Cousins, Phys.Rev. D57 (1998) 3873.

[141] S.Barwick, HENAP meeting (Venice, Feb. 2001), Amanda collaboration meeting in March 2001.

[142] S.Hundertmark, Amanda collaboration meeting in Oct. 2000.

[143] P.Meszaros and E.Waxman, astro-ph/0103275.

[144] D.Guetta, Review talk, to appear in the Proc. of the XXIst Rencontres de Moriond "Very High Energy Phenomena in the Universe", Les Arcs, France, Jan. 20-27 (2001), astro-ph/0104045.

[145] C.Schuster, M.Pohl, R.Schlickeiser, Neutrinos from AGN as diagnostic tool, submitted to A&A

[146] E.Waxman, submitted to PRL, astro-ph/0102317.

[147] T.Weiler, submitted to Astro. Part. Phys, astro-ph/0001233.

[148] D.Bakari et al., hep-ex/0004019.

[149] G.Giacomelli and L.Patrizii, Lecture at the Fifth School on Non-Accelerator Particle Astrophysics, Trieste, 29 June - 10 July 1998, hep-ex/0002032.

[150] E.Andres et al., Astropart.Phys.13 (2000) 1.

[151] see report on neutrino analysis on Zeuthen IceCube webpage.

[152] C.Spiering, Nucl.Phys.Proc.Suppl. 91 (2000) 445-452.

[153] L.Köpke and C.Weinheimer, Amanda Internal report.

[154] K.Scholberg, Nucl.Phys.Proc.Suppl. 91 (2000) 331-337.

[155] Pierre Auger Observatory, see `http://www.auger.org/`.

[156] J.E. Dickinson *et al.*, NIM **A440** (2000) 95.

[157] D. Nygren et al., Digital Optical Module & System Design for a km-Scale Neutrino Detector in Ice, LBNL INPA Internal Report, March 20, 1998.

[158] R. G. Stokstad, RAP - A Method for Absolute Time Calibration of a Large Array based on a digital Optical Module System, LBNL-43200, October 9, 1998.

[159] R. G. Stokstad, Consequences of a Local Coincidence for a Large Array in Ice, LBNL-41476, May 1998.

[160] J. Jacobsen and R. G. Stokstad, Consequences of a Local Coincidence for a Large Array in Ice II: Local Coincidences in AMANDA B-10 1997 Data, LBNL INPA Internal Report, October 9, 1998.

[161] J. Jacobsen and R. G. Stokstad, Consequences of a Local Coincidence for a Large Array in Ice III: Monte Carlo Simulations, LBNL INPA Internal Report, October 24, 1998.

[162] See `http://www.rational.com/products/rose` for details about the Rational Rose model-driven software development system.

[163] See `http://www.sf.net` for details about the Sourceforge software development system.

[164] See `http://cedar.web.cern.ch/CEDAR/` for details about the EDMS document handling system.

[165] For Gaudi documentation, see `http://proj-gaudi.web.cern.ch/proj-gaudi`.